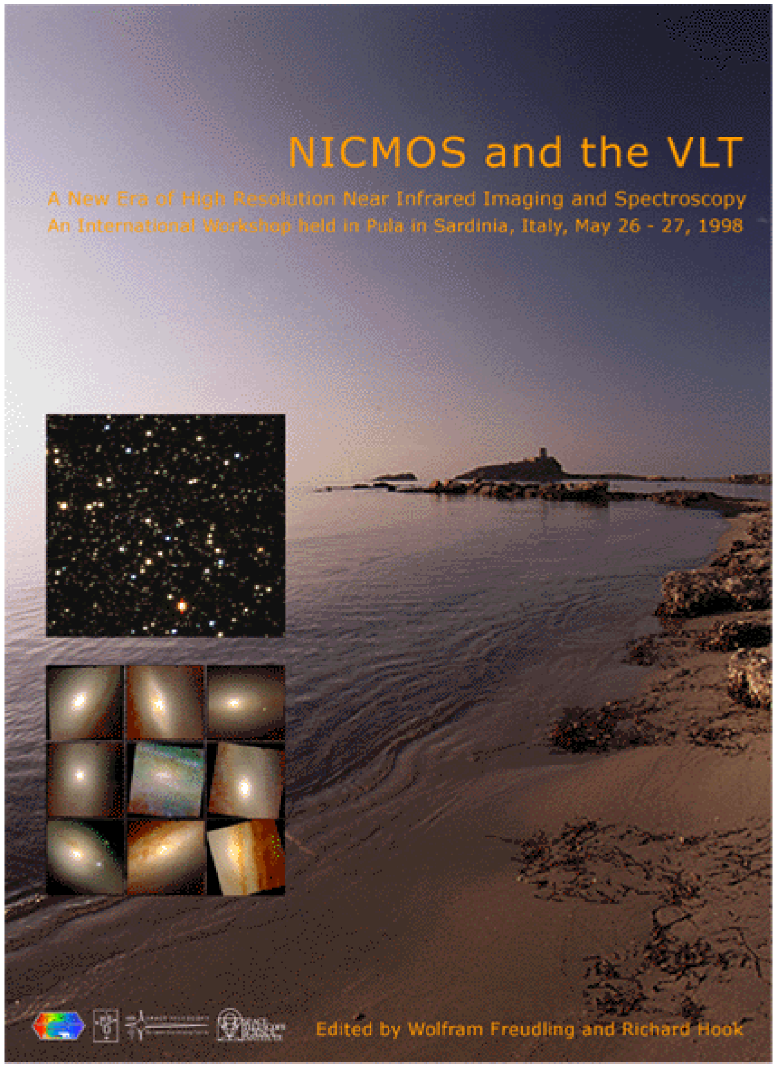

NICMOS and the VLT

A New Era of High Resolution Near Infrared Imaging and Spectroscopy

An International Workshop held in Pula, Sardinia, Italy
May 26-27, 1998
Edited by Wolfram Freudling and Richard Hook
PDF version by Norbert Pirzkal

ESO Conference and Workshop Proceedings No.55

EUROPEAN SOUTHERN OBSERVATORY
Karl-Schwarzschild-Str. 2, D-85748 Garching, Germany

ISBN 3-923524-58-7

Cover Illustration: The background image used on the cover is taken from a photograph by Bob Fosbury showing the bay in Sardinia close to where the conference took place. It is reproduced at far lower resolution than the original. The upper insert is one of the ESO VLT firstlight images and is a true colour view of the core of the globular cluster Messier 4. It was constructed from 2 minute exposures taken on 22nd May 1998 and reaches a limiting B magnitude of about 24 in 0.53 arcsec seeing. More details of the VLT first light are given on page 2. The lower insert is taken from the paper of Peletier et al. (page 162) and shows multi-colour NICMOS/WFPC2 imaging of the bulges of nearby galaxies. It is used by permission of the authors.

Contents

Preface

On May 26 & 27, 1998, about 50 participants met for the workshop “NICMOS and the VLT” in Pula, Sardinia, Italy. The goal of the workshop was to review what has been achieved with the Near Infrared and Multi Object Spectrograph (NICMOS) on board of HST, what can be achieved in the remaining lifetime of the instrument, and how NICMOS observations can be optimized taking into account the availability of IR imaging and spectroscopy on ESO’s Very Large Telescope (VLT) in the near future. The workshop took place at a time when the expected remaining lifetime of NICMOS was about 7 months, and the first call for proposals for VLT was about 3 month away. The timeliness of the workshop was underlined by the fact that first light for the VLT occurred in the midst of this meeting, which has not been anticipated at the time the date for the workshop was set. Also at the time of the workshop, the prospects for extending the lifetime of NICMOS through the installation of a cryo-cooler have improved enough to warrant a serious consideration of this possibility. A technical expert presentation on this topic was also given at the workshop and is published here.

Considerable NICMOS expertise was present through the participation of a large fraction of the the NICMOS IDT as well as the STScI and ST-ECF NICMOS groups. On the VLT side, the IR instrumentation was presented by the ESO head of IR instrumentation and news of the VLT first light was brought directly from the ESO headquarters in Garching. The presence of experts as well as the pleasant atmosphere of the workshop fostered numerous discussions outside the formal program.

From the beginning, our plan was to publish proceedings of this workshop very shortly after the workshop. The interesting and timely presentations given during the meeting strengthen the case for distributing them in written form as soon as possible. These proceedings will now be mailed less than two months after the workshop. This achievement was made possible by the cooperation of the authors who contributed to this volume, the hard work of Britt Sjoeberg the workshop secretary, a fast cover design from Ed Janssen and help with the printing arrangements from Kurt Kjär at ESO. The Astronomical Society of the Pacific and Harry Payne at STScI also allowed us to use their LaTeX style files and other software to ease the preparation of this volume. Bob Fosbury made available several beautiful high quality photographs of the meeting and its surroundings which appear within this volume and on the cover, although regrettably in much poorer quality reproductions. Norbert Pirzkal provided invaluable help in reformatting and checking some papers.

We would like to thank them all.

Garching, June 1998
Wolfram Freudling (Workshop Chair) & Richard Hook (Principal Editor)

Participant List

Alessandra Aloisi, Osservatorio Astronomico di Bologna, Via Zamboni 33, I-40126 Bologna, Italy (aloisi@astbo3.bo.astro.it)

Almudena Alonso-Herrero, University of Arizona, Steward Observatory, 933 N. Cherry Avenue, Tucson, AZ 85721, USA (aalonso@as.arizona.edu)

Eric Becklin, University of California at Los Angeles, Astronomy and Astrophysics; Dept. of Physics, 405 Hilgard Ave., Los Angeles, CA 90095-1547, USA (becklin@sofia.astro.ucla.edu)

Piero Benvenuti, ST-ECF, Karl-Schwarzschild-Str. 2, D-85748 Garching, Germany (pbenvenu@eso.org)

Peter Bizenberger, Max-Planck-Institut für Astronomie, Königstuhl 17, D-69117 Heidelberg, Germany (biz@mpia-hd.mpg.de)

John Black, Onsala Space Observatory, S-439 92 Onsala, Sweden (jblack@oso.chalmers.se)

Andrew Bunker, University of California at Berkeley, Department of Astronomy, 601 Campbell Hall, Berkeley, CA 94720-3411, USA (bunker@bigz.berkeley.edu)

Howard Bushouse, Space Telescope Science Institute, Science Software Group, 3700 San Martin Drive, Baltimore, MD 21218, USA (bushouse@stsci.edu)

Luis Colina, Space Telescope Science Institute, 3700 San Martin Drive, Baltimore, MD 21218, USA (colina@stsci.edu)

Michael Corbin, University of Arizona, Steward Observatory, 933 N. Cherry Avenue, Tucson, AZ 85721-0065, USA (mcorbin@as.arizona.edu)

Guido De Marchi, European Southern Observatory, Science Office, Karl-Schwarzschild-Str. 2, D-85748 Garching, Germany (demarchi@eso.org)

Nadine Dinshaw, University of California, Santa Cruz, Lick Observatory, Santa Cruz, CA 95064, USA (nadine@ucolick.org)

Christophe Dumas, Jet Propulsion Laboratory, MS 183-501, 4800 Oak Grove Drive, Pasadena, CA 91109, USA (dumas@nicmos.jpl.nasa.gov)

Robert Fosbury, ST-ECF, Karl-Schwarzschild-Str. 2, D-85748 Garching, Germany (rfosbury@eso.org)

Wolfram Freudling, ST-ECF, Karl-Schwarzschild-Str. 2, D-85748 Garching, Germany (wfreudli@eso.org)

Donald Hall, University of Hawaii, Institute for Astronomy, 2680 Woodlawn Drive, Honolulu, HI 96822-1839, USA (hall@ifa.hawaii.edu)

John Hill, University of Arizona, Steward Observatory, 933 N. Cherry Avenue, Tucson, AZ 85721, USA (jhill@as.arizona.edu)

Dean C. Hines, University of Arizona, Steward Observatory, 933 N. Cherry Avenue, Tucson, AZ 85721, USA (dhines@as.arizona.edu)

Richard Hook, ST-ECF, Karl-Schwarzschild-Str. 2, D-85748 Garching, Germany (rhook@eso.org)

Rachel Johnson, Institute of Astronomy, Madingley Road, Cambridge, CB3 0HA, United Kingdom (raj@ast.cam.ac.uk)

Marek Kukula, Space Telescope Science Institute, NICMOS / SSD, 3700 San Martin Drive, Baltimore, MD 21218, USA (kukula@stsci.edu)

Michael Lindqvist, Onsala Space Observatory, S-439 92 Onsala, Sweden (michael@oso.chalmers.se)

Patrick Lowrance, University of California at Los Angeles, Astronomy and Astrophysics; Dept. of Physics, 405 Hilgard Ave., Los Angeles, CA 90024, USA (lowrance@astro.ucla.edu)

John MacKenty, Space Telescope Science Institute, Science Support Division / NICMOS Group, 3700 San Martin Drive, Baltimore, MD 21218, USA (mackenty@stsci.edu)

Juan-Manuel Martín-Fleitas, GTC Project, Via Lactea, s/n, E-38200 La Laguna, Spain (jmartin@ll.iac.es)

Patrick McCarthy, Carnegie Institution of Washington, The Observatories, 813 Santa Barbara Street, Pasadena, CA 91101, USA (pmc2@ociw.edu)

Roland Meier, University of Hawaii, Institute for Astronomy, 2680 Woodlawn Drive, Honolulu, HI 96822, USA (meier@uhifa.ifa.hawaii.edu)

Alan Moorwood, European Southern Observatory, Infrared Instruments and Detectors, Karl-Schwarzschild-Str. 2, D-85748 Garching, Germany (amoor@eso.org)

Anna Pasquali, ST-ECF, Karl-Schwarzschild-Str. 2, D-85748 Garching, Germany (apasqual@eso.org)

Reynier Peletier, University of Durham, Department of Physics, South Road, Durham, DH1 3LE, United Kingdom (R.F.Peletier@dur.ac.uk)

Norbert Pirzkal, ST-ECF, Karl-Schwarzschild-Str. 2, D-85748 Garching, Germany (npirzkal@eso.org)

Marcia Rieke, University of Arizona, Steward Observatory, 933 N. Cherry Avenue, Tucson, AZ 85721, USA (mrieke@as.arizona.edu)

Werner Schmutz, ETH Zürich, Institut für Astronomie, CH-8092 Zürich, Switzerland (schmutz@astro.phys.ethz.ch)

Glenn Schneider, University of Arizona, Steward Observatory, 933 N. Cherry Avenue, Tucson, AZ 85721-0065, USA (gschneider@as.arizona.edu)

Ethan Schreier, Space Telescope Science Institute, 3700 San Martin Drive, Baltimore, MD 21218, USA (schreier@stsci.edu)

Nick Scoville, California Institute of Technology, Astronomy 105-24, Pasadena, CA 91125, USA (nzs@astro.caltech.edu)

Ralf Siebenmorgen, ESA Satellite Tracking Station, Infrared Space Observatory, Villafranca del Castillo; P.O. Box 50727, E-28080 Madrid, Spain (rsiebenm@iso.vilspa.esa.es)

David Silva, European Southern Observatory, Data Management and Operations, Karl-Schwarzschild-Str. 2, D-85748 Garching, Germany (dsilva@eso.org)

Bradford Smith, University of Hawaii, Institute for Astronomy, 82-6012 Pu'uhonua Road, Napo'opo'o, HI 96704-8226, USA (brad@mahina.ifa.hawaii.edu)

William Sparks, Space Telescope Science Institute, NICMOS / SSD, 3700 San Martin Drive, Baltimore, MD 21218, USA (sparks@stsci.edu)

Elizabeth Stobie, University of Arizona, Steward Observatory, 933 N. Cherry Avenue, Tucson, AZ 85721, USA (bstobie@as.arizona.edu)

Susan Stolovy, University of Arizona, Steward Observatory, 933 N. Cherry Avenue, Tucson, AZ 85721, USA (sstolovy@as.arizona.edu)

Lisa Storrie-Lombardi, Carnegie Observatories, 813 Santa Barbara St., Pasadena, CA 91101, USA (lisa@ociw.edu)

Richard Terrile, Jet Propulsion Lab., Earth and Space Science, Mail Stop 183-501, Pasadena, CA 91109, USA (rich.terrile@jpl.nasa.gov)

Rodger Thompson, University of Arizona, Steward Observatory, Tucson, AZ 85721, USA (rthompson@as.arizona.edu)

Ray Weymann, Carnegie Institution, Observatories, 813 Santa Barbara Street, Pasadena, CA 91101, USA (rjw@ociw.edu)

Hans Zinnecker, Astrophysikalisches Institut Potsdam, An der Sternwarte 16, D-14482 Potsdam-Babelsberg, Germany (hzinnecker@aip.de)

Figure 1. Some of the participants enjoying the relaxed Mediterranean atmosphere

Part 1. VLT Status and Instruments

NICMOS and the VLT
Pula, Sardinia, May 26-27th 1998
Wolfram Freudling and Richard Hook, eds.

VLT First Light

Abstract. First light for the ESO VLT unit telescope 1 occurred during the workshop. David Silva, head of the ESO user support, brought the news and associated press release information directly from ESO headquarters in Garching. Some of the ESO press releases which demonstrate the working of the VLT UT1 are reprinted here.

1. Omega Centauri Tracking Test

Omega Centauri is the most luminous globular cluster in our Galaxy. As the name indicates, it is located in the southern constellation Centaurus and is therefore observable only from the south.

The image shown (Figure 1) here was obtained with the VLT on May 16, 1998, in red light (R band), i.e. while the mirror was still uncoated. It is a 10-minute exposure of the center of Omega Centauri and it demonstrates that the telescope is able to track continuously with a very high precision and thus is able to take full advantage of the frequent, very good atmospheric conditions at Paranal. The images of the stars are very sharp (full-width-at-half-maximum (FWHM) = 0.43 arcsec) and are perfectly round, everywhere in the field. This indicates that the tracking was accurate to better than 0.001 arcsec/sec during this observation.

At a distance of about 17,000 light years, this cluster is barely visible to the naked eye as a very faint and small cloud. When Omega Centauri is observed through a telescope, even a small one, it looks like a huge swarm of numerous stars, bound together by their mutual gravitational attraction.

Most globular clusters in our Galaxy have masses of the order of 100,000 times that of the Sun. With a total mass equal to about 5 million solar masses, Omega Centauri is by far the most massive of its kind in our Galaxy.

2. Image Quality of the VLT

Superb image quality is the prime requirement for the VLT. The VLT should take full advantage of the exceptionally good "seeing" conditions of the Paranal site, i.e. moments of a particularly stable atmosphere above the site, with a minimum of air turbulence.

In this diagram (Figure 2), the measured image quality of the VLT UT1 astronomical images is plotted versus the "seeing", as measured by the Seeing Monitor, a small telescope also located on top of the Paranal Mountain.

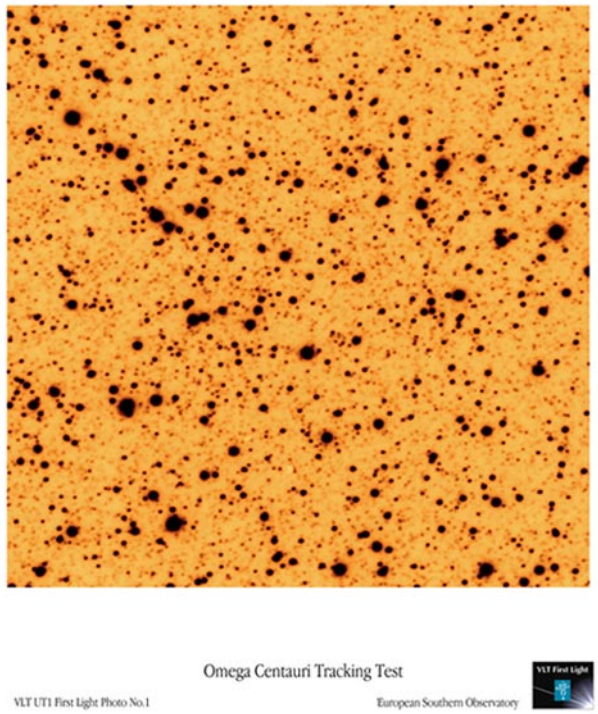

Figure 1. Omega Centauri Tracking Test

The dashed line shows the image quality requirement, as specified for the VLT at First Light. The dotted line shows the specification for the image quality, three years after First Light, when the VLT will be fully optimized. The fully drawn line represents the physical limit, when no further image distortion is added by the telescope to that introduced by the atmosphere.

The diagram demonstrates that First Light specifications have been fully achieved and, impressively, that the actual VLT performance is sometimes already within the more stringent specifications expected to be fulfilled only three years from now.

Various effects contribute to degrade the image quality of a telescope as compared to the local seeing, and must be kept to a minimum in order to achieve the best scientific results. These include imperfections in the telescope optical mirrors and in the telescope motion to compensate for Earth rotation during an exposure, as well as air turbulence generated by the telescope itself. The tight specifications shown in this figure translate into very stringent requirements concerning the quality of all optical surfaces, the active control of the 8.2-m mirror, the accuracy of the telescope motions, and, in the near future, the fast “tip-tilt” compensations provided by the secondary mirror, and finally the thermal control of the telescope and the entire enclosure.

The only way to achieve an image quality that is “better than that of the atmosphere” is by the use of Adaptive Optics devices that compensate for the atmospheric distortions. One such device will be operative on the VLT by the year 2000, then allowing astronomers to obtain images as sharp as about 0.1 arcsec.

In this diagram, both seeing and telescope image quality are measured as the full-width-at-half-maximum (FWHM) of the light-intensity profile of a point-like source. The uncertainty of the measurements is indicated by the cross in the lower right corner.

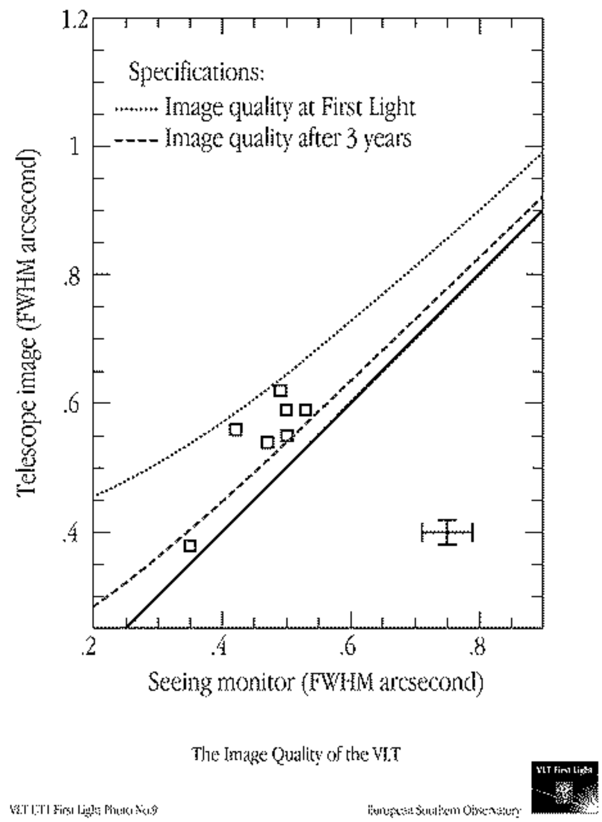

Figure 2. Image Quality of the VLT

3. Total Optical Control

The VLT active optics system fully controls the primary and secondary mirrors. In figure 3, images of stars are shown that were obtained during tests in which the control system forced the optical elements to produce three different image aberrations, namely triangular, round (defocus) and linear (astigmatism). This is done by applying different forces to each of the 150 individual active actuators on which the 8.2-m main mirror rests and to the position of the secondary mirror. In the case of the triangular aberration, the mirror was made to resemble Napoleon's hat. It is worth noting that the deviation of the mirror from its optimum shape is only 0.015 millimeters.

The great power of this system is demonstrated by the fact that the resulting stellar images can take on (nearly) any desired form. The optical system is also consistently brought back to its optimal form, producing the sharp images of a real star, shown in the lower row.

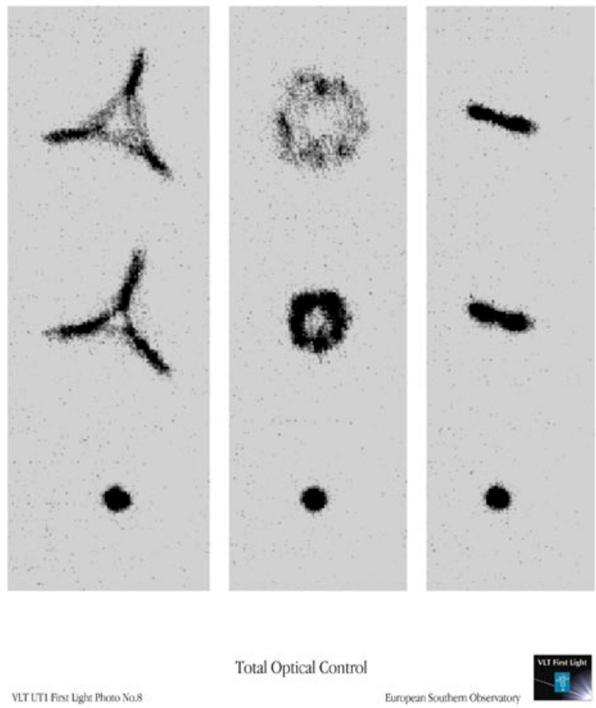

Figure 3. Total Optical Control

The control of the two mirrors is such that no significant aberrations remain after the corrections are applied. The accuracy of the control of shape of the primary mirror results in an average error of order 0.00005 millimeters. The telescope is only limited by the Earth's atmosphere. In space, the optical quality of the mirrors under active control could be diffraction limited.

NICMOS and the VLT
Pula, Sardinia, May 26-27th 1998
Wolfram Freudling and Richard Hook, eds.

Near IR Astronomy with the ESO VLT

Alan Moorwood

European Southern Observatory, Karl-Schwarzschild-Str. 2, D-85748 Garching

Abstract. The ESO VLT situated on Cerro Paranal in Chile comprises four 8.2m plus three 1.8m movable auxiliary telescopes providing 8 Nasmyth, 4 Cassegrain, and 1 incoherent combined focus plus a variety of interferometric options. First light was achieved with the first unit telescope (UT1) on 25th May 1998 with results which fully demonstrate the quality of both the telescope and the site. Six infrared instruments for the unit telescope foci plus three for interferometry are at various phases of design and development. Together, they provide for direct imaging in wide fields; diffraction limited imaging with adaptive optics and interferometry; polarimetry; long slit, multi-object and integral field spectroscopy at resolving powers ranging from a few hundred to 10^5. The status and expected capabilities of these instruments is summarized together with a brief overview of the highest priority science goals which can be anticipated now.

1. Introduction and Overview

ESO's VLT situated on Cerro Paranal in Chile comprises four 8.2m plus three 1.8m moveable auxiliary telescopes. In addition, the site will host a 2.5m wide field survey telescope to be built by the Capodimonte Observatory, Naples and operated by ESO. The site is dry; photometric more than 80% of the time and delivers a median seeing of 0.65 arcsec. The small telescopes can be combined with each other optically to form the VISA interferometer or with the large telescopes to form VIMA. The large telescopes can also be incoherently combined. Each of the large telescopes provides two Nasmyth and a Cassegrain focus. Of these twelve foci, eleven are planned to be equipped with 'common user' instruments and one will be reserved for innovative visitor instruments. UT1 will be equipped with a laser guide star system plus the NAOS Shack-Hartman adaptive optics system used with CONICA and the MACAO curvature sensing AO system to be used with SINFONI (and later interferometry and possibly CRIRES). Of the main instruments, three (ISAAC,UVES and CRIRES) plus MACAO are being developed by ESO and the rest by consortia of mostly, but not exclusively (e.g Australia is producing a fibre positioning unit) European Institutes. In the case of externally contracted instruments, ESO generally covers the capital cost while the Institutes provide manpower and expertise in exchange for guaranteed observing time. Even in the case of the subcontracted instruments, however, ESO is usually involved in the design and provides most of the detectors and part of the instrument control systems.

Current status of the project is that first light of the first 8.2m Unit Telescope was achieved on 25th May 1998. The FWHM $\simeq$ 0.32" visible images obtained and shown at this Workshop clearly demonstrate the excellent quality of both the telescope and the site. Science Verification with a visible test camera is planned for the second half of August after which the first major instrument, FORS (visible imaging, polarimetry, spectroscopy and MOS spectroscopy) will be installed. The first IR instrument, ISAAC (1-5μm imaging, polarimetry and spectroscopy), which has been built at ESO, will be installed in November 1998. Both of these instruments will be finally commissioned and used for Science Verification observations in early 1999 and made available to visiting astronomers in April 1999. With regard to the regular operation of the VLT it should be noted that ESO is also developing a complete data flow system comprising instrument simulators, software for pre-preparing observation/instrument sequences in the form of Observation Blocks, flexible scheduling software, data and calibration pipelines and an archive. At the beginning it is expected that about 50% of the observing will be performed by ESO in service mode and the rest with the visiting astronomer present at the Observatory.

For those interested, more comprehensive information on the VLT and its instruments can be found on ESO's Web Site (http://www.eso.org/instruments/).

2. Infrared instruments for the VLT

2.1. Instrument Summary

The already approved infrared instruments for the VLT are:

ISAAC: 1-5μm Infrared Spectrometer and Array Camera (P.I. A. Moorwood, ESO) which is currently undergoing final testing in Garching prior to shipment to Paranal in June for installation at UT1 in Nov 1998. A derivative 1-2.5μm instrument, SOFI, is already in operation at the 3.5m NTT telescope on La Silla (Moorwood, Cuby and Lidman, 1998, The Messenger, 91,9).

CONICA: Coude Near Infrared Camera (P.I. R. Lenzen, MPIA, Heidelberg) - an historical name as this instrument will be used for diffraction limited 1-5μm imaging, polarimetry and spectroscopy with the NAOS, Nasmyth Adaptive Optics System on UT1 (P.I. G. Rousset, ONERA). The two systems will be integrated in Europe in late 1999 and installed at the VLT in mid-2000.

SINFONI: Single Far Object Near IR Investigation (P.I. N. Thatte, MPIE, Garching) which will be used with the ESO developed MACAO AO system (P.I. D. Bonaccini, ESO) for integral field spectroscopy. SINFONI will be used by the MPIE first at Calar Alto and then transferred to the VLT in 2001.

NIRMOS: Near IR Multi-Object Spectrometer (P.I. O. Le Fèvre, LAS. Marseille) for 1-1.8μm wide field imaging and spectroscopy at R $\simeq$ 2500 of up to 170 objects simultaneously. This instrument is in the detailed design phase together with its twin visible instrument VIMOS. It will be installed in 2001.

CRIRES: Cryogenic IR Echelle Spectrometer (P.I. G. Wiedemann, ESO) for very high (10^5) resolution IR spectroscopy, probably in combination with a MACAO type curvature sensing AO system. Is in detailed design phase and with aim of exploiting many of the ISAAC technical developments. To be installed in 2002.

VISIR: VLT Mid Infrared Imager Spectrometer (P.I. P.-O. Lagage, SAp, Saclay) for 8-27μm imaging and spectroscopy.

A brief overview of the main instrumental modes is given in Table 1. Taken together, they cover a large fraction of the spatial and spectral resolution phase space with multi-object and integral field capabilities entering as major new modes opened up with the development of large format IR array detectors.

Table 1. VLT Infrared Instrument Modes

Name	$\lambda\lambda\mu$m	Pixel(“)	Field	Spectroscopy	MOS
ISAAC	1-5	0.07-0.5	2.5x2.5’	300-5000	-
CONICA	1-5	0.014 - 0.1	73” dia	300-1800	-
NIRMOS	1-1.8	0.2	14x14’	2500	170
SINFONI	1-2.5	0.035-0.25	10”	2500/6000	int. field
CRIRES	1-5	0.1	NA	10^5	no
VISIR	8-27	0.075 - 0.2	1x1’	100 - 2 10^4	no

In addition, three interferometric instruments are at the conceptual design stage - AMBER (1-2.5μm imaging/spectroscopy), MIDI(8-13μm) and PRIMA (2-5μm phase referenced imaging and astrometry).

2.2. IR Detectors

The infrared detectors to be used in the different instruments are summarized below.

- Rockwell 1-2.5μm 1024x1024 Hawaii (ISAAC, SINFONI)
- Rockwell 1-2.5μm 2048x2048 funded by University of Hawaii, SUBARU and ESO (4 in NIRMOS)
- SBRC 1-5μm 256x256 (ISAAC)
- SBRC 1-5μm 1024x1024 Aladdin (CONICA, ISAAC, 2-3 in CRIRES)
- SBRC 8-27μm 240x340 (VISIR)

In all cases, the IRACE acquisition system, developed by ESO initially for ISAAC will probably be used. It is a modular (nominally 32 channel) high speed (20 Mpix/s), low noise (limited by detector) system employing a GByte/sec link and an Ultrasparc processor for image pre-processing (Meyer et al., 1997, The Messenger, 86, 14). Although most modes will be background limited, it is expected that some modes involving the highest spatial and spectral resolution in the near infrared will reach the limits set by the intrinsic detector noise and dark current which are now at the incredible level of only a few e^- and around 20e^-/hour respectively as measured on Rockwell Hawaii arrays with IRACE.

2.3. Performance

It is beyond the scope of this article to reproduce the expected performance of all the instruments in all their modes. Typically, however, background limited imaging in the near infrared is expected to reach point source 3σ limits in 1 hr of around J = 25. H = 24 , Ks = 23 under the best seeing condition, and up to about 2 magnitudes fainter at the diffraction limit with AO. Continuum limits for medium resolution (R $\simeq$ 3000) spectroscopy are expected to be in the range 20-22 mag. but strongly wavelength dependent due to the OH sky lines. At this resolving power, however, a large fraction of the J and H bands can be observed between the strong OH lines allowing 1 hr line flux limits of a few x 10^{-18} erg cm^{-2} s^{-1}.

3. Science

The combined instrument complement of the VLT provides for a wide range of visible and infrared capabilities from deep imaging and spectroscopic surveys to high spatial and spectral resolution observations of individual objects using adaptive optics and interferometry. Science objectives are therefore expected to embrace much of contemporary astronomy and the following is only a brief summary of some of the currently envisaged science areas in which infrared observations are expected to be of particular importance.

Large scale structure. Surveys for high z clusters and evolution of structures at $z \leq 3$. Measurement of dynamics to constrain the formation epoch and distortions in the expansion field to map dark matter and the total mass density of the Universe. (NIRMOS, ISAAC).

Cosmological parameters. Distances from Cepheids and relative distances from fundamental plane and Tully - Fisher scaling relations and supernovae. Time delay in gravitationally lensed quasars. Refine values for H_0, q_0 and Λ (CONICA, SINFONI, ISAAC).

High redshift galaxies. Galaxy formation and evolution. Photometric redshift (in combination with visible) and emission line surveys (Ly_α, H_α, [OII]) plus follow-up spectroscopy to determine star formation rate as a function of z, size, morphology, mass (ISAAC, NIRMOS, CONICA, SINFONI).

Gamma-ray bursts. Spectroscopy of optical counterparts (ISAAC, CONICA, SINFONI).

Galaxy nuclei. Stellar populations/dynamics. Black hole masses. Test unified AGN theories. Quasar host galaxies. (CONICA, SINFONI, VISIR, VLTI).

Stars. Abundances, circumstellar shells, mass loss, magnetic fields (CRIRES, VISIR).

Star formation. Measure IMF to lowest masses in star forming clusters. Outflows and dynamics of protostellar discs (ISAAC, CONICA, SINFONI, CRIRES, VISIR).

Extrasolar planets. Direct detection by imaging and/or velocity modulation of planetary spectral features (CRIRES, CONICA, VISIR, VLTI).

Protoplanetary systems. Thermal imaging of protoplanetary discs (VISIR, CONICA, VLTI).

Solar system. Composition and dynamics of planetary atmospheres. Detection, chemistry and mineralogy of faint outer solar system bodies (ISAAC, CONICA, SINFONI, VISIR).

NICMOS and the VLT
Pula, Sardinia, May 26-27th 1998
Wolfram Freudling and Richard Hook, eds.

CONICA: The high resolution near-infrared camera for the ESO VLT

Peter Bizenberger, Rainer Lenzen, Heinrich Bellemann, Clemens Storz, Andreas Tusche, Karl Wagner

Max-Planck-Institut für Astronomie Königstuhl 17, 69117 Heidelberg, Germany

Reiner Hofmann

Max-Planck-Institut für Extraterrestrische Physik Gießenbachstr., 85748 Garching, Germany

Abstract. The high resolution near infrared camera (CONICA) for the first VLT unit telescope is under development. It serves as a multi-mode instrument for the wavelength region between 1.0 and 5.0 microns, providing diffraction-limited spatial resolution when combined with the adaptive optic system NAOS of the VLT (Rosset et al. 1998). CONICA offers broad band, narrow band and Fabry-Perot direct imaging capabilities, polarimetric modes using Wollaston prisms or wire-grid analyzers, as well as long-slit spectroscopy up to a spectral resolution of R $\approx$ 2400 per pixel. This paper describes the design and status of CONICA, focusing on the cryo-mechanics and optical performance and the resulting observational capabilities.

1. Introduction

The CONICA infrared camera is being built for diffraction limited observations in the spectral range from 1 - 5 μm. This camera is for use on the first unit of the VLT (ESO) and is built by a consortium of two institutes, the MPI für Astronomie (Heidelberg) and the MPI für Extraterrestrische Physik (Garching) with additional assistance from ESO. Combined with an adaptive optics system (NAOS) CONICA will offer diffraction-limited observing capabilities at an 8 m telescope. These capabilities include direct imaging, imaging spectroscopy, long slit spectroscopy and imaging polarimetry. The optics and cryo-mechanics are designed for implementation of an ALADDIN 1024 x 1024 InSb focal plan array (FPA). The imaging scale can be adapted for correct sampling of the wavelength dependent diffraction limited beam between about 14 and 55 mas/pixel, corresponding to fields of view between 14x14 and 56x56 arcsec respectively. The instrument will be completely remote controlled. The general design of CONICA has been presented in earlier publications (Lenzen & Hofmann 1995; Lenzen et al. 1998b), so this paper concentrates on the optical and cryo-mechanical design and the resulting observational capabilities.

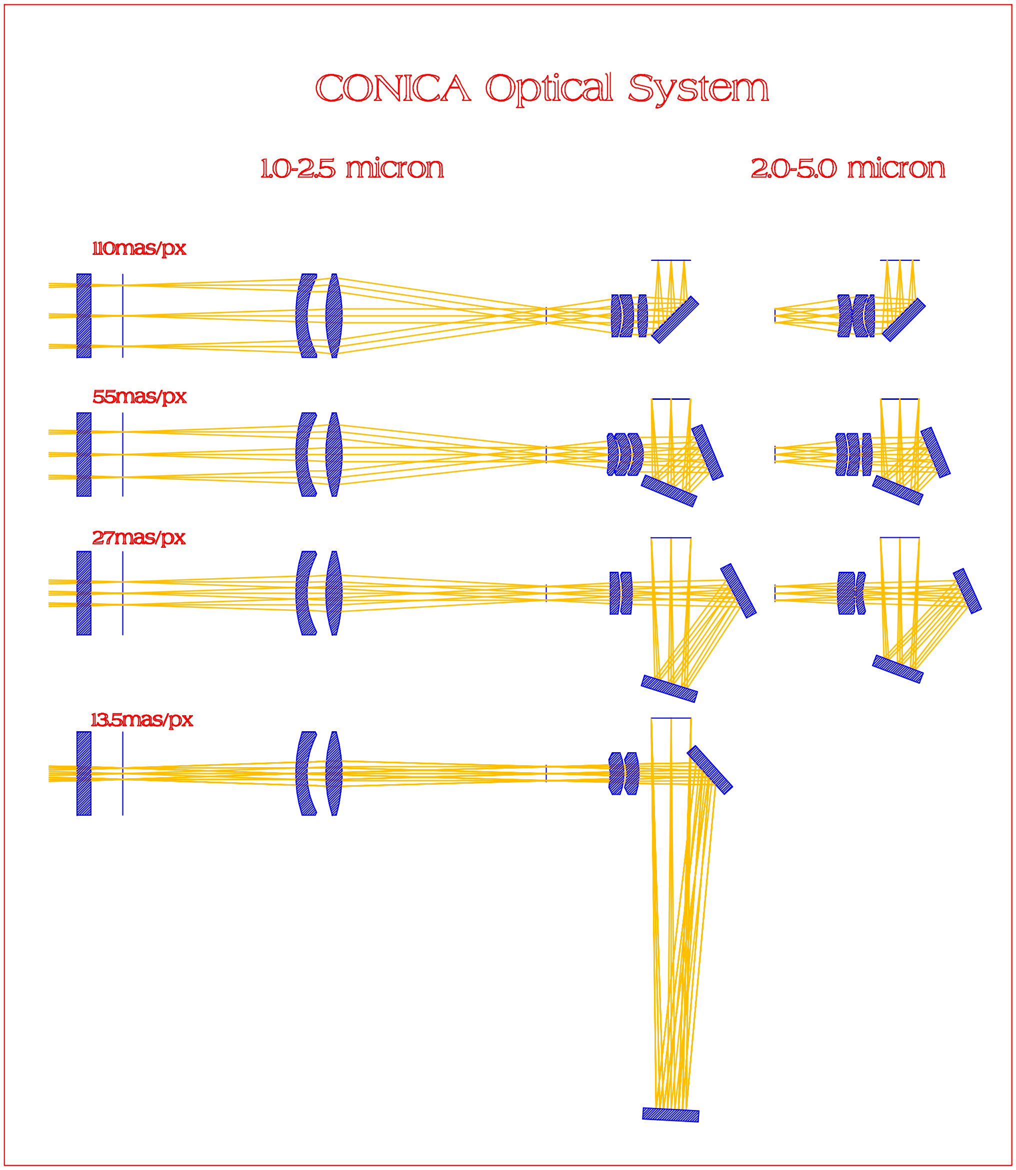

Figure 1. Overview of all CONICA camera systems

2. Design of Imaging Optics

In order to provide an double-sampling over the wavelength band from 1 - 5 μm, the imaging scale is designed to be variable. Three discrete image scales (13, 27 and 55 mas/pixel) sample the wavelengths of interest. These optics are designed to illuminate a 1024 x 1024 array with 27 μm pixel pitch without vignetting. A fourth set of camera optics is available for a larger pixel scale of about 110 mas/pixel which leads to a field of view of about 73 arcsec in diameter. For each scale (except the slowest camera) the camera systems are split in two wavelength regions, one for 1.0 - 2.5 μm and a second for 2.0 - 5.0 μm. Thus, there are seven imaging systems in total, all of which can be used within the K-band (Figure 1). The complete imaging optics are realized as a re-imaging system. Inside the cryostat, just behind the plane-parallel CaF_2 entrance window, lies the instrument focal plane. A number of field-limiting masks, slits, coronographic masks or special stripe masks for Wollaston applications can be inserted here. The beam is then collimated by an achromatic LiF/BaF_2 doublet giving a well collimated beam and a pupil image all over the wavelength region. Residual chromatic errors are compensated by the individual camera systems. Even though the whole optical system is achromatic, the detector position in the back focal plane of the optics can be remotely adjusted during operation.

3. Analyzing Optics

CONICA can take 40 filters (1 inch diameter), mounted close to the pupil position. A set of standard broad-band filters, as well as 15 individual narrow band filters are available. In addition, there is a set of blocking filters for the Fabry-Perot. All filters lie behind the pupil, so there is no shift of the pupil image due to different filter thickness. All filters are tilted by 6 degrees to avoid ghost images.

A cryogenic Fabry-Perot can be inserted into the collimated beam, giving spectroscopic imaging for all available imaging scales at a spectral resolution R $\approx$ 1800 within the K-band.

At present, three grisms of medium resolution R $\approx$ 350 - 2400 per pixel allow long-slit spectroscopy with diffraction limited spatial resolution. An additional grism is on order to cover the whole range of resolution for all wavelengths. Two of the grisms are direct ruled KRS5 for operation at longer wavelengths (up to 5 μm). The remaining two grisms are replica grisms for the wavelength range from 1.0 - 2.5 μm (Table 1)

For polarimetric applications two Wollaston prisms and four wire-grid analysers are mounted. Both types of analyzers are suitable for the whole wavelength range.

In front of the cooled camera, a tunable atmospheric dispersion compensator (TADC) at ambient temperature corrects the chromatic dispersion of the atmosphere for higher airmasses. Particularly for the J band a correction is essential, since the dispersion at an airmass of 2 is at the order of the diffraction limited FWHM at this wavelengths. For longer wavelengths, this effect is negligible, allowing the TADC to operate at ambient temperature.

All these analyzing components have been tested in an instrument very similar to CONICA. Since autumn 1997, an infrared camera called Omega Cass (Lenzen et al. 1998a) has been available at the 3.5 m telescope on Calar Alto in Spain. Omega Cass is equipped with the same capabilities as CONICA, including the adaptive optic system ALFA (Hippler et al. 1998). The only difference to CONICA is the smaller telescope and the reduced operating wavelength range of 1.0 - 2.5 μm of the HgCdTe detector array.

4. Cryo-mechanical Design

Since CONICA will be sensitive up to the thermal NIR region of 5.0 μm the whole imaging and analyzing optics are cooled below 80 K (except the TADC). The radiation shield and the internal cryogenic structure are thermally coupled to the first stage of a

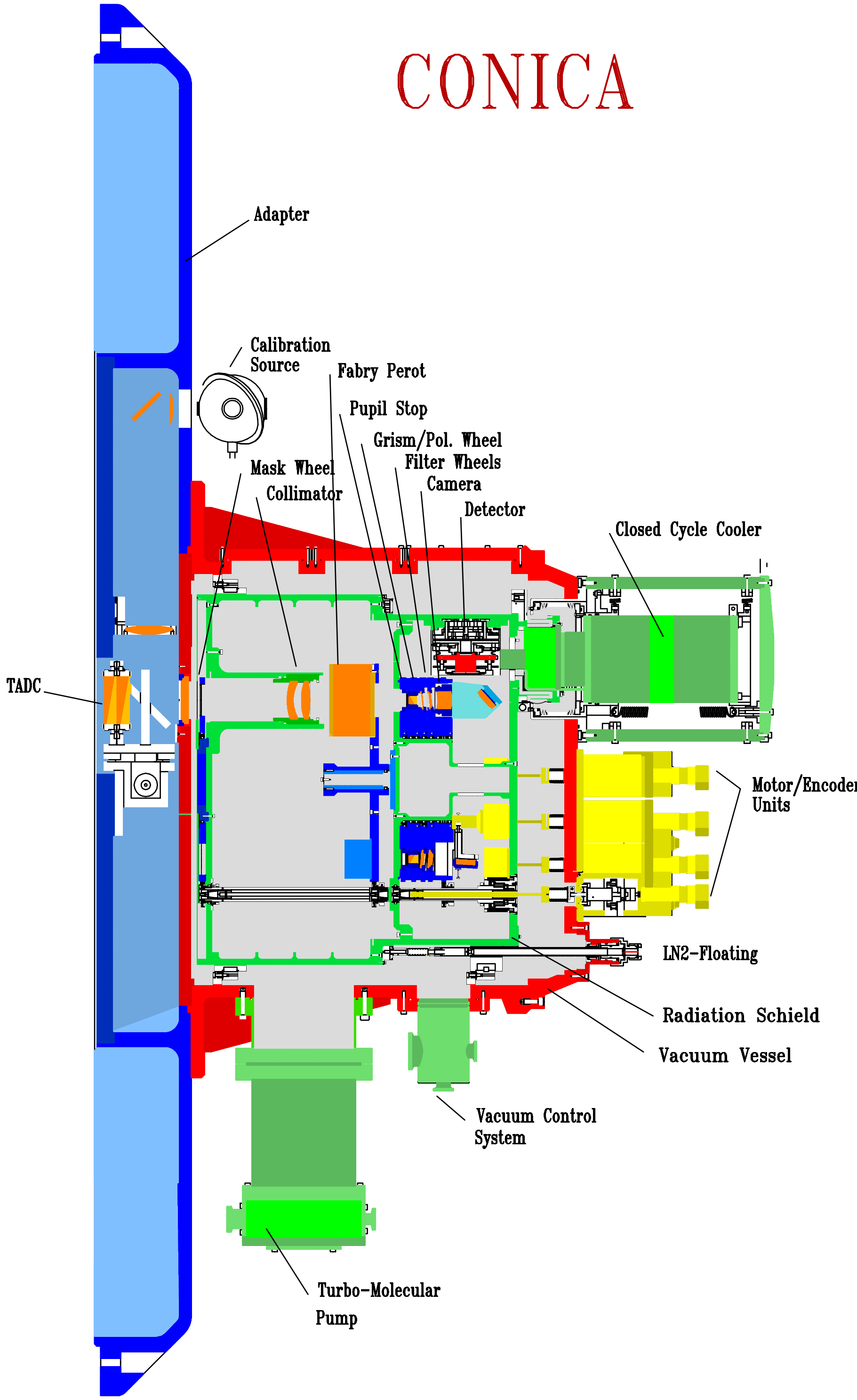

Figure 2. Overview of the CONICA cryo-mechanical design.

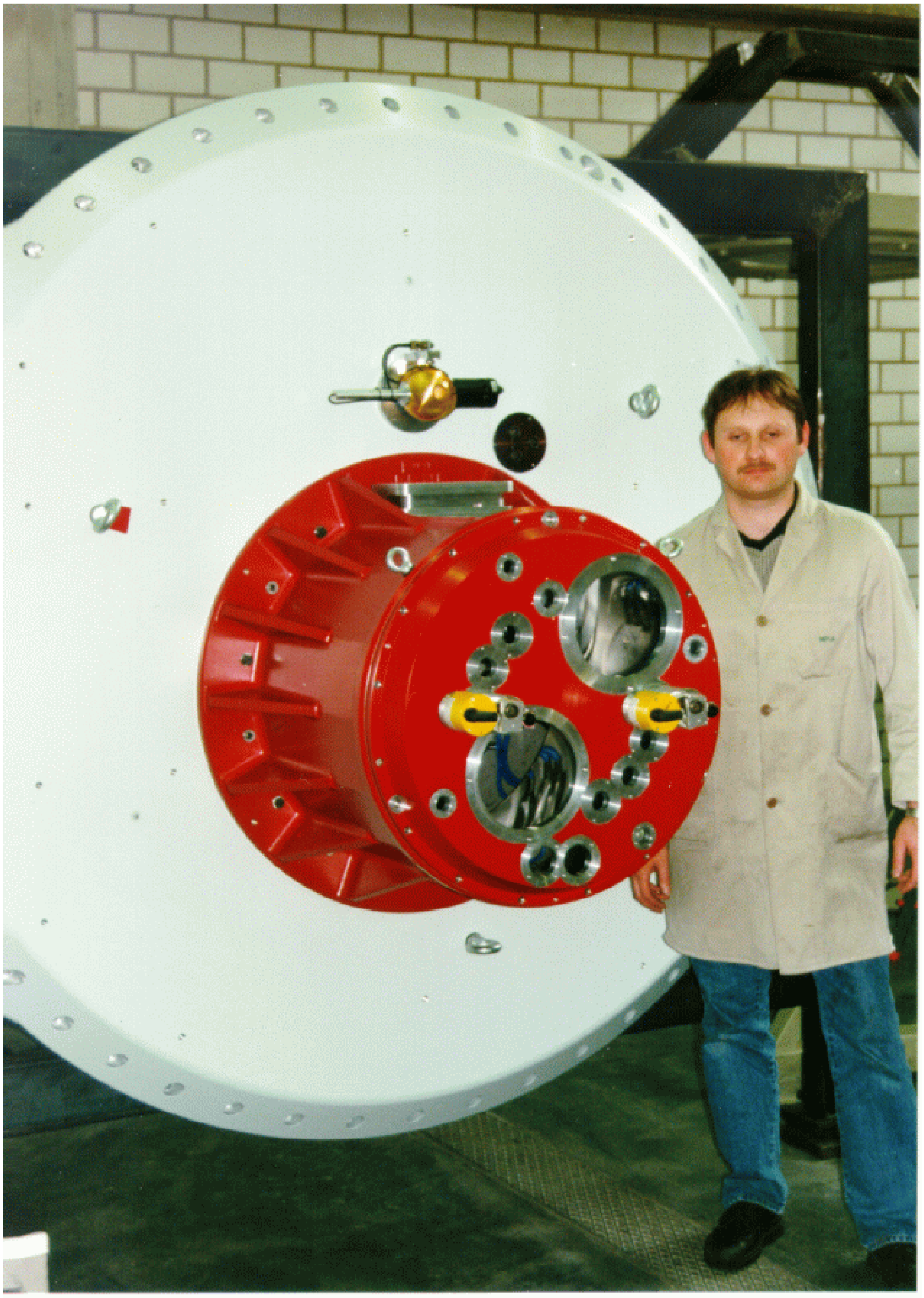

Figure 3. CONICA and Mr. Böhm. The dewar is mounted on the interface flange to NAOS.

Table 1. Wavelength ranges and resolution of the CONICA grisms. Data for the 55 mas/pixel camera.

Grism No.	Order	$\lambda_0[\mu m]$	R @ λ_0 [1/pixel]	wavelength range [μm]	comment
1	2	3.25	349-975	1.72 - 4.80	direct ruled
	3	2.18	”	1.16 - 3.21	KRS5
	4	1.65	”	0.90 - 2.42	
2	1	4.00	1496 - 2460	3.04 - 5.00	direct ruled
	2	2.02	”	1.54 - 2.51	KRS5
	3	1.36	”	1.04 - 1.69	
3	2	2.30	1544 - 2426	1.80 - 2.5	replica
	3	1.56	”	1.23 - 1.92	
	4	1.18	”	0.93 - 1.45	
4	1	1.80	416 - 1374	0.84 - 2.5	replica
	2	0.92	”	0.44 - 1.41	

two-stage Gifford-McMahon closed cycle cooler. As the environmental temperature of the detector array can determine instrumental sensitivity (particularly for spectral applications), special care has been taken to reach temperatures below 80 K for all surfaces which are directly seen by the detector. Finite element analysis has been performed to check the expected temperature distributions.

The array itself is thermally coupled to the second stage of the closed cycle cooler. The operation temperature can be stabilized at any value between 30 K and 40 K. The optimum operating temperature for the InSb detector is expected to be $\approx$ 35 K. The typical cool down process has been tested and stabilized conditions can be reached within less than 24 hours. This relatively short time is achieved by floating a tube system surrounding the radiation shield with liquid nitrogen.

CONICA uses a cold shutter for integration times shorter than the frame read time of about 50 ms and for seeing selection in case bad seeing disrupts the NAOS image quality during long integrations. For the shutter drive, a modified magnetic head drive of a hard disk unit is used. This system works at LN_2 temperatures and allows beam switching within a few milliseconds and repeat rates of more than 10 Hz. It is driven by newly-developed electronics which are controlled by one command bit and produce current pulses to accelerate and decelerate the shutter arm. Figure 2 shows a schematic of the dewar and mounting flange. Figure 3 is an image of the first integration of the dewar and mounting flange with the head of our workshop as a scale.

5. Performance

Table 2 shows the calculated limiting magnitudes of point sources for 3 σ in one hour integration time, assuming a Strehl ratio of 70 % down to a wavelength of 2.0 μm and a total efficiency of 65 % including telescope, optics, filter and detector. NAOS is calculated with 100 % throughput since no other numbers are known yet. The R = 50 row in the table represents narrow band imaging. R = 500 is an indicator for the detection limits in spectroscopy mode, but these numbers vary for other resolutions. The R = 1800 is for the Fabry-Perot mode which is only available in the K band.

Table 2. Limiting magnitudes for CONICA.

Band	J	H	K	L	M
Scale [mas/pixel]	13.6	13.6	27.2	27.2	54.6
BB imaging	26.9	25.7	25.0	19.9	16.7
R = 50	25.2	24.3	23.3	18.5	15.6
R = 500	23.7	22.8	21.7	17.2	14.5
R = 1800	-	-	19.7 - 18.8	-	-

Acknowledgments. We are grateful to the ESO staff members who have been involved in developing components for CONICA.

References

Hippler S., Glindemann A., Rohloff R., Wagner K., “ALFA: The MPIA adaptive optics system with lasers for astronomy project”, in Infrared Detectors and Instrumentation for Astronomy, A.M. Fowler, ed. Proc. SPIE 3353-33, 1998

Lenzen R., Bizenberger P., Salm N., Storz C., “Omega Cass: A new multi-mode NIR-imager/spectrometer for Calar Alto”, in Infrared Detectors and Instrumentation for Astronomy, A.M. Fowler, ed. Proc. SPIE 3354-33, 1998a

Lenzen R., Hoffmann R., “Status of the high resolution near infrared camera CONICA for the VLT (ESO)”, in Infrared Detectors and Instrumentation for Astronomy, A.M. Fowler, ed. , Proc. SPIE 2475 pp. 268-278, 1995

Lenzen R., Hoffmann R., Bizenberger P., Tusche A., “CONICA: The high resolution near-infrared camera for the ESO VLT”, in Infrared Detectors and Instrumentation for Astronomy, A.M. Fowler, ed. Proc. SPIE 3354-44, 1998b

Rosset G., Lacombe F., Puget P., Hubin N., Gendron E., Madec P., Rabud D., Conan J., Mouillet D., Lagange A., Rigaut F., “Design of the Nasmyth adaptive optics system (NAOS) of the VLT”, in Infrared Detectors and Instrumentation for Astronomy, A.M. Fowler, ed. Proc. SPIE 3353-26, 1998

Part 2. NICMOS Calibration and Analysis Software

NICMOS and the VLT
Pula, Sardinia, May 26-27th 1998
Wolfram Freudling and Richard Hook, eds.

The STScI NICMOS Calibration Pipeline

H. Bushouse, C. Skinner, J. MacKenty, and D. Axon

Space Telescope Science Institute, 3700 San Martin Drive, Baltimore, MD 21218, Email: bushouse@stsci.edu

E. Stobie

U. of Arizona, Steward Observatory, Tucson, AZ 85721

Abstract. The Space Telescope Science Institute (STScI) data reduction and calibration pipeline for the Near-Infrared Camera and Multi-Object Spectrometer (NICMOS) is composed of two major tasks, CALNICA and CALNICB. CALNICA applies instrumental calibration to all images, while CALNICB applies specialized processing to sets of images associated with a single astronomical target. This paper describes some of the technical aspects of the NICMOS data file formats, the CALNICA and CALNICB software, as well as details and examples of the processing that these tasks perform.

1. Introduction

The STScI NICMOS calibration pipeline is composed of two major tasks, CALNICA and CALNICB. CALNICA applies instrumental calibration to all images and includes basic corrections such as dark current subtraction, detector non-linearity correction, and flat-fielding. CALNICA operates on one image at a time. It takes as input the raw science data files produced by the Generic Conversion process in the STScI OPUS environment. Its outputs are fully calibrated files and, for MultiAccum observations only, an intermediate calibrated file.

CALNICB is only applied to associated NICMOS observations and is executed after all images in an association have first been calibrated with CALNICA. CALNICB combines images into mosaics and also removes background signal from the images. Its inputs are an association table, which contains information about the images in the association, and the calibrated images produced by CALNICA. Its outputs are an updated version of the association table and background-subtracted mosaic images, produced by combining the associated input images.

2. CALNICA/CALNICB Common Features

Both CALNICA and CALNICB are built as host-level tasks and can therefore be executed directly from the host operating system level (e.g. Unix or VMS), or they can be executed from within the IRAF environment in the STSDAS `hst_calib.nicmos` package. The tasks are completely data driven in that they derive all information that is necessary to guide the processing from values of the input image header keywords and, in the case of CALNICB, the association table. Some user-setable parameters are available for tailoring reprocessing efforts. These parameters use default values when operating in the OPUS pipeline.

The run-time file format for all data I/O is FITS files with IMAGE and BINTABLE extensions. All NICMOS images are represented by five data arrays, stored as five IMAGE extensions in a single FITS file. The group of five data arrays is known as an image set, or "imset". MultiAccum-mode exposures, which produce multiple intermediate detector readouts during the course of an exposure, have multiple imsets stored in the FITS files. Each imset is comprised of the science image (extension name "SCI"), a statistical error image ("ERR"), a data quality flag array ("DQ"), an array giving the number of data samples at each pixel ("SAMP"), and an exposure time per pixel array ("TIME").

All input and output files conform to the same file structure and organization, which allows output files to be reused as input if desired. All data processing steps involving reference data (e.g. dark and flat-field images) propagate statistical uncertainties from the ERR arrays and data quality flags from the DQ arrays of the reference data into the science data being processed. Furthermore, all steps involving image combination propagate the number of samples (SAMP) and their total exposure time (TIME) used to compute each resulting science (SCI) image value.

3. CALNICA Processing

The overall flow of CALNICA processing is shown in Figure 1. Included in this figure are the names of the image header keywords that are read by CALNICA to determine the names of reference files (left column) and the names of the keyword "switches" used to turn each step on or off.

CALNICA applies basic instrumental calibrations to individual NICMOS observations. For MultiAccum-mode observations, the processing steps are repeated for each imset in the input file. The most significant calibration steps are the subtraction of dark current, correction for non-linear photometric response, and correction for pixel-to-pixel gain variations (flat-fielding). MultiAccum-mode observations receive some specialized processing, including correction for source signal present in the initial or "zeroth" detector readout, subtraction of the zeroth readout from all subsequent readouts, and combination of the multiple readouts into a single image, which includes cosmic-ray and bad pixel rejection. Details of some of these steps are discussed below. For details regarding all of the individual processing steps see Bushouse (1997a, 1997b).

3.1. Dark Current Subtraction

The subtraction of dark current is a critical step in processing NICMOS data because it actually includes corrections for several instrumental effects (see Skinner, Bergeron, & Daou 1997; Bergeron & Skinner 1997). The actual detector dark current is quite small for all three NICMOS cameras, being at most 0.05 e^-/sec. There are two other much larger instrumental signatures superimposed on the darks. The first is a bias level or DC offset which exhibits a signal gradient across each quadrant of an image. This is the so-called "shading", which is a noiseless signal than can reach levels of tens or even hundreds of DN (data numbers). The other effect is known as amp glow and appears as an elevated signal in the corners of NICMOS images. This signal is due to a small

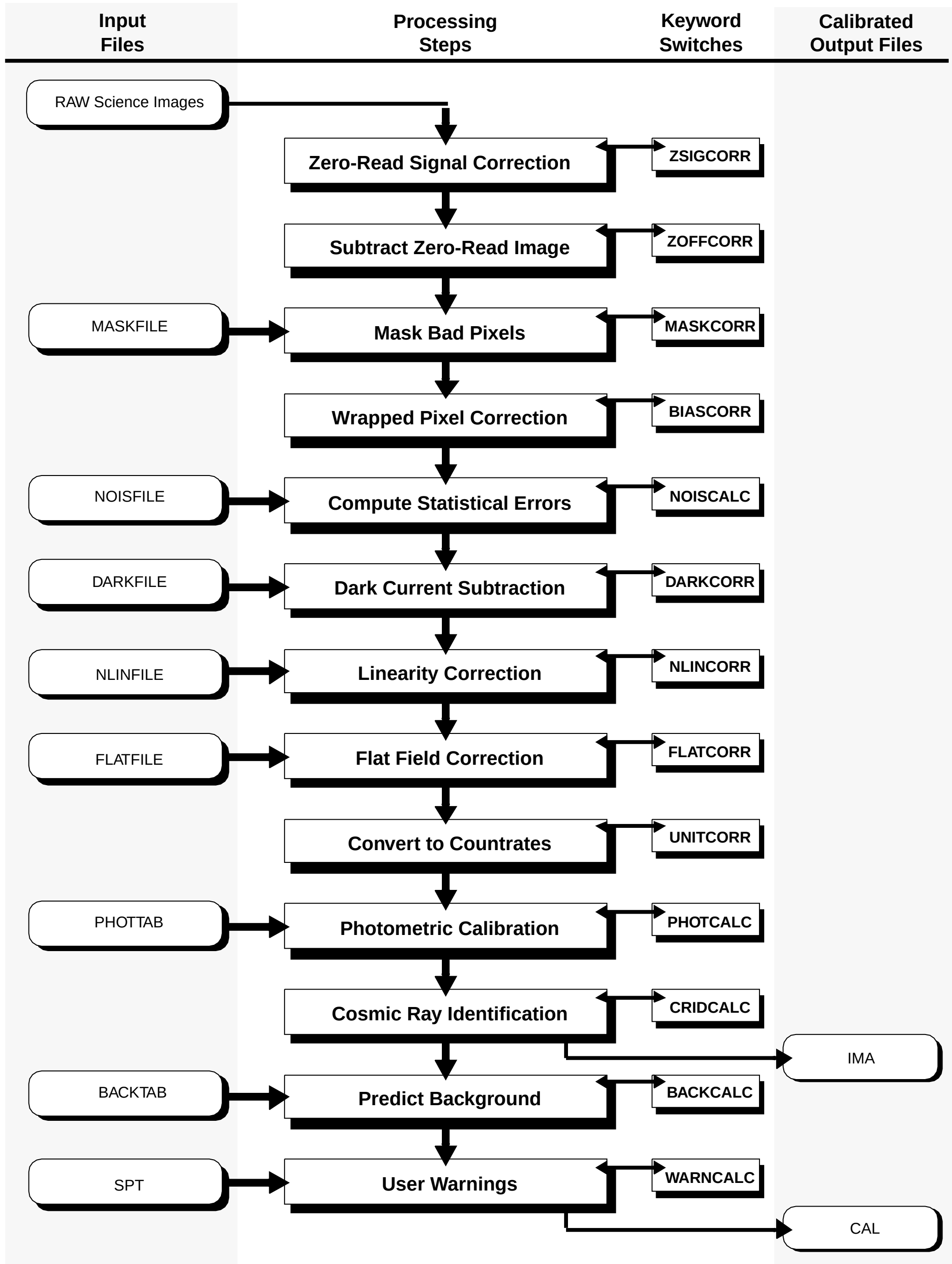

Figure 1. CALNICA Processing Flow.

amount of IR radiation emitted by the readout amplifiers, which are situated near the detector corners.

Fortunately, both the shading and the amp glow signal levels are very repeatable, and depend variously upon the number of readouts and the time since the last detector reset. Hence a proper subtraction can be achieved by applying dark current reference images having the exact same readout sequence and exposure times. CALNICA automatically selects the appropriate imset from the dark current reference file that has an exposure time matching that of the science data being processed.

3.2. Detector Non-Linearity

This step corrects for the non-linear response of the detectors. The response can be conveniently divided into three regimes. In the low signal regime, the detector response is linear, hence no correction is applied. In the mid-level regime, the response deviates from true linearity in a way that is correctable using a first-order polynomial of the form

$$SCI(corrected) = (c_1 + c_2 * SCI) * SCI \tag{1}$$

where c_1 and c_2 are the polynomial coefficients. The coefficients are stored, on a pixel-by-pixel basis, in the "COEF" and "ERR" image extensions in the NLINFILE reference file. In the high signal regime, where pixels begin to saturate, no correction is applied to the data, but a saturation flag value is set in the DQ image. The DN levels defining the boundaries between the regimes are also stored on a pixel-by-pixel basis in two "NODE" image extensions in the NLINFILE. The linear regime typically extends up to $\sim$14500 DN, and the non-linear regime to $\sim$27500 DN, above which saturation begins to occur.

3.3. MultiAccum Zeroth Read Signal

Because NICMOS does not have a shutter, signal from bright sources can accumulate during the $\sim$0.2 second long period that elapses between resetting the detector and taking the initial, or zeroth, readout that begins an exposure. Any signal present in the zeroth read will be removed when the zeroth read image is subtracted from all subsequent readouts by CALNICA, but this can lead to an error in the linearity correction that is applied to a given pixel, since the linearity correction depends on the total amount of charge that accumulated in the pixel.

The ZSIGCORR step of CALNICA computes the count rate for each pixel by differencing the zeroth and first readouts from one another and then estimates the amount of signal that would have accumulated in the zeroth read during its 0.203 second effective exposure time. This zeroth read signal is carried through to the NLINCORR step, where it is added back into the signal level for each pixel before determining its correction. After applying the linearity correction, the zeroth read signal is again removed.

3.4. Combining MultiAccum Readouts

Once all the individual readouts of a MultiAccum observation have received all the necessary instrumental calibration steps, they are combined into a single image, identifying and rejecting both cosmic-ray hits and bad pixels in the process. The accumulated counts as a function of increasing exposure time for each pixel are fitted with a first-order polynomial, using a standard weighted least-squares algorithm. Readouts already flagged as bad in the DQ array (e.g. due to saturation) are not used in the fit. The distance of each readout value from the fit is computed and cosmic-rays are identified by their characteristic negative-to-positive residual transition from one readout to the

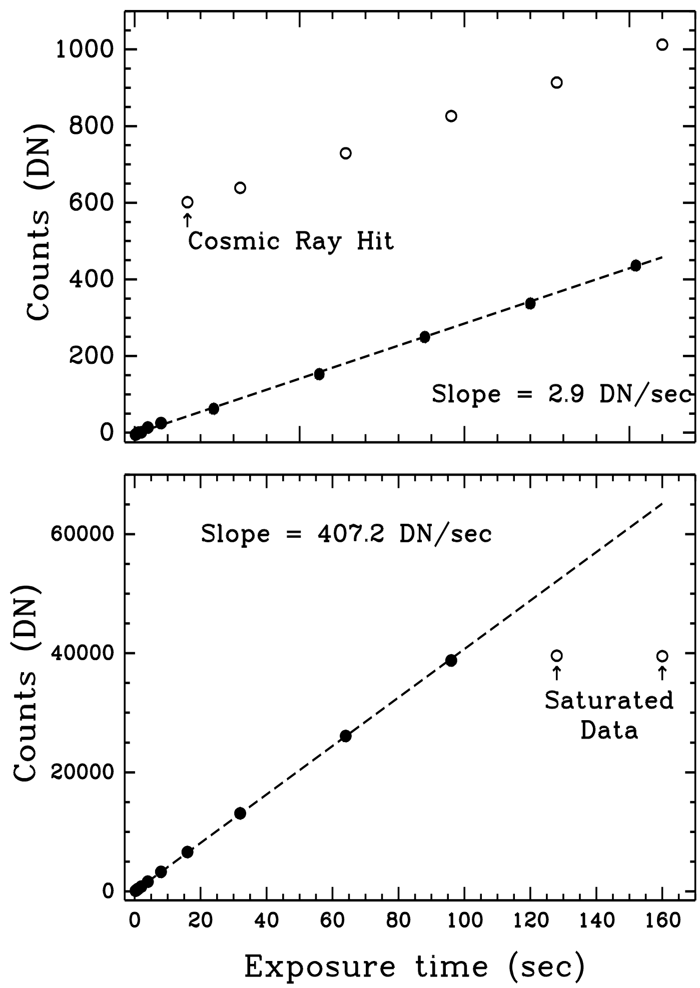

Figure 2. MultiAccum Ramp Fitting Examples.

next. Readouts containing a hit are rejected and the fit is recomputed. This process is repeated until no new hits are identified. The slope of the fit gives the final count rate for the pixel. The total number of non-rejected readouts and their exposure time are recorded in the SAMP and TIME arrays of the final output image.

Figure 2 shows some examples of the MultiAccum fitting process. The top panel shows the results for a pixel that had a cosmic-ray hit. The open circles are the original data values, while the filled circles are the result of removing the signal from the readout containing the CR hit. The bottom panel shows a pixel that has the last two readouts flagged as saturated and therefore not used in the fit.

4. CALNICB Processing

The overall flow of CALNICB processing is shown in Figure 3. CALNICB is used exclusively for processing associated sets of images, all of which must have already been calibrated using CALNICA. A NICMOS image association is defined to be a

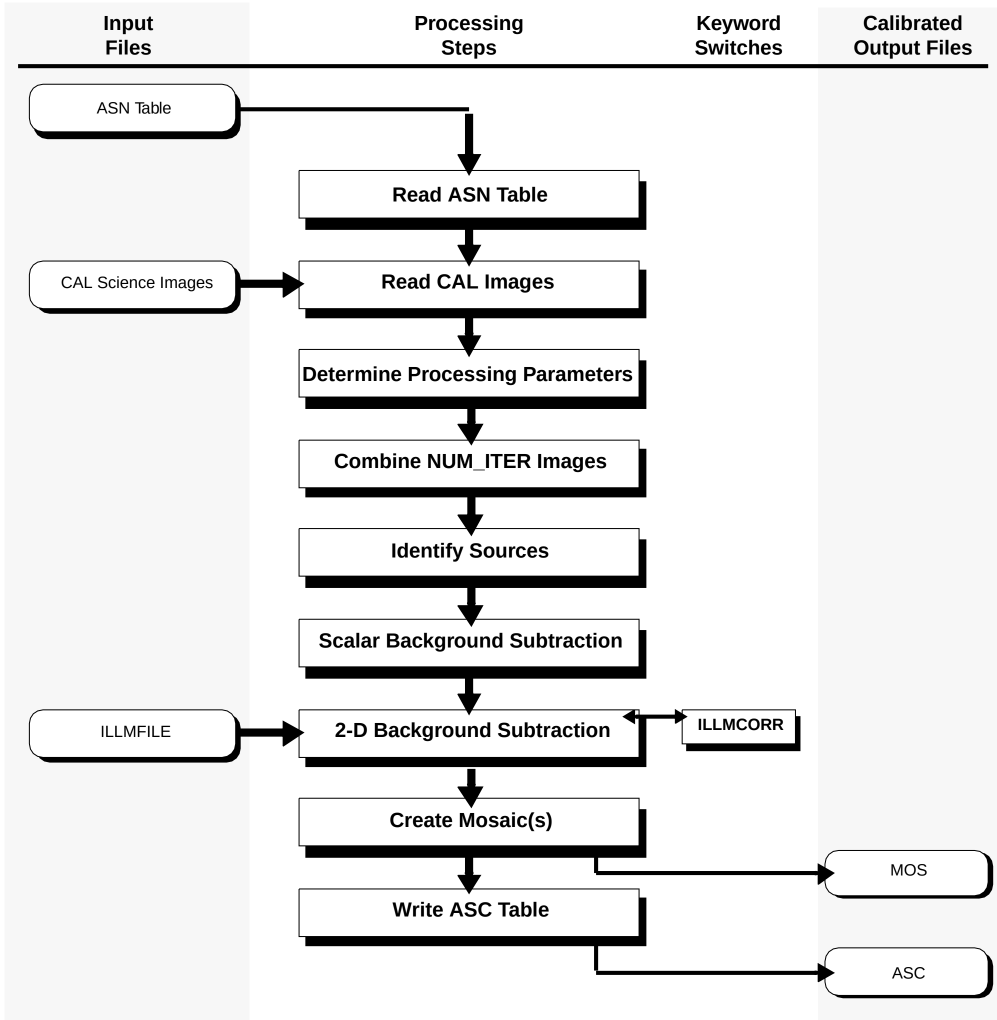

Figure 3. CALNICB Processing Flow.

logical grouping of multiple observations of a single astronomical target. Associations are typically used for:

- making multiple exposures at a single sky position so that cosmic-ray rejection can be performed by later combining the images
- dithering the telescope field of view to remove the effects of bad pixels or flat field residuals
- building image mosaics of large angular-size targets
- chopping the field of view off of the target to measure the telescope thermal background signal

To make it easier for observers to plan dithered and chopped sets of observations, STScI created several predefined observing patterns which automatically dither or chop the telescope field of view through a grid of observing positions on the sky (see MacKenty et al. 1997, chapter 10).

The major processing steps of CALNICB include the combination of images taken at individual sky positions, the measurement and subtraction of the thermal background signal, and the mosaicing of images within an observing pattern. The following sections describe some of these operations in a bit more detail. For more information, see Bushouse (1997a, 1997c).

4.1. Input Data

CALNICB, as run in the STScI pipeline, is completely data driven, getting all the information it needs to guide the processing from the association table that accompanies the individual images, and from header keywords in the images themselves. Some user-setable task parameters are available in CALNICB versions 2.2 and later, for use when running CALNICB interactively (see below). The association table (denoted “ASN”) is a FITS file with a BINTABLE extension containing the list of file names that make up the association to be processed by CALNICB, as well as the file names of all output mosaic image files (denoted “MOS”) to be produced. CALNICB determines which names in the list are input files and which are output files based on the MEMTYPE column in the ASN table. Input files have a MEMTYPE prefix of “EXP” (exposure), while output files have a prefix of “PROD” (products). Furthermore, association members that are observations of the target of interest have a MEMTYPE suffix of “TARG” (target), while observations of sky background locations (which are only produced by using chop patterns) have a suffix of “BCKn”, where n is the background region number in the pattern (see Table 1). One MOS image will always be produced for the target, and chop patterns will result in one MOS image being produced for each background region observed.

Once CALNICB has determined the list of input images from the ASN table, it reads various keywords from the image headers to determine exactly what processing needs to be performed. Certain keywords, such as PATTERN (pattern type), NUMPOS (number of pattern positions), and NUMITER (number of exposure iterations at each position) have the same value in all images and are therefore only read from the first image in the association. Others are image specific, such as PATT_POS (position number of each image in the pattern) and World Coordinate System (WCS) keywords, have unique values in each image and are therefore read from each image. From this information CALNICB determines what type of pattern was used, how many positions are in the pattern, how many images there are at each pattern position, the relative positions of each image in the pattern, how many output MOS images need to be produced, and which input images go into which MOS image.

4.2. Combining NUMITER Images

If there is more than one image at each pattern position, CALNICB will combine the images at each position into a single image. The offsets between each image at a given position are computed from their WCS information, using the first image at each pattern position as a reference. These offsets are then refined using a cross-correlation technique. The images are then aligned with their reference image, using bilinear interpolation, and then combined. The combining process computes the ERR-weighted mean for each SCI image value, with rejection of DQ-flagged pixels and iterative sigma clipping. The number of non-rejected samples, and their total exposure time, are saved in the SAMP and TIME images.

4.3. Identifying Sources

This step flags (in the DQ images) pixels suspected of containing flux from a source. This is accomplished using a 3-stage process. First, pixels that are greater than 5 sigma above the median signal level in each image are identified as candidate source pixels. Second, in order to filter out spurious identifications, only those candidates having two or more neighboring pixels also identified as containing a source are retained. Finally, the surviving pixels have their source DQ flags "grown" to their four immediate neighbors.

4.4. Scalar Background Subtraction

This step computes and subtracts a scalar (or "DC") background signal from all images in the association. This is accomplished as follows. First, the median signal level in each BCK image in the association is computed. The computation excludes bad and source-flagged pixels and uses iterative sigma clipping to avoid any possible contamination. If there are not any BCK images in the association (e.g. the observations are from a pure dither pattern), the same computation is performed on the target images. The resulting background levels for each image are then averaged to compute the overall mean background level for the whole association. This overall mean is then subtracted from all images. The mean background level is recorded in the MEAN_BKG keyword in the output association (denoted "ASC") table.

4.5. 2-D Background Subtraction

This step subtracts the ILLMFILE reference image from the associated images. It is intended to remove any spatial variations in the telescope background thermal pattern, but to date, little if any such spatial variations have been seen. Thus the ILLMFILEs currently in use at STScI contain dummy data (constant zero values). CALNICB recognizes that the files are dummy and skips the subtraction.

4.6. Creating Mosaics

This step performs the final combination of images to produce the output mosaics. The process is very similar to the step that combines the NUMITER images at each pattern position. The relative offsets for each image in a given mosaic are first computed from their WCS information, using the first image in each mosaic as a reference. The offsets are refined using cross-correlation, and then the images are aligned using bilinear interpolation and combined. The combining process computes the ERR-weighted mean of overlapping pixels, rejecting those with non-zero DQ values and applying an iterative sigma clipping. The number of non-rejected samples and their total exposure time are saved in the output SAMP and TIME images of the MOS files.

4.7. Updating the Association Table

The final step of CALNICB creates a new association (ASC) table. The ASC table is a copy of the input ASN table, with four new columns of information appended. An example of an ASC table is shown in Table 1. The new columns are BCKIMAGE, MEANBCK, XOFFSET, and YOFFSET. The BCKIMAGE column indicates whether

Table 1. Example Association (ASC) Table.

MEMNAME	MEMTYPE	BCKIMAGE	MEANBCK (DN/sec)	XOFFSET (pixels)	YOFFSET (pixels)
n3uw01a1r	exp-targ	no	INDEF	0.00	0.00
n3uw01a2r	exp-targ	no	INDEF	-0.15	0.00
n3uw01a3r	exp-bck1	yes	0.28	0.00	0.00
n3uw01a4r	exp-bck1	no	INDEF	0.00	0.20
n3uw01a5r	exp-targ	no	INDEF	0.32	0.00
n3uw01a6r	exp-targ	no	INDEF	0.00	0.00
n3uw01a7r	exp-bck2	yes	0.26	0.00	0.00
n3uw01a8r	exp-bck2	no	INDEF	0.00	0.00
n3uw01a9r	exp-targ	no	INDEF	0.00	0.00
n3uw01a0r	exp-targ	no	INDEF	0.00	-0.15
n3uw01010	prod-targ	no	INDEF	INDEF	INDEF
n3uw01011	prod-bck1	no	INDEF	INDEF	INDEF
n3uw01012	prod-bck2	no	INDEF	INDEF	INDEF

or not a given image was used in the scalar background computation. The example shown in Table 1 is for a TWO-CHOP pattern, with NUMITER=2, and NUMPOS=5. So there are two images at each of the five pattern positions and two of the positions are background (BCK) regions. Thus, in this example, only the images at the BCK positions were used to compute the scalar background level. The MEANBCK column records the background signal computed for each individual image. The XOFFSET and YOFFSET columns record the computed offsets for each image relative to its reference image.

4.8. CALNICB User Parameters

As mentioned above, beginning with CALNICB v2.2, there are a few parameters available to interactive users for tailoring the CALNICB processing. The `subbkg` parameter allows you to turn the scalar background subtraction step on or off. The `meanbkg` parameter allows you to use the mean scalar background value of all images, or subtract the value derived for each image from itself. The `readbkg` and `readoffsets` parameters allow you to use an ASC table as input to CALNICB and have it read either the image background or offset (or both) values from the table, rather than computing them. The `crthresh` parameter sets the cosmic-ray rejection threshold used during image combining, and the `xcwin` parameter sets the size of the cross-correlation search window box.

References

Bergeron, L. E., & Skinner, C. J. 1997, in The 1997 HST Calibration Workshop, eds. S. Casertano, et al. (Baltimore: STScI), 240[1]

[1] http://icarus.stsci.edu/∼stefano/newcal97/pdf/bergeronl.pdf

Bushouse, H. 1997a, in The 1997 HST Calibration Workshop, eds. S. Casertano, et al. (Baltimore: STScI), 223[2]

Bushouse, H. 1997b, Instrument Science Report NICMOS-97-028 (Baltimore: STScI)[3]

Bushouse, H. 1997c, Instrument Science Report NICMOS-97-029 (Baltimore: STScI)[4]

MacKenty, J. W., et al. 1997, NICMOS Instrument Handbook, Version 2.0 (Baltimore: STScI)[5]

Skinner, C. J., Bergeron, L. E., & Daou, D. 1997, in The 1997 HST Calibration Workshop, eds. S. Casertano, et al. (Baltimore: STScI), 171[6]

[2] http://icarus.stsci.edu/~stefano/newcal97/pdf/bushouseh.pdf

[3] http://www.stsci.edu/ftp/instrument_news/nicmos/isreports/isr_028.ps

[4] http://www.stsci.edu/ftp/instrument_news/nicmos/isreports/isr_029.ps

[5] http://www.stsci.edu/ftp/instrument_news/nicmos/nicmos_doc_handb.html

[6] http://icarus.stsci.edu/~stefano/newcal97/pdf/skinnerc1.pdf

NICMOS and the VLT
Pula, Sardinia, May 26-27th 1998
Wolfram Freudling and Richard Hook, eds.

Status and Goals of the NICMOS Calibration Plan

L. Colina[1]

Space Telescope Science Institute, 3700 San Martin Drive, Baltimore, MD 21218, Email: colina@stsci.edu

Abstract.

This document summarizes the goals and status of the various calibration programs that form the basis of the NICMOS Cycle 7 calibration plan. Pointers to technical reports and/or WEB pages showing the results of the analysis and providing detailed information are also given.

1. Introduction

Astronomers working with ground-based telescopes are used to get simultaneously their calibrations (i.e. darks, flats, standards, etc) and scientific data. The extension of this practice to satellites in general, and HST in particular, would make a very inefficient use of telescopes in orbit as the fraction of available observing time devoted to calibrations would increase very dramatically.

The approach taken by STScI regarding the calibrations of HST instruments is that STScI is responsible for (a) the definition of the goals and objectives of the calibrations, (b) the implementation and execution of the calibration programs, (c) the analysis of the calibration data, and (d) the delivery of the calibration products in the form of reference files and/or technical reports. This approach has two benefits, first, it saves a considerable amount of telescope time (about 10% of the total number of orbits allocated to a given instrument go into its calibration) and second, it generates an homogeneous database of calibrations that would be difficult to create otherwise.

This document summarizes the content, goals and status of the Cycle 7 calibration plan for NICMOS and also points to the WEB pages where detailed information on specific topics of interest can be found.

2. Cycle 7 Calibration Plan. Overview and Goals

The NICMOS calibrations available during Cycle 7 are based on three distinct calibration activities. First, NICMOS was extensively tested on the ground. These tests included a limited amount of calibration, particularly during the System Level Thermal Vacuum (SLTV) testing. Second, a period following the installation of NICMOS into HST for testing and initial calibration was completed during the first three months on or-

[1] Affiliated with the Astrophysics Division, Space Science Department, ESA

bit. This activity is known as the Servicing Mission Observatory Verification (SMOV). Finally, the routine Cycle 7 calibration plan is now underway.

It is important to distinguish between the various goals of these calibration activities. SLTV was intended to demonstrate the proper functioning of NICMOS and to obtain an initial calibration of a subset of its capabilities. SMOV was intended to demonstrate that the instrument is functioning as expected, based on the SLTV experience, to characterize those parameters not measurable during SLTV (e.g. the thermal background generated by the HST optics), to establish necessary operation parameters (e.g. plate scale), and to begin the calibration of NICMOS. A complete calibration of NICMOS various operating modes is conducted during Cycle 7 with SMOV being used to demonstrate that the planned calibrations are in fact feasible.

As a consequence of the camera 3 (NIC3) defocus, the Cycle 7 calibration plan[2] that went into operation in June 1997, did put the emphasis on the calibration of NIC1 and NIC2 cameras executing only a limited number of calibration programs for NIC3. Revisions[3] to the original cycle 7 calibration plan took place after experience with the detectors was gained during the first 5 months of Cycle 7 (i.e. in November 1997), and most recently in March 1998. The first revision supplemented the original version with programs designed to cover the calibration of NIC3 during the first campaign. The second revision included programs aimed at the calibration of modes of operation not covered in the previous versions. In this version, few additional programs were also added to monitor the behaviour of the detectors during the warming-up phase of NICMOS.

In its present form, the Cycle 7 calibration plan consists of several calibration programs that are grouped in one of four different categories: special calibration programs, routine monitoring programs, NIC3 specific programs and Cycle 9 oriented programs (see Table 1):

- Special Calibration programs. These programs are designed to obtain a detailed characterization of the detectors and knowledge of their different modes of operation, including imaging polarimetry and grism spectroscopy. The outputs of these programs provide the reference files and tables needed for the calibration of data obtained with NICMOS.

- Routine Monitoring Programs. These calibration programs are designed to monitor the status of the detectors and to follow the temporal evolution of their performance. Dark and flat-field exposures, as well as photometric and focus measurements for all three cameras are presently taken every four weeks.

- NIC3 Specific Calibration Programs. Most programs requesting the NIC3 camera as prime have been scheduled during two observing campaigns (January and June 1998) when the secondary mirror of HST was moved to get NIC3 in focus. The special calibration programs for NIC3, including plate scale, absolute photometry measurements and the characterization of the grisms, have been executed during these campaigns.

---

[2] http://www.stsci.edu/ftp/instrument_news/NICMOS/nicmos_calprod.html

[3] http://www.stsci.edu/ftp/instrument_news/NICMOS/nicmos_calprod.html

- Cycle 9 Oriented Calibration Programs. The installation of a cryocooler during the third servicing mission is presently under consideration. If the cryocooler is installed, NICMOS will resume observations in Cycle 9 although operating at a temperature higher than during Cycle 7. A small set of calibration programs, mostly darks and flats, will be executed during the warming-up phase of NICMOS at the end of its lifetime in Cycle 7. These programs will help to assess the behaviour and performance of the detectors for Cycle 9 observations.

Table 1. NICMOS Cycle 7 Calibration Plan as of May 1998

ID	Proposal Title	Accuracy	Status	Results
	Routine Monitoring Program			
7596	Darks Monitoring	10 DN	In progress	Under analysis
7607	Photometric Monitoring	2%	Finished	Available
7608	Focus Monitoring	1 mm	Finished	Available
7690	Flats Monitoring	1%	In progress	Under analysis
7901	Focus Monitoring II	1 mm	In progress	Available
7902	Photometric Monitoring II	2%	In progress	Available
7903	Grism Dispersion Monitoring	0.01 μm	In progress	Under analysis
	Special Calibration Programs			
7039/40	Plate Scale Calibration	0.1%	Finished	Available
7611	Thermal Background	–	Finished	Available
7688	ACCUM Darks	10 DN	Finished	Under analysis
7689	NIC2 Narrow-band Flats	1%	Finished	Available
7690	Internal Lamp Flats	1%	Finished	Available
7691	Photometric Zero Point	5%	Finished	Available
7692	Polarizers	1%	In progress	Under analysis
7693	Pupil Transfer Function	2%	Finished	Available
7703-10	MULTIACCUM Darks: pre-fix	10 DN	Finished	Available
7775	Earth Flats	5%	Finished	Under analysis
7789,93-99	MULTIACCUM Darks: post-fix	10 DN	Finished	Available
7904	Photometric Zero Point: red stars	5%	Finished	Under analysis
7938	FOM-focus Test	–	Finished	Available
7956	NIC1 Narrow-band Flats	1%	Finished	Under analysis
7957	Lamp Flats II	1%	To be executed	Not available
7958	Polarizers II	1%	To be executed	Not available
7960	Persistence Test	–	Finished	Under analysis
	NIC3 Specific Calibration Programs			
7695	GRISM Wavelength Cal.	0.01 μm	Finished	Available
7696	GRISM Abs. Sensitivity	20%	Finished	Available
7806	GRISM Revalidation	0.01 μm	Finished	Available
7813	NIC3 HDF Darks	–	Finished	Not available
7814	NIC3 Lamp Flats	1%	Finished	Available
7815	NIC3 Earth Flats	–	Finished	Under analysis
7816	NIC3 Photometric Zero Point	5%	Finished	Available
7959	GRISM Calibration II	–	2nd campaign	Not available
	Cycle 9 Oriented Calibration Programs			
7961	Flats: Warming up	–	To be executed	Not available
7962	Focus: Warming up	–	To be executed	Not available
7963	Darks: Warming up	–	To be executed	Not available

The NICMOS calibration programs may each be examined by using their ID number and the HST Program and Schedule Information page[4]. The reference calibration files and tables created as a result of the various calibration programs are available on

[4] http://presto.stsci.edu/public/propinfo.html

the NICMOS Reference Files List page[5]. Instrument science reports (ISR) and/or published conference papers presenting the latest calibration results can be found on the NICMOS Documentation WEB page[6].

3. Cycle 7 Calibration Plan. Status of the Specific Programs

3.1. Detector Performance

All three detectors are being characterized to the same extent. High quality darks were obtained for all available MULTIACCUM sequences during June and early July 1997 (proposals ID 7703 to 7710). The mode of operation of the detectors was modified in August 1997 (amplifiers are now kept on all the times instead of keeping them off, and switching them on only when exposures start) and as a consequence a new set of darks were obtained (proposals ID 7789, 7793 to 7799). As a result, there are now two separate set of dark references files that should be used for pre-fix[7] data (i.e. data obtained before August 22, 1997) and post-fix[8] data (i.e. data obtained after August 21, 1997), respectively.

Changes in the detectors darks are being monitored with a monthly periodicity (proposal ID 7596). These data are currently being analysed and show indications that darks are changing with time. A strategy to create incremental darks is under investigation and will be provided in the future to users. Dark frames have also been obtained for a limited subset of ACCUM exposure times (proposal ID 7688) but the analysis has not yet been completed. Observers using ACCUMs with exposure times different than those provided by the calibration program will require to interpolate, producing therefore a less satisfactory calibration of their data.

3.2. Flat Fields

The pixel-to-pixel and the large scale responses of NICMOS filters are provided by high signal-to-noise flat-fields[9] generated using internal lamp exposures. Flat-field exposures for all NIC1 and NIC2 polarizers, broad- and medium-band filters were obtained during July and August 1997 (proposal ID 7690). Flat-fields for all narrow-band NIC1 and NIC2 filters were taken in May 1998 (proposal ID 7956) and February 1998 (proposal ID 7689), respectively. Lamp flats for all NIC3 filters were taken separately in December 1997, just before the first NIC3 campaign (proposal ID 7814).

The temporal evolution of the pixel-to-pixel response as a function of camera and wavelength is being monitored on a monthly basis using a subset of filters in the three cameras (proposal ID 7690).

The operating temperature of NICMOS has been rising steadily during Cycle 7. As a consequence, variations in the pixel-to-pixel and large scale sensitivity are expected.

[5] http://www.stsci.edu/ftp/instrument_news/NICMOS/nicmos_doc_cal_list.html

[6] http://www.stsci.edu/ftp/instrument_news/NICMOS/nicmos_doc.html

[7] http://www.stsci.edu/ftp/instrument_news/NICMOS/nicmos_doc_cal_list.html#DRKMULPRE

[8] http://www.stsci.edu/ftp/instrument_news/NICMOS/nicmos_doc_cal_list.html#DRKMULPOST

[9] http://www.stsci.edu/ftp/instrument_news/NICMOS/nicmos_doc_cal_list.html#FLT

A second set of internal lamp flat-field exposures (proposal ID 7957) will be taken in August/September 1998 for those filters for which the reference flats are based on data taken in July/August 1997, i.e. all medium- and broad-band NIC1 and NIC2 filters.

3.3. Image Anomalies

Several image anomalies have been found in NICMOS exposures. While in general the pipeline calibration appears to work well, on occasion one or more anomalies will occur. Complete descriptions of these anomalies including work-arounds, if available, can be found on the NICMOS Image Anomalies WEB page[10].

3.4. Focus Monitoring

The focus of all three cameras is being monitored throughout the entire Cycle 7. During the first few months focus measurements were obtained every other week with the three cameras (proposal ID 7608). The frequency of this monitoring program decreased to once a month after the first NIC3 campaign. In its present form, measurements of NIC3 focus are obtained every month while the other two cameras are monitored on a bimonthly basis (proposal ID 7901). The results of the focus monitoring program are posted regularly on the NICMOS focus WEB page[11].

3.5. Point Spread Function

No calibration program aimed at measuring the point spread function of the three cameras as a function of wavelength and location was included in the Cycle 7 calibration plan. Observers requiring PSFs in specific filters and/or locations within the field of view, were advised to include these in their own program. NICMOS PSFs can also be modeled using Tiny Tim V4.3. Tiny Tim software can be retrieved from the Tiny Tim WEB site[12].

3.6. Plate Scale

Plate scale measurements for all three cameras were performed early during the SMOV phase as part of the NICMOS aperture location (proposal ID 7039). Additional detailed measurements of plate scale and camera distortions were performed taking a series of images of the star cluster NGC 1850. In each camera 5 images were taken, displaced from each other without rotation (proposal ID 7040).

The results of the program 7040 are already available and have been presented in a technical report by Cox and collaborators (OSG-CAL-97-07[13]). Additional information regarding plate scale measurements can also be found on the NICMOS Plate Scale WEB page[14].

---

[10] http://www.stsci.edu/ftp/instrument_news/NICMOS/nicmos_anomalies.html

[11] http://www.stsci.edu/ftp/instrument_news/NICMOS/nicmos_doc_focus.html

[12] http://scivax.stsci.edu/~krist/tinytim.html

[13] http://www.stsci.edu/ftp/instrument_news/NICMOS/nicmos_doc_isr.html

[14] http://www.stsci.edu/ftp/instrument_news/NICMOS/nicmos_doc_platescale.html

3.7. Thermal Background

The absolute level and stability of the thermal background as seen by the NICMOS cameras was already measured as part of the SMOV program. The Cycle 7 calibration program extended the SMOV program with images obtained in the F237M (NIC2) and F222M (NIC3) filters (proposal ID 7611). Images were taken during June and July 1997 as pointed parallel observations to map possible changes in the thermal background as a result of temperature changes in HST optics.

The analysis of these data is now complete and the results can be found in a recent instrument science report (NICMOS-98-010) written by Daou & Calzetti[15].

3.8. Photometry

The photometric characterization of NICMOS comprises various aspects covered by different calibration programs. The absolute photometry for all available filter plus camera combinations has been obtained by observing the two primary NICMOS absolute spectrophotometric standards, the white dwarf G191-B2B and the solar analog P330E (proposal ID 7691 for NIC1 and NIC2 and proposal ID 7816 for NIC3). Images of additional calibration standards (white dwarfs, solar analogs and red stars) have also been taken to help defining the transformations between HST and ground-based JHK photometric systems (proposal ID 7904 for NIC1 and NIC2 and proposal ID 7816 for NIC3).

The photometric stability of all three NICMOS cameras as a function of time and wavelength is being monitored on a monthly basis with observations of an absolute spectrophotometric standard (P330E) in a subset of filters covering the entire NICMOS wavelength range (proposal IDs 7607 and 7902).

Relative photometry as a function of the position in the detectors has been measured for each camera using images of the solar analog P330E in a few filters. The grid used for this program consisted of 144 positions covering the entire field-of-view in each camera (proposal ID 7693).

Results regarding NICMOS photometric performance can be found on the NICMOS Photometry Update page[16].

3.9. Polarizers

The instrumental polarization and zero position angle of NIC1 and NIC2 polarizers have been measured taking images of two bright near-infrared polarized standards, HDE283812 and CHA-DC-F7. Changes in the polarization as a function of position within the detectors will also be measured by moving one of the polarized targets in a spiral pattern across the detector. Additional images of the HST unpolarized standards HD64299 and BD+32d3739 have also be taken (proposal IDs 7692 and 7958).

The analysis of these data is in progress but preliminary results can be found in the contribution of Dines, Schmidt & Lytle to the 1997 HST Calibration Workshop[17].

---

[15] http://www.stsci.edu/ftp/instrument_news/NICMOS/nicmos_doc_isr.html

[16] http://www.stsci.edu/ftp/instrument_news/NICMOS/nicmos_doc_phot.html

[17] http://www.stsci.edu/ftp/instrument_news/NICMOS/nicmos_doc_isr.html

3.10. Coronograph

NICMOS coronograph consists of a laser-ablated hole in the NIC2 mirror on the field divider assembly (FDA). One of the effects of the dewar expansion and subsequent contraction has been a change in the relative geometry of the NIC2 detector relative to the FDA. For the coronograph, this has caused the apparent location of the coronographic hole to drift relative to the fixed acquisition aperture on NIC2. Because it is necessary to center a star in the coronographic hole to within 1/4 pixel or better, a new addition to the NICMOS onboard software has been implemented to locate the coronographic hole at the beginning of each observation.

The long term drift of the NIC2 coronographic hole has been continuously monitored during Cycle 7 using internal lamp flat exposures obtained as part of the focus monitoring program (proposal IDs 7608 & 7901). The latest information on the status of the coronograph can be found on the NICMOS Coronographic Hole page[18].

3.11. Grisms

The wavelength dispersion solutions for all three NIC3 grisms have been computed using the emission lines of the compact planetary nebulae HB12 during the first NIC3 campaign (proposal ID 7695). The absolute sensitivities of the three grisms were derived using observations of the two primary NICMOS absolute spectrophotometric standards (G191-B2B and P330E; proposal ID 7696). A check on the stability of the wavelength and absolute sensitivity will be performed during the second NIC3 campaign in June 1998 (proposal ID 7959). Finally, the stability of the wavelength calibration for grism G141 is measured on a by-monthly basis (proposal ID 7903).

The analysis of the calibration programs executed during the first NIC3 campaign has been completed and the results can be found on the NICMOS ST-ECF WEB page[19].

4. Summary

This paper has summarized the status of NICMOS Cycle 7 calibration plan as of May 1998. The calibration of NICMOS is an ongoing effort that will continue long after the nitrogen is exhausted and Cycle 7 observations are finished. Calibration proposals will be executed during the warming-up phase of NICMOS and will stop soon before the shut-down of the instrument.

The calibration of NICMOS detectors is not yet in a stable situation. Improvements in the calibration pipeline continue, new reference files are being delivered as the analysis of the calibration data is completed and new technical reports presenting the results of the calibration programs are posted continuously on the NICMOS WEB page[20].

---

[18] http://www.stsci.edu/ftp/instrument_news/NICMOS/nicmos_doc_coron.html

[19] http://ecf.hq.eso.org/nicmos/nic3_calib/

[20] http://www.stsci.edu/ftp/instrument_news/NICMOS/topnicmos.html

Acknowledgments. The definition, implementation and analysis of all the calibration programs that form part of the NICMOS Cycle 7 calibration plan has been a project that involving a large number of persons including members of the STScI NICMOS team (D. Axon, E. Bergeron, D. Calzetti, D. Daou, D. Gilmore, S. Holfeltz, J. Mackenty, J. Najita, K. Noll, C. Ritchie, A. Schultz, C. Skinner, W. Sparks, A. Storrs, A. Suchkov), the instrument definition team (R. Thompson, M. Rieke, G. Schneider and D. Hines), and the ST-ECF (W. Freudling and N. Pirzkal).

References

Aurière, M. 1995, in ASP Conf. Ser., Vol. 77, Astronomical Data Analysis Software and Systems IV, ed. R. A. Shaw, H. E. Payne & J. J. E. Hayes (San Francisco: ASP), 109

Canizares, C. R., Grindlay, J. E., Hiltner, W. A., Liller, W., & McClintock, J. E. 1978, ApJ, 224, 39

Djorgovski, S., & King, I. R. 1984, ApJ, 277, L49

Hagiwara, K., & Zeppenfeld, D. 1986, Nucl.Phys., 274, 1

Hénon, M. 1961, Ann.d'Ap., 24, 369

King, I. R. 1966, AJ, 71, 276

King, I. R. 1975, in Dynamics of Stellar Systems, ed. A. Hayli (Dordrecht: Reidel), 99

King, I. R., Hedemann, E., Hodge, S M., & White, R. E. 1968, AJ, 73, 456

Kron, G. E., Hewitt, A. V., & Wasserman, L. H. 1984, PASP, 96, 198

Lynden-Bell, D., & Wood, R. 1968, MNRAS, 138, 495

Newell, E. B., & O'Neil, E. J. 1978, ApJS, 37, 27

Ortolani, S., Rosino, L., & Sandage, A. 1985, AJ, 90, 473

Peterson, C. J. 1976, AJ, 81, 617

Spitzer, L. 1985, in Dynamics of Star Clusters, ed. J. Goodman & P. Hut (Dordrecht: Reidel), 109

NICMOS and the VLT
Pula, Sardinia, May 26-27th 1998
Wolfram Freudling and Richard Hook, eds.

Photometric Performance of NICMOS

L. Colina[1], S. Holfeltz & C. Ritchie

Space Telescope Science Institute, 3700 San Martin Drive, Baltimore, MD 21218, Email: colina@stsci.edu, holfeltz@stsci.edu, ritchie@stsci.edu

Abstract. This review covers several aspects of NICMOS photometric performance including the selection of the primary spectrophotometric standards, the absolute calibration of NICMOS detectors and their photometric stability. Special issues like relative photometry across the detectors, intra-pixel sensitivity, red leaks and transformations between the HST and ground-based photometric systems are mentioned. Finally, a summary of the different sources of uncertainty when performing photometric measurements with NICMOS is presented.

1. Introduction

The near-infrared wavelength range was opened to HST with the installation of the Near-Infrared Camera and Multi-Object Spectrometer (NICMOS) in February 1997, during the second HST servicing mission. Unaffected by atmospheric absorption and emission, NICMOS covers the entire 0.8 μm to 2.5 μm wavelength range. Similarly, NICMOS, being above the atmosphere, is not forced to adopt filter bandpasses like those used at ground-based observatories matching the near-infrared atmospheric windows. In practice NICMOS does not have a set of filters matching any of the standard ground-based photometric bands and this poses a challenge when trying to achieve precise absolute photometry. On the other hand, NICMOS absolute calibration requires a set of faint spectrophotometric standards covering the entire 0.8μm $-$ 2.5μm wavelength range. Such a set of standards didn't exist before and the selection and generation of NICMOS standards represented additional challenges.

This paper reviews several aspects of NICMOS photometric performance. Details on NICMOS absolute spectrophotometric standards are given in section 2. Section 3 discusses NICMOS absolute photometry. The photometric stability of the cameras and the relative photometry across the detectors are mentioned in sections 4 and 5, respectively. Special issues like intra-pixel sensitivity, red leaks and transformations between HST and ground-based systems are treated in sections 6, 7 and 8, respectively. Finally, several sources of uncertainty when performing absolute calibration with NICMOS are summarized in section 9. This paper does not mention the performance of NICMOS grisms and polarizers as they will be the topic of separate contributions by W. Freudling and D. Hines, respectively.

[1] Affiliated with the Astrophysics Division, Space Science Department, ESA

The reader is recommended to visit the NICMOS Photometry WEB page[2] to check for the latest news regarding the photometric performance of NICMOS.

2. Absolute Spectrophotometric Standards

The absolute calibration of the ultraviolet and optical instruments onboard HST is based on the existence of absolute flux calibrated spectra of a few pure hydrogen white dwarfs (WD) and hot stars, the so called HST set of absolute spectrophotometric standards (Colina & Bohlin 1994; Bohlin, Colina & Finley 1995; Bohlin 1996). The absolute calibration of this set of HST absolute standards in the UV and optical is based on a detailed model spectrum of a hot pure hydrogen white dwarf standard (G191-B2B), transformed into an absolute flux scale using synthetic photometry techniques and accurate Landolt visual photometry (Bohlin, Colina & Finley 1995). This model spectrum covers also the entire NICMOS wavelength range and therefore G191-B2B has been selected as the primary NICMOS white dwarf standard.

An alternative method for calibrating NICMOS uses solar analogs (Campins et al. 1985). Three faint solar analogs were selected by the NICMOS Instrument Definition Team (IDT), and observed on the ground at JHK (E. Green and E. Persson, private communication). Spectra of these three solar analogs were taken with the HST Faint Object Spectrograph (FOS) in the 0.2 μm - 0.8 μm wavelength range to study how accurately their spectral energy distribution matched that of the Sun (Colina & Bohlin 1997). The absolute flux distribution of these three solar analogs covering the ultraviolet to near-infrared range was obtained combining a scaled version of an absolute flux calibrated solar reference spectrum (Colina, Bohlin & Castelli 1996a) with the FOS spectra (Colina & Bohlin 1997). In the near-infrared, the solar reference spectrum was generated computing the energy output of a solar photospheric model using the most recent version of Kurucz ATLAS code (see Colina, Bohlin & Castelli 1996 for details). Of the three solar analogs, the star P330E shows an optical spectrum consistent, within the observational errors, with that of the Sun. P330E has therefore been selected as the primary NICMOS solar analog standard.

3. Absolute Photometry

A preliminary on-orbit absolute photometric calibration of all three NICMOS cameras was obtained in July 1997 soon after the end of the Servicing Mission Observatory Verification (SMOV) phase. This preliminary update was based on on-orbit measurements of a couple of standard stars in 4/5 filters per camera, covering the entire NICMOS wavelength range. The accuracy of the absolute calibration obtained in this way was 10% - 15% for most filters (Colina & Rieke 1997).

An update to the NIC1 and NIC2 photometry, and corresponding photometric keywords that get populated during the calibration pipeline process, was delivered in March 1998. This update is based on the complete NIC1 and NIC2 on-orbit absolute photometry calibration program executed in August 1997 (proposal ID 7691).

---

[2] http://www.stsci.edu/ftp/instrument_news/NICMOS/nicmos_doc_phot.html

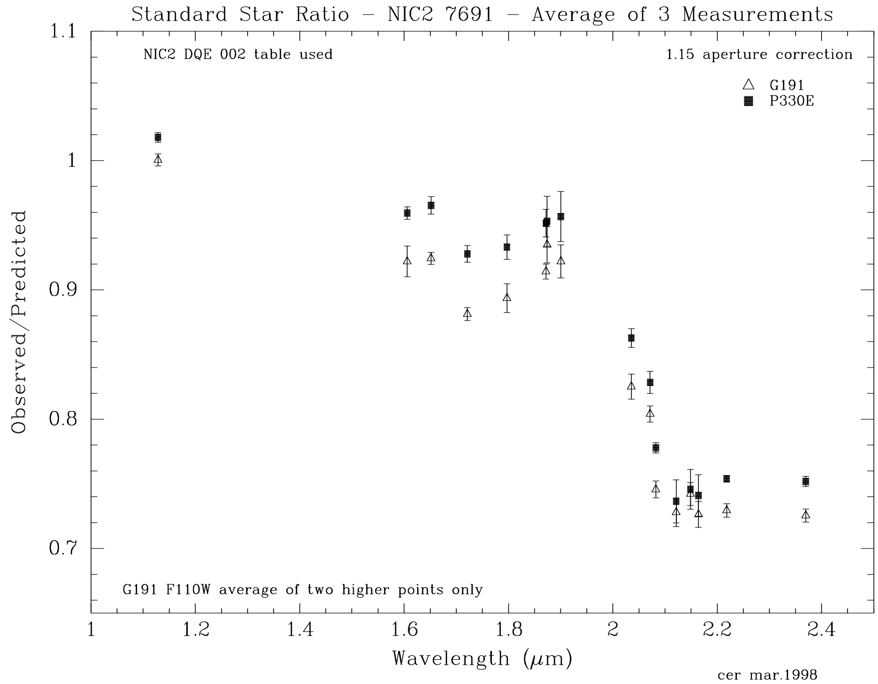

Figure 1. Observed/predicted countrate ratios for stars G191-B2B (white dwarf) and P330E (solar analog) in all NIC2 filters before corrections to the pre-launch predicted countrates were applied.

Images of G191-B2B and P330E were taken through all available NIC1 and NIC2 narrow-, medium- and broad-band filters (32 in total). Independent measurements of each of the stars were taken at three separated positions around the center of the detectors.

Countrates (i.e. counts per second) were measured in the final calibrated images using a 0.5 arcsec radius aperture in both cameras. The total countrates for a nominal infinite aperture have been computed applying an aperture correction equivalent to multiplying the 0.5 arcsec aperture countrates by 1.15, irrespectively of filter.

The observed total countrates obtained in this way were compared with the pre-launch predicted total countrates obtained using synthetic photometry (SYNPHOT) on the spectra of the primary standards for all NIC1 and NIC2 filters (see figure 1 for NIC2 results).

Images of G191-B2B and P330E were also taken with NIC3 during the first NIC3 campaign in January 1998 (proposal ID 7816). To minimize pixelation effects, the countrates were measured in the final calibrated images using a 1.0 arcsec radius. The total countrates for a nominal infinite aperture have been computed applying an aperture correction equivalent to multiplying the 1.0 arcsec aperture countrates by 1.075, irrespectively of filter.

For each filter, the average of the observed/predicted countrates for each of the two stars was used to correct the pre-launch predicted countrates and match them with the observed countrates. These corrections were applied in practice by renormalizing the filter throughputs without changing their shape and without modifying the QE curve

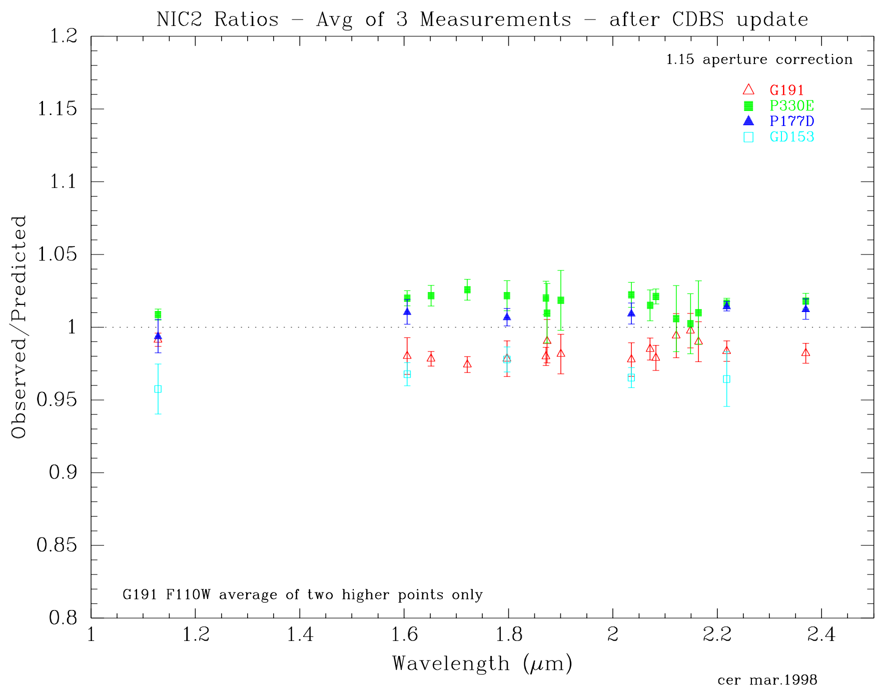

Figure 2. Observed/predicted countrate ratios for the standard stars G191-B2B, GD153 (white dwarfs) and P33OE and P177D (solar analogs) in NIC2 filters after corrections to the pre-launch predicted countrates were applied.

of the detectors. Once the corrections were in place (see figure 2 for NIC2 results), SYNPHOT was used to compute the updated photometric countrate to flux conversion factors for all NIC1 and NIC2 filters.

The main results of the absolute photometry measurements are valid for all three cameras and can be summarized in the following points:

- On average, the pre-launch predicted countrates were off by $\sim$ 10% and $\sim$ 25% in the $0.9 - 2.0$ μm and $2.0 - 2.5$ μm wavelength range, respectively.
- The white dwarf and solar analog absolute photometric scales, as defined by the stars G191-B2B and P330E respectively, have a systematic difference of about 2% in the $0.9 - 1.2$ μm region and of about 4-5% for wavelengths longer than 1.4 μm.
- Measurements of the two primary standards and two additional standards indicate that absolute photometry to better than 5%, and as good as 2%-3% for bright sources can be achieved.

4. Photometric Stability

The long term photometric stability of all three NICMOS cameras is being monitored during Cycle 7 by taking images of a standard star (the solar analog P330E) every

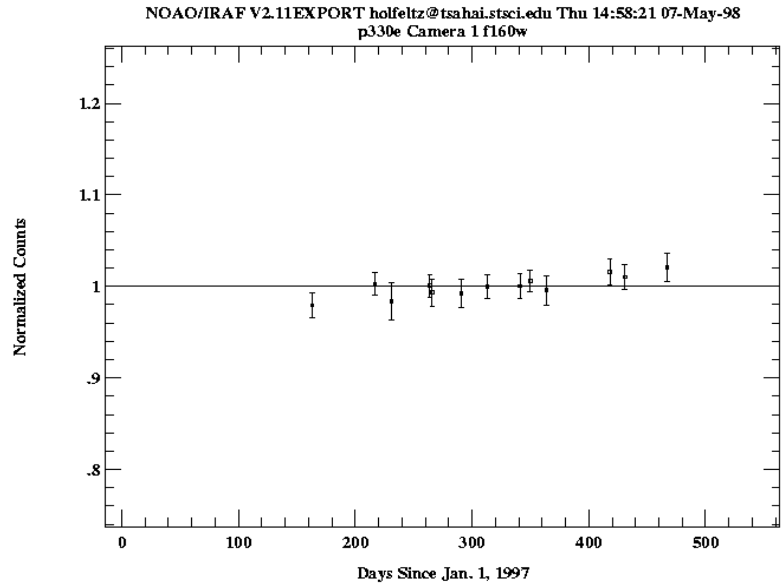

Figure 3. Results of the on-going photometric monitoring program for camera NIC1 and filter F160W.

four weeks. The standard star is observed through several filters spanning the entire wavelength range of NICMOS.

During the period already covered by the monitoring (May 1997 - April 1998), no significant deviations (i.e. larger than 2%) have been measured and the cameras have been photometrically stable to better than 2% (see figures 3 and 4 for an example of the stability of cameras NIC1 and NIC2 at 1.6 μm).

The temperature of the detectors has been rising continuously since the beginning of Cycle 7 and will continue to do so during the next few months. As the temperature increases, the sensitivity of the detectors changes and this could eventually be reflected in changes in the countrates, and therefore in the photometry. Updates with the new results of the photometric monitoring program are posted on a monthly basis on the NICMOS Photometry WEB page.

5. Relative Photometry Across Detectors

Relative photometry across the detectors has been measured for a few filters in all three cameras. Images of the absolute standard P330E (solar analog) were taken at 144 different detector positions using filter F160W for NIC1 and filters F110W and F222M for NIC2 and NIC3 (proposal ID 7693). Data with camera 3 were obtained during the first NIC3 campaign while this camera was in focus. All images were calibrated using on-orbit darks and flats obtained with internal lamps.

The results show that relative photometry for cameras 1 and 2 is better than 2% in the filters for which measurements are available (see figure 5 & 6 for the NIC2 results). Since the images obtained as part of this calibration program have been calibrated using the on-orbit darks and flats reference files available to the observers, there is no reason

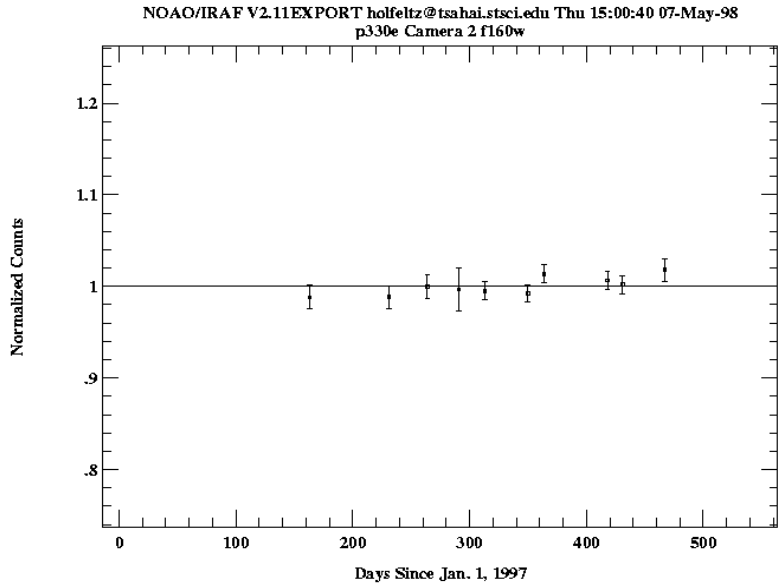

Figure 4. Results of the on-going photometric monitoring program for camera NIC2 and filter F160W.

to believe that a relative photometry at the 2% level, or better, can not be obtained for the rest of the filters in these two cameras, if on-orbit flats are used in the calibration.

The results for camera 3 have to be treated with more caution. For the F110W filter, the one sigma deviation from the mean (11%) is dominated by intra-pixel sensitivity variations (see next section) and not by residuals in the large scale structure of the flats. The results for the F222M filter show that a differential photometry of better than 2% can also be achieved in this camera.

6. Intra-pixel Sensitivity and NIC3 Photometry

As with many other array detectors, the sensitivity of NICMOS detectors is lower near the edges of the pixels than in their centers. It is as though there were small regions of reduced sensitivity along the intra-pixel boundaries. In practical terms this effect means that for a source whose flux changes rapidly on a size comparable with or smaller than the pixel size, the measured countrate, and therefore flux, will depend on where the center of the source lies with respect to the center of the pixel. Because this position is not known a priori, this effect introduces some uncertainty in the flux calibration for a point source.

For NICMOS detectors, this uncertainty is largest for camera 3 at short wavelengths, in which the PSF is largely undersampled. Calibration tests show that uncertainties are indeed largest (11%) in the blue filter (F110W; figure 7), decrease as the wavelength increases ($\sim$ 6% for F160W) and are not measurable at long wavelengths (2 μm and beyond). The effect of the intra-pixel sensitivity on the photometry is less important for observations of extended targets and outside the NIC3 campaigns when the camera is out of focus.

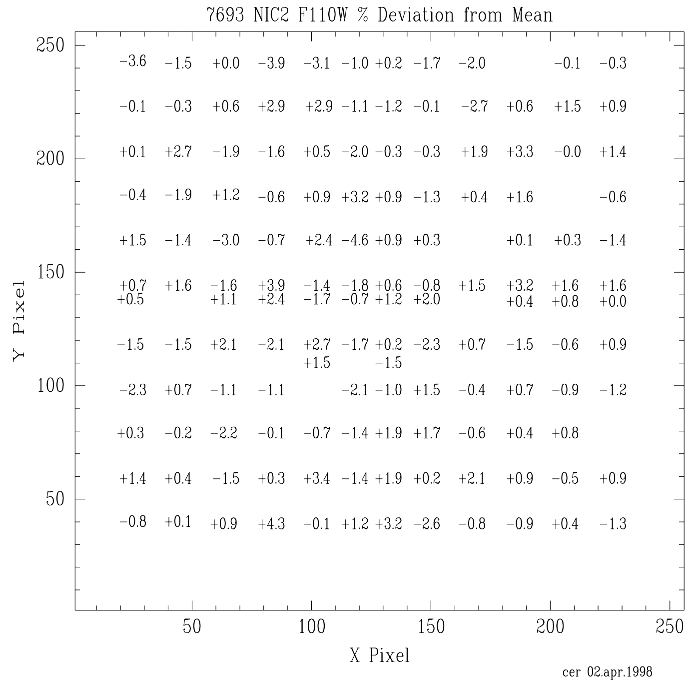

Figure 5. Results of the relative photometry test for filter F110W in camera NIC2. Values indicate the deviations in % from the average.

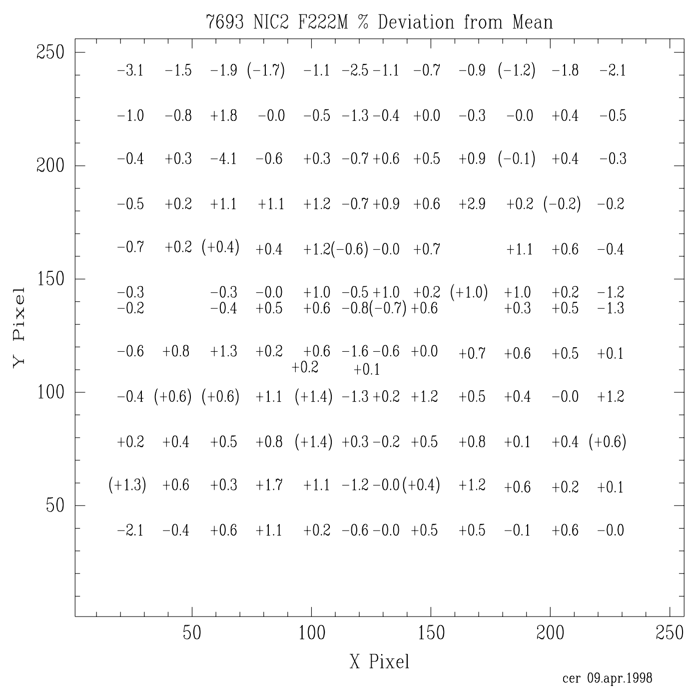

Figure 6. Results of the relative photometry test for filter F222M in camera NIC2. Values indicate the deviations in % from the average.

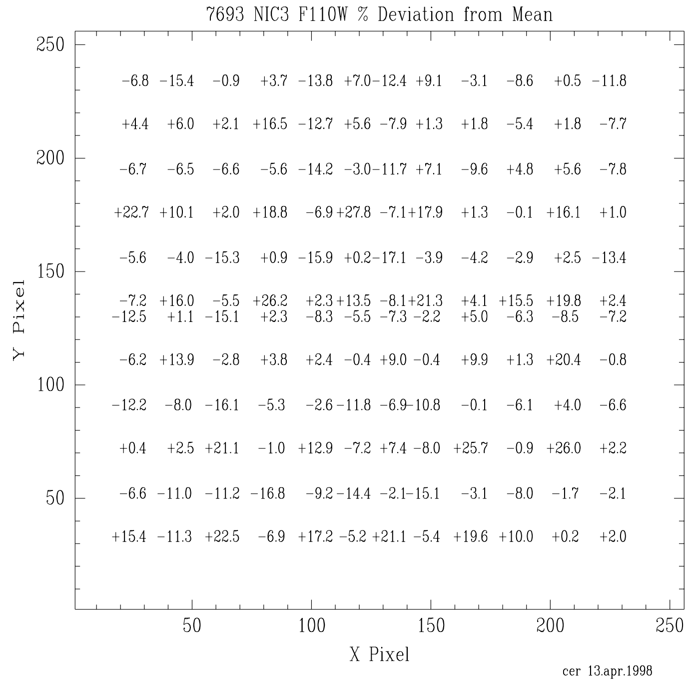

Figure 7. Results of the relative photometry test for filter F110W in camera NIC3. Values indicate the deviations in % from the average. The large deviations observed in this filter are due to the intra-pixel sensitivity variations at short wavelengths.

For high precision photometry and to compute the amount of photometric uncertainty in a given filter, in particular filters in the $1.0 - 1.8$ μm wavelength range, several measurements with subpixel dithering are recommended.

A calibration program designed to quantify the impact of the intra-pixel sensitivity in the NIC3 photometry will be executed in June 1998 during the second NIC3 campaign. The results of this program will be available on the NICMOS photometry WEB page soon after the analysis of the data is completed.

7. Red Leaks

Many very red targets will be observed with NICMOS at short wavelengths (i.e. $\sim$ 1 μm). For these sources the flux at $\sim 2.2\mu$m - 2.5μm could be orders of magnitude larger than at $\sim 1.0\mu$m and therefore exceptionally good out-of-band blocking would be required. The filters for which red leaks might be a problem are F090M, F095N, F097N, F108N, F110M, F110W, and F113N. Images of a red star (Oph S1, J$-$K $\sim$ 3) have been obtained as part of the Cycle 7 calibration plan, the analysis is underway and the results will be posted on the NICMOS Web page. However, photometry of a somewhat less red star (BRI0021, J$-$K $\sim$ 1.3) show no indications of red leaks. Strategies involving observations in multiple filters to model the source spectral energy distribution would be required for very red stars, if red leaks were present.

8. HST versus Ground-based Photometric Systems

The standard HST JHK system is formed by the F110W, F160W and F222M filters. NICMOS images are calibrated in units of *Janskys* and conversions to magnitudes are obtained defining the flux of a zero magnitude star in these filters. The spectrum of a zero magnitude star is defined by the model spectrum of Vega (see Colina, Bohlin & Vastelli, 1996b for details), correcting its flux to match the observed fluxes (i.e multiplying it by 1.05) and assuming Vega has a magnitude equal to 0.02 in all NICMOS bandpasses, as per calibration of Campins, Rieke & Lebofsky (1985).

The set of standard stars observed by HST (Table 1) contains blue stars (white dwarfs), intermediate color stars (solar analogs) and very red stars, and covers a large range in color ($-0.2 \leq J-K \leq 3.0$). This set of standards, together with ground-based measurements, will be used by the NICMOS Instrument Definition Team (M. Rieke and collaborators) to transform the HST magnitudes onto the CIT Arizona system.

Table 1. HST magnitudes for NICMOS standards.

Star	Type	F110W	F160W	F222M
G191-B2B	white dwarf	12.49	12.71	12.83
P330E	solar analog	12.01	11.57	11.49
GD153	white dwarf	14.04	14.23	14.36
P177D	solar analog	12.47	12.02	11.93
BRI0021	red standard	12.45	11.28	10.48
OPH-S1	red standard	9.48	7.45	6.36
CSKD21	red standard	12.26	9.73	8.61

9. NICMOS Photometry. Sources of Uncertainty

There are various sources of uncertainties when performing photometry with NICMOS that could affect the final accuracy of the measurements. In the following, several systematic uncertainties and special cases are mentioned.

9.1. Absolute Spectrophotometric Standards

The white dwarf G191-B2B and the solar analog P330E are NICMOS primary spectrophotometric standards. To assess the accuracy of the G191-B2B model in the near-infrared, two atmosphere flux distributions for exactly the same physical parameters were computed independently by two different experts in this field. The largest differences in the continuum fluxes of the two independent models are 3.5% in the near-infrared at 2.5μm (Bohlin 1996).

The spectral energy distribution of P330E in the 0.4μm - 0.8μm range is the same as the solar reference spectrum, within the uncertainties of the FOS measurements (Colina & Bohlin 1997). Also, the near-infrared spectrum of P330E, created by rescaling the reference spectrum of the Sun (see Colina & Bohlin 1997 for details), agrees to within 2% - 3% with ground-based near-infrared photometry.

In summary, the accuracy of the absolute spectral energy distribution of NICMOS primary standards introduces a systematic uncertainty of about $2\% - 3\%$ in the absolute calibration of the filters.

9.2. Relative Photometry Across Detectors

The photometric values provided in the headers of the images are obtained from measurements of standard stars positioned in the central regions of the detectors. The results of the relative photometry characterization of NICMOS cameras (see section 5 above) indicate that relative photometry to better than 2% can be achieved for all filters in cameras NIC1 and NIC2, and for long wavelength filters ($\geq 2.0\ \mu$m) in NIC3.

9.3. Intra-pixel Sensitivity Variations

No evidence of intra-pixel sensitivity effects has been observed in cameras NIC1 and NIC2. However, as mentioned already (see section 6), the intra-pixel sensitivity affects NIC3 photometry in the $1.0 - 1.8\ \mu$m wavelength range and errors as large as 10-20% can be present, if images are taken without a subpixel dithering strategy. Therefore, subpixel dithering is recommended for high precision photometry.

9.4. PSF Variations

Changes in focus are observed on an orbital timescale due mainly to thermal breathing of the telescope. In addition to this short term PSF variation there is an additional long term NICMOS component, as the cryogen evaporates and the dewar relaxes. This last effect is critical for NIC3 images where the focus of the camera has changed significantly during Cycle 7. In addition, PSF changes as a function of position in the detector. All these effects are believed to affect at the few percent level photometry obtained with small apertures. However, no quantitative measurements are available and therefore Tiny Tim simulations are recommended to study these effects, if high precision is required.

9.5. Aperture Corrections

The photometric conversion factors provided in the header of NICMOS images have been obtained by doing aperture photometry on standards using fixed radius apertures (see section 3 for details). It is often difficult to measure the total flux of a point source using large apertures where the flux contribution from the extended wings of the PSF, diffraction spikes, and scattered light is also included. This is in particular true in crowded fields where the extended wings of well resolved sources could overlap with each other. To take into account aperture correction effects it is advisable to use Tiny Tim PSFs to measure the encircled energy curve of growth as explained in the HST Data Handbook (Voit 1997).

9.6. Color Dependence of Flatfields

The strong wavelength dependence of NICMOS flat-fields limits the photometric accuracy of sources with extreme colors observed in broad-band filters. Simulations with a very red source (J-K = 5 equivalent to a 700K black-body) indicates that these photometric errors are small, around 3% or less (MacKenty et al. 1997). Targets redder than J-K $\sim$ 5 could have photometric errors in excess of 3% for some of the filters.

9.7. Velocity shifts and Photometry with Narrow-band Filters

The photometric conversion factors for all NICMOS filters are obtained from observations of continuum, emission line free, standards. The integrated flux in$erg\ sec^{-1}\ cm^{-2}$ can be obtained as a function of the full width half maximum of the filter and the PHOTFLAM parameter as explained in the HST Data Handbook (Voit 1997). However, if the target has large velocity shifts the emission line does not coincide with the peak transmission of the filter, the line flux will be in error (few to several percent, depending on the filter and velocity shift) and a correction to account for the displacement is required. A method is indicated in the HST Data Handbook (Voit 1997).

Acknowledgments. One of us (L.C.) has benefited from several discussions with Dr. R. Bohlin and Dr. M. Rieke regarding various photometric issues.

References

Bohlin, R.C. 1996, AJ 111, 1743

Bohlin, R.C., Colina, L., & Finley, D.S. 1995, AJ 110, 1316

Campins, H., Rieke, G.H., & Lebofsky, M.J. 1985, AJ 90, 896

Colina, L., & Bohlin, R.C. 1994, AJ 108, 1931

Colina, L., & Bohlin, R.C., & Castelli, F., 1996a, AJ 112, 307

Colina, L., & Bohlin, R.C., & Castelli, F., 1996b, ISR CAL/SCS-008

Colina, L., & Bohlin, R.C. 1997, AJ 113, 1138

Colina, L., & Rieke, M. 1998, The 1997 HST Calibration Workshop, Ed. S. Casertano et al. page 182

MacKenty, J.W. et al. 1997, NICMOS Instrument Handbook, Version 2.0 (Baltimore: STScI)

Voit, M. 1997, HST Data Handbook, Version 3.0 (Baltimore: STScI)

NICMOS and the VLT
Pula, Sardinia, May 26-27th 1998
Wolfram Freudling and Richard Hook, eds.

The Photometric Performance of the NICMOS Grisms

W. Freudling and N. Pirzkal

Space Telescope – European Coordinating Facility
European Southern Observatory
Karl-Schwarzschild-Str. 2
85748 Garching
Germany
Emails: wfreudli@eso.org, npirzkal@eso.org

Abstract.
In addition to broad band, medium band and wide band filter sets, the NICMOS Camera 3 (NIC3) filter wheel contains three grisms. These grisms provide low-resolution slitless spectroscopic capabilities. This article describes the wavelength and throughput calibration of the grisms and discusses the photometric performance of the NICMOS grism mode.

1. Introduction

The NICMOS grisms in camera 3 (NIC3) provide low-resolution slitless spectroscopic capabilities. There are three grisms: G096 covering 0.8 to 1.2 μ; G141 for 1.1 to 1.9 μ and G206 for the 1.4 to 2.5 μ region. The resolution of the first order spectra on all grisms is about 200 per pixel. Second order spectra contain on the order of 1 to 2% of the total detected flux for each object on the grism images. In general, only part of the second order spectra are located on the detector. Since there are no slits, an image of the same field through a matching wide-band filter is needed to obtain a zero point for wavelength calibration. A matching filter with similar throughput as the grism is available for each of the grisms. A standard procedure for the grism observations is to spend a small fraction of the total integration time to obtain the undispersed image.

The optimum focus position for NIC3 is beyond the reach of the PAM focusing mechanism, i.e. NIC3 can only be perfectly focused by moving the secondary mirror of HST. Since such a move prevents other HST instruments from being focused, it is carried out only during special NIC3 campaigns, the next one is planned for June 1998. The optimum position of the focus has continuously been moved over the last few month to a more favorable location. Wavelength and throughput calibration observations have been carried out both during and outside of NIC3 campaigns.

2. Extraction and Calibration of Spectra

A detailed description of the methods used to extract spectra from a grism image with a matching direct image is given in Pirzkal & Freudling (1998a, b and c). Here, we

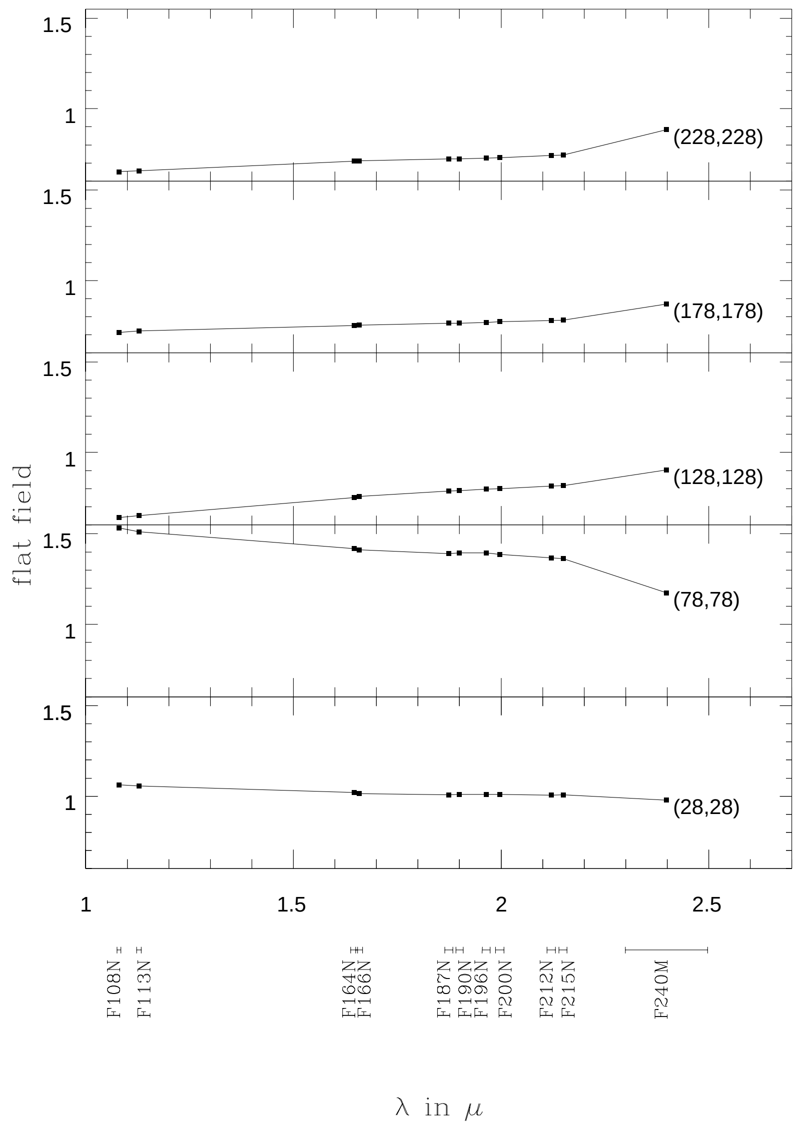

Figure 1. Wavelength dependence of the pixel response for selected pixels on the NIC3 detector. The points are the values of the flat fields of the narrow-band flatfields for the indicated pixel location. The filters used are shown in the bottom of the figure. It can be seen that the pixel response is strongly wavelength dependent and differs for different position on the detector.

briefly summarize the steps relevant for the discussion of the grism calibration given below.

The first step in the extracting is the removal of the background from the location covered by the spectrum. All calibration observations were of sufficient s/n so that the background contribution to the spectrum is small and no differences were found using different background removal procedures.

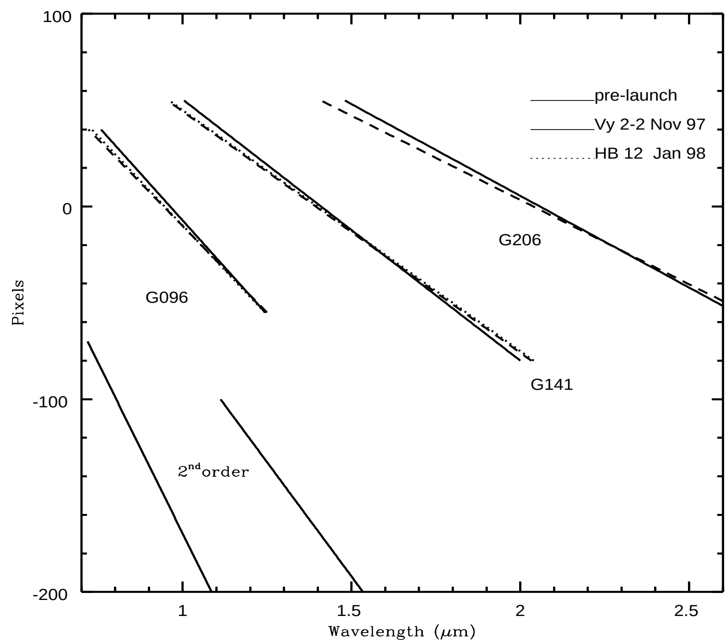

Figure 2. Wavelength as a function of the position within the spectra. The positions are relative to the position of the object on the direct image. Pre-launch measurements as well as in-orbit measurements within and outside of one of the NIC3 campaigns are shown. For the first order spectra, two in-orbit measurement shown derived from 2 different calibration objects and at 2 different epochs are shown, one before the first NIC3 campaign, and one within the first NIC3 campaign.

The flux F_l for a given wavelength bin l is computed from the background subtracted grism image by summing the count rates $g_{x,y}$ at pixel position (x,y)

$$F_l = \sum t_{x,y,l} \cdot w_{x,y,l} \cdot g_{x,y} \tag{1}$$

where the sum is over all pixels contributing to wavelength bin l, $w_{x,y,l}$ is the weight for a given wavelength and pixel position, and $t_{x,y,l}$ is the wavelength dependent inverse sensitivity at a given position on the detector.

For the errors, the error estimate for each pixel is taken from the array 'err' of the input grism image. The error estimate for each wavelength is then the quadratic sum over the same region,

$$\varepsilon_l = \sqrt{\sum (t_{x,y,l} \cdot w_{x,y,l} \cdot \varepsilon_{i,l})^2}. \tag{2}$$

The pixels included in the sums are determined by the position of the object on the direct image, and the location of the spectra relative to the direct image. This relative location is parameterized as a shift and a rotation of the spectrum relative to the rows of the image which contains the object on the direct image. These parameters have been determined for each grism and separately for the first and second order.

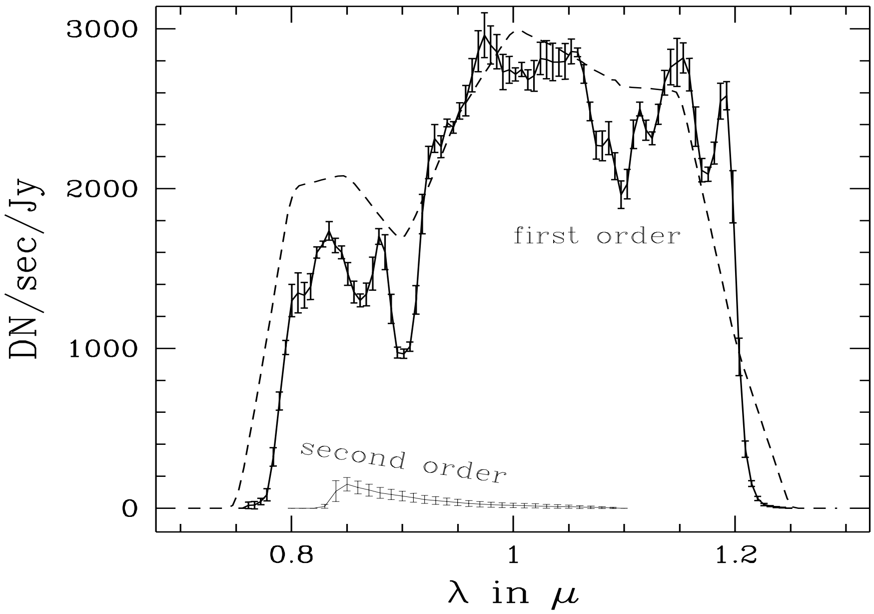

Figure 3. Inverse sensitivity curves for G096 as measured during the first NIC3 campaign in January 1998. For the first order, pre-flight estimates are shown for comparison as a dashed line. The errors are the rms of the different extracted spectra divided by the square root of the number of spectra. The integrated flux in the second order is about 1.5% for a flat spectrum.

For the extraction of the calibration spectra, boxcar functions have been used for the weights. For the flux calibration, fairly large apertures have been used to assure that all the flux is contained in the box.

The inverse sensitivity $t_{x,y,l}$ can be written as $i_l \cdot q_{x,y,l}$, where for a given wavelength l, the function $q_{x,y}$ presents an appropriate normalized monochromatic flatfield. Unfortunately, narrow-band flatfields for the NIC3 camera which can be used to approximate monochromatic flatfields are available only for a very limited number of wavelengths. Figure 1 illustrates the situation. The wavelength dependence of the flatfield response of individual pixels differs substantially over the detector. Currently, the only way to estimate the pixel response for a given wavelength is to use this limited data set and interpolate between the wavelengths of the available filters. The limited measurements of this response is a major contribution to our uncertainty in the flux calibration.

The purpose of the wavelength calibration is to find the relation between the pixel position relative to the undispersed objects l and the wavelength $\lambda(l)$. The purpose of the flux calibration is to find the inverse sensitivity $i(\lambda)$ as a function of wavelength in mJy/DN/sec.

3. Wavelength Calibration of NICMOS Grisms

NICMOS has no internal lamps for wavelength calibration. Therefore, objects with strong IR line emission must be used for in-orbit wavelength calibration. For slitless spectroscopy, wavelength calibrators should be compact. The best wavelength calibrators for NICMOS seem to be compact planetary nebulae. The Planetary nebulae Vy

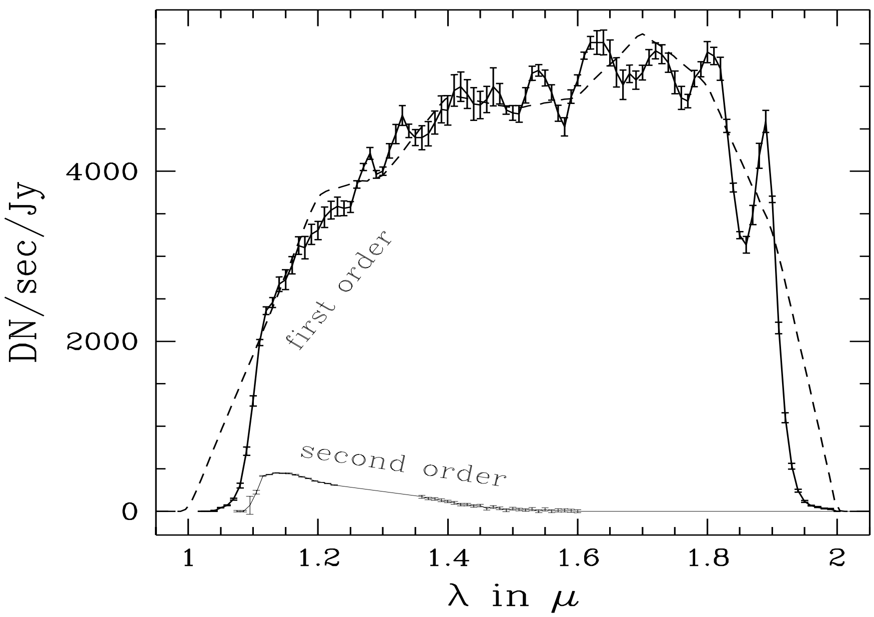

Figure 4. Inverse sensitivity curves for G141 as measured during the first NIC3 campaign in January 1998. For the first order, pre-flight estimates are shown for comparison as a dashed line. Note the region in the second order spectrum sensitivity without error bars. For that region, no measurements could be carried out. The superimposed curve in that region is an interpolation. The total amount of flux in the second order is about 1.8% for a flat spectrum.

2-2 and HB12 have been used for that purpose. Currently, HB12 is routinely used for monitoring the wavelength dispersion.

The dispersion of the grisms, i.e. the wavelength as a function of position relative to the coordinate of the object on the direct images, have been parameterized as linear relations. Polynomials of higher order have been tried but did not result in better fits. The parameters of the the dispersion relation were determined by correlation of the extracted spectra with ground based spectra of Vy 2-2 provided by Hora et al., 1998. The in-orbit measurements of the dispersion relation are significantly different from the pre-launch measurements, but no significant changes in the parameters of the relation have been observed in the repeated in-orbit measurements. As an illustration, the dispersion relations for 2 epochs are plotted in figure 2 and compared to the pre-launch measurements. The main uncertainty in the wavelength calibration is the exact location of the object on the direct image. The uncertainty for an individual spectrum is about 0.5 pixels. This translates into an uncertainty of the wavelength calibration of less than 0.005μ. Within this uncertainty, no dependence of the dispersion relation on the position on the NICMOS detector. Similarly, no systematic change in time has been detected so far.

The dispersion relations of second order spectra were determined by cross-correlating the extracted spectra of both orders and using the calibration of the first order with the ground-based data.

4. Throughput Calibration

The white dwarf G191-B2B and the solar analog P330 have been adopted as flux calibrators for NICMOS. Each grism calibration observations consists of at least three different direct image / grism image pairs, with the calibrator positioned at different locations on the NICMOS detector for each individual observation. The first order spectrum from each pair of images was extracted in instrumental units (DN/sec).

For both calibrators, model spectra scaled to measurements at shorter wavelengths are available, for details see Colina (1998, this workshop). The spectra as given by Colina & Bohlin 1997 (for the solar analog P330), and Bohlin & Colina & Finley 1995 and Bohlin 1996 (for the white dwarf G191-B2B) have been used for the grism calibration.

Inverse sensitivity curves for first order spectra were derived by dividing the individual spectra by the model spectrum of the respective calibrator and computing the average of all spectra from the two flux calibrators. Figures 3, 4 and 5 show the derived sensitivities for G096, G141 and G206, respectively. The uncertainty for each point in the sensitivity curves is the rms from all extracted spectra divided by the number of spectra.

Inverse sensitivity curves for second order were derived from archive grism images taken for the public parallel program. Spectra were extracted for bright objects with both first and second order spectra on single grism images. The relative extracted flux for both orders in combination with the first order sensitivity calibration was used to derive the sensitivity of the second order. Since the field of view of grism observations do not allow for both orders to be completely contained in single images, several images had to be used to derive the sensitivity for the whole wavelength range of grisms G098 and G141. The available data did not allow to derive a calibration for the second order of G206.

5. Photometric Accuracy of Extracted Spectra

The sensitivity curves for the first order spectra presented in the previous section have typical uncertainties per point of about 5 to 10%. These errors have been estimated from the differences of individual extracted spectra. We have separated the inverse sensitivity by the calibrator used to derive them and found that integrated over the whole bandpass systematic differences are smaller than 2%. Statistical error as computed from the error array of the grism images are also small compared to the errors shown above. The origin of the uncertainty in the sensitivities are differences in the spectra extracted at different positions on the detector. Presumably, these differences are due to our lack of knowledge of the difference in the wavelength dependence of the individual pixel response. As mentioned in section 2., these differences are currently approximated by the response of narrow-band flats which do not sample the full range of wavelength of the grisms very well. For that reason, the flux calibration of a single spectrum can be up to 20 to 30% uncertain. This is within the goal of the original calibration plan.

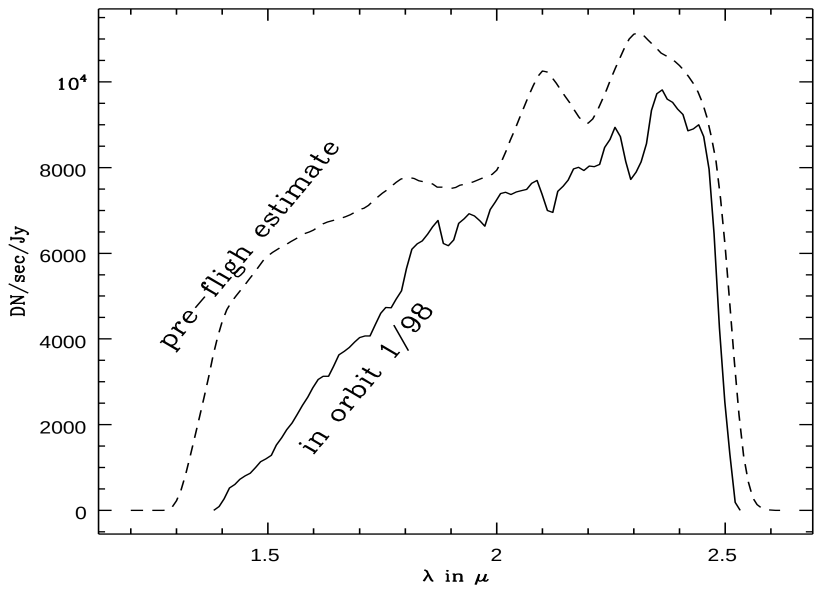

Figure 5. Inverse sensitivity curves for G206 as measured during the first NIC3 campaign in January 1998. The pre-flight estimates are shown for comparison as a dashed line.

6. Summary

We are carrying out wavelength and flux calibrations of the NICMOS grisms. The uncertainty in the flux calibration is about 5-10% for the first order spectra, the uncertainty in the wavelength calibration is less than 0.005μ. Files with the most recent calibration data can be obtained from http://ecf.hq.eso.org/nicmos/. The monitoring of wavelength and throughput calibration will continue until the end of 1998.

References

Bohlin & Colina & Finley 1995, AJ 110, 1316

Bohlin 1996, AJ 111, 1743

Colina, 1998, this proceedings.

Colina & Bohlin 1997, 113, 1138

Pirzkal, N., Freudling, W., this proceedings.

Pirzkal, N., Freudling, W., 1998a, NICMOSlook manual, Version 2.1 (Garching: ST-ECF)

Pirzkal, N., Freudling, W., 1998b, Calnic C Manual, Version 2.1 (Garching: ST-ECF)

Hora, Latter & Deutsch, 1998, in preparation

NICMOS and the VLT
Pula, Sardinia, May 26-27th 1998
Wolfram Freudling and Richard Hook, eds.

ST-ECF Grism Spectrum Software for NICMOS Grism Data

N. Pirzkal & W. Freudling

Space Telescope - European Coordinating Facility, Karl-Schwarzschild-Str. 2, D-85748 Garching, Germany

Abstract. A unique capability of NICMOS is its grism mode which permits slitless spectrometry at low resolution. Extracting spectra from a large number of NICMOS grism images requires a convenient interactive tool which allows a user to manipulate direct/grism image pairs. NICMOSlook and Calnic-C are IDL programs designed for that purpose at the Space Telescope – European Coordinating Facility[1]. NICMOSlook is a graphical interface driven version of this extraction tool, while Calnic C is a program which performs the same functionality in a “pipeline“ approach.

1. NICMOSlook and Calnic C

NICMOSlook and Calnic-C are two programs that were designed to take advantage of the fact that the NICMOS grism mode typically consists of taking both a direct and a grism image. Both NICMOSlook and Calnic-C use the direct image to determine which objects are to be extracted, their location, size, and orientation. The programs allow the user to extract spectra using a range of extraction techniques.

NICMOSlook, which has an IDL user interface based on STISlook from Terry Beck, is designed to allow a user to interactively and efficiently extract spectra from a small batch of data. The user maintains full control over the extraction process. NICMOSlook was designed to be most useful to users who want to quickly examine data or fine tune the extraction process.

The stand-alone version, Calnic C, is meant to be used on larger sets of data and requires only a minimum amount of user input. Both programs can be fully configured and extended through the use of a few configuration and calibration files. Figure 1 presents an overview of the spectral extraction process.

2. Features overview

2.1. Image Display

NICMOSlook provides a variety of display options to examine the direct and grism images (Figure 2). These options include color tables, zoom factors, row/cut plots, and blinking between the two images. Some basic image filtering and processing capabili-

[1] http://ecf.hq.eso.org

ties are also available to facilitate the identification of objects.
Calnic-C outputs Postscript finding charts which contain the direct and grism images with the objects and spectra clearly numbered and marked (Figures 4 and 5).

2.2. Object Identification

With NICMOSlook, objects can be identified automatically using either the DAOFIND algorithm, by using a text file containing the objects coordinates, or can be provided interactively by the user by marking specific objects in the direct image. NICMOSlook and Calnic-C account for the size and orientation of the objects when extracting their spectrum (Figure 3).
Calnic-C uses the more sophisticated SExtractor (Bertin 1996) program to automatically locate and determine the size and orientation of objects in the direct images. Calnic-C can also be made to extract only objects that are listed in an input list.
With both programs, and if using an input object list, the RA and DEC of objects can be used rather than simply the pixel coordinates of the objects in the direct image. This feature requires that a WCS be available in both the direct and grism images FITS headers.

2.3. Determination of the location of the spectrum

The positions of the objects are used in combination with the appropriate coordinate transformation to determine the location and extend of spectra in the grism image. The zeroth, first, and second spectral orders can be automatically located on the grism image (Figure 3). The direct and grism images do not need to have been taken with exactly the same telescope pointing since NICMOSlook and Calnic-C can additionally make use of the WCS information to locate the spectra in the grism image.

2.4. Spectral Extraction

Weighted or unweighted spectral extractions can be performed. Objects can be extracted as point sources (In which case, a Tiny Tim profile is used during the spectral extraction) or as extended objects (In which case a spectral profile is determined by first computing the profile of the object in the direct image).

2.5. Background Subtraction

The programs estimate the amount of background light in a spectrum. A region containing no spectrum is first identified in the vicinity of the spectrum of interest (Figure 6). This region is then either used to scale a pre-computed model background, or is linearly interpolated to estimate the level of the background were the spectrum is located.

2.6. Wavelength and Flux calibrations

A wavelength is assigned to each pixel of the spectrum in the grism image using the knowledge of where the object is located in the direct image and using the dispersion relation of the grism used. A flatfield is then constructed by taking into account that different pixels in the grism image correspond to different wavelengths. NICMOSlook and Calnic-C compute the flatfield coefficient of a specific pixel at a specific wavelength by interpolating the narrow band filter flatfield coefficients of the same pixel. Inverse sensitivity curves are then applied to the extracted spectra to produce a final extraction product that is wavelength and flux calibrated (Figures 7 and 8).

2.7. Deblending

An attempt can be made to automatically remove the spectral contamination caused by the presence of nearby objects. The only assumption made by the method used is that the shape of the object is not wavelength dependent.

2.8. Spectral lines search

Emission and absorption lines are automatically identified in the resulting spectra, and the continuum emission is automatically determined.

2.9. Result Output

The final data products are plots on the screen (Figures 7 and 8), binary FITS tables and postscript files with the spectra, error estimates, object parameters derived from the direct imaging, and details of the spectrum extraction process (Figure 9). Calnic-C additionally outputs finding charts to locate the objects and their spectra in the direct and grism images

3. Supported platforms and availability

- NICMOSlook is written entirely in IDL. It runs under either IDL 4.0 or IDL 5.0.
- The "pipeline version" Calnic C shares most of the code of NICMOSlook but also requires the successful compilation of SExtractor 1.0a (Bertin 1996) which is written in C..
- NICMOSlook, Calnic C, and their respective User's Manual can be downloaded from *http://ecf.hq.eso.org/nicmos*

References

Bertin, E., Arnouts, S., 1996, A&A, 117, 393

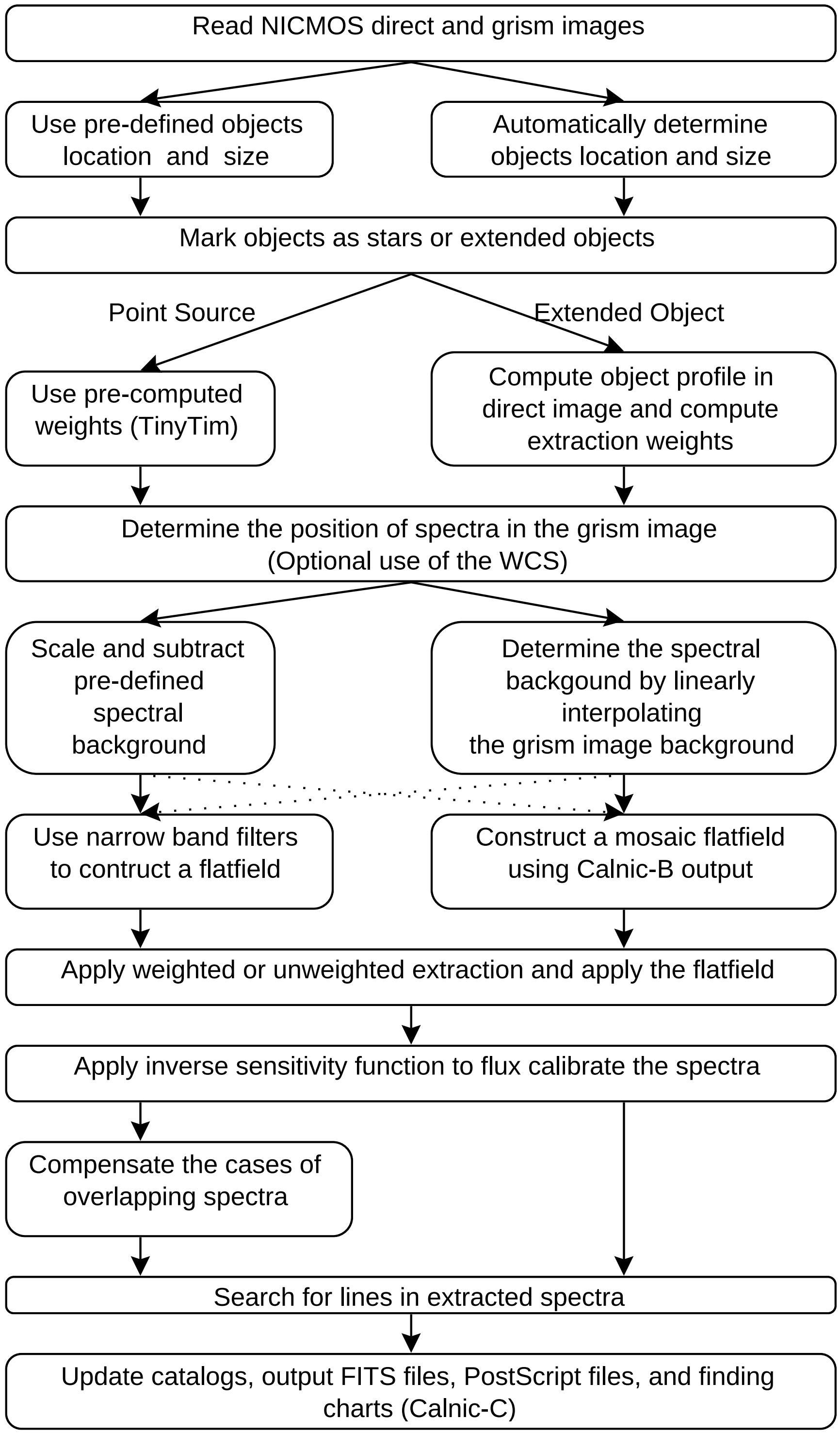

Figure 1. Overview of NICMOSlook and Calnic-C

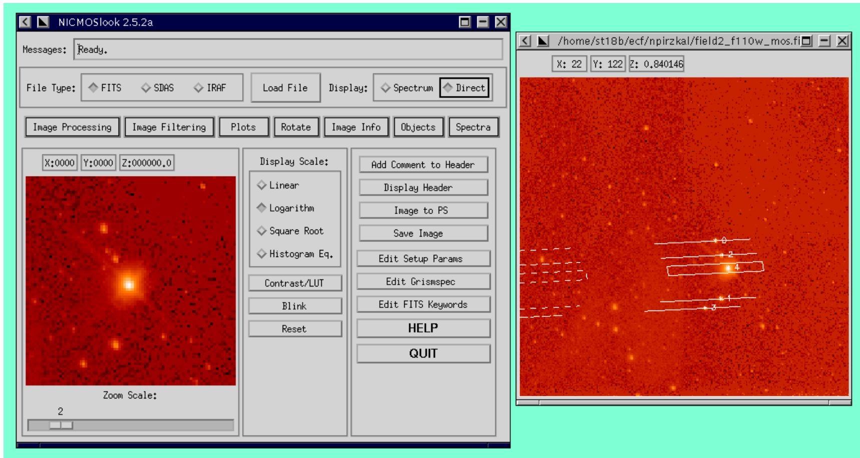

Figure 2. The NICMOSlook user interface

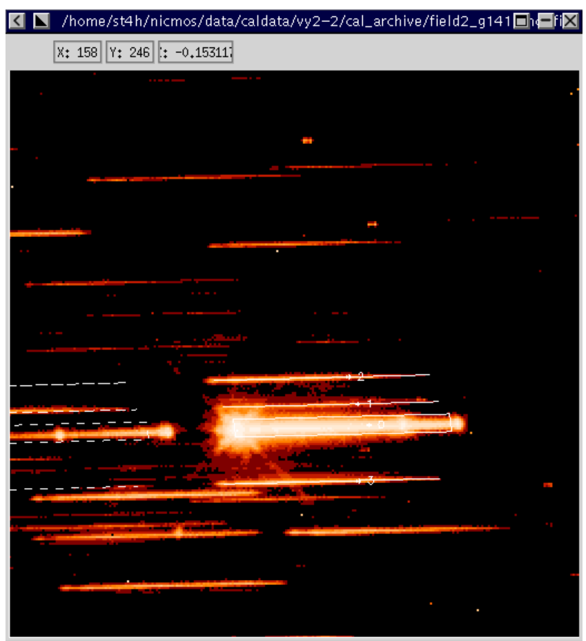

Figure 3. Grism image displayed by NICMOSlook with the identified objects marked. First order spectra are marked with full lines, second order spectra are marked with dashed lines

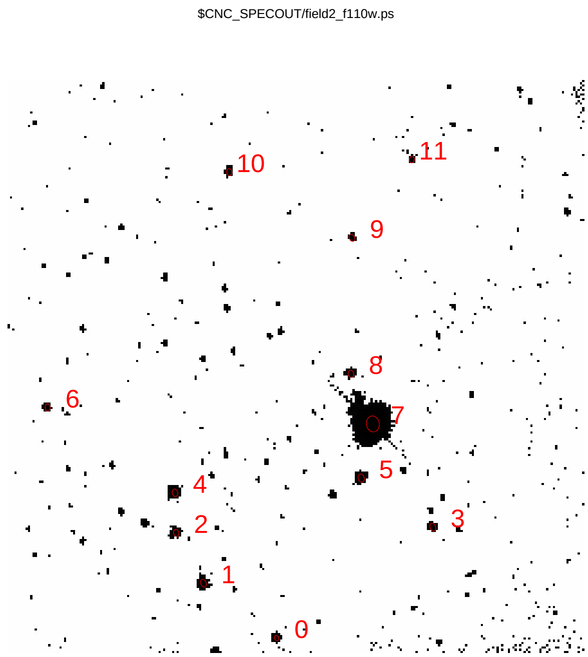

Figure 4. Direct image Postscript finding chart output by Calnic-c

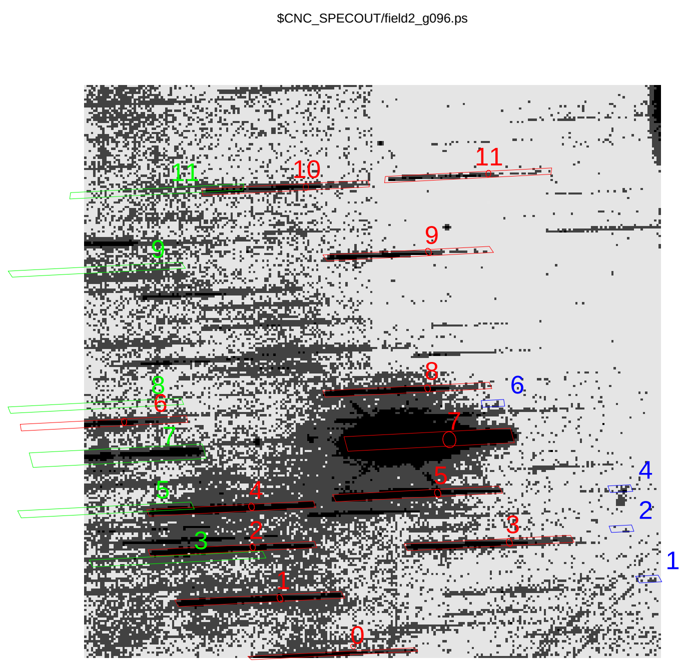

Figure 5. Grism image Postscript finding chart output by Calnic-c

Figure 6. Display of the areas used to determine the background spectral contamination

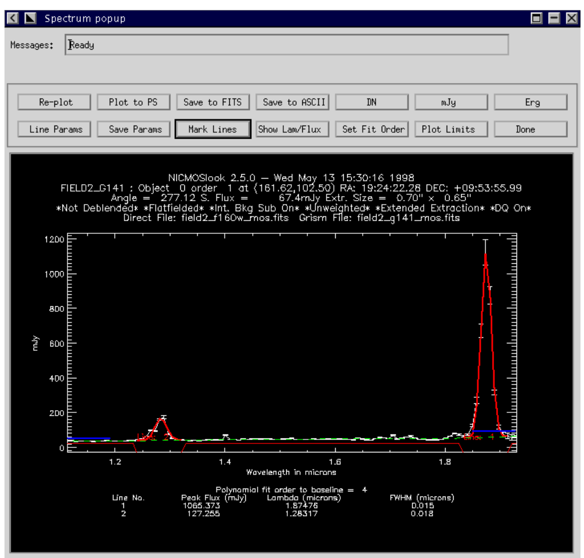

Figure 7. Result of a first order extraction of Vy-22

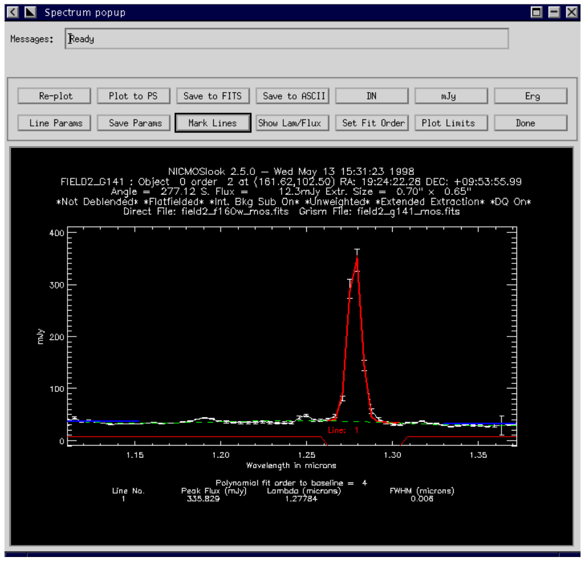

Figure 8. Result of a second order extraction of Vy-22

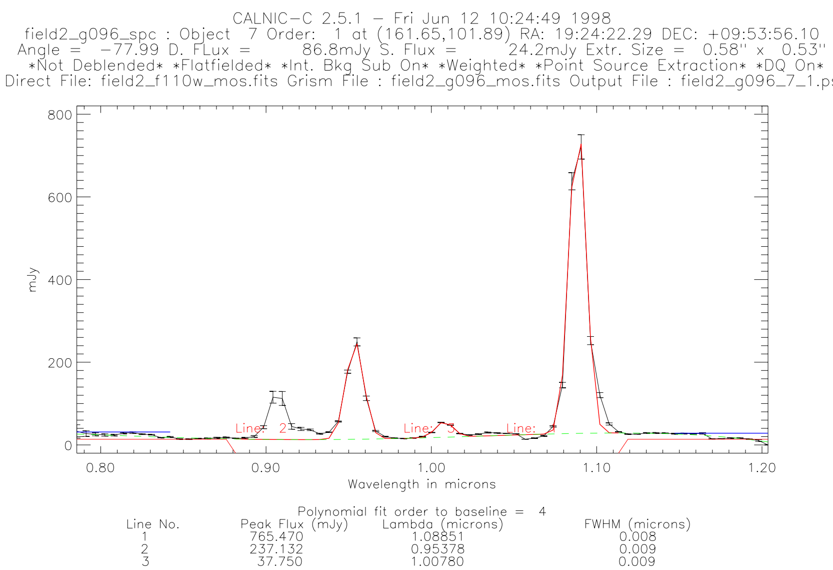

Figure 9. Postscript output of Calnic-C

NICMOS and the VLT
Pula, Sardinia, May 26-27th 1998
Wolfram Freudling and Richard Hook, eds.

Imaging Polarimetry with NICMOS

D. C. Hines[1]

Steward Observatory, The University of Arizona, Tucson, AZ 85721

Abstract. The Near Infrared Camera and Multi-Object Spectrometer (NICMOS) contains optics which enable imaging polarimetry at 1 & 2 microns with unprecedented detail. The preflight Thermal Vacuum tests revealed that each polarizer has a unique polarizing efficiency, and that the position angle offsets differ from the nominal positions of 0°, 120° & 240°. Therefore, to properly reduce polarimetry data obtained with NICMOS, a new algorithm different from that needed for an ideal polarizer was developed. I discuss this new algorithm, its successful application to NICMOS observations, and its more general use for data obtained with other instruments. I also present estimates of the NICMOS Instrumental Polarization, and discuss both the sensitivity of the Grisms to polarized light and the accuracy of NICMOS imaging polarimetry for faint and low polarization objects.

1. Introduction

Studies of polarized light have brought about profound changes in our understanding of astronomical objects, especially within the last two decades with the advent of sensitive, large format imaging arrays such as optical CCDs and the NICMOS3 infrared arrays. Imaging of linearly polarized light from young stellar objects, bipolar nebulae, radio galaxies and hyperluminous infrared galaxies has shown that disks of dusty gas play a key role in the birth and death of stars, and can strongly influence the appearance of quasars and QSOs.

The Near Infrared Camera and Multi-Object Spectrometer (NICMOS) contains optical elements which enable high spatial resolution, high sensitivity observations of linearly polarized light from $0.8 - 2.1\mu$m. The filter wheels for Camera 1 (NIC1) and Camera 2 (NIC2) each contain three polarizing elements sandwiched with band-pass filters. The design specifies that the position angle of the primary axis of each polarizer (as projected onto the detector) be offset by 120° from its neighbor, and that the polarizers have identical efficiencies. While this clean concept was not strictly achieved, the reduction techniques described below permit accurate polarimetry using both the short- and long-wavelength cameras over their full fields of view.

[1]NICMOS Project, The University of Arizona

2. Thermal Vacuum Tests

Preflight thermal vacuum tests on NICMOS included an extensive characterization of the polarimetry optics. We also measured the overall sensitivity of the non-polarimetry optics to polarized light. A polarizing element attached to the CIRCE standard light source provided uniform illumination of the entire field of view with light of known polarization and position angle.

Polarizing efficiencies[2] and absolute polarizer position angles (relative to the NICMOS entrance aperture) were derived for each polarizer in NIC1 and NIC2 from images obtained at 20° increments of the calibration polarizer position angle. The same method, but without the NICMOS polarizers in place, was used to to evaluate the polarization signature imparted by the mirrors which comprise the NICMOS imaging system, and to characterize the sensitivity of the NIC3 Grisms to polarized light.

The Thermal Vacuum tests showed that:

- Each polarizer in each camera has a unique polarizing efficiency.
- The offsets between the position angles of the polarizers within each filter wheel differ from their nominal values of 120°.
- The instrumental polarization caused by reflections off the mirrors in the NICMOS optical train is small ($\lesssim 1\%$).
- The Grisms are slightly sensitive to the orientation of incoming polarized light, with G206 showing the largest variation in intensity ($\sim 5\%$) for completely polarized light. This effect scales with percentage polarization and will be negligible for the majority of astronomical situations.

3. The HSL Algorithm for Reducing NICMOS Polarimetry Observations

The "standard theory" polarimetry reduction algorithm outlined in the original NICMOS Manual (Axon et al. 1996) assumes that the polarizers have uniform and perfect (100%) polarizing efficiencies, and that the position angles of the primary axis of the polarizers are offset by exactly 120°. The thermal vacuum tests showed that the NICMOS polarizers are not ideal, so a more complex technique is required. The new algorithm developed by Hines, Schmidt & Lytle (1997; hereafter HSL) is presented below.

The observed signal from a polarized source of total intensity I and linear Stokes parameters Q and U measured through the k^{th} polarizer oriented with a position angle[3] ϕ_k is

$$S_k = A_k I + \varepsilon_k (B_k Q + C_k U), \tag{1}$$

---

[2]Polarizer efficiency is defined as $\varepsilon = (S_{\rm par} - S_{\rm perp})/(S_{\rm par} + S_{\rm perp})$, where $S_{\rm par}$ and $S_{\rm perp}$ are the respective measured signals for a polarizer oriented parallel and perpendicular to the axis of a fully polarized beam.

[3]Polarizer position angle as measured from the NICMOS Aperture Offset Angle of 224.52°, about the aperture center toward the +U3 axis.

where

$$A_k = \frac{1}{2} t_k (1 + l_k),\; B_k = A_k \cos 2\phi_k,\; C_k = A_k \sin 2\phi_k,$$

and ε_k is the polarizing efficiency, t_k is the fraction of light transmitted for a 100% polarized input aligned with the polarizer's axis, and l_k is the fraction transmitted (exclusive of that involved in t_k) when the incoming light is perpendicular to the axis of the polarizer (see Table 1). The values of t_k were initially determined by the filter manufacturer, and were not accurately remeasured in thermal vacuum tests (HSL). However, recent observations of unpolarized and polarized standard stars have allowed us to refine these values.

Table (1) presents the properties of the individual polarizers as determined in preflight thermal vacuum tests and by the on-orbit standard star observations. Table (2) lists the coefficients derived from these parameters for use solving Eq. (1).

Table 1. Characteristics of the NICMOS Polarizers

Filter	ϕ_k[a]	ε_k	t_k (on-orbit)[b]	l_k	Comments
POL0S	1.42	0.9717	0.7660	0.0144	...
POL120S	116.30	0.4771	0.5946	0.3540	Possible "ghost" images
POL240S	258.72	0.7682	0.7169	0.1311	...
POL0L	8.84	0.7313	0.8981	0.1552	...
POL120L	131.42	0.6288	0.8551	0.2279	...
POL240L	248.18	0.8738	0.9667	0.0673	...

[a] As measured from the NICMOS aperture 224.52° about the +U3 axis.

[b] Derived from on-orbit observations of the unpolarized standard BD 32° 3739 (Schmidt, Elston & Lupie 1992).

Table 2. Coefficients for Simultaneous Solution of Equation (1)[a]

Filter	A_k	$\varepsilon_k B_k$	$\varepsilon_k C_k$
POL0S	+0.3936	+0.3820	+0.0189
POL120S	+0.4025	−0.1166	−0.1526
POL240S	+0.4054	−0.2876	+0.1195
POL0L	+0.5187	+0.3614	+0.1152
POL120L	+0.5250	−0.0411	−0.3276
POL240L	+0.5159	−0.3262	+0.3111

[a] Based on thermal vacuum data and the on-orbit determination of t_k (Table 1).

After solving the system of equations (Eq. 1) to derive the Stokes parameters at each pixel (I,Q,U), the percentage polarization (p) and position angle (θ) at that pixel are calculated in the standard way:

$$p = 100\% \times \frac{\sqrt{Q^2+U^2}}{I}, \theta = \frac{1}{2}\tan^{-1}\left(\frac{U}{Q}\right).$$

[*Note that the arc-tangent function is implemented differently on different systems and programming environments, so care must be taken to ensure that the derived angles place the electric vector in the correct quadrant.*]

4. On-Orbit Calibration

Observations of a polarized star (CHA-DC-F7: Whittet et al. 1992) and an unpolarized (null) standard (BD 32° 3739: Schmidt et al. 1992) were obtained with NIC1 and NIC2 (Cycle 7 CAL 7692, 7958: Axon). The observations used a four position, "spiral-dither" pattern with 20.5 pixel offsets to improve sampling and alleviate the effects of bad pixels, cosmic rays, some persistence, and other image artifacts. Two epochs were chosen such that the differential telescope roll between observations was $\sim 135^\circ$.

Since the thermal vacuum tests showed that the imaging system had little effect on the observed polarization, any measured polarization in the null standard was attributed the t_k term in the HSL algorithm. Applying our refined coefficients to the polarized star data yielded a measured percentage polarization within 0.3% of the published value. Table 3 presents the results.

Table 3. Polarization Measurements of CHA-DC-F7

Band	p (%)	σ_p[a] (%)	θ (°)	σ_θ[a] (°)
J (ground)[b]	3.19	0.05	118	2
1μm (Epoch 1)	3.44	0.5	111	4
1μm (Epoch 2)	3.31	0.5	108	4
K (ground)[b]	1.19	0.01	126	4
2μm (Epoch 1)	0.97	0.2	119	6
2μm (Epoch 2)	1.00	0.2	119	6

[a]Conservative upper limits for the uncertainties were estimated from the variation between results obtained from individual "dither" positions in each epoch.

[b]Whittet et al. (1992)

5. On-Orbit Results

Polarimetry data were obtained for IRC +10216 and CRL 2688 with NIC1 and NIC2 respectively as part of the Early Release Observations program. Descriptions of the observations can be obtained on the STScI website via the Cycle 7 proposal number or PI name (ERO 7120: Skinner; ERO 7115: Hines). Overall, the NICMOS and ground-based polarimetry agree remarkably well, once the NICMOS polarimetric images have been binned to match the spatial resolution of the ground-based images.

5.1. NIC1 – IRC +10216

Figure 1 presents the NICMOS polarimetry results for IRC +10216 (Skinner et al. 1997) compared with the ground-based data from Kastner & Weintraub (1994). The polarization map derived by processing the NICMOS data with the new HSL algorithm (center panel) agrees well with the ground based data. In contrast, polarization images derived by using the "standard theory" underestimate the polarization and lead to incorrectly oriented electric vector position angles. Variations of the percentage polarization in relatively uniform regions of the HSL-reduced IRC +10216 data suggest uncertainties $\sigma_{p,\mathrm{meas}} \lesssim 1-3\%$ (in percentage polarization per pixel), and comparison with the

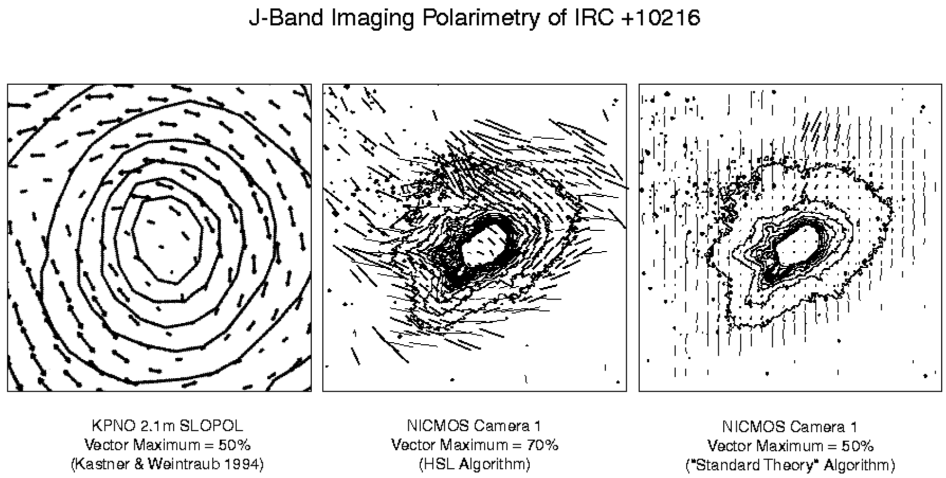

Figure 1. (after HSL) J-Band Imaging Polarimetry of IRC +10216 observed from the ground (Kastner & Weintraub 1994), compared with data obtained using NICMOS Camera 1 and reduced with the HSL and "standard theory" algorithms. The data reduced with the HSL algorithm agree well with the ground based data. For clarity, the NICMOS polarization vectors are plotted for 5×5 pixel bins, and the faintest and brightest intensity contours have been omitted.

ground-based data suggests an uncertainty in the position angles $\sim 2^\circ$ in a 5×5 pixel bins (Fig. 1).

5.2. NIC2 – CRL 2688

Figure 2 presents the NICMOS polarimetry results for CRL 2688 compared with observations obtained from the ground (Sahai et al. 1998). In this case the ground-based data are of exceptional quality and allow a more detailed comparison than for IRC +10216. Overall, the NICMOS and ground-based data agree quite well and show centrosymmetric patterns of position angle within the polar lobes.

Other, more subtle, features of the polarization morphology that are seen in the ground-based polarization map are reproduced precisely in the NICMOS map, confirming that the NICMOS polarimetry is well calibrated. However, the superior resolution of the NICMOS data reveals polarization features that are not apparent in the ground-based polarization map. In particular we note the very high polarizations ($\sim 70 - 80\%$) in the arcs and filamentary structures — features that are washed out (beam averaged) in the ground-based images resulting in lower observed polarization. As for IRC +10216,

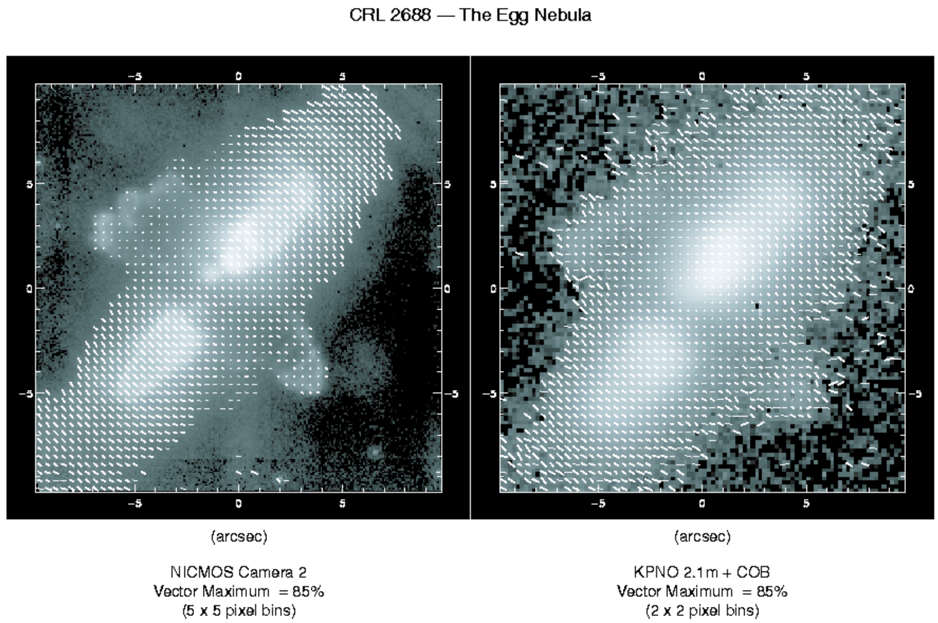

Figure 2. (after HSL) 2μm Imaging Polarimetry of CRL 2688 (The Egg Nebula) using NICMOS Camera 2, and the Cryogenic Optical Bench (COB) attached to the 2.1m at Kitt Peak (courtesy of J. Kastner). For clarity, the vectors in the NICMOS and COB data are binned by 5×5 and 4×4 pixels respectively.

uncertainties in the spacecraft data are estimated to be $\sim 1-3\%$ in percentage polarization, and $\sim 2^\circ$ in the position angles.

6. NICMOS Imaging Polarimetry

As illustrated by the calibration data and EROs discussed above, the NICMOS system is capable of producing accurate imaging polarimetry. The refined coefficients of the HSL algorithm enable investigation of polarization to lower limits than had originally been estimated by HSL.

Limiting Polarization: Because the errors for percentage polarization follow a Rice distribution, precise polarimetry requires measurements such that $p/\sigma_{p,\mathrm{meas}} > 4$ (Simmons & Stewart 1985). Therefore, uncertainties $\sigma_{p,\mathrm{meas}} \approx$ 0.5-3% (per pixel) imply that objects should have minimum polarizations of at least 2-12% per pixel. Binning the Stokes parameters before forming the percentage polarization (p) and the position angles reduces the uncertainties by $\sim 1/\sqrt{N}$, where N is the number of pixels in the bin. Uncertainties as low as 0.2% should be achievable with bright objects.

Limiting Brightness of the Target: In a perfect photon-counting system, $\sigma_{p,\mathrm{phot}} \approx \sqrt{2/E}$, where E is the total number of photons counted. For CRL 2688, the signal strength even in regions of low intensity (e.g. the H_2-emitting torus) should have produced $\sigma_{p,\mathrm{phot}} \lesssim 1\%$. We measure $\sigma_{p,\mathrm{meas}} \approx 1-3\%$, which suggests the presence of other noise sources (e.g. flat-field errors).

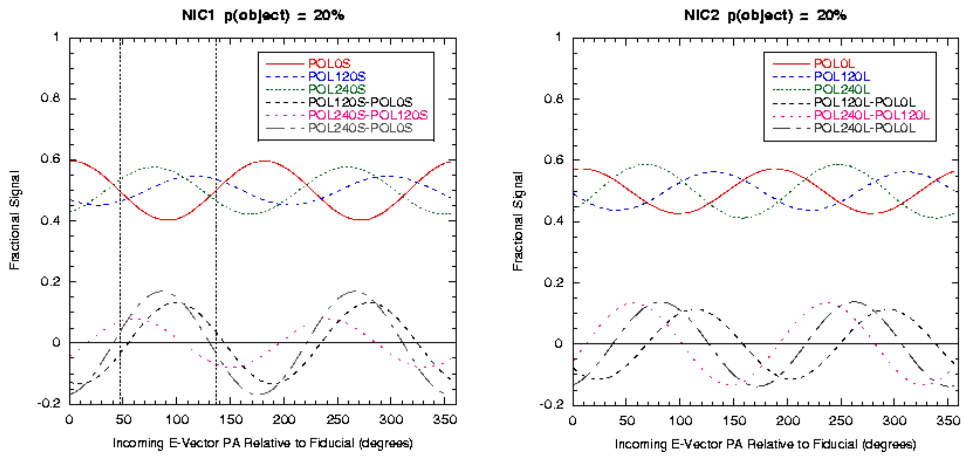

Figure 3. (after HSL) Fractional signal measured in each NICMOS polarizer as a function of incident electric vector position angle (PA) for 20% polarized light. The lower curves are the differences in fractional signal between images taken with successive polarizers. The vertical dashed lines in the left panel (NIC1) represent the position angles of the incoming electric vector where these differences are all small, and thus produce the largest uncertainties in the polarization.

Position Angle of Incoming Polarization Relative to NICMOS Orientation: The non-optimum polarizer orientations and efficiencies cause the uncertainty in polarization to be a function of the position angle of the electric vector of the incoming light. For observations with low signal-to-noise ratios (per polarizer image), and targets with lower polarizations, the difference between the signals in the images from the three polarizers becomes dominated by (photon) noise rather than analyzed polarization signal. Therefore, observations that place important incoming electric vectors at $\approx 45^\circ$ and $\approx 135^\circ$ in the NICMOS aperture reference frame should be avoided in NIC1. No such restriction is necessary for NIC2.

7. Future Directions

Further analysis of the Cycle 7 calibration data, and comparisons between NICMOS and ground-based observations of GTO and GO targets should allow even more improvements in the HSL coefficients. A detailed error analysis of the HSL algorithm is also in progress.

We have demonstrated that NICMOS can produce highly accurate images in polarized light despite its non-ideal polarimetry optics. The HSL algorithm may be useful in processing data from other instruments that use polarimetry designs like NICMOS, such as the Faint Object Camera and the Advanced Camera for Surveys.

Acknowledgments. It is a pleasure to thank B. Stobie, L. Bergeron and A. Evans for assistance with the (non-polarimetric) data calibration. Special thanks to Joel Kastner for the use of his COB observations of CRL 2688 in advance of publication, and to the late Chris Skinner for his initial processing of the IRC +10216 data. DCH acknowledges support from the NICMOS project under NASA grant NAG 5-3042.

References

Axon, D., Auer, R., Baggett, W., Blades, C., Daou, D., Gilliland, R., Kutina, R., Ritche, C., & Stevens, M., 1996, NICMOS Instrument Handbook Version 1,0, Space Telescope Institute

Hines, D.C., Schmidt, G.D. & Lytle, D., 1997 in The 1997 *HST* Calibration Workshop, ed. S. Casertano et al. (Baltimore: STScI) [HSL]

Kastner, J. & Weintraub, D. 1994, ApJ, 434, 719

Sahai, R., Hines, D. C., Kastner, J. H., Weintraub, D. A., Trauger, J. T., Rieke, M. J., Thompson, R. I. & Schneider, G., 1997, ApJ, 492, L163

Schmidt, G.D., Elston, R. & Lupie, O.L., 1992, AJ, 104, 1563

Skinner, C.J., et al., 1997, in prep.

Simmons, J.F.L. & Stewart, B.G, A&A, 1985, 142, 100

Thompson, R. I, Rieke, M., Schneider, G., Hines, D.C., & Corbin, M.R., 1997, ApJ, 492, L95

Whittet, D.C.B., Martin, P.G., Hough, J.H., Rouse, M.F., Bailey, J.A. & Axon, D.J., 1992, ApJ, 386, 562

NICMOS and the VLT
Pula, Sardinia, May 26-27th 1998
Wolfram Freudling and Richard Hook, eds.

Some Experiments with the Restoration of NICMOS Camera 2 Images of OMC-1

Richard N. Hook

Space Telescope – European Coordinating Facility, European Southern Observatory, Karl Schwarzschild Str-2, D-85748, Garching, Germany, e-mail: rhook@eso.org

Susan R. Stolovy

University of Arizona, Steward Observatory, Tucson, AZ 85721, USA, e-mail: sstolovy@as.arizona.edu

Abstract. Imaging of the core of the OMC-1 region using NICMOS camera 2 through the F212N and F215N filters shows a wide variety of interesting structure on scales of 0.2” at a very high dynamic range (Stolovy et al. 1998). The application of image restoration techniques, including multi-channel variants of the Richardson-Lucy technique, offers the chance to enhance structure on the finest scales and also to suppress the prominent and richly structured point-spread functions of the many bright stars in the images. These methods are described and some preliminary results are presented.

1. Introduction

The NICMOS cameras on HST at longer wavelengths allow well-sampled diffraction limited imaging with a very high dynamic range which is achieved using multiple non-destructive readouts of the arrays. During the check-out phase, soon after NICMOS was installed, images were taken of the OMC-1 region using the F212N and F215N narrow-band filters to isolate the 2.12 μm molecular hydrogen line. These images formed part of the NICMOS early release (ERO) data and their scientific content has been described in Stolovy et al. (1998).

The high dynamic range, good sampling, excellent signal-to-noise ratio and stable point-spread function of these NICMOS images suggests that image restoration methods may be able to significantly enhance them. It was hoped that such processing, which enhances contrast and resolution, could permit better study of the complex morphology of the highly structured environment close to the BN object. A particular problem with NICMOS images is that the point-spread functions exhibit rich structure as a result of the complex obscuration pattern in the pupil coming from both the HST OTA and the cold mask in the NICMOS dewar. Also, for very bright sources such as BN, the diffraction spikes can cover the entire array. The second aim of this work was to try to suppress PSF structure in these images so allow the underlying image to be better seen.

This work is currently in progress and the results presented must be regarded as highly provisional.

2. Data Processing

The standard NICMOS data reduction was performed using a customized version of the CALNICA software developed at STScI. There were seven images at each position on the target and these were combined to produce five processed images in each filter at different pointings and orientations with significant overlaps. The five images through the F212N filter form the basis of the image restoration attempts. This filter includes both the molecular hydrogen emission and the continuum and hence shows the most diffuse structure. It also allows us to simultaneously look for sharpening of H_2 features as they tend to be spatially anti-correlated with the continuum emission (see Figure 3 of Stolovy et. al 1998).

The first phase of the image restoration was to obtain an adequate PSF. For the central frame which includes the very bright BN object a PSF from the Tiny Tim simulator (Krist & Hook 1997) was used. The most recent version of this code contains residual aberrations measured by phase retrieval as well facilities for defocus and compensation for cold-mask shifts in the pupil. For the outer frames a PSF extracted from a star in a relatively uncrowded region was extracted and scaled after suitable background subtraction. The empirical PSF matched the central structure somewhat better than the Tiny Tim one but had inadequate signal in the outer parts to model the full PSF of the BN object and small errors in the background subtraction led to significant artifacts.

Standard image restoration in crowded fields with strong, varying, background lead to artifacts around bright stars. These are typically circular dark rings centred on stars and were found to be very pronounced in this NICMOS data. Instead of taking a direct approach, a two channel variant of the Richardson-Lucy method was employed (Lucy 1994; Hook & Lucy 1994, Hook et al. 1994). This method used a list of positions of known point-sources which have fixed positions in combination with a background image which is constrained to be smooth on a user-specified scale. As iterations proceed the intensities of the points model the stars and the background is modelled in the other channel. This second background channel is constrained to be smooth by the addition of an entropic term in the objective function being maximised. In the original version of this method (known as PLUCY) the points were represented as delta functions in an image and hence had to be centred in pixels. In a newer enhancement (CPLUCY) this constraint is removed and the stars can be assigned positions freely at a subpixel level. This method was found to effectively remove the outer parts of stars images although minor residuals are visible close to the centres.

In the very difficult case of the bright BN object the diffraction rings are largely cleaned up but there are residuals further out in the spider spikes. The two-channel restoration of the central frame is shown in Figure 1. A bright point-source, approximately 0.9 arcsecs to the NW of the BN object becomes apparent when the blobs in the diffraction pattern very close to the centre are suppressed. The exact nature of the point is unclear but it does not appear to be a ghost image from the filter.

After these cleaned images were produced they were block replicated by a factor of two and then restored using the standard Richardson Lucy algorithm to sharpen up structure in the background after the stars have been suppressed. The results were then mosaiced using the drizzling task in IRAF and the result is shown in Figure 2. Some residuals are apparent in places but are localized.

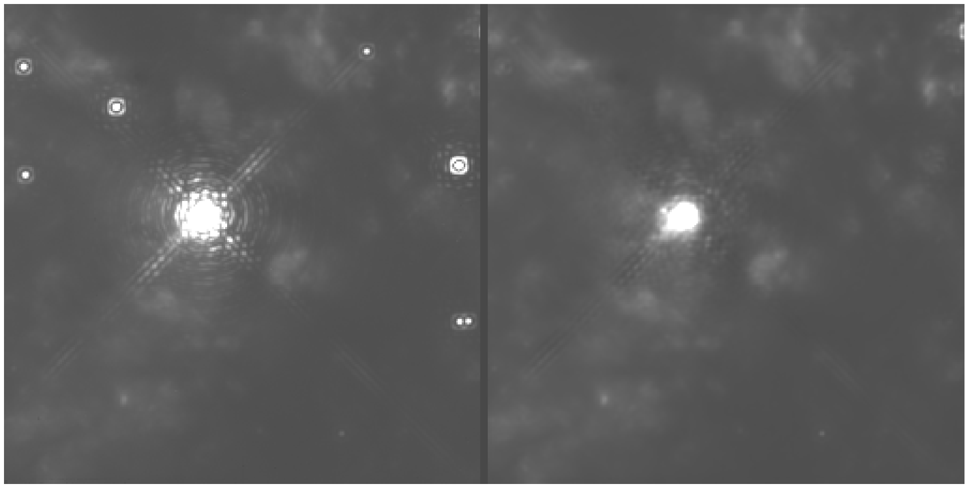

Figure 1. A two channel restoration of the central NICMOS 2 image of the BN object through the F212N filter.

3. Discussion

The application of image restoration allows many fine-scale structures in these images to be more clearly seen and less affected by the PSFs from bright stars. This has allowed the region close to the BN object to be better studied than before and a point source 0.9 arcsecs to the NW has been noted but its exact nature is unclear. It may be a bright blob of dust and gas reflecting light from BN or it could be a previously undiscovered star. There is also intriguing faint asymmetric diffuse structure close to BN. The restorations are limited by the accuracy of the PSFs available. Tiny Tim does a good but not perfect job in this case, presumably because of an incomplete knowledge of the geometrical parameters of the NICMOS camera - residual aberrations, cold-mask shifts and so forth. Empirical PSFs taken from the images do not have enough signal to map the outer spider diffraction features which are visible around the BN object.

This deconvolution technique was successful in enhancing details in the extended molecular hydrogen “fingers” and “bullets” (see Stolovy et al. 1998). The southern, illuminated edge of the continuum “Crescent” feature north of BN is also sharpened.

This work is in progress and will be extended to determining the best way to generally deconvolve narrow-band emission line images from NICMOS. This effort is complicated by the fact that the line and continuum filters have different PSFs. In this case, the F215N image would normally be subtracted from the F212N image to produce the molecular hydrogen image.

References

Krist, J.E., Hook, R.N., 1997, “The Tiny Tim Users Guide (V4.4)”, October 1997

Hook, R.N. & Lucy, L.B., “Image Restorations of High Photometric Quality. II. Examples”, in “The Restoration of HST Images and Spectra”, STScI, 86

Hook, R.N., Lucy, L.B., Stockton, A. & Ridgway, S., 1994, ST-ECF Newsletter 21, 16

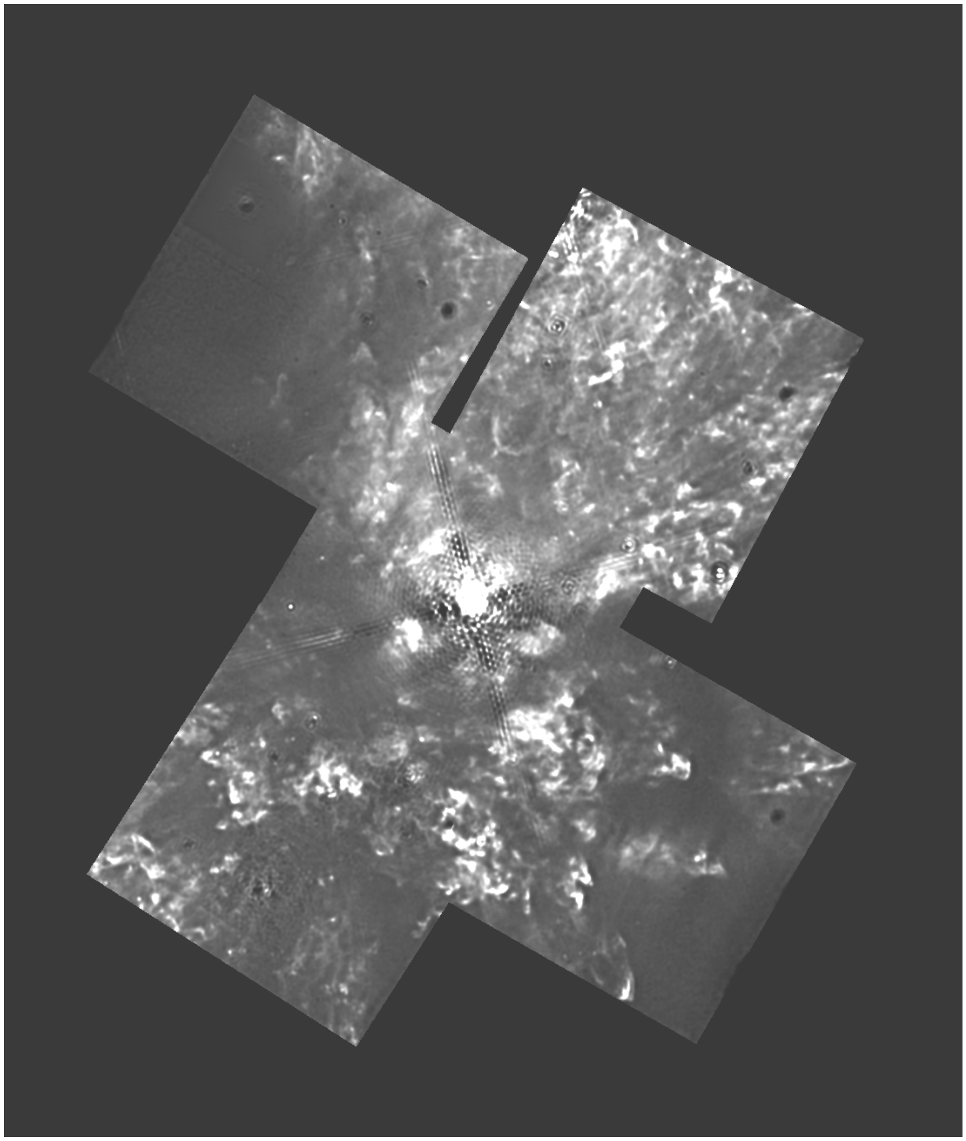

Figure 2. A mosaic of the sharpened restorations of the five F212N images of OMC-1

Lucy, L.B., 1994, "Image Restorations of High Photometric Quality", in "The Restoration of HST Images and Spectra", STScI, 79

Stolovy et al., 1998, ApJ, 492, L151

NICMOS and the VLT
Pula, Sardinia, May 26-27th 1998
Wolfram Freudling and Richard Hook, eds.

NICMOS Software at the University of Arizona

E. Stobie, D. Lytle, I. Barg, and A. Ferro

NICMOS Project, University of Arizona, Tucson, AZ 85721, E-mail: bstobie@as.arizona.edu

Abstract. The NICMOS Software Group at the University of Arizona has built a number of software tools for processing NICMOS data. These tools have been developed entirely within IDL or have IDL interfaces to other existing software. We will describe each of these tools.

1. Introduction

The NICMOS Software Group at the University of Arizona has developed a number of software tools in IDL[1] in support of data calibration and analysis for the NICMOS Instrument Definition Team.

2. Software Group

The NICMOS Software Group at the University of Arizona is composed of four members:

- Irene Barg - NICMOS database management
- Anthony Ferro - system software
- Dyer Lytle - science software
- Elizabeth Stobie - science software

3. Programming Environment

Group members develop both batch programs and interactive programs with graphical user interfaces using IDL. In some cases, GUI's are developed for pre-existing software developed in other programming environments. All software is developed and tested under the Solaris and Linux Operating Systems. Users may retrieve any of the software in one of two ways:

- by FTP - `ftp://nicmos.as.arizona.edu/pub/NICMOS/software`
- from website - `http://nicmos/as.arizona.edu`

[1] IDL (Interactive Data Language) is an interactive analysis and visualization program written by Research Systems, Inc..

4. Programs Available

The software tools developed within the software group at the University of Arizona may be divided into six main categories: observation planning, calibration, editing, display, analysis, and general utilities.

4.1. Planning

Cntrate, a graphical user interface (GUI) layered on the IRAF/STSDAS countrate task which evaluates the countrate for a given target and observing mode.

HSTField, a procedure based on the IDL program, Overlay, developed by Eliot Malumuth at Goddard Space Flight Center, but has been heavily modified to our purposes at the University of Arizona. The program displays an image of the sky with an overlay of the Space Telescope apertures. The user may pick the prime aperture, orient the telescope, mark guide stars, get RA and Dec as well as Ecliptic coordinates.

Simimage, an IDL GUI layered on the IRAF/STSDAS task "simimg", which computes simulated images for the HST imaging instruments FOC, NICMOS, STIS, and WFPC2. Simimage allows a convenient mechanism for determining the necessary parameters and provides a display of the final result as both an image and shaded surface plot. Simimage will also produce a group of dithered images across the object field.

4.2. Calibration

Buildref, an IDL program for building reference files from single FITS images by stitching together single-image FITS files into multi-extension FITS files. The user provides a command file that specifies the input images to be combined, the method of combination, and any keyword additions or changes that should be made to the standard NICMOS header template files that are used. The outputs of the program are NICMOS standard multi-extension FITS files that are compatible with calnica.

Calnica, an IDL replication of the calnica task in IRAF/STSDAS. Its single argument is the list of files to process. The outputs are a calibrated image with associated extensions and, in the case of multiaccum data, an intermediate file with each readout fully calibrated excluding the cosmic ray rejection. If no _IMA file is desired, the user may include the command, 'noima' at the beginning of the list file.

Quad_Edit, an interactive program for reviewing the bias levels from one quadrant of a NICMOS image to another and adjusting the individual quadrants. The final result may be saved to a FITS file.

4.3. Editing

Cal_Edit, an interactive program used to edit FITS header keywords in preparation for re-calibrating NICMOS data with Calnica. The display consists of a list of the calibration switch values and when appropriate their associated reference files. Both calibration switches and reference files may be modified easily using the action and radio buttons in the widget.

FHE, (FITS Header Editor), an IDL program for editing headers of groups of FITS files. It is particularly well suited to editing FITS files with multiple image extensions. Any keyword in the primary header or any extension header (excluding the reserved FITS keywords) may be edited. Keywords may be modified, added, or deleted.

FPHE, (FITS Primary Header Editor), an IDL program designed for editing the primary headers of FITS files with image extensions. It is an optimized version of FHE which edits the headers in place and therefore will only modify the primary headers. Keywords may be modified, added, or deleted.

Maskedit, an interactive program used to edit bad pixel masks. The inputs are the FITS data image and the FITS mask image. There are various keywords that can be used on input to scale the image and to set the "good pixel" value for the mask. The program displays the data image and marks the "bad" pixels based on values in the mask image (bad pixels are circled). The user may then set or unset masked pixels using the mouse buttons. Finally, the new, edited, mask may be saved to a file.

4.4. Display

Multi_Disp, an interactive program for creating a display of multiple sub-images from sections of one or more images where each sub-image has its own zoom factor and image stretch. Each sub-image may have a single line caption. The user may select the number of sub-images per row and column with the default rowsize=4 and the default colsize=6. Each of the individual sub-images may be saved to a FITS file and the entire display may be saved and restored.

SDW, (Super Display Widget), an interactive program designed to be a general purpose FITS image viewer. It allows general image display of multi-extension FITS files, zooming, bad pixel masking, log scaling, rudimentary pixel editing, min/max scaling, general IDL colormap adjustment, cursor readback, spread sheets of pixel values, header display, and access to all image extensions of a NICMOS multi-extension file.

Trucolor, a program for displaying and printing true color images by loading the three display color tables, red, green, and blue with separate images and overlaying the result. Each color table can be scaled individually to obtain the desired "look". The images may also be log scaled to bring up background detail. This program works on systems with 8-bit or 24-bit color display and produces appropriate output postscript files when the print button is pressed.

4.5. Analysis

FLC, (FITS List Calculator), a program to process large groups of FITS files together by creating data lists. The program parser supports a simple command syntax including the ability to process pre-defined scripts, do-loops, and if-then-else constructs as well as arithmetic operators, native IDL commands, and operating system commands. The program has an image scan feature to view a list of images in a movie-like format, a more detailed graphics display which includes the image header, full image, single quadrant or zoomed region of the image, and the image histogram. There are also windows for editing pixels in an image and for building lists. The program supports four data types: lists, images, arrays, and scalars. The user may customize the number of each data type by editing the user definitions file. Several mathematical functions for lists are pre-defined for convenience including the computation of image statistics, pixel statistics, medians, means, and first differences. A sample display of FLC appears in Figure 1.

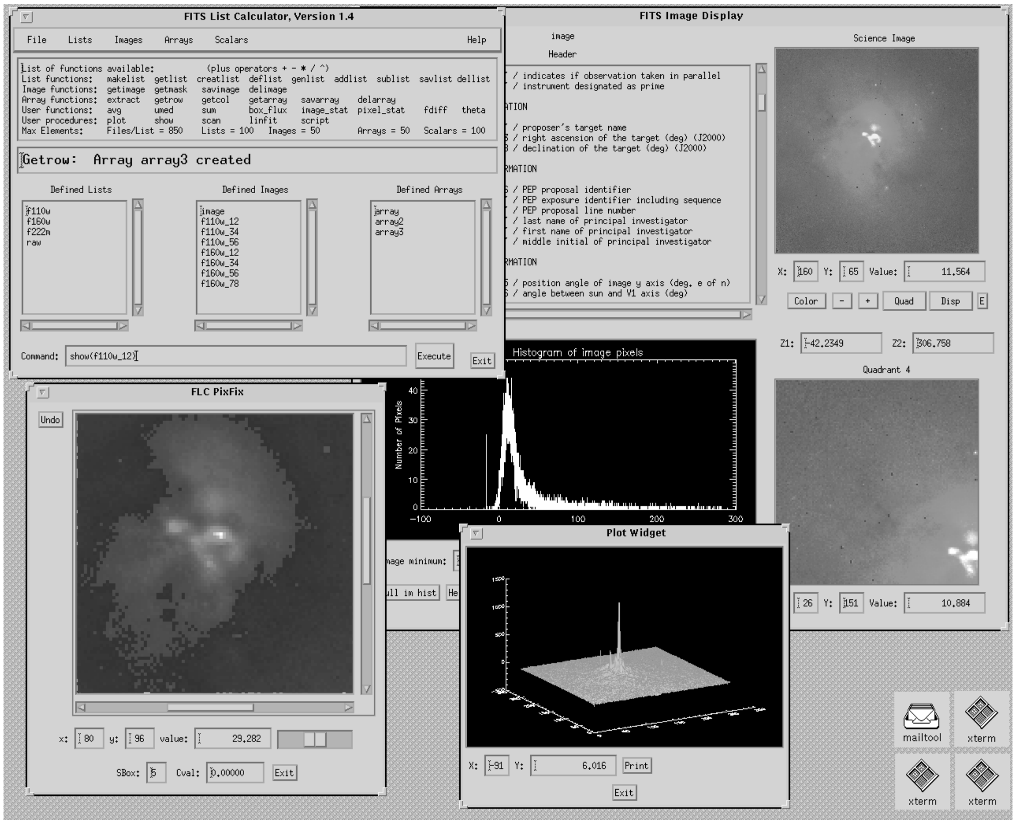

Figure 1. Many of the display and text windows used by FLC.

IDP3, (`Image Display Paradigm #3`), a program for manipulating data images employing a powerful but easy-to-use graphical user interface. It allows the user to work with a collection of images and display one or more images in a graphics window simultaneously. Images may be individually moved, scaled, and rotated to bring image features into registration. Each image may be displayed by adding it to the composite image in the display, by subtracting it from the composite image or by one of the other various image functions (divide, XOR, average, etc.). Idp3 provides a region-of-interest pop-up tool for intensive examination of sub-regions of the main display. There are cross-section plots, masks, surface plots, statistics, spreadsheets displays and other tools at the user's disposal. Final combination images may be saved to FITS files. These output images contain descriptive headers detailing the settings in IDP3 at the time the image was written. A sample display of IDP3 appears in Figure 2.

Lucy, a program that generates a deconvolved image from an input image and point spread function (PSF) using the algorithm developed independently by Richardson

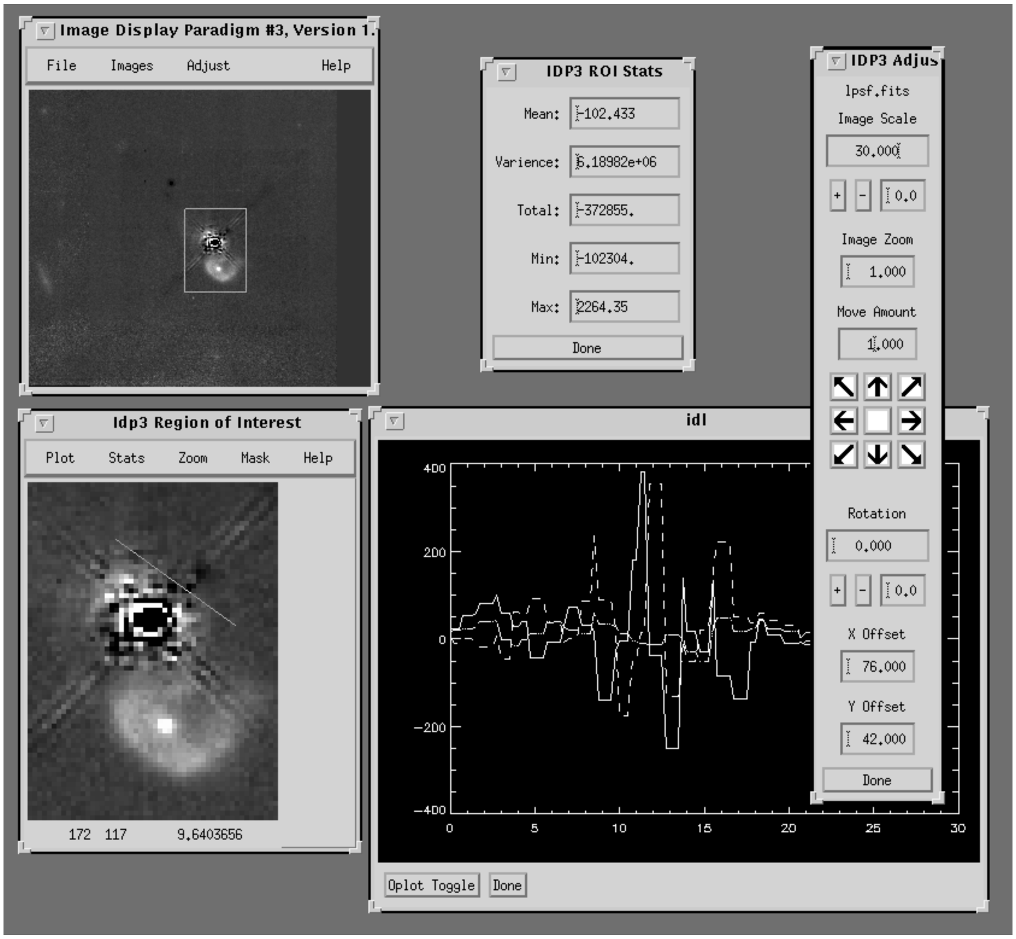

Figure 2. Many of the display and text windows used by IDP3.

(1972) and Lucy (1974). The widget is based on the original and accelerated algorithms with optional damping developed by White (1993) at STScI. The IDL program displays the original data as well as the result at the end of each iteration.

Niclook, a quick look analysis tool for NICMOS data. The widget contains three display windows: full window, zoom window, and graphics window. Statistics may be computed for the full or zoom window. World coordinates may be overlaid on the full window and coordinates may be printed for any pixel in either the full or zoom window. Image arithmetic may be done on any of the five loaded images using arithmetic operators or IDL functions. Two images may be blinked in the full window. All commands are logged in a journal file.

Nicmosaic and Nicstikum, tools for mosaicing NICMOS images. The inputs for Nicmosaic are a list of images to mosaic and, optionally, a table of position data previously output from “Nicmosaic”. If no table is given, the program attempts to line up the input images as best it can based on the world coordinate information in the image headers. Image rotation and fractional pixel shifts are used to accomplish this alignment. Once the data are loaded, the user may select two of the images (called the primary and the secondary images) and blink these two images. The user may then shift and rotate the selected primary image to improve the alignment using the buttons and value fields provided. On exiting, a table of positions is written that can be used by the program “Nicstikum” to create a final, mosaic image.

Nicphot, an IDL graphical user interface wrapper for the DoPHOT stellar photometry program written by Mario Mateo, Abhijit Saha, and Paul Schechter. Nicphot provides facilities for computing the FWHM of an object, determining the image background, editing the DoPhot parameter file, executing DoPHOT, and displaying the result with detected objects removed. Since DoPHOT requires the image data as 16-bit integers Nicphot will rescale the data and create a new FITS file with extension `.FITSX` if the data are not 16-bit integers.

Polar and Polarplot, two programs that have been written for the analysis of NICMOS polarization data. “Polar” is a program that takes three images (one from each polarizer) as input, solves the linear equations, and produces as output the “I”, “Q”, “U”,“P”, and “Θ” images. “Polarplot”, shown in Figure 3, allows the user to overlay the polarization vectors on the intensity image. This program has many user adjustable parameters to customize the plot such as intensity image color table manipulation, axis, contour map, and polarization vector color manipulation, contour overlay, and thresholds for polarization intensity.

4.6. Utilities

Delread, a batch program to delete one or more readouts (imsets) from a `_raw` or `_ima` multiaccum file.

Keydump, a batch program for printing select keywords from the headers of NICMOS data files. All keyword values are taken from the primary header of the file (`_raw, _ima, _cal, _mos`). If the positions option is selected the target right ascension and declination are printed in addition to the other header information. When the refiles option is selected the values of the reference file keywords are printed.

Kwlist, a batch program to print a table of keyword values for the specified list of files. The desired keywords are defined in a string array and the files to be read are defined in an ASCII text file. The information is printed to the user’s screen and to the specified output file.

Nic_Help, an interactive tool for querying the help files of all IDT developed software. All programs are listed and as one is selected a single line description is given. The user may display or print the entire help file.

Simplefits, a batch program to separate the readouts (`IMSETs`) of NICMOS raw (`_raw`) or intermediate (`_ima`) multiaccum files into individual FITS files. The output files contain a single header (merging the primary and science image extension headers) and the science image. All other image extensions (`ERR, DQ, SAMP,` and `TIME`) are discarded.

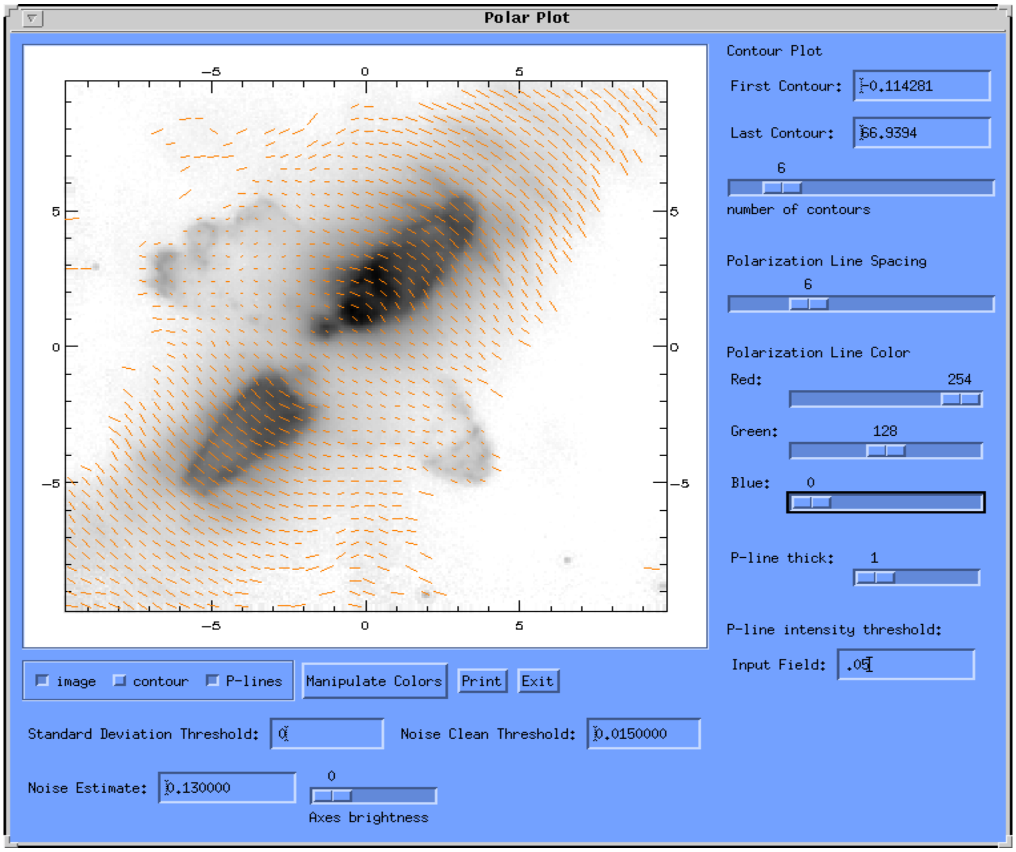

Figure 3. Example Polarplot display, an intensity image is shown over-plotted with polarization vectors.

Unstitch, a batch process to separate the readouts (`IMSETs`) of multiaccum files into different files. Output files are named by replacing the last character of the `IPPPSSOOT` designation with the readout number. Readouts count from one to a maximum of 26 in forward time order (normal NICMOS files are in reverse time order). The inputs are an ASCII text file of filenames and an optional path parameter.

5. Web Interface to NICMOS Archive

In order to support our geographically diverse team members, we have developed a number of web based forms and scripts to allow them to search for and retrieve data sets. To minimize the network traffic, we have developed our own database system at the University of Arizona, which includes NICMOS data to which we have access. Via the web this database can be queried to locate specific data of interest. Authorized users can then request copies of the data via the network.

Selected proposal types (GTO/NIC, CAL, PAR, ENG, and SMOV) are monitored daily and are downloaded to a database servers at Steward Observatory. The data stored locally represents a small sub-set of the data in the HST data archive at the Space Telescope Science Institute. In addition, a database of observed and simulated (generated by the Tiny Tim program) NICMOS point spread functions (PSFs) is being developed for team use. Information about the UofA NICMOS Databases may be obtained by following the appropriate links from the web site: `http://nicmos.as.arizona.edu/`.

Acknowledgments. We are grateful to the NICMOS Instrument Definition Team members and their Post Docs for their input and support in our software development. Their patience in testing software as it evolves is much appreciated.

References

Richardson, W.H., 1972, J. Opt Soc. AM 62, 55

Lucy, L. B., AJ 79, 745

White, R. W., 1993, Restoration, Newsletter of STScI's Image Restoration Project, 11

NICMOS and the VLT
Pula, Sardinia, May 26-27th 1998
Wolfram Freudling and Richard Hook, eds.

STScI NICMOS Software

H. Bushouse

Space Telescope Science Institute, 3700 San Martin Drive, Baltimore, MD 21218, Email: bushouse@stsci.edu

Abstract. The Space Telescope Science Institute (STScI) has various software tools available for calibrating and analyzing Near Infrared Camera and Multi-Object Spectrometer (NICMOS) datasets. These include the tasks used in the STScI pipeline, tools to generate the reference files used by the calibration pipeline tasks, and general image analysis, manipulation, and arithmetic tasks.

1. Introduction

All STScI NICMOS tasks can be run from within the IRAF/STSDAS environment and are written either in the native IRAF SPP language, the ANSI C language, or as IRAF cl scripts. The two main tasks used to calibrate and reduce NICMOS observations are `calnica`, which applies instrumental calibrations, and `calnicb`, which processes associated sets of observations. There are also several tools available for use in generating the calibration reference files needed by `calnica`, such as bad pixel masks, detector read noise images, detector non-linearity corrections, and dark current and flat field images. Any existing IRAF and STSDAS tools can be used for the analysis of NICMOS datasets, but there are several that have been written specifically for the five data array grouping (known as image sets) that is used for storing NICMOS images. These tasks include tools for displaying images with overlayed data quality masks, image set arithmetic and statistics, and image set combining. There are also prototype tools for measuring and removing residual DC offsets from calibrated NICMOS images. Brief descriptions of these tasks are given in the following sections.

2. Calibration Pipeline Tasks

The two calibration pipeline tasks are `calnica` and `calnicb`. `Calnica` is used to apply instrumental calibrations to individual datasets, while `calnicb` is used to process associated sets of NICMOS images. The calibrations applied by `calnica` include the removal of standard instrumental signatures, such as dark current subtraction, detector non-linearity correction, and flat fielding, as well as NICMOS-specific processing, such as subtraction of MultiAccum-mode zeroth read images, and the combining of MultiAccum readouts into a single image.

`Calnicb` is applied to associated sets of NICMOS images, which must have already been processed with `calnica`. Major steps performed by `calnicb` include the combination of multiple images obtained at individual sky positions, calculation and subtraction of the HST thermal background signal, and mosaicing of images obtained in a dither pattern.

See Bushouse et al. (this volume) for more details about the calibration pipeline tasks.

3. Reference File Tools

There are several tools available within the STSDAS package `hst_calib.nicmos` that can be used to generate some of the reference files used by the `calnica` pipeline task. They are:

- msbadpix - Detects bad pixels in NICMOS images and produces a bad pixel mask (MASKFILE reference file)
- msreadnoise - Measures readout noise in NICMOS images and produces a read-noise image (NOISFILE reference file)
- msstreakflat - Processes Earth "streak flat" images and produces a destreaked flat field image (FLATFILE reference file)
- ndark - Builds a NICMOS DARKFILE reference file from individual dark current images
- nlincorr - Computes a polynomial fit to the non-linear NICMOS response and produces a NLINFILE reference file

4. Image Analysis and Reduction

The STSDAS packages `hst_calib.nicmos` and `toolbox.imgtools.mstools` contain the tasks listed below, which are useful for image analysis. The tasks with names beginning with the letters "ms" are set up to handle the five data array grouping of NICMOS images, known as "image sets".

- markdq - Mark data quality (DQ) flags on a displayed image
- ndisplay - Display an image and superimpose DQ flags
- pstack - Plot a stack of pixel values from a MultiAccum image
- msarith - Image arithmetic
- mscombine - Combine images with rejection of outliers
- msstatistics - Compute image statistics

5. Under Development

In addition to the software tasks listed above, which are all available in STSDAS v2.0.1, there are several tasks which, at the time of this writing, are still under development.

The most notable of these are various tasks that measure and remove the quadrant-dependent DC offsets, often known as "pedestal", which appear in some NICMOS images. Two of these experimental tasks are `nped` and `pedsky`, both of which are currently implemented as IRAF cl scripts. They estimate the pedestal level in each image quadrant by attempting to minimize the flat-field residuals that get imposed on the image when the flat-field is applied to the constant pedestal level. Once the algorithms are completely developed, they will be rewritten and released as public STSDAS tasks.

Part 3. NICMOS Science

NICMOS and the VLT
Pula, Sardinia, May 26-27th 1998
Wolfram Freudling and Richard Hook, eds.

NICMOS Coronagraphic Surveys-Preliminary Results

Glenn Schneider

University of Arizona, Tucson, AZ

Abstract. A search for previously unknown low-mass (giant planet and brown dwarf) companions to stars in the solar neighborhood, and circumstellar dust disks around main sequence stars by direct coronagraphic imaging has been undertaken by the NICMOS Instrument Definition Team (IDT). Observations of a carefully selected candidate list of $\sim$100 stars began on February 28, 1998, more than a year after the start of the NICMOS mission. Using a differential imaging strategy, as originally demonstrated in the second Servicing Mission/Observatory Verification (SMOV) program, we were able to achieve statistically significant detections of substellar companions at 1.6μm with a ΔH of $\sim$10 at separations as close as 0.5" (corresponding to 2.5 AU at 5 pc), with increasingly better performance at increasing radii. With nearly two dozen candidates now observed, and a better understanding of the focal plane stability and target acquisition precision we report on the efficacy of the program for detecting transitional objects into the 3 to 5 Jupiter mass regime.

1. Introduction

A systematic survey of nearby stars for giant planet and brown dwarf companions, and circumstellar (or protoplanetary) disks, is a cornerstone of the NICMOS IDT's Environments of Nearby Stars (EONS) program. In carrying out this survey we are attempting to address some fundamental questions in the arena of stellar and planetary system formation. We seek to learn if indeed there is there a continuity of objects across the sub-stellar mass spectrum bridging the main sequence to planetary objects. If so then at what distances will such objects be found from their primaries and how might this be biased by the characteristics of their primaries or companion objects? What implications will such discoveries have for our understanding of formation mechanisms?

Shedding light on these, and related questions, is a major element of the NASA's Origins initiative which contains at it's core the establishment of scientific activities to investigate the birth and early evolution of stars and planets (Dressler, 1996). The NICMOS IDT embraced this theme in the establishment and formulation of our EONS search program. From the ill-constrained low-mass end of the mass-luminosity function ($<\sim$0.2 solar masses) through the transitional regime of brown dwarfs ($<\sim$0.08 solar masses), and down into the realm of giant planets NICMOS provides a unique resource for exploration. The EONS search programs were designed to identify low-mass and sub-stellar companions and over two decades in the mass-spectrum as well as circumstellar disks which may be potential harbingers of planetary formation.

2. The EONS Coronagraphic Surveys

The design, fabrication, and incorporation of a coronagraph into NICMOS camera 2, as discussed in detail by Schneider, et al. (1998), allows us to push our investigations into previously and other-wise unreachable corners of the observational parameter spaces associated with the close environments of stars. The NICMOS coronagraph is capable of providing detections of non-stellar companions as faint as H = 22, 10 to $\sim$13 magnitudes fainter then their primaries at separations of 0.375" to $\sim$3.0", should they exist. The EONS programs concentrate on these astrophysically and dynamically interesting spatial regions of the search parameter space. For the stars in our sample this covers minimum physical separations of 1.2-50 AU at the inner spatial detection limit. The lower mass limit depends on age, distance, and spectral type, but can be as low as 3 to 5 $M_{Jupiter}$ for many of our targets. The EONS surveys are segregated into three complementary observing programs (designated 7226, 7227 and 7233 by STScI), delineated primarily by the principle characteristics of the candidate stars,which cover the full accessible range of the observable sub-stellar search space.

The 7226 candidate list contains 43 very young main-sequence stars with mean distances of $\sim$30 pc. The median age for the candidates with well established ages is $<\sim$90 Myrs and contains at least 6 candidates with ages as young as $<$10 Myrs (see Fig. 1), including several members of the TW Hyd association. Because of the extreme youth of these objects any low-mass brown dwarf and planetary companions will still be in a higher luminosity phase and thus easily detectable. For example, in its first 10 Myrs a 10 $M_{Jupiter}$ brown dwarf would have a luminosity exceeding 10^{-4} solar luminosities (Kulkarni, 1997). Typical separations observable with NICMOS are near the empirical maximum in the binary distribution of stars ($\sim$20 to 40 AU), which also corresponds to the mean distance of the giant planets in our own solar system.

The 7227 candidate list contains 31 M-dwarf stars which are (a) nearby (d $<\sim$6 pc) with spectral types later than $\sim$M3.5, (b) young (age $<\sim$100 Myr) with (d $<\sim$25 pc), and (c) spectrally the latest known (i.e.,"ultra-cool" stars later than $\sim$M8.5), with some overlaps (see Fig. 2). Because of the proximity of many of the stars in this sample to the sun, companions as close as 1.2 AU from their primaries may be detected at the inner radius of our search space.

The 18 candidate stars in the search for circumstellar dust disks (7233) are primarily main sequence stars with IRAS IR excesses, $\tau(dust) > 10^{-3}$, and other indicators of the possible presence of disks. In addition to H-band imaging for the brighter stars in this program we are obtaining multi-spectral images at 1.71μm ($HCO_2 + C_2$ continuum), 2.04μm (methane band), and in the line spectra of Paschen-α (1.87μm) and Bracket-γ (2.15μm).

Our EONS surveys are obtaining single-color coronagraphic images aimed at discovering sub-stellar companions utilizing the F160W filter (1.4 - 1.8μm) where the NICMOS coronagraphic performance is optimized. This wavelength band also corre-

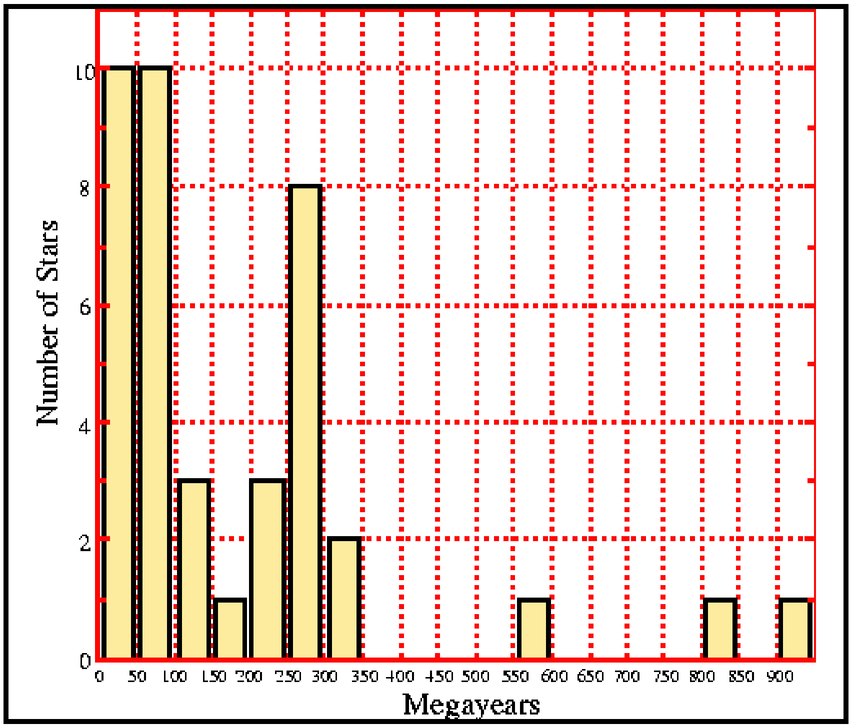

Figure 1. Distibution of stellar ages for the young stars candidates (7226)

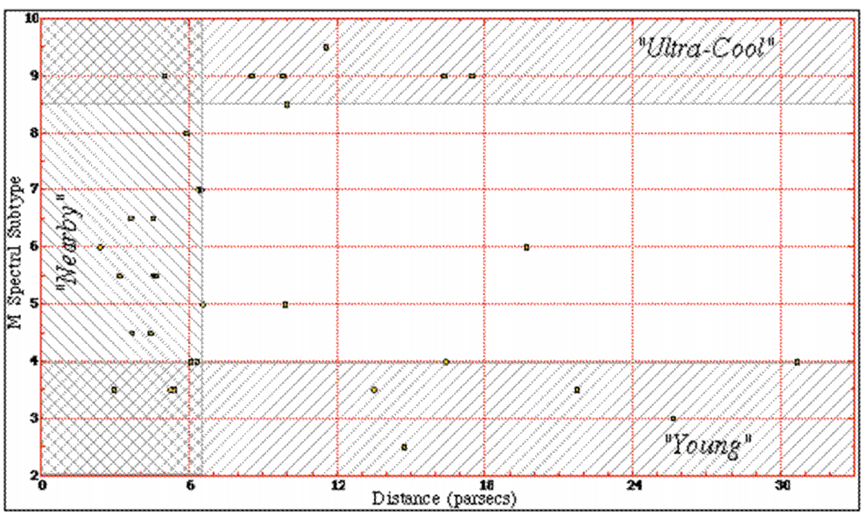

Figure 2. M-dwarf candidate distances and spectral sub-types (7227).

sponds to the strong emission in GL 229B (Burrows, et. al, 1997), GD 165B (Zuckerman & Becklin, 1992) and several of the DENIS survey candidate brown dwarfs (Delfosse, et. al, 1997), as well as to strong reflections in Jupiter and Titan. Putative discoveries of brown dwarf and giant planet companions arising from the above single-epoch searches must be subsequently confirmed and the objects characterized in follow-up second-epoch observations.Such follow-up observations are required to sort out field-objects from true companions by common proper motions and/or color indices and to obtain multi-color imaging to establish luminosity ratios of such companions. All of the stars in the M-dwarf survey, and most of those in the young stars program, have sufficiently high proper motions to allow follow-up confirmatory observations to be carried out in the shortened NICMOS lifetime. It is anticipated that for some regimes of the search-space ground-based follow-up using facilities such as Keck, Lick, or VLT may be possible.

3. Anticipated and Current Coronagraphic Performance

An aggressive 17-orbit commissioning, performance verification, and calibrationprogram executed during SMOV allowed us to ascertain the true performance limits of the coronagraph (Schneider & Lowrance, 1997; Schneider, et. al, 1997) and optimize both its operation and our observing programs. Performance profiles for NICMOS camera 2 direct, coronagraphic, and differential imaging derived from that test program are shown in Figure 1 of Lowrance, et. al. (1998), elsewhere in these conference Proceedings. By subtracting coronagraphic PSFs at different spacecraft roll angles the background diffracted and scattered energy in the unocculted PSF-wings of an occulted primary star can be reduced to approximately one-millionth the peak intensity of the star at a radial distance of 1”, or about 10^{-5} at 0.5”. This is an improvement of more than two orders of magnitude over the already low backgrounds afforded by the diffraction-limited, highly stable, PSF. This represents a very significant gain over the current generation of AO ground-based coronagraphs (Sandler, 1997) and is unique to NICMOS+HST. The basic observational strategy, also described by Lowrence,et al., is illustrated in Fig. 3.

Due to a now recognized, and understood, deficiency in the target acquisitionprocess the anticipated performance levels of differential coronagraphic observations (as demonstrated in SMOV) have been somewhat compromised. As a result the limiting sensitivities, and ultimate detection limits for observations made in the first three months of the EONS programs have fallen short of their performance goals due to locally increased backgrounds of two stellar magnitudes or more in a spatially dependent fashion. Corrective action for subsequent observations has been taken in the form of an operational workaround, and a soon to be implemented flight software upgrade. A strategy for recovery of these early coronagraphic data has been devised by the NICMOS IDT.

The first 34 coronagraphic target acquisitions in the EONS program exhibited large (up to $\sim$1 pixel) pointing errors due to the above mentioned flight S/W problem. Acquisitions are done in pairs, approximately 20 minutes apart, in the same target visibility period. The spacecraft is rolled 30^o between acquisitions to obtain coronagraphic images at two orientations. The origin of the graph in Fig. 4 is the desired placement of the target in the coronagraphic hole (the “low scatter point” of the coronagraph). To achieve the detection limits and sensitivities required for the full search space of the EONS programs afforded by the coronagraph the maximum deviation from the low

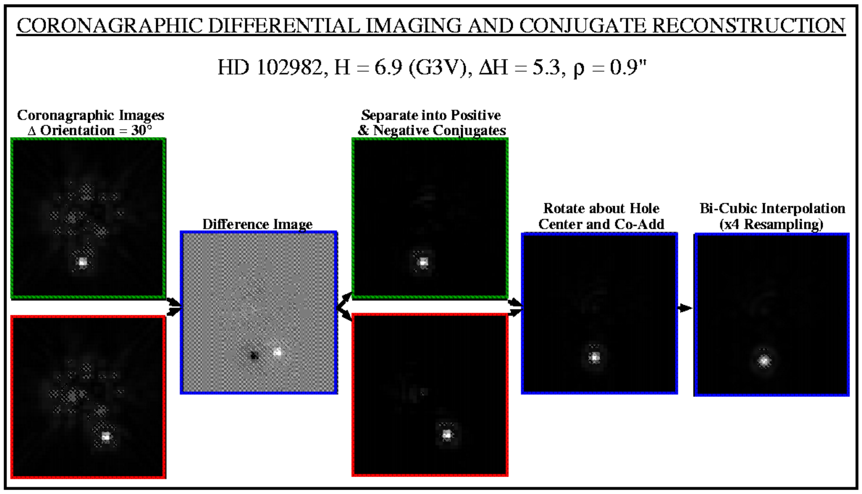

Figure 3. A candidate star is placed in the coronagraph and observed at two orientations differing by 30^o, by rolling the spacecraft. The coronagraphic PSF co-rotates with the detector, a companion rotates about the center of the coronagraphic hole. The images are subtracted to remove theprimary PSF, and the image conjugates (positive and negative residuals) are un-rotated and coadded. Bi-cubic interpolative resampling is done only to show the recovery of the first Airy ring for this low-mass companion star.

scatter point for an acquisition pair should be no more than 0.25 pixels, with a dispersion for the two points in the pair of no more than 0.1 pixels.

To “recover” the observations targets with similar mis-pointings may bepaired and subtracted after appropriate flux-scaling. In the absence of large spacecraft “breathing” excursions, the magnitude of the subtraction residuals is greatly reduced. This is demonstrated in Fig. 5. The subtraction of two identically exposed and reduced, but differentially mis-pointed, coronagraphic images of the same target (805-06 in Fig. 4) is shown in the top left panel. The field was rotated 30 degrees about the target star between observations. The differential pointing error resulted in a mis-registartion of the target in the coronagraphic hole by 0.16 pixel (with an absolute pointing error of $\sim$1.3 pixels).The panel on the top right shows the subtraction of the “positive roll” image of the same target (805) using a much better position-matched flux-scaled PSF (S62).The registration of the two PSF cores was three times better then the roll subtraction shown on the left. (The large dark spot below the target is a moderately bright field star in the reference PSF image). The visually obvious improvement in the image subtraction is quantified in the histogram of subtraction residuals. Using a more closely position matched PSF the FWHM of the residual distribution function is reduced by a factor of 4. Unfortunately, only a few such weii matched mis-pointing pairs exist for the already obtained data. The NICMOS IDT is now designing a post S/W fix observing program to obtain reference/calibration coronagraphic PSFs to recover, to a large degree, the observations already in hand.

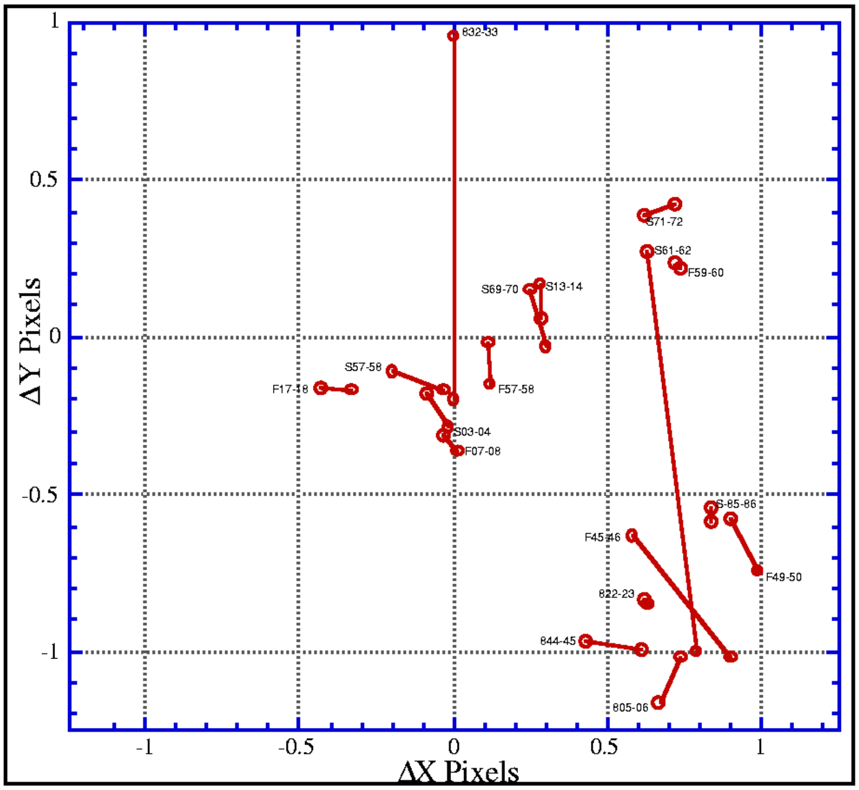

Figure 4. Pointing errors for the first 17 targets observed in the EONS programs. Paired acquisitions should be < 0.1 pixels apart and centered within 0.25 pixels of the low-scatter point (0,0) of the coronagraph. The geometrical radius of the coronagraphic hole is 4 pixels.

4. Summary

Due to the complexities of commissioning the camera 2 coronagraph the EONS search programs received a late start in the NICMOS mission. At this date approximately 1/5 of the sub-stellar companion and circumstellar disk survey observations have been completed. The problem in the target acquisition process resulted in degraded pointing and target centration performance for these observations. None-the-less, the instrumental performance levels of the coronagraph itself, as originally demonstrated in SMOV, continue to meet the needs of the EONS programs. Remedial actions have been taken to mitigate the pointing problem for the remainder of the NICMOS lifetime, and an effective strategy to recover the sensitivity and detection limits from observations taken in the first three months of the program has been developed. With these in place weare confident that NICMOS will allow us to successfully probe the circumstellar environments of nearby stars and address the fundamental questions related to theorigins of stellar and planetary systems raised in our introductory comments.

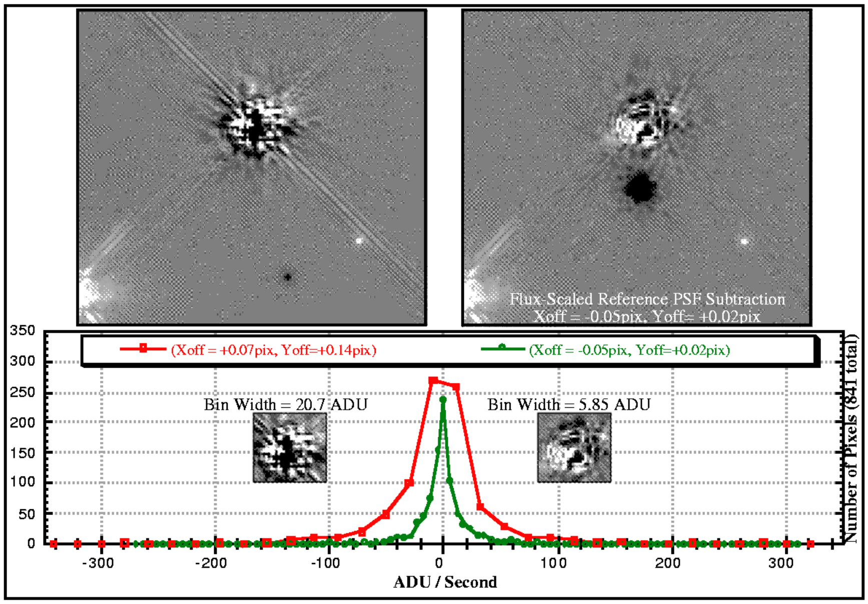

Figure 5. Significant degradation in performance (increase in PSF subtraction residuals) results from small pointing errors. The improvement in performance by subtracting a better position matched (flux-scaled) PSF is illustrated (right). The residual brightness gradient near the hole is due to the small remaining pointing offsets between the two differenced images.

5. Acknowledgments

We would like to thank both STScI and Goddard Space Flight Center's Code 512 for their responsiveness in the consideration and implementation of corrective actions for the augmented target acquisition pointing deficiencies.

This work is supported by the National Aeronautics and Space Administration under NASA grant NAG-5-3042.

References

Burrows,A., Hubbard,W., Lunine,J., Marley,M., Huillot,T., Saumon,D. & Friedman,R., 1997,APS Conf. Series 119, 9.

Delfosse,X., Tinney,C.G., Forveille,T., Epchtein,N., Bertin,E., Borsenberger,J., Copet,E., deBatz,B., Fouque,P, Kimeswenger,S., Le Bertre,T., Lacombe,F., Rouan,D. & Tiphene,D., Astron. Astrophys. 327, L25.

Dressler,A., 1996, HST and Beyond: Exploration and the Search for Origins, AURA Inc.

Kulkarni,S., 1997, Science 276, 1350.

Lowrance,P.J., Becklin,E.E., Schneider,G., Hines,D., Kirkpatrick,D., Koerner,D., Low,F., McCarthey,D., Meier,R., Rieke,M., Smith,B.A., Terille,R., Thompson,R., & Zuckerman,B.,1998, ESO Conference Proceedings (NICMOS and the VLT), in press.

Sandler,D., 1997, ASP Conf. Series 119, 175.

Schneider,G. & Lowrance,P.J., 1997, SMOV/7052 Test Report, ($http://nicmosis.as.arizona.edu/gschneid/7052\_PS/$)

Schneider,G., Smith,B.A, Terrile, R.J. & Meier, R., 1997, SMOV/7157 Test Report, ($http://nicmosis.as.arizona.edu/gschneid/7157\_PS/$)

Schneider,G., Thompson,R.I., Smith,B.A. & Terrile,R.J., 1998, SPIE Conference Proceedings Series 3356, in press.

Zuckerman,B. & Becklin,E.E., 1992, ApJ 386, 260.

NICMOS and the VLT
Pula, Sardinia, May 26-27th 1998
Wolfram Freudling and Richard Hook, eds.

A Coronagraphic Search for Substellar Companions to Young Stars

P.J. Lowrance[1], E.E. Becklin[1], G. Schneider[2], D. Hines[2], J.D. Kirkpatrick[3], D. Koerner[4], F. Low,[2] D. McCarthy,[2] R. Meier[5], M. Rieke,[2] B.A. Smith[5], R. Terrile,[6] R. Thompson,[2] B. Zuckerman[1]

[1]*University of California, Los Angeles, CA*

[2]*University of Arizona, Tucson, AZ*

[3]*Infrared Processing and Analysis Center (IPAC), Pasadena, CA*

[4]*University of Pennsylvania, Philadelphia, PA*

[5]*Institute for Astronomy (IFA), University of Hawaii, Honolulu, HI*

[6]*Jet Propulsion Laboratory (JPL), Pasadena, CA*

Abstract.

We are using NICMOS to search for very low-mass stellar and sub-stellar companions around nearby, young, main-sequence stars. With the coronagraph on Camera 2 and the F160W filter (1.4-1.8μm), we search in the region $0.4''$-$4''$ from the target star. To greatly reduce the scattered light near the hole, we image at two roll angles centered on the star and separated by 30 degrees. The lower mass limit of a detectable companion depends on the mass, age, and distance of the target star as well as the angular separation between star and companion. For several of our targets that are 10-50 Myr old, this lower mass limit could be as low as 10 Jupiter masses.

We display preliminary results using this technique. A stellar-like object with ΔH=5.3 was discovered $0.''9$ from HD 102982. From the distance and age of the primary, this companion is most likely a low-mass M star. Recent observations demonstrate that we can obtain a S/N = 5 (clear detection) on a secondary with ΔH=12 at a separation of 1”.

1. Introduction

Searches for sub-stellar companions to main sequence stars and white dwarfs began about a decade ago utilizing both infrared (photometric) and optical (radial velocity) techniques. Brown dwarfs are objects thought to form like stars, but with insufficient mass ($\leq 0.08 M_{\odot} = 80 M_{Jupiter}$) to sustain hydrogen (H) burning within their interior. In contrast, giant planets like those in our solar system are thought to form through agglomeration of H and He around a rocky, icy core within a protoplanetary disk around a star. Planets are usually split into Jovian (gaseous) and Terrestrial (rocky), but brown dwarfs are more like Jovian planets than Jovian planets are like Terrestrial planets. Some have suggested brown dwarfs might be a third class of planets, since they should not be classified as stars, as they do not have thermonuclear fusion in their cores.

The best brown dwarf candidate for several years was the companion to the white dwarf GD 165 (Becklin& Zuckerman 1998, Zuckerman & Becklin 1992). For eight years it had the coolest temperature ($\approx$1800K) of any dwarf star, but it remained unclear if it was a very low-mass star or high-mass brown dwarf. Recent "all-sky" near-infrared surveys (2MASS & DENIS) may soon clarify whether 1800K objects are minimum-mass stars or brown dwarfs. In 1995, the first undisputed brown dwarf was discovered as a companion to the M1V star GL 229 (Nakajima et al. 1995). The methane feature in the infrared spectrum of the companion clearly constrains its temperature below 1000K (Oppenheimer et al 1995), and models place its mass between 30 and 50 M_J (Burrows et al 1997).

The last two years have brought many discoveries. Presently, we now have several suspected isolated brown dwarf objects in the Pleiades star cluster and solar neighborhood, and several planets around main-sequence stars. Yet, GD 165B and GL 229B remain the only substellar *companions* to have been *directly* imaged. Low-mass objects are intrinsically faint and therefore hard to detect directly close to bright stars. With the resolution and current infrared capability of NICMOS on the Hubble Space Telescope, we can now attempt this daunting task.

1.1. Searching around young stars

Brown dwarfs and giant planets are more luminous when they are young, as they are still at a large radius, gravitationally contracting, and hot. Models of substellar objects (Burrows et al 1997) show that $L \sim t^{-1.3}M^{2.24}$ based on cooling curves derived from atmospheric physics. If these models are correct, we can expect a brown dwarf/planet of $10M_J$ will be above $10^{-6}L_\odot$ when it is $\leq 10^8$ years old.

Numerous young stars within $\sim$ 50 pc of the sun have ages similar to the Pleiades ($\approx 10^8$yrs). This is deduced via inter-comparison of lithium abundance, Hα emission, Ca H & K line emission, kinematics, X-ray emission, and rotational velocity. Age estimates can be calibrated against samples of T Tauri stars and stars in young, nearby clusters such as the Pleiades and the Hyades and distances can be determined from parallax measurements. As part of our GTO program we have assembled a list of $\sim$50 stars thought to be young and close, with median age and distance of 0.1 Gyrs and 33pc, respectively.

The main problem with trying to image brown dwarfs or giant planets around main-sequence stars is the overwhelming brightness of the primary. A substellar companion could be as much as 10^8 times fainter than the star it orbits. A brown dwarf makes up some of this in the infrared, where it radiates most of its power, and is brighter with youth, but the primary can still be 10^4 times brighter. The orbit of a high mass planet is thought to be rather close to the star, as well, so high resolution, achievable from space, is needed. We will conduct our imaging survey with the coronagraph on Camera 2 at 1.6μm (F160W), which corresponds roughly to the H-band filter on the ground.

However, not all sources in the field of view around the primary will necessarily be companions. Background objects could be stars or galaxies. With the excellent resolution on NICMOS, galaxies are easy to distinguish since they appear extended. As for point sources, the ultimate determinant of companionship is common proper motion. The target stars have been chosen for location away from the galactic plane: $| b | > 15^\circ$. Therefore, we expect less than 0.02 background stars within $4''$ at H=22 for each star (D.McCarthy, private comm). Detections will be followed up with additional direct imaging to confirm companionship. For a candidate close-in ($< 4''$), for which the proper motion is enough ($> 0.''08$/yr), we will follow up with a later orbit on NICMOS. This will require giving up another object on our list. NICMOS has a limited lifetime and will be unusable after Dec 98. If the candidate is farther from the target star than $4''$, then ground-based follow-up will be possible to check proper motion. For close objects with smaller proper motions, or those we are unable to follow-up, we must wait for Adaptive Optics (AO) at Keck or Lick observations for confirmation. Keck might have a workable AO system by the first part of 1999 (Larkin, private comm).

Because the coronagraph is in a corner of the detector, this survey will only fully sample $0.''5$ to $4''$ around the primary star. At the average distance of 30 pc, this corresponds to 15-120 AU. This will sample the empirical maximum in the binary distribution of stars as well as the average distance of the giant planets in our own solar system (Duquennoy & Mayor 1991).

2. Observations with NICMOS

Our observational strategy places the target stars behind the coronagraph on Camera 2. The coronagraph is actually a hole in one of the mirrors of the optical path and combined with a Lyot stop, reduces the amount of light in the Airy rings of the point spread function rather than merely blocking light. With the target behind the coronagraph, we reduce the amount of light at the edge of the coronagraph by a factor of 4-6 (figure 1) compared to direct imaging. We have developed an observing strategy to go even deeper, as explained below.

The Hubble Space Telescope has the ability to slew in three directions: x, y, and θ. In order to keep the target star in the same position behind the coronagraph, as well as simplify the removal of the stellar profile, we designed two observations of the star at different spacecraft orientations ($\Delta\theta$) separated by 30 degrees. Therefore, the observing strategy is to place the young star behind the coronagraph, observe in the F160W filter (1.4-1.8μm) for about 700s, roll the telescope 30 degrees, and observe again for 700s. When we subtract the two images, the background from the star should subtract out (not quite completely due to some scattering) and if there are any additional objects in the field, two images (positive and negative) of each should remain (see figure 2). In the Orbital Verification testing (SMOV) of the camera, we found that this strategy worked as expected.

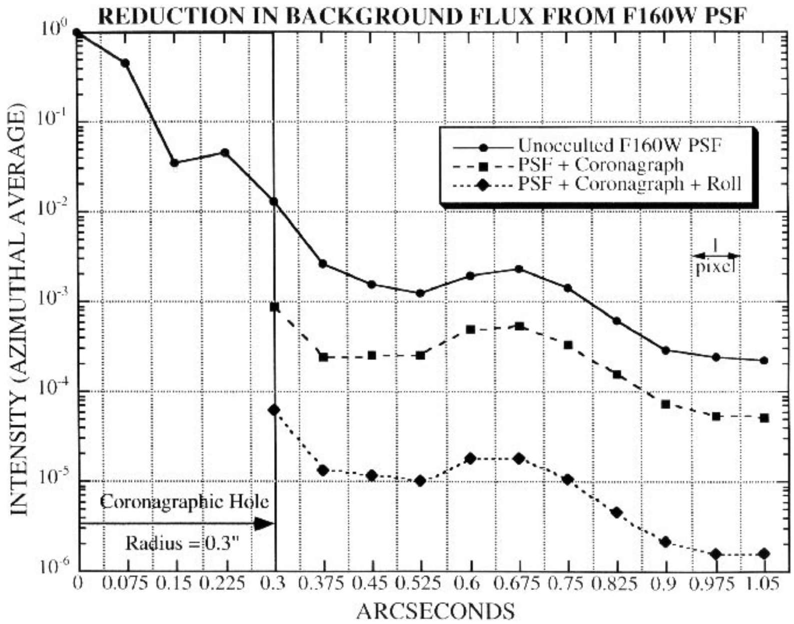

Fig.1: Measured background as an azimuthal average relative to the central pixel of a unocculted image in F160W (H-band) on the NICMOS camera. The background flux is reduced by placing the star behind the coronagraph (dashed line), and reduced even more from the roll subtraction of two images (dotted line). Results of SMOV test 7052 (Schneider & Lowrance, 1997)

According to models (Burrows et al 1997), a 0.1 Gyr old, 20 M_J brown dwarf will have an absolute H magnitude = 13.51 which corresponds to an apparent magnitude of 16.10 at the typical distance of our targets (d=30pc). In figure 1, early observations demonstrated that the background is 10^{-5} less than the star at $0.''5$. With a background $\approx$12 magnitudes fainter than our typical 6th magnitude target star, a 16.10 magnitude object should be easily detectable.

3. Preliminary Results

We present one of of first stars observed, HD 102982, a G3V star, m_H=6.9, 42 parsecs from the Sun. The NICMOS images revealed a stellar object $0.''9$ away which is fainter at H by 5.3 magnitudes. If it is a companion, then M_H=9.08 places it between M5 and M6 in photometric spectral class (Kirkpatrick & McCarthy 1994). The age of the star was thought to be close to the Pleiades age (0.1 Gyr) from X-ray luminosity (Lampton et al 1997) and Calcium H & K emission (Henry et al 1996). At this young age, the companion would be a candidate brown dwarf at the edge of 75 M_J. However, a recent finding (Soderblom et al 1998) shows the primary to be a spectroscopic binary with a period less than one month. This suggests that the activity once thought to be a signature of youth is more likely a product of a tidally-locked close binary system.

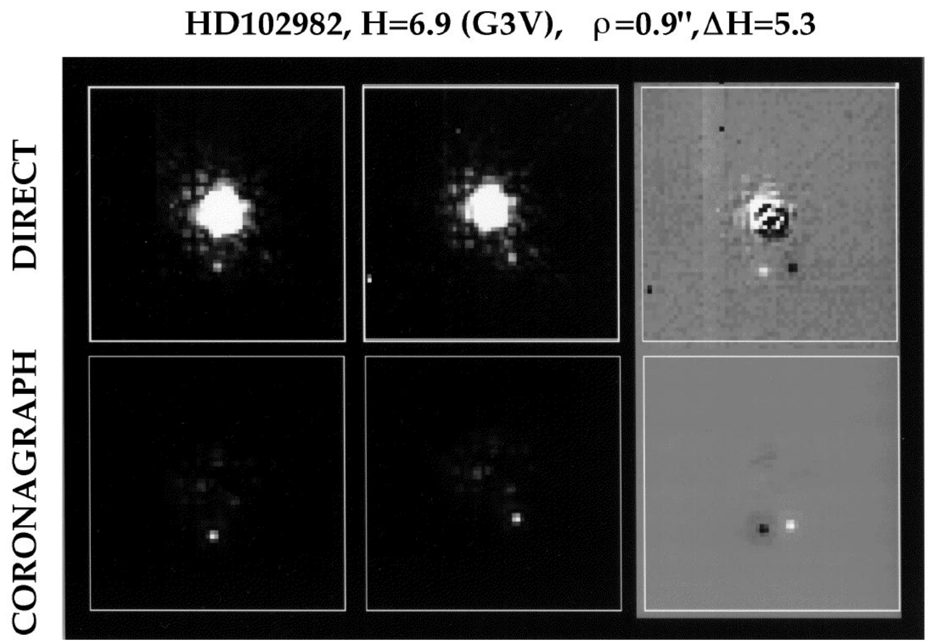

Fig.2: HD 102982 images with direct imaging (top panels) and with coronagraphic imaging (bottom panels). The direct images are from the acquisition with the F165M filter and are scaled to the F160W image. The far right panels are the subtraction of the two roll orientations; thus a positive and negative image exist.

4. Summary

The observations of HD 102982 demonstrate our ability to detect substellar objects. The possible companion has a S/N≈1600 (it is visible in the 0.2s acquisition image) with the roll subtraction for a Δmag≈5. From these observations, we should expect a Δmag≈12 for a S/N=5 (a clear detection) at this separation of $1''$. Around this star, that would be a brown dwarf, and around some of our youngest stars, this brightness corresponds to $\leq 10M_J$ (age=15Myr). Clearly, we will be exploring down to the high-mass planet range with this survey.

To detect brown dwarfs or possible extra-solar giant planets, we are undertaking a coronagraphic imaging survey of young stars. We present images of a possible companion, probably a low-mass M star, to the star HD102982 which demonstrates our ability to detect substellar objects. Every substellar companion discovered with this survey will add to the mere handful already known, and its spectrum would be of tremendous value in determining the physics of objects between 10-60M_J.

References:

Becklin,E.E. & Zuckerman,B. 1988, Nature 336, 656

Burrows,A., Hubbard,W. Lunine,J., Marley,M., Huillot,T., Saumon,D., Friedman,R., 1997, ASP Conf. Servies, 119, 9.

Duquennoy & Mayor 1991, A&A 248, 485
Henry,T.J., Soderblom,D.R., Donahue,R.A., & Balinus,S.L. 1996, AJ 111, 439
Kirkpatrick, J.D. & McCarthy,D.W.,Jr 1994, AJ 107, 333
Lampton.M., Lieu,R., Schmitt,J.H.M.M., Bowyer,S., Voges,W., Lewis,J. & Wu,X. 1997, ApJS 108, 545
Larkin, J. 1998 (private communication)
McCarthy,D.W.,Jr 1996 (private communication)
Nakajima,T., Oppenheimer,B.R., Kulkarni,S.R., Golimowski,D.A., Matthews,K. & Durrance,S.T. 1995, Nature 378, 464
Oppenheimer,B., Kulkarni,S., Matthews,K., Nakajima,T. 1995, Science 207, 1478.
Schneider,G. & Lowrance,P.J. SMOV/7052 Test Report (http://nicmosis.as.arizona.edu/gschneid/7052_PS/)
Soderblom,D.R., King,J., Henry,T.J. 1998, AJ in press
Zuckerman,B. & Becklin,E.E. 1992, ApJ 386, 260

NICMOS and the VLT
Pula, Sardinia, May 26-27th 1998
Wolfram Freudling and Richard Hook, eds.

The Stellar Population in the NICMOS Parallel Fields

A. Pasquali, G. De Marchi and W. Freudling

ST European Coordination Facility - ESO, Karl-Schwarzschild-Strasse 2, Garching bei München, Germany, D-85748, E-mail: apasqual@eso.org

Abstract. We present the preliminary results of the analysis of the NICMOS/GRISM parallel observations from programs #7811, 7922 and 7907. Images and spectra have been reduced and calibrated through CALNICC and NICMOSLOOK. We have used the morphology and the radial profile of the objects identified by CALNICC on the direct images together with the SExtractor class parameter defined by CALNICC for each object to separate stars from galaxies. We here discuss the stars/galaxies distributions in the J and H bands and their corresponding color-magnitude diagrams obtained from both imaging and spectroscopic data.

1. The NICMOS Parallel program

NICMOS Camera 3 is being used in parallel mode to observe galactic fields at both high and low galactic latitudes. One of the scientific goals of the NICMOS campaign is to detect substellar objects, such as brown dwarfs and objects close to the stellar mass-cutoff. The astrophysical relevance of these stellar categories covers many issues, from the star formation mechanisms to the physics of stellar atmospheres, the nature of the dark matter and the galactic structure.

Parallel observations are mostly made in the J and H bands. For each telescope pointing, they comprise direct imaging through the F110W and the F160W filters and grism spectroscopy with the G096 and G141 grisms. Acquisitions are typically of about 250 s and 900 s for imaging and spectroscopy, respectively. The corresponding program IDs are 7811, 7907 and 7922.

The data are processed using the NICMOS pipeline; dithered exposures of the same fields are associated and combined into one image, which is then the input for CALNICB. The direct and grism combined images are used for each pointing by CALNICC in order to identify the objects in the field, derive their J, H photometry from the direct image and extract and calibrate their low dispersion spectra from the grism acquisition.

2. Some Statistics

We have reduced and analysed so far the NIC3 data obtained for 52 independent field pointings. Out of these, only 13 fields have been observed through both F110W and F160W filters and G096 and G141 grisms; 22 have been imaged only in F160W and the corresponding G141, and only 17 have been acquired through F110W and G096.

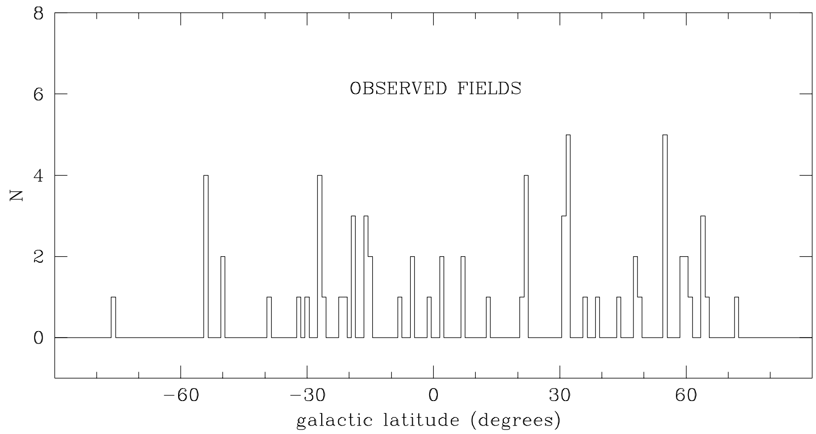

Figure 1. NICMOS parallel fields distribution in galactic latitude.

Most of the fields are at high galactic latitude; as Figure 1 shows, only 8 pointings are within $|b| = 10^o$, i.e. the galactic disk. We have run CALNICC over the data in order to identify the objects in each frame, measure their fluxes and CLASS parameter through SExtractor, which has been implemented in CALNICC for object identification and photometry. The CLASS parameter may be considered as a sort of ellipticity indicator, so that those objects having CLASS $\geq$ 0.85 may be classified as point sources. Since the CLASS parameter seems to be sensitive to variable sky background, we have also traced the radial profile for each identified object and given more weight to the latter to distinguish stars from galaxies. Figure 2 shows the distribution of the objects classified either as stars or galaxies from their radial profiles as a function of their CLASS parameter. It is clear that there is an excellent agreement between the CLASS- and radial-profile- classifications in the case of galaxies, while there may be $\sim$ 30% contamination for the stars sample. We have classified a total of 418 stars and 546 galaxies down to the magnitude set by a detection limit of 5σ above the local background. It is then interesting to correlate the number of stars and galaxies with the galactic latitude of the analysed field pointings. The ratio of stars to galaxies has been plotted in Figure 3 as a function of galactic latitude: a clear increase in the number of detected stars over galaxies is seen towards the galactic bulge and disk. The aperture fluxes measured by SExtractor in CALNICC have been transformed into the HST instrumental magnitudes for both stars and galaxies by reading the inverse sensitivity PHOTLAM from the images header and adopting a zero-point of 21.1 mag. Subsequently, the instrumental F110W and F160 W magnitudes have been translated into the Vegamag system magnitudes by subtracting 2.3 mag and 3.7 mag, respectively. These magnitudes are more similar, although not identical, to J and H in the Johnson - Cousin system. Since 4 fields were observed several times through both filters, we have been able to estimate from them our photometric uncertainty, which turns out to be $\leq$ 0.1 mag in both bands for magnitudes brighter than 19, while it increases up to 0.5 down to the limiting magnitude. Figure 4 describes the photometric properties of our samples: stars are characterized by a limiting magnitude of 23 in J and 22.5 in H. Their distribution peaks at about 20 in J and H with a bright tail extending up to 11.5 in J and 11 in H. The limiting magnitude for galaxies is somewhat fainter: 23.5 in J and 23 in H. Galaxies peak at about 22 in J and 21 in H and can be as bright as 16 mag in J and 15 mag in H.

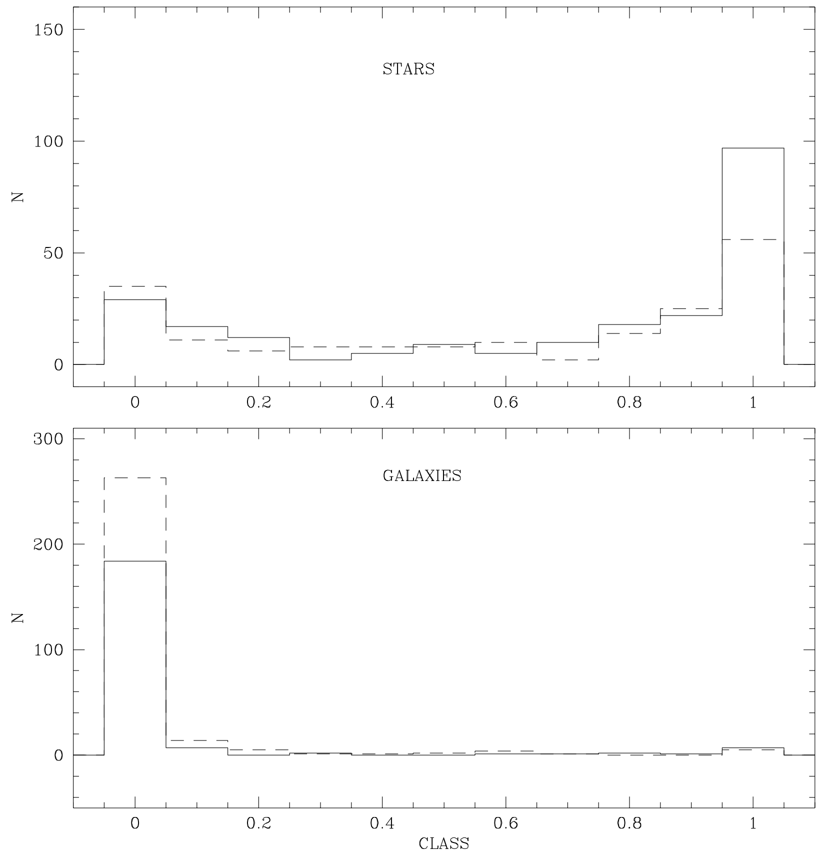

Figure 2. Histograms of stars and galaxies classified by their radial profile as a function of their CLASS parameter. The solid and the dotted lines represent objects detected in the F110W and F160W images, respectively.

These limiting magnitudes are of course set by the relatively short exposure times and also by the fact that, at fainter magnitudes, galaxies are more easily detected than stars due to their extended structure.

3. The Stellar Population

We have here restricted our analysis to the stellar sample. We have used the 13 field pointings observed in both F110W and F160W filters to construct the color-magnitude diagram in Figure 5, where the magnitudes are not dereddened. The distribution peaks around (J-H) = 1, typical of late spectral types; it is however broadened between 0.5 and 1.5 because of the photometric uncertainty, which becomes quite large ($\sim$ 0.5 mag) for those stars close to the limiting magnitude. It is known that the (J-H) color is not particularly sensitive in discriminating stars of different late spectral type and metallicity; to do this, at least a second color is required. To better understand the spectral type of the objects in Figure 5, we have defined the color (I-J)' as (I' - J'), where I' is the magnitude in a box filter between 0.8 μm and 0.9 μm and J' covers the range 1.05 μm to

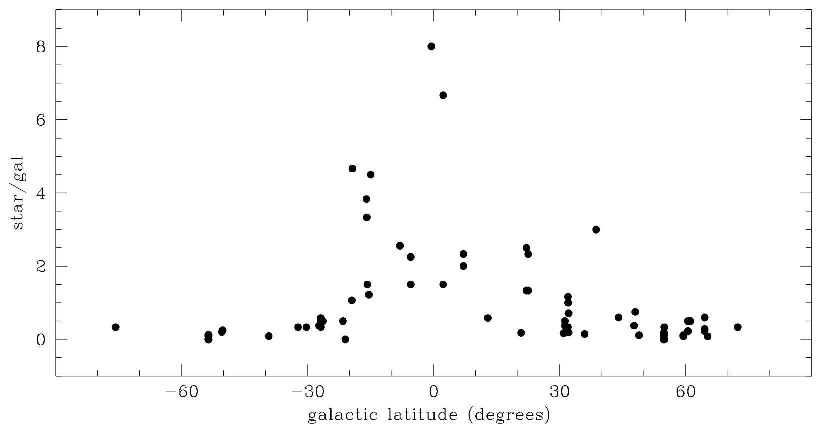

Figure 3. The number ratio of stars to galaxies for the individual 52 pointings as a function of galactic latitude.

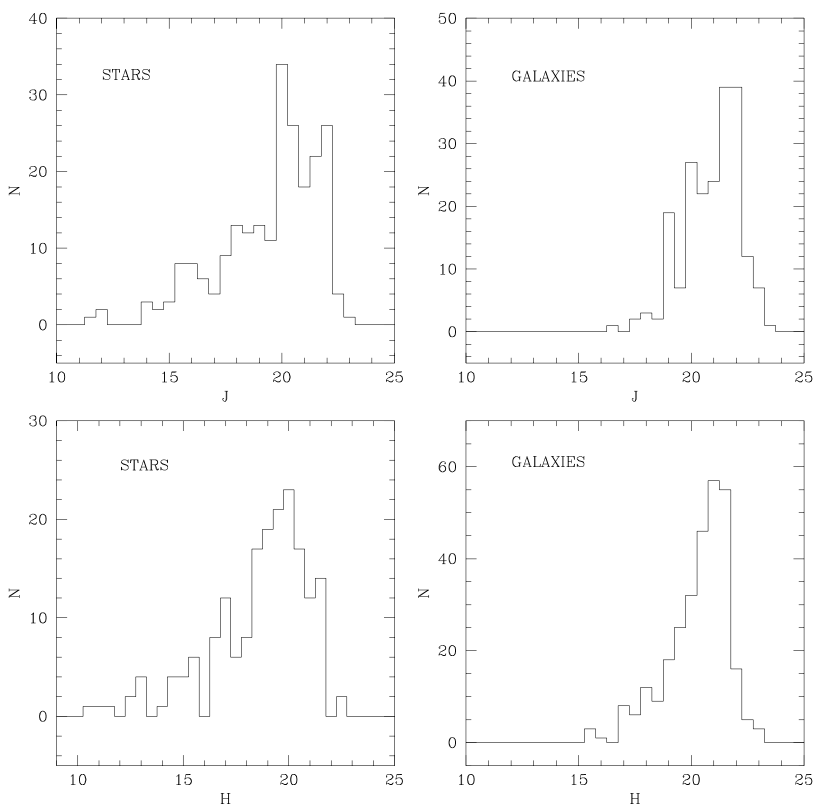

Figure 4. The magnitude distributions of stars and galaxies in the J and H bands.

1.15 μm. We have measured the (I-J)’ color using the G096 grism spectra for all stars in the 13 fields brighter than J = 20 which ensures a good spectral S/N ratio. We have also computed the (I-J)’ color for stars of late spectral type in the BPGS library available in

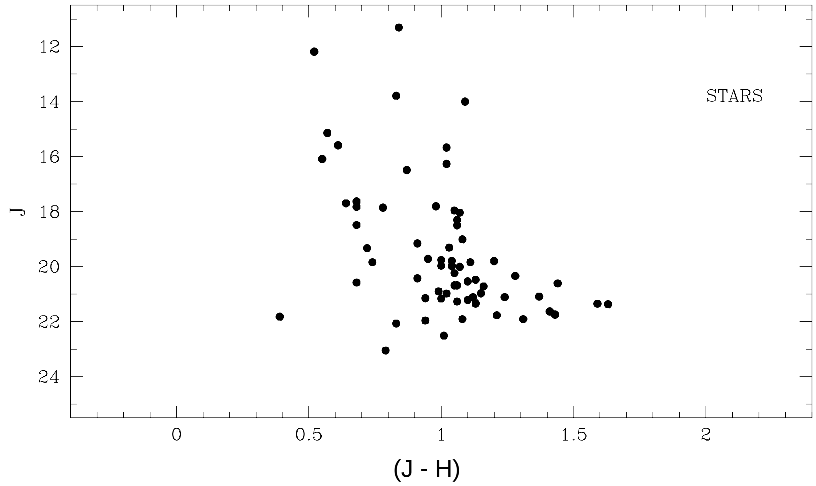

Figure 5. The observed color-magnitude diagram of the stars detected in 13 fields imaged through both F110W and F160W filters.

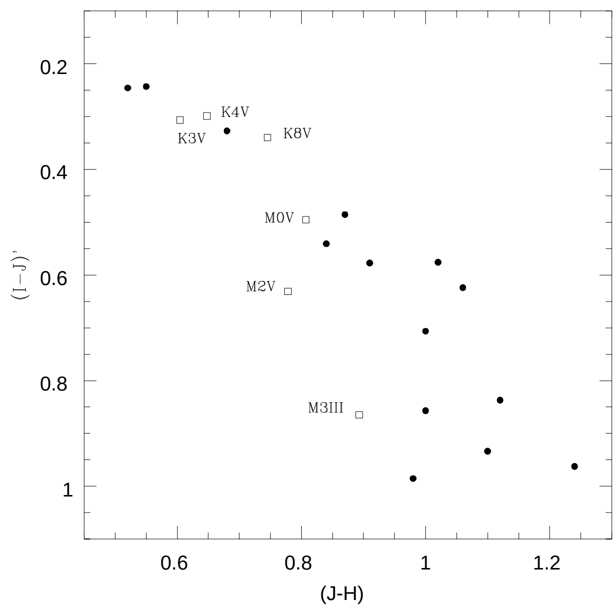

Figure 6. The observed two colors diagram of the stars detected in 13 fields imaged through both F110W and F160W filters (black dots). Also plotted are the colors derived from the BPGS library spectra (open squares).

IRAF in order to build a comparison grid of known spectral types. The resulting two colors diagram is shown in Figure 6, where the (I-J)' and (J-H) colors of the detected stars are not corrected for reddening. The comparison shows that the detected stars are mostly dwarfs of K and M spectral types.

We have also adopted an alternative approach to the problem of deriving stellar spectral types. In fact, we have been able to cross-identify 13 stars out of 418 with the US Navy Observatory Catalogue which has provided us with photographic B and V magnitudes, subsequently scaled to the Johnson system. The typical B and V photometric error is of 0.25 mag and 0.5 mag for stars at positive and negative galactic latitude, respectively, and the cross-identification is uncertain by about 1 arcsec. For the 13 cross-identified stars we have estimated the reddening from the HI maps of Stark *et al.* (1992), which give the HI column density for each position in the sky. HI column densities have been transformed into E(B-V) through the relation of Diplas & Savage (1994): N(HI) = 4.93×10^{21}E(B-V), and we have used the E(B-V) values derived in this way to correct for reddening the available B, V, J and H magnitudes. We have been able at this point to trace the Spectral Energy Distribution (SED) for the 13 stars and match each of these to the SEDs derived from the BPGS spectra. The best fits are shown in Figures 7 and 8, where the errorbars are those of the USN Observatory Catalogue for the B and V bands, and are set to 0.1 mag for the NICMOS J and H bands being brighter than 19 mag (cfr. Sect. 2). Although fits generally get worse at B and V magnitudes fainter than 18, we may conclude that they add a noticeable component of G dwarfs to the previous population of K and M dwarfs (cfr. Figure 6).

We will extend the present analysis to the remaining data of the NIC3 Parallel Campaign and follow up this study by addressing two main astrophysical issues: the spatial distribution, the Luminosity Function (LF) and hence the Initial Mass Function (IMF)of galactic low mass stars.

Acknowledgments. We would like to thank Norbert Pirzkal for supporting the data reduction software during this work. We would also like to thank Luca Pasquini for useful discussions.

References

Diplas, A., & Savage, B. D. 1994, ApJ, 427, 274

Stark, A. A., Gammie, C. F., Wilson, R. W., Bally, J., Linke, R. A., Heiles, C., & Hurwitz, M. 1992, ApJS, 79, 77

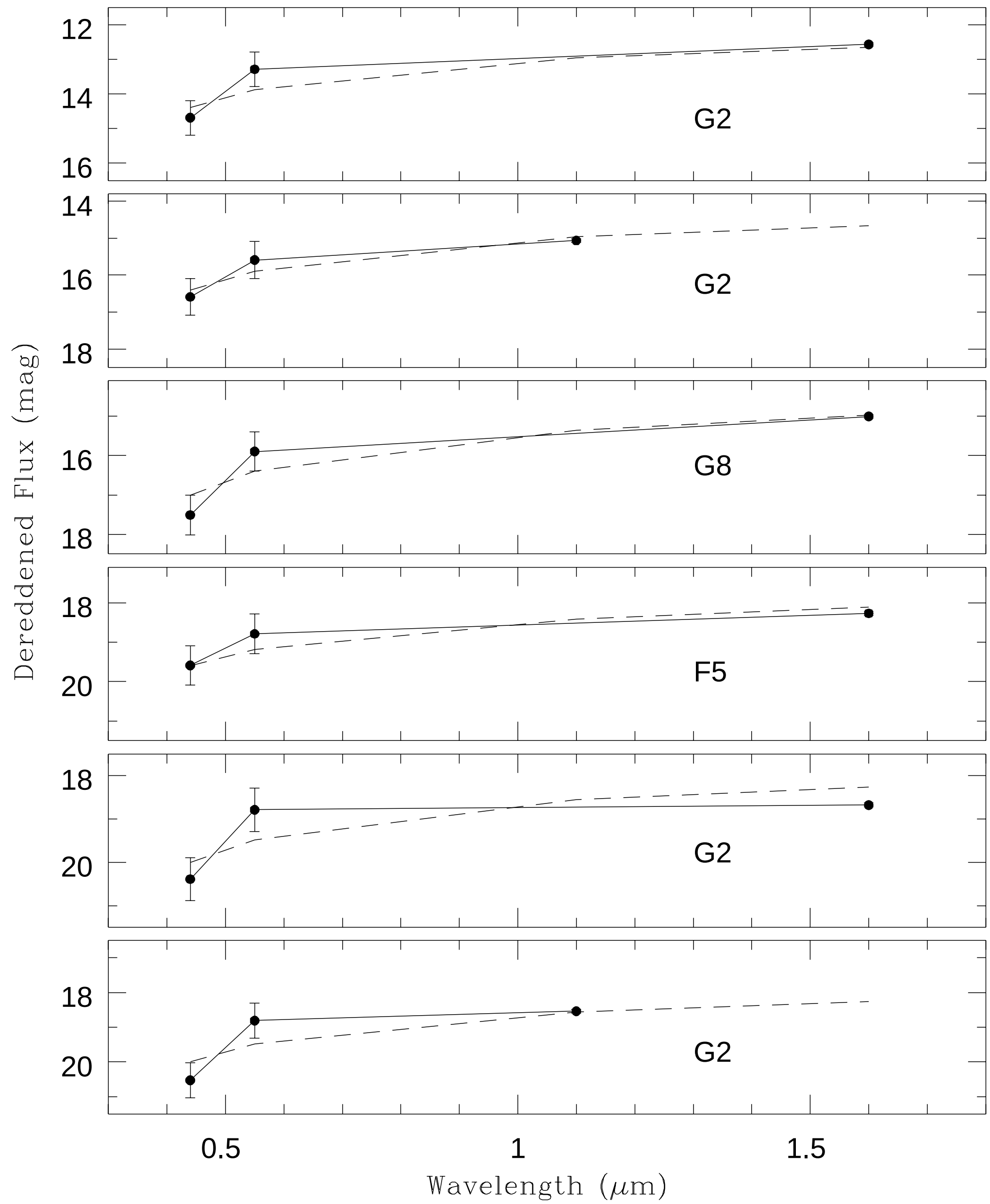

Figure 7. Fits to the observed, dereddened SEDs.

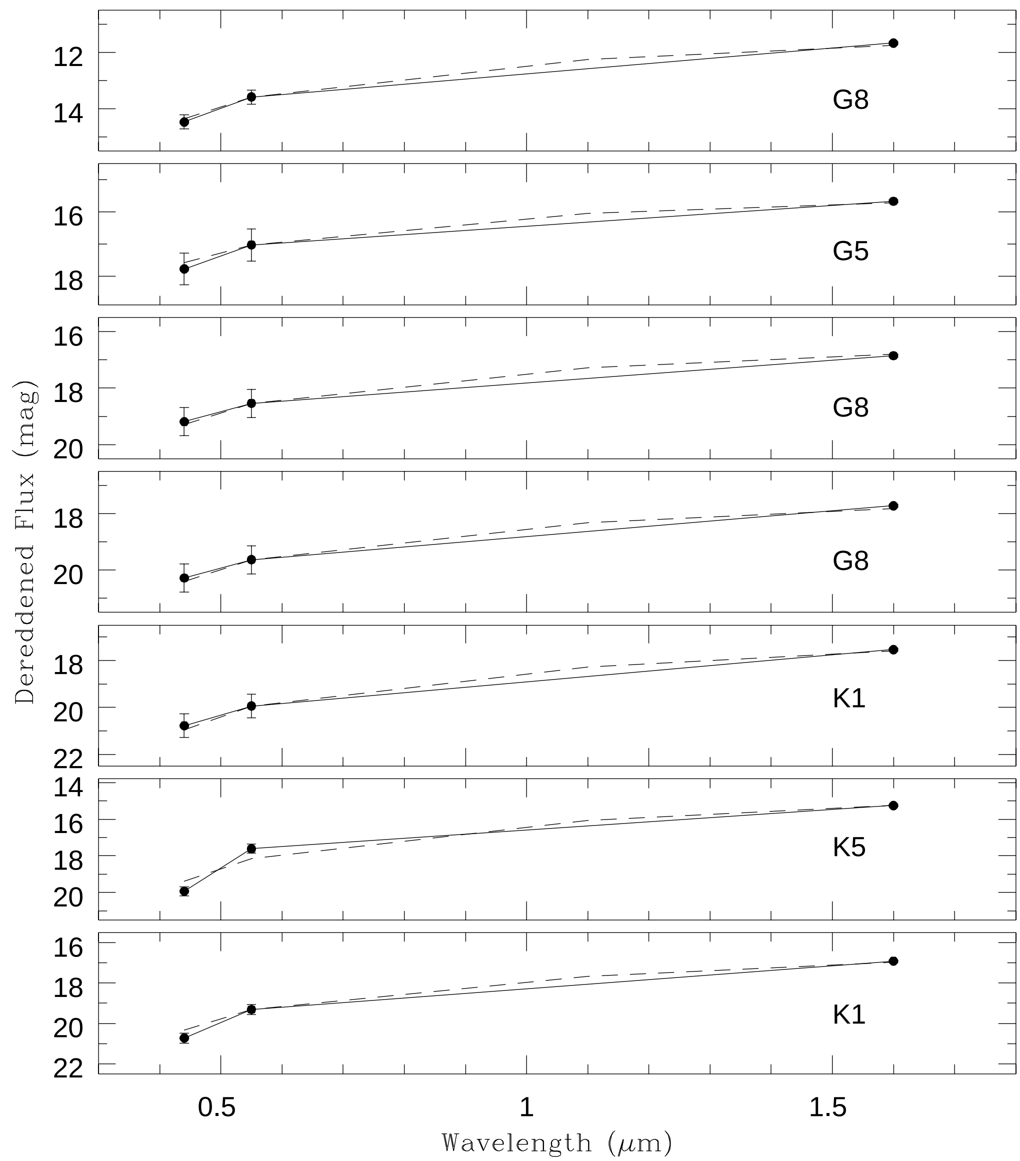

Figure 8. Fits to the observed, dereddened SEDs.

NICMOS and the VLT
Pula, Sardinia, May 26-27th 1998
Wolfram Freudling and Richard Hook, eds.

The Evolution of Stars seen with ISOCAM - the Need for NICMOS and VLT Follow Up.

R. Siebenmorgen

ISO Science Operations Centre, Astrophysics Division of ESA, Villafranca del Castillo, P.O. Box 50727, E-28080 Madrid

Abstract. Three examples are presented of how ISOCAM[1] sees the process of stellar evolution. i) Standard staring and coronographic observations with ISOCAM towards BD+31 643 are presented. The morphology of the detected emission is quite similar to a proto-planetary disk. ii) The class 0 object HH108MMS is detected at 15 mic. in absorption against the diffuse interstellar background. This detection confirms its protostellar nature. iii) A ring of organic matter is detected around the pre–main–sequence Herbig AeBe star HD97300. The images show extended emission, an elliptical ring structure of size about 0.045x0.03 pc as well as two peaks of emission, separated by about 3” (240 AU). One of the two peaks coincides with the position of HD97300, while the other may be an embedded companion. The data show that the emission in this region is dominated by the infrared emission bands centered at 6.2, 7.7, 8.7, 11.3 and 12.5μm, with a very small contribution from continuum emission at longer wavelengths. The spectra are fit with a three component dust model which includes organic molecules such as polycyclic aromatic hydrocarbons, very small graphite and very small silicates, as well as large grains. The fit to the ISOCAM data is very good if one applies a classical oscillator model for the infrared emission bands. The new fitting procedure allows to estimate the total mass of the ring, which is $0.03M_\odot$.

1. Introduction

The Infrared Space Observatory (ISO) completed its observations at 14:00 CET on 16th of May 1998. The targets of ISO had been all over in the Universe: in the Solar System, towards Comets and the Zodiacal Light, Giant Molecular Clouds, Protoplanetary Disks, the Galaxy and still further away to Interacting Systems and QSO in distant Cluster. The observatory performed a total of 40000 IR observations and successfully executed as of end March 1998 a total of 26220 science observations. In this contribution I present three observations performed with the infrared camera ISOCAM (Cesarsky et al., 1996) on board of ISO (Kessler et al., 1996). Those observations are dedicated to the process of stellar evolution. Together with L. Metcalfe and K. Okumura we observed in a coronographic mode a potential proto planetary disk system.

[1] Based on observations with ISO, an ESA project with instruments funded by ESA Member States (especially the PI countries: France, Germany, the Netherlands and the United Kingdom) with the participation of ISAS and NASA.

This experiment is somehow unique since no real coronograph was mounted on ISO. The second experiment, performed with E. Krügel and R. Chini, shows the detection of a protostar in absorption against the diffuse background. I close discussing the nature of a ring detected around a Herbig Ae/Be star (Siebenmorgen, Natta, Krügel, Prusti, 1998).

2. A Proto-Planetary Disk around BD+31 643 ?

Recently Kalas & Jewitt (1997) discovered a circumbinary disc in scattered light around BD+31 643 (B5 V) in the young cluster IC 348. The disk has quite a similar morphology as the scattering disk of β Pictoris. Although the disk around BD+31 643 is much larger.

Together with L. Metcalfe and K. Okumura we pointed with ISOCAM towards this target and detected at 15 μm emission in a disk like structure, extending at least 45" or 15000AU at the distance of the star (300pc).

Further we employed a "coronographic" observing mode of ISOCAM and detected a disk like quite asymmetrical emission structure at 4.5 μm. The "coronagraphic" ISOCAM mode rejects the light of the central source by causing it to fall off the edge of the small Fabry-mirror and thus allowing for a high enough dynamic range to detect faint emission nearby a bright target (Metcalfe, Siebenmorgen, Okumura, 1998).

3. The Protostellar Candidate HH108MMS

Although the definition of a protostar is debatable, the detection of such an object is likened to finding the holy grail. No wonder that numerous detections of protostars have been claimed during the last two decades. However, with improving technical equipment, all sources turned out to be more or less evolved young stellar objects.

A promising approach of searching for true protostars is to investigate regions of ongoing star formation at mm/submm wavelengths. In a systematic investigation of all known Herbig Haro energy sources at mm/submm wavelengths which includes mapping of dark clouds at high spatial resolution with IRAM 30m, SEST, JCMT; a new class of young stellar objects (assigned to "Class 0") have been found. All of them are strong mm/submm sources and among them are the coldest and densest dust condensations ever found (for instance, Chini et al. 1993, AA272,L5). Their known characteristics are:

a) From spectral energy distributions (SED) between 350 and 1300 microns the typical dust temperatures are about 10K.

b) Associated masses, as derived from the dust emission, are comparable or greater than the Jeans mass.

c) Molecular line data indicate that the molecules are partially frozen out.

It was predicted that Class 0 are opaque enough to be detected in absorption against the diffuse background (e.g. Buss & Yorke 1990; Fig. 10 in Siebenmorgen et al. 1992)

The ISOCAM image I took in collaboration with E. Krügel and R. Chini towards the Class 0 source HH108MMS (Chini et al. 1997) shows indeed this source in absorption against the diffuse background (Figure 1).

Although there is blending with zodiacal light, one can derive from the absorption feature an optical depth at 15μm of about 4. This translates into a visual extinction of

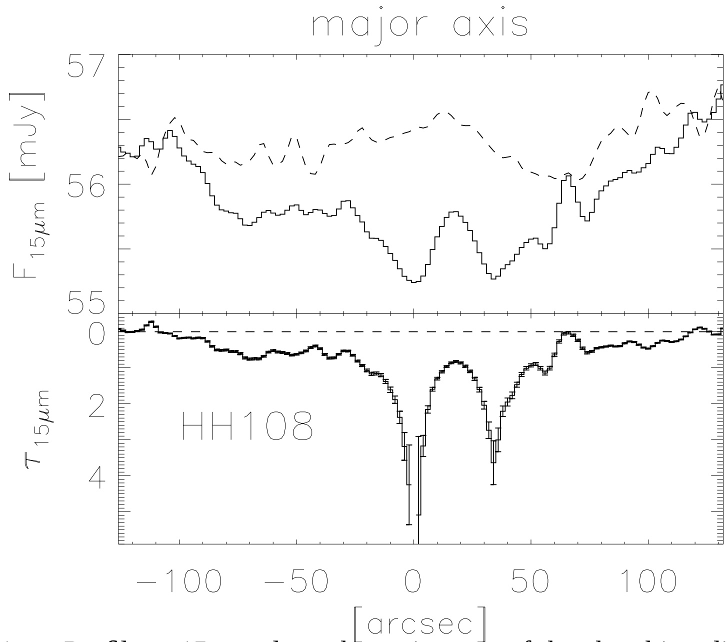

Figure 1. Profile at 15 μm along the major axis of the absorbing disk like structure centered at the position of HH108MMS is shown as histogram in the upper panel. The background flux is indicated as dashed line. The optical depth at 15 μm shown in the lower panel is derived by taking the minimum source flux as zero point.

Av more than 80mag. The direct measurement of dust extinction at this wavelength allows to confine the dust properties in this object which are certainly modified in the cold and dense environment of the protostar (Krügel & Siebenmorgen 1994). The ISOCAM image suggests that besides the core, we see in HH108MMS an extended disk in absorption against the diffuse interstellar background which makes this source even more remarkable (Siebenmorgen, Krügel, Chini, 1998).

4. A Ring of Organic Molecules around HD 97300.

Imaging spectroscopy of the pre-main–sequence star HD 97300, was obtained with ISOCAM. Those data are from a program which aimed at investigating the nature of the mid-infrared emission associated to Herbig AeBe stars. They are discussed in more detail by Siebenmorgen, Natta, Krügel, Prusti (1998) and some other “first” results are given by Siebenmorgen et al., 1997.

The young star HD 97300 is located in the Chamalion I cloud (Whittet et al. 1997), at distance $D \sim 188$ pc. We report the detection of an extended, ring-like structure around HD 97300, whose emission is dominated by the infrared emission bands at 6.2, 7.7, 8.7, 11.3 and 12.5 μm, (hereafter IEBs), observed in our own and other galaxies wherever neutral matter is exposed to UV radiation (see the many papers presenting CVF and SWS spectra in the special issue of *Astronomy and Astrophysics* on ISO published in November 1996).

4.1. Results

Fig. 2 shows the images of HD 97300 obtained in the four CAM narrow-band filters centered at 6.0 μm (lw4), 6.8 μm (lw5), 11.3 μm (lw8) and 14.9 μm (lw9). The morphology of the object is very similar in the four filters: we can see extended emission centered on the star and an elliptical ring of size $\sim 50 \times 36''$ around it. This same morphology is also seen in the CVF images at all frequencies, with very similar characteristics.

The ring is not symmetric around the star, but is much more extended in the SE than in the NW direction. The off-center location of the star with respect to the ring may be the effect of a density gradient in the SE–NW direction in the outer region of the Chamalion I cloud where HD 97300 lies. The position of the star in our images coincides with the emission peaks seen near the center in lw4 and lw5, and with the secondary peak of the emission seen in lw8, roughly at the same position. In the lw8 and lw9 filters we detect a second peak of emission, about $3''$ (240 AU) north of the star.

Fig. 3 shows CVF spectra between 5.8 and 13.8 μm in 8 positions roughly aligned along P.A. = 142.4^o. This line intersects the star, as well as the emission minimum and the ring seen in the SE direction. The location of the 8 positions is indicated in Fig. 2. In all positions, we detect strong IEBs over a weak continuum.

4.2. The IEBs Carriers

To acquire a better understanding the spectra of Fig. 3 are fit using the three component dust model of Siebenmorgen and Krügel (1992). This model computes the emission per unit mass of dust heated by radiation of known intensity and spectral distribution. We use $T_\star$=10700 K (Rydgren 1980) and luminosity $L_\star$=35 $L_\odot$(van den Ancker et al., 1997). The computed spectra are smoothed to the CVF spectral resolution. We adjust the PAH parameters and vary the gas column density $N_{\rm H}$ until a satisfactory fit is obtained.

The simplest picture we can construct to model the band shapes is to consider that the bands can be described by classical oscillators. The absorption coefficient (σ_ν; Schutte et al. (1993)) of such a driven damped oscillator is a Lorentzian profile

$$\sigma_\nu \;=\; \frac{\sigma}{2\pi} \cdot \frac{\gamma}{(\omega-\omega_0)^2+(\gamma/2)^2} \; , \tag{1}$$

where $\omega = 2\pi\nu$.

Note that an excited level in an atom has an average lifetime $t_{\rm L} = A^{-1}$, where A is the Einstein coefficient for spontaneous transition, the probability to find the atom there decays like e^{-At}. Because of Heisenberg's uncertainty principle $\Delta E \cdot \Delta t \geq \hbar$, the energy of the upper level is then only defined to an accuracy $\Delta E = A\hbar$. This leads naturally to a Lorentzian emission profile, and A may be identified with the damping constant, $\gamma = A$. In this picture, the line width is determined by the timescale Δt. For PAH resonances with a width of $\simeq 0.1\mu$m, the characteristic time Δt would be 10^{-12} s. This would imply immense values for A (10^{12} s^{-1}) as well as for the associated dipole moment $\mu \sim 10^5$ Debye because $A \propto \mu^2\omega^3$. A way out of the dilemma would be to assume that the IEBs arise from a superposition of many narrow lines.

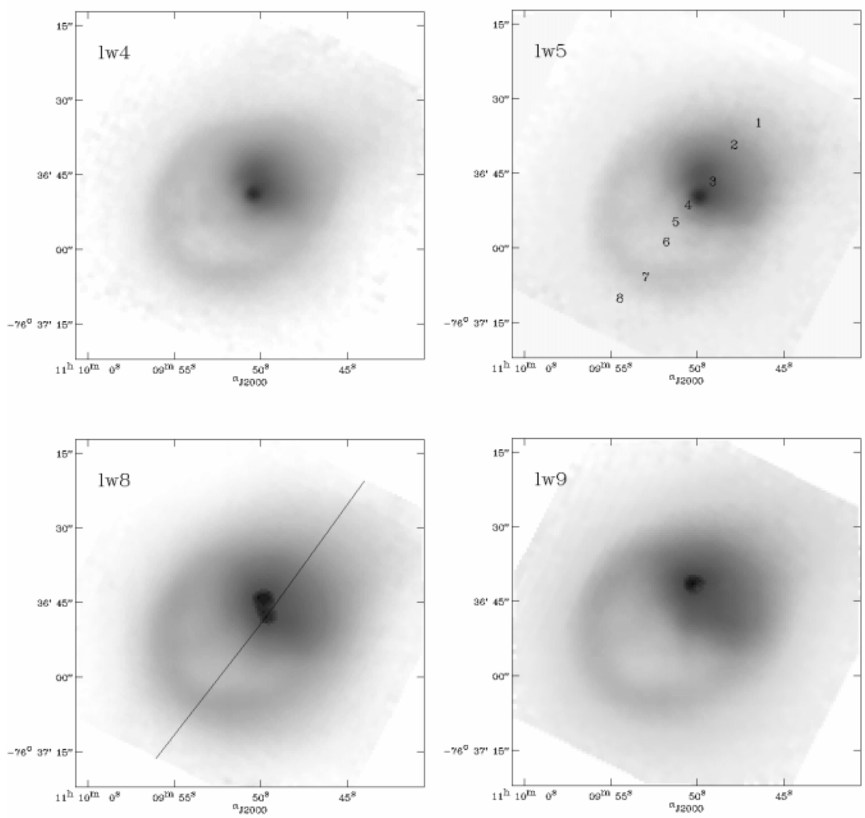

Figure 2. Logarithmic grey scale images of HD 97300 of the four narrow-band filters. The images are re-sampled to 0.5″ pixel scale. The numbers in the lw5 image indicate the positions of the CVF spectra shown in Fig. 3.

4.3. Mass of Circumstellar Material

An interesting possibility opened with our model is to derive the mass of circumstellar material from the observed intensity of the PAH features.

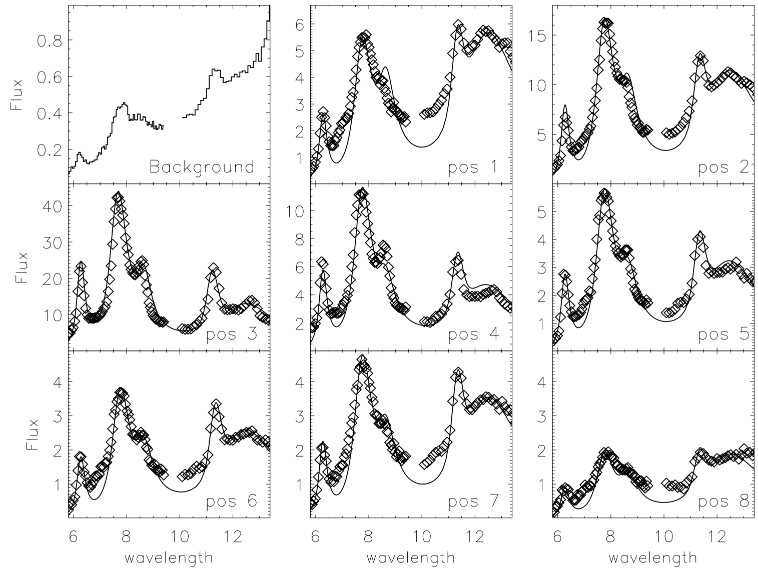

Figure 3. CVF spectra of HD 97300 in the 8 positions shown in Fig. 2. Position 4 is closest to the star; Position 6 coincides roughly with the minimum of emission seen in the images; position 7 with the ring. The background emission has been measured in the upper-left corner of the imaged area. Each spectrum has been measured over a single pixel, i.e., over an area of $3'' \times 3''$. The uncertainties are typically smaller than a few %. Data are shown by diamonds and the best-fit models by the full lines.

We know the geometry of the emitting region, i.e., the approximate distance of the grains from the star. For a given distance and stellar luminosity, the integrated 6 to 14μm flux is directly proportional to the number of C atoms in PAHs. This is because the PAHs account for the total emission in this spectral region. The fraction of C atoms in PAHs is known to within a factor of three, so we can directly convert the carbon column density $N_{\rm C}$ derived by fitting the feature intensities into a hydrogen column density $N_{\rm H}$. The uncertainty on $N_{\rm H}$ is probably comparable to the uncertainty that affects its determination from sub-millimeter continuum observations (see, for example, Krügel & Siebenmorgen, 1994). The mass of gas and dust can then be computed from the values of $N_{\rm H}$ averaged over the region of interest.

We derive a total mass of the circumstellar material in a region of about 0.03 pc radius ($33''$) of about $0.07\mathrm{M}_\odot$ of which $0.03\mathrm{M}_\odot$ is in the elongated ring structure.

4.4. The Origin of the Ring

The presence of PAHs in the ring indicates that it is made of interstellar matter, rather than of matter ejected from the star. Its morphology suggests that the ring structure has been created by the interaction of the star with the surrounding matter.

It is possible that the ring results from the interaction of a stellar wind with the environment. In this hypothesis, the material in the ring is swept-up gas and the ring coincides with the inner wall of a three-dimensional cavity created by the wind. A second possibility is that the ring is due to the action of the radiation pressure from the star working on the grains.

Finally, it is interesting that HD 97300 is not the only Herbig AeBe star with a ring. A similar structure (although about 3.5 times larger) is seen in scattered light in the younger and more deeply embedded star LkHα198 (Leinert et al. 1991). In that case also the ring has an elliptical shape and the exciting star is shifted from its center.

5. Summary

I presented three examples of the evolution of stars as seen with ISOCAM. All those cases are again a good demonstration of the high sensitivity of ISO.

However, the hypothesis of a proto-planetary disk structure of BD+31 643 must be further confirmed and we want to know if there could be planets in the outer parts of the binary disc? Nearby IRAS18331-0035 and HH108MMS there are other absorbing “knots” visible in the ISOCAM images. One wants to uniquely resolve them. To unambiguously measure the spectral energy distribution of the secondary peak of HD 97300 one needs a higher spatial resolving power. One is wondering if we see a deeply embedded companion?

With these kind of questions we have an immediate response to the data presented: we need higher spatial resolving power. Some higher resolution observations are certainly existing in the NICMOS data base but just in this moment becoming available with the first light of the VLT.

References

Boss A., and Yorke H., 1990, ApJ 353, 236

Cesarsky D., Lequeux J., Abergel A. et al., 1996b, A&A 315, L305

Chini R., Krügel E., Haslam H., et al. 1993, AA272,L5

Chini R., Reipurth B., Sievers A., , Haslam H., et al. 1997, AA

Kessler M.F., Steinz J.A., Anderegg M.E. et al., 1996, A&A 315, L27

Kalas, P., and Jewitt D., 1997, Nature 386, 52

Krügel E., and Siebenmorgen R., 1994, AA 288, 929

Leinert Ch., Haas M., Lenzen R., 1991, A&A 246, 180

Metcalfe L., Siebenmorgen R., Okumura K., in prep.

Rydgren A.E., 1980, AJ 85, 444

Schutte W.A., Tielens A.G.G.M, Allamandola L.J., 1993, ApJ 415, 397

Siebenmorgen R., Krügel E., 1992, A&A 259, 614

Siebenmorgen R., Krügel E., Mathis J.S., 1992, A&A 266, 501

Siebenmorgen R., Prusti T., Krügel E., Natta A., 1997, Proc. First ISO Workshop on Analytical Spectroscopy, 6–8 October 1997 (ESA SP-419, December 1997).

Siebenmorgen R., Natta A., Krügel E., Prusti T., 1998, A&A subm.

Siebenmorgen R., Krügel E., Chini R., in prep.

van den Ancker M.E., Thé P.-S., Tjin A Djie H.R.E., Catala C., de Winter D., Blondel P.F.C., and Waters L.B.F.M., 1997, AA 324, L33

Whittet D.C.B., Prusti T., Franco G.A.P., Gerakines P.A., Kilkenny D., Larson K.A., Wesselius P.R., 1997, A&A 327, 1194

NICMOS and the VLT
Pula, Sardinia, May 26-27th 1998
Wolfram Freudling and Richard Hook, eds.

Unusual H_2 Emission near a Compact Source in Orion

M. Lindqvist and J.H. Black

Onsala Space Observatory, S–439 92 Onsala, Sweden
Email: michael@oso.chalmers.se, jblack@oso.chalmers.se

Abstract.

Preliminary results are reported for high-resolution imaging of parts of the Orion Bar. Data have been obtained through a variety of filters with the Near-Infrared Camera and Multi-Object Spectrometer (NICMOS) on Hubble Space Telescope. One striking feature is a small source of almost pure H_2 line emission, which is located near one of the compact sources in Orion reported by O'Dell and collaborators (HST–18 = 203–504). We suggest how some physical properties may be inferred from narrow-band fluxes.

1. Introduction

Molecular hydrogen (H_2) emits strong near-infrared lines, both in regions where it is thermally excited at high temperatures ($T > 1000$ K, e.g. in molecular shocks), and in the illuminated boundaries of molecular clouds (photon-dominated regions or PDRs) where it is excited by UV pumping. In the case of UV fluorescence, when the illuminating radiation is fairly uniform, observed fluctuations in the H_2 line intensity will trace fluctuations in density and column density in the boundary layer of the molecular cloud. This was one of our motivations in obtaining high-resolution images of H_2 emission in the Orion Bar with NICMOS. The Orion Bar is the visible ionization boundary of the Orion Nebula, southeast of the Trapezium. It is a well studied example of a Photon-Dominated Region (PDR) where the boundary of a molecular cloud is illuminated by intense ultraviolet radiation from hot stars (Hogerheijde et al. 1995, Jansen et al. 1995). Direct observations of the excited H_2 emission with $\approx 0\farcs1$ resolution offer the possibility to trace the small-scale structure of such a boundary region.

The Orion Bar region also harbors Herbig-Haro objects, notably H-H 203 and H-H 204 (also known as M42 H-H 3 and H-H 4, respectively) and some of the compact sources and proplyds identified by O'Dell and collaborators (O'Dell, Wen & Hu 1993; O'Dell & Wen 1994).

2. Observations

We obtained a series of images across the bright rim of the Orion Bar near the peaks of mm-wave molecular line emission with NICMOS cameras $1-3$ (NIC1, NIC2, NIC3) in several filters on 1998 February 18. Only preliminary results from NIC2 are discussed here. The NIC2 camera has a field of view of $19\farcs2 \times 19\farcs2$ and a plate scale of $0\farcs076$ pixel^{-1} (Thompson et al. 1998). Images were obtained in two narrow-band (1%

resolution) filters, F212N (centered on the H_2 $v = 1-0$ S(1) line) and F215N (line-free continuum for thermal emission), as well as in two medium-band filters, F171M, and F180M.

The data have been reduced through the pipeline processing with the CALNICA software, which carries out the subtraction of dark current, flat-fielding, and linearity corrections. Multiple exposures have been combined in a mosaic by further processing with CALNICB software.

The full mosaic in filters F212N and F215N shows that the Bar region is threaded by a complicated pattern of thin filaments, clearly highlighted by their H_2 line emission. When the excitation of the H_2 vibration-rotation spectrum is near-thermal at high temperatures ($T \geq 1000$ K), the contrast in flux between F212N and F215N images should be quite high. When the excitation is caused by ultraviolet fluorescence at relatively low densities ($n(H_2) \leq 10^6$ cm^{-3}), strong lines appear in both bands and the contrast is not so large (see §3 below). Where the extended emission shows up in both bands, it is likely that fluorescence makes a large contribution to the observed emission. The appearance and interpretation of the extended emission will be discussed in more detail elsewhere.

We focus here on a very striking feature of the narrow-band images. There is a very compact source which shows up conspicuously in the F212N image but is nearly undetected in the F215N image. It is located $1\farcs6$ from a much brighter stellar source, which has equal brightness in the two narrow-band filters. This stellar source coincides with the compact source HST 18 discovered by O'Dell, Wen & Hu (1993) in their WF/PC survey of the Orion Nebula region. Although many of the compact sources in that work were identified as "proplyds" (= protoplanetary disks), this particular object was considered unlikely to be of the proplyd type, possibly an H-H object instead. In the subsequent study of proplyds (O'Dell & Wen 1994), this source was given the designation 203–504 and was listed as associated with a variable star, number 644 (far-red magnitude I=13.5), in the catalogue of Jones and Walker (1988). The image containing this star and our H_2-emitting condensation is shown as a contour diagram in Fig. 1. The infrared image of the star is evidently unresolved ($0\farcs2$ diameter FWHM), while the H_2 condensation is extended ($\approx 0\farcs46$ FWHM) in F212N. Close inspection of a WF/PC narrow-band image in Hα shows that the H_2 condensation coincides with a small, dark area in the bright emission, but the contrast is not high. The fluxes of the star in the two narrow-band filters are equal, approximately 7.0 mJy, which corresponds to a K magnitude of approximately 12.5. In F212N, the integrated flux corresponds to a surface brightness (over $0\farcs46$) of $I \approx 2.4 \times 10^{-3}$ erg s^{-1} cm^{-2} sr^{-1}. The marginally detected source at the position of the H_2 condensation in F215N is consistent with a point source at K=18.0 mag. The ratio of integrated fluxes $f_{212}/f_{215} = 24$. In F171M, we measure a weak source at the H_2 position, which is not obviously extended. The ratio of integrated fluxes, corrected for bandwidth, is $f_{212}/f_{171} = 4.6$.

3. Discussion

Proplyds are seen as dark silhouettes in projection against the Orion Nebula and are believed to be circumstellar disks. NICMOS observations of several proplyds in Orion have recently been discussed in several papers (Chen et al. 1998; McCaughrean et al. 1998; Stolovy et al. 1998). Although O'Dell et al. 1993 suggested that HST 18 is probably not of the proplyd form, it is interesting that it appears to be associated with the compact source of H_2 emission that we have found. The evidence of an association consists of (1) the small angular offset and (2) the extension of H_2 emission contours along an axis directed away from the star HST 18. At the distance of Orion KL, $d = 480$ pc (Genzel et al. 1981), the angular distance between the star and the H_2 condensation corresponds to 770 AU in projection on the sky. The angular extent of the H_2 emission, $0\farcs46$, corresponds to 220 AU (3.3×10^{15} cm).

In fact, O'Dell and Wen (1994) proposed that HST 18 is an Herbig-Haro (H-H) object. H-H objects are collisionally excited nebulae produced by supersonic outflows ejected by young stellar objects (YSOs). Although HST 18 shows Hα and [N II] line emission based on the WF/PC images, our infrared images of that source appear stellar. The suggestion of an H-H object does not seem compelling. It is impossible to decide whether the compact source of H_2 emission nearby is excited by a shock or by some other thermal process without a spectrum. However, the flux ratios in the narrow-band images can distinguish between pure fluorescent emission and some form of thermal excitation. We have computed thermal emission spectra of H_2 at temperatures $T = 1000$, 2000, and 3000 K, and convolved these with the NICMOS filter response functions. The predicted flux ratios at these three temperatures are $f_{212}/f_{215} = 950$, 43, and 15, respectively. The flux ratio in a typical fluorescence spectrum (cf. Black & van Dishoeck 1987) is $f_{212}/f_{215} = 2.7$. The observed ratio of integrated fluxes, $f_{212}/f_{215} \geq 24$, is thus inconsistent with pure fluorescence; it would imply a temperature $T \leq 2500$ K for fully thermal emission. There is a large number of H_2 lines within the bandpass of the F171M filter. The observed, bandwidth-corrected ratio of integrated fluxes $f_{212}/f_{171} = 4.6$ is in harmony with thermal emission at $1500 < T < 2400$ K. The corresponding value of the ratio predicted for pure fluorescence is 0.84. As shown by Sternberg & Dalgarno (1989), UV-pumping of H_2 emission produces a spectrum more like the thermal spectrum, when the density is high enough that the excited H_2 is partly de-excited by collisions (i.e. partly thermalized). The position of our H_2 condensation is close to one of the peaks of emission in the C 65α and C 91α recombination lines, which trace the density of the PDR that is maintained by the light of the Trapezium stars (Wyrowski et al. 1997). The ambient interstellar density in this direction is moderately high, $(0.5 - 2.5) \times 10^5$ cm^{-5}. Thus it is conceivable that the H_2 emission arises in an even denser condensation in the PDR through partly thermalized UV fluorescence. Spectroscopy will be needed to decide definitively the nature of this source. Chen et al. 1998 suggested that the H_2 emission from their circumstellar disks (proplyds) cannot be excited by a mechanism internal to the source; they concluded that it is more likely that the H_2 is excited by UV fluorescence from one of the hot stars nearby.

The observed flux ratios for our source are consistent with thermal emission at $T \approx 2000$ K. The observed surface brightness of the H_2 condensation requires a column density of molecules $N(H_2) = 7.5 \times 10^{18}$ cm^{-2} thermalized at this temperature. Such a column density spread over the small measured extent of the source corresponds to a total hydrogen mass of only 2.7×10^{26} g or 0.046 earth-masses. If nothing else, this is an indication of the remarkable sensitivity of NICMOS to small amounts of excited hydrogen.

Acknowledgments. We gratefully acknowledge the efforts of the NICMOS Science Team over the years and of the NICMOS project staff at NASA Goddard Space Flight Center and STScI. Our work is a part of the NICMOS/GTO science and has been generously supported by a contract through the University of Arizona.

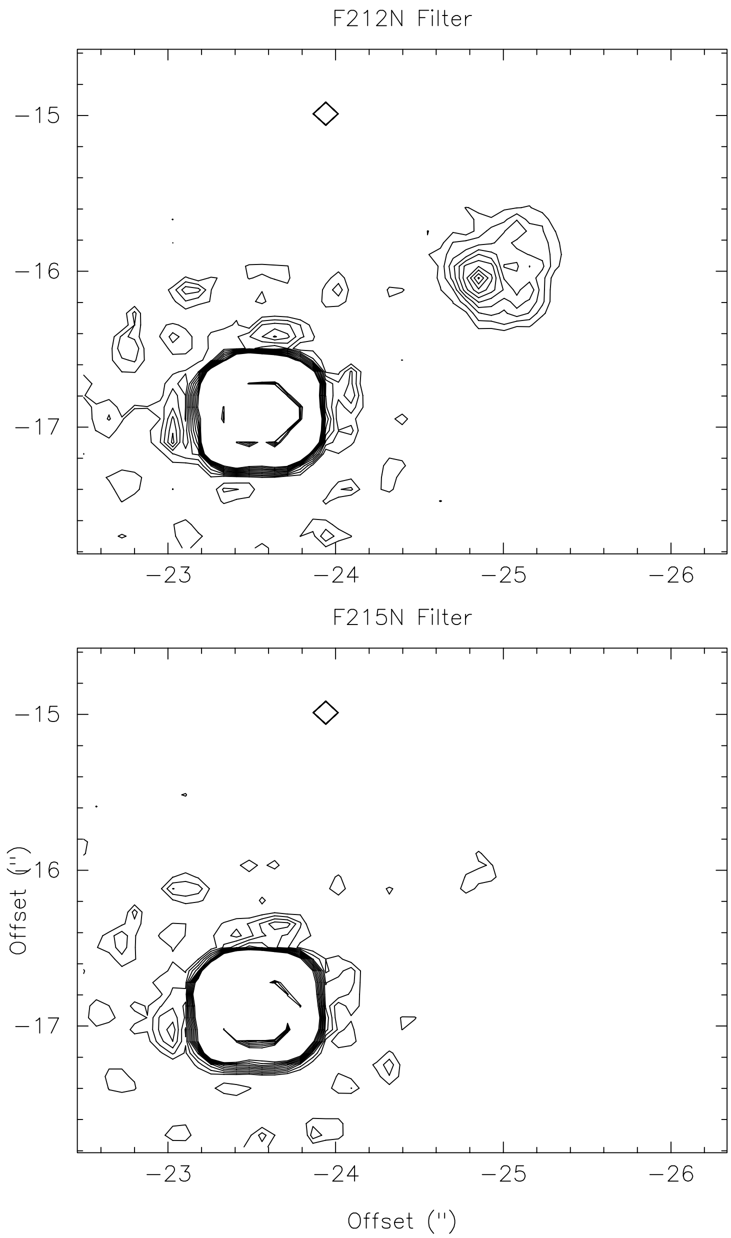

Figure 1. The top panel shows the H_2 emission (F212N) taken with NIC2. The bottom panel shows the adjacent "continuum" band (F215N). Note the large contrast between the H_2 emission and the continuum emission in the source at offsets (–24.8,–16.0).

References

Black J.H., van Dishoeck E., 1987, ApJ, 322, 412

Chen H., Bally J., O'Dell C.R., McCaughrean M.J., Thompson R.I., Rieke M., Schneider G., Young E.T., 1998, ApJ, 492, L173

Genzel, R., Reid, M.J., Moran, J.M., Downes, D., 1981, ApJ, 244, 884

Hogerheijde, M., Jansen, D.J., van Dishoeck, E.F., 1995, A&A, 294, 792

Jansen, D.J., Spaans, M., Hogerheijde, M.R., van Dishoeck, E.F., 1995, A&A, 303, 541

Jones, B.F., Walker, M.F., 1988, AJ, 95, 1755

McCaughrean M.J., Chen H., Bally J., Erickson E., Thompson R.I., Rieke M., Schneider G., Stolovy S.R., Young E.T., 1998, ApJ, 492, L157

O'Dell C.R., Wen Z., Hu X., 1993, ApJ, 410, 696

O'Dell C.R., Wen Z., 1994, ApJ, 436, 194

Sternberg, A., Dalgarno, A., 1989, ApJ, 338, 197

Stolovy S.R., Burton M.G., Erickson E.F., Kaufman M.J., Chrysostomou A., Rieke M., Schneider G., 1998, ApJ, 492, L151

Thompson R.I., Rieke M., Schneider G., Hines D.C., Corbin M.R., 1998, ApJ, 492, L95

Wyrowski, F., Schilke, P., Hofner, P., Walmsley, C.M. 1997, ApJ, 487, L171

NICMOS and the VLT
Pula, Sardinia, May 26-27th 1998
Wolfram Freudling and Richard Hook, eds.

HST NICMOS Observations of Circumstellar Matter Around CYG X-3

W. Schmutz

Institute of Astronomy, ETH Zentrum, CH-8092 Zürich, Switzerland

W. D. Vacca, L. Close, and J. Rayner

Institute for Astronomy, Honolulu, Hl 96822

T. R. Geballe

Joint Astronomy Centre, Hilo, Hl 96720, USA

H. Schild and R. Walder

Institute of Astronomy, Zürich, Switzerland

Abstract. Models of the evolution of massive binaries predict that only a few such objects should survive the common envelope phase and result in systems containing a compact object plus a Wolf-Rayet star (c+WR). According to these models, a vast amount of stellar material is lost during the common envelope phase prior to the c+WR phase. We are attempting to test these models by searching for the presence of such circumbinary material around the only known c+WR object: Cyg X-3. Since the large reddening towards Cyg X-3 prevents any investigation in the optical, deep infrared exposures of Cyg X-3 with the NICMOS NIC-2 camera aboard HST and the Paα narrow band filter have been used to image the system at high spatial resolution.[1]

The HST images have only recently been acquired and their analysis is currently underway. Here we report the possible detection of emission at a distance of about $0\farcs3$. This result is preliminary and needs confirmation by NIC-1 observations with its better sampling of the stellar profile.

1. Introduction

Cyg X-3 is one of the most luminous X-ray sources in the sky. On the basis of its periodic X-ray variability, it has been interpreted as a binary system in which substantial mass transfer occurs from a companion onto a collapsed object (Bonnet-Bidaud & Chardin 1988). Unfortunately, the enormous reddening toward Cyg X-3 ($E_{B-V} > 5$) effectively prevents any optical studies of this system ($V > 24$, $I \approx 20$, $K \approx 12$). However,

[1] Based on observations with the NASA/ESA Hubble Space Telescope obtained at the Space Telescope Science Institute, which is operated by the Association of Universities for Research in Astronomy, Inc., under NASA contract NAS5-26555.

recent infrared observations of Cyg X-3 have provided important information regarding the nature of this object. The first *K*-band spectrum of the system, obtained by van Kerkwijk et al. (1992), revealed strong and broad emission lines of He I and He II and it was suggested that the mass donor is a Wolf-Rayet (WR) star. Schmutz et al. (1996) found that the *K*-band emission lines exhibited periodic wavelength shifts, presumably due to the orbital motion of the WR star around the compact companion. The mass function for the system was found to be 2.3 and reasonable estimates of the mass of the WR star yielded a mass of the compact object of $\approx 17\ M_\odot$; thus, the compact object is an excellent black hole candidate. These results strengthen the suggestion that Cyg X-3 is representative of the endpoint of massive binary evolution.

Despite theoretical predictions for the formation of systems composed of a WR star and a compact companion (van den Heuvel & de Loore 1973), observational searches for such objects had yielded negative results (Willis et al. 1989; Moffat 1992; St-Louis et al. 1993) until the observation by van Kerkwijk et al. (1992). The evolutionary steps for the formation of such a system are O+O $\Rightarrow$ RSG+O $\Rightarrow$ WR+O $\Rightarrow$ SN+O $\Rightarrow$ c+O $\Rightarrow$ c+RSG $\Rightarrow$ c+WR, where c denotes a compact object. Numerical calculations (Iben & Livio 1993) indicate that the common envelope phase (c+RSG) is the critical phase in the evolution, and few c+WR systems are expected to exist as a result of the complete disruption of the secondary during this phase. The fact that only one c+WR system has been found to date indicates that it is indeed rare for a system to survive the common envelope phase. Thus Cyg X-3 provides an excellent and completely unique laboratory for testing the models of massive binary evolution.

2. Prediction of Circumbinary Material

It has been estimated that on the order of a few tens of solar masses of material was lost during the common envelope phase of Cyg X-3 and various models predict that the material should be concentrated in the orbital plane (Livio & Soker 1988; Terman et al. 1994). The current fast wind from the WR star should interact with this slowly expanding circumbinary material. This situation should lead to a "ring" of condensed matter around the system, probably broken up into individual knots due to Rayleigh-Taylor and other instabilities (Garcia-Segura & Mac Low 1995), similar to the ring observed around SN 1987A. This is demonstrated in Fig. 1, which presents predictions for the density contours resulting from a 2-D numerical simulation in which a fast stellar wind collides with a slowly expanding shell (Folini & Walder 1998, personal communication; see also Walder & Folini 1998). Localized density enhancements such as those seen in this figure would be observed as knots. The formation of high density knots is even more pronounced if the time dependence of the cooling is taken into account, as this leads to further compression and enhancement. The dense regions are relatively cool (with low gas pressure) and the material is ionized by the X-ray emission from the black hole and the strong Lyman continuum flux from the Wolf-Rayet star. Shock heated layers are expected to have fairly low density and therefore contribute little to the emission measure of the the strong nebular recombination lines.

The size of the expected emission region should depend on the velocity of expansion of the shell of material expelled during the common envelope phase and on the time since the common envelope phase. The expansion velocity in turn, is given by the accumulated momentum from the wind that accelerated the shell's mass. (The initial expansion from the shell can probably be neglected.) For a typical duration of the WR

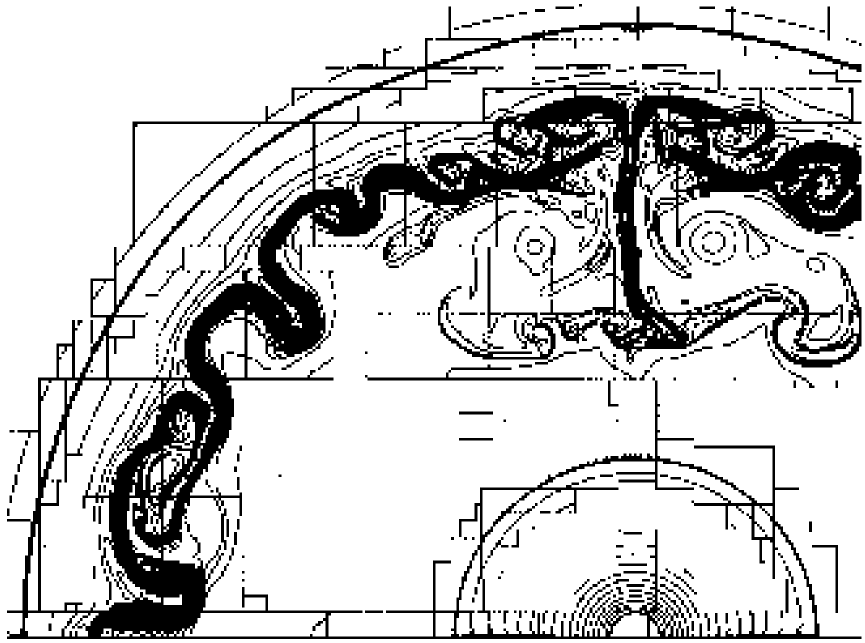

Figure 1. 2-D simulation of the collision of a fast wind with a slowly expanding shell. The developing Rayleigh-Taylor instabilities are traced by density contours. The rectangular grid outlines different levels of the adaptive mesh refinement algorithm. This figure demonstrates that we should expect many small regions with high density rather than a shell with uniform density. The concentration into high density knots is even more pronounced when time-dependent cooling is included in the calculations.

phase, $\sim 3 \times 10^5$ yr, and an assumed average expansion of $\sim 1\,\mathrm{km\,s^{-1}}$, we estimate an extension of 0.3 pc. At 10 kpc, the commonly adopted distance of Cyg X-3 (Dickey 1983), this corresponds to an angular separation of $6''$. This estimate is highly uncertain, and a search for nebular emission at both larger and smaller separations is also necessary. For example, typical sizes of WR ring nebulae are on the order of a few pc (Tutukov 1982), i.e. on the order of $20''$ at a distance of Cyg X-3.

The morphology of the emission nebula can provide observational constraints for the predictions of the common envelope mass loss and the nebular emission can be used to place constraints on the initial mass of the system. Contamination by swept up interstellar material can be excluded as the source of any possible nebular emission detected relatively close to Cyg X-3 (i.e. anywhere within the field of view of the NIC-2 camera), because the predicted SN explosion prior to the common envelope phase should have cleared out this region. Detected nebular Paα emission would therefore allow us to calculate the circumstellar mass and obtain an estimate of the lower limit for the initial mass of the WR star. This assumes that most of the ionized material is density bounded. Alternatively, if the nebula is ionization bounded, then we can probe the far UV radiation field, especially if we detect the nebula in the light of He I, [Fe II], and [S III]. In either case, an unambiguous detection of nebular emission close to Cyg X-3 would confirm the predicted common envelope phase with its dramatic mass loss.

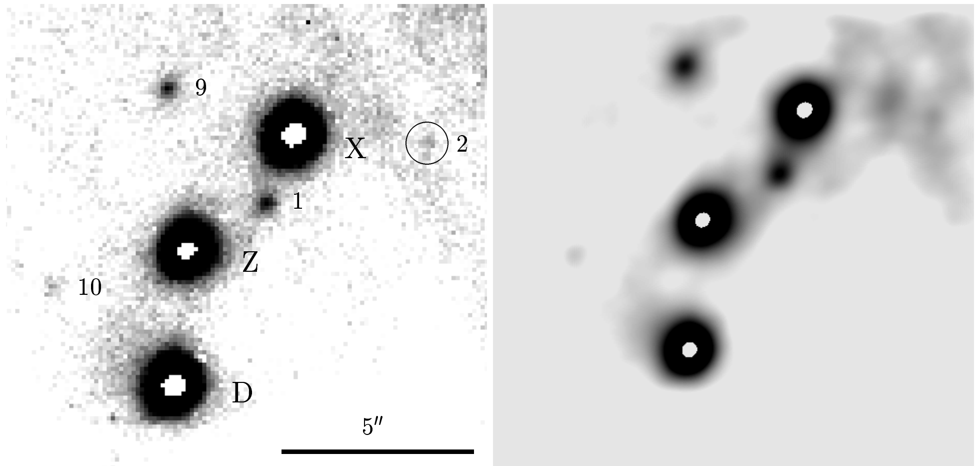

Figure 2. Left panel: H-band image of an 18” x 18” field around Cyg X-3, obtained with the Adaptive Optics system on the CFHT 3.6 m telescope on 15 July 1997 (Vacca et al. 1998). North is up and East is to the left. The FWHM is approximately $0.''5$; the white cores of sources X and D have diameters approximately equal to the FWHM. Sources are labeled according to Joyce (1990) and Fender & Bell-Burnell (1996); X denotes Cyg X-3. Right panel: The H-band image of the left panel after 300 iterations with the algorithm of Lucy-Richardson, with the PSF made from Z and D. The stellar cores (white) now have a FWHM of about $0.''2$.

3. Previous Observations

There is observational evidence for extended nebular emission associated with the Cyg X-3 system. Spectroscopic observations of Cyg X-3, obtained with $\approx 1''$ seeing and slit sizes, reveal the presence of narrow emission lines superimposed on the broad WR emission features. An example of this emission can be seen in Figs. 3 and 4 of Schmutz et al. (1996). These narrow lines are much stronger than any variable emission features often seen on top of the WR emission lines in the spectra of WR binary systems and attributed to the wind-wind collision zones (Moffat et al. 1996). Therefore, the narrow emissions in Cyg X-3 are probably not related to the WR wind but originate at larger distances from the system.

We have recently obtained ground-based near-infrared images of Cyg X-3, using adaptive optics (AO) techniques, which also seem to suggest that extended nebular emission may be present in this system. In Fig. 2 (from Vacca et al. 1998) we present our H-band image, obtained with the University of Hawaii Adaptive Optics system on the CFHT. The total integration time for this image was 600 sec. It was constructed by co-adding 20 individual frames, each with an exposure time of 30 sec. The FWHM of this image is about $0.''5$. Because the only suitable reference star that can be used to make the AO wavefront corrections is $30''$ away from Cyg X-3 and has a brightness of only V=15 (both values are at the limit of what can be used in current AO systems), our exposure resulted in a PSF which is slightly elongated to the SE, in the direction of this reference star. Nevertheless, this image indicated that we *may* have detected extended emission to the west of Cyg X-3 in the region of object #2. Unfortunately the detection is marginal because of problems with the flat-fielding and background sky subtraction. But it is sufficiently far from the point sources that we thought it might be real until we saw the HST NICMOS images. In fact, it is an artifact resulting from the flat-fielding.

Recently, Ogley et al. (1997) have reported that Cyg X-3 appears to be slightly extended in their deep *K*-band images and they suggested that a second point source, a factor of 11 fainter than the primary object, was located within $0''.56$ of Cyg X-3. (Dilution by a second stellar object might also explain why the broad WR emission lines seen in the *K*-band spectra have unusually small equivalent widths for a WR star (van Kerkwijk et al. 1992; van Kerkwijk 1993; Schmutz et al. 1996). However, our AO images (Fig. 2; Vacca et al. 1998), do not confirm this suggestion. Despite the slight elongation of our PSF, a second point source with the claimed separation and brightness would be easily recognizable on our image. (We also do not find a second source in the *K*-band image). NICMOS images, with their much smaller PSF cores, easily settle this question and place much stricter limits on the brightness and separation of any possible additional source.

4. NICMOS Observations

Cyg X-3 was observed with HST and NICMOS over 3 orbits on 1998 March 13. We used the NIC-2 camera in combination with the narrow band filters F187N, centered on Paα, and F190N, for the adjacent continuum region. For both filters we obtained 4 dither positions with $2''$ step size. The total exposure times were 68 min and 34 min for the filters F187, and F190N, respectively. For the analysis presented here we used the mosaiced images as delivered by the standard STScI pipeline. The standard processing leaves a clearly visible offset in the bias levels of the four detector quadrants but otherwise, particularly in terms of image sharpness, the processing resulted in excellent images.

In Fig. 3 we show the resulting image of the Cyg X-3 $19'' \times 19''$ field. All previously known sources in the field are clearly detected; a comparison with Fig. 2 shows the presence of objects 1, 2, 9, and 10. In addition, there are about half a dozen newly discovered faint objects in the image.

5. Discussion

With the HST NICMOS observations we were searching for 4 types of emission:

1. nebular emission close ($< 1''$) to Cyg X-3;
2. nebular emission in the vicinity of Cyg X-3 ($\approx 5''$);
3. extended nebular emission in the general area of Cyg X-3;
4. continuum emission from a source at about $0''.5$ from Cyg X-3.

Each of these items corresponds to a possibility discussed in the Sects. 2 and 3. The easiest item to discuss is item #4. Ogley et al. (1997) suspected an object about 2.6 mag fainter and $0''.56$ to the west of the main object. In Fig. 4 we show the cores of the stellar images of the objects X, Z, and D. The lightest grey level represents emission about 4 mag fainter than the central pixel. We conclude that at the time of our HST

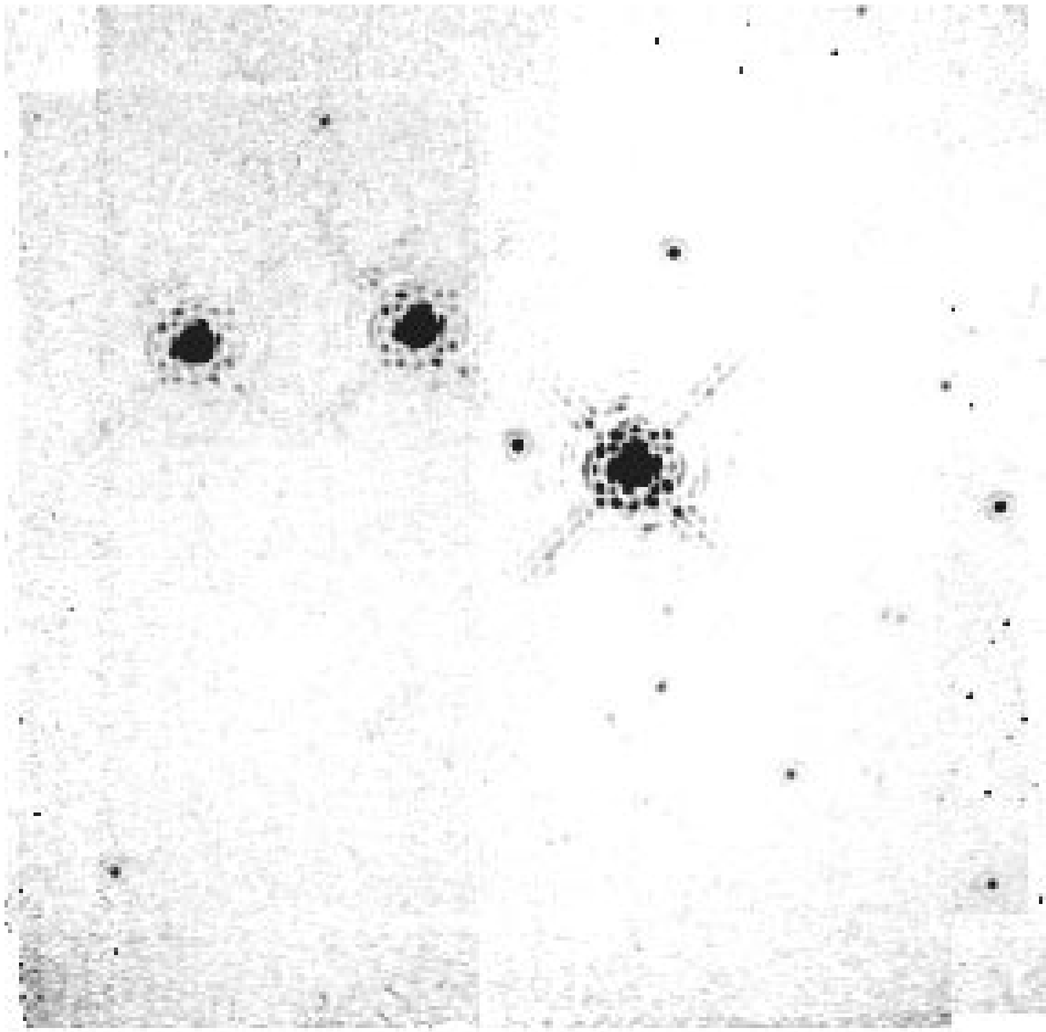

Figure 3. Mosaiced NIC-2 image of 4×17 min exposures through the Paα filter F187N. The observation angle was 79.4°, i.e. north is approximately to the right and east to the top. The field of view of one NIC-2 exposure is $19\farcs2 \times 19\farcs2$ and the mosaiced image has an extension of 286×286 pixels or $21\farcs45 \times 21\farcs45$. The strongest source near the center is Cyg X-3 and the next brightest object to the south-east is star Z. Star D is the object to the south of star Z about as bright as Z. The grey scale representation is chosen to enhance faint features just above the background. Due to this representation the different bias offsets in the four detector quadrants are very obvious.

observation there was no object present with the brightness and distance suggested by Ogley et al. (1997). Thus, we confirm the results of Vacca et al. (1998) based on AO images.

We can also address item #2 relatively easily. Using the intensities of the stars D and Z we scale the image F190N with a factor of 0.97 to that of F187N and we produce a difference image F187N−F190N. An investigation of this difference image

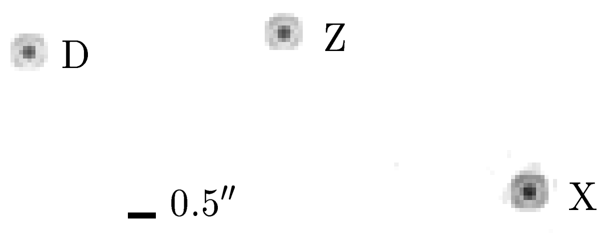

Figure 4. As Fig. 3 but the grey scale representation chosen such that the cores of the stellar images are visible.

does not reveal any extended emission. The only signatures left above the background are strong Paα emission at the location of Cyg X-3 and imperfect cancelations of the stellar images of star D and Z that leave paired positive and negative intensities. (The negative-positive residuals from stars D and Z integrate to zero intensity, of course, because we have used them to scale the continuum observation to that of the Paα.) The strength of the Paα excess emission of Cyg X-3 is 40% of the continuum. This value agrees very well with the emission strength estimated from ground-based spectroscopy of Cyg X-3 (see Fig. 4 of Schmutz et al. 1996). In fact, the emission is not from Paα at all, but rather the broad He II 6-8 stellar wind line.

With the difference image described above we have also addressed, in part, item #3. However, if there is a nebular structure like a ring nebulae around Wolf-Rayet stars then this would be outside the field of the NIC-2 camera. We also have Paα images of NIC-1 and NIC-3 that are obtained in parallel with the NIC-2 exposures. With the parallel exposures we probe regions about 30″ and 80″ to the west of Cyg X-3. Although these images are not in focus they would still allow to detect extended nebular emission. In the difference images of NIC-1 and NIC-3 there is also no obvious nebular emission. Of course, with this parallel exposures we are only covering only a small fraction of the total area out to, say, 100″. Thus, item #3 cannot be addressed conclusively with our HST NICMOS observations.

The only remaining issue is item # 1, nebular emission close (i.e. $< 1''$) to Cyg X-3. The detection of such emission requires a deconvolution of the stellar image of Cyg X-3. As can be seen on Fig. 3 the point-spread function (PSF) of NICMOS is quite complicated. But the good news is that it is supposed to be very reproducible, apart for some "breathing" effects which change the focus during an orbit. The best PSF template available for these observations is that of Cyg X-3 itself on the F190N image. The difference in wavelength is small so that the F190N PSF is only about 1.6% more extended than that expected for the F187N image. For the preliminary analysis presented here we disregard this difference. In Fig. 5 we present the results of a deconvolution with the Lucy-Richardson restoration algorithm as implemented in MIDAS. In the left panel we see that our PSF agrees very well with the Paα image of star D; the deconvolution of this star has produced a diffraction limited point source with no residual wings. On the other hand, the profile of the deconvolved image of Cyg X-3 is more extended than a pure point source. There is an extended structure to the east and a less bright one to the west. Therefore, Cyg X-3 appears to be more extended in Paα than it is in the continuum image. The number of iterations turned out to be

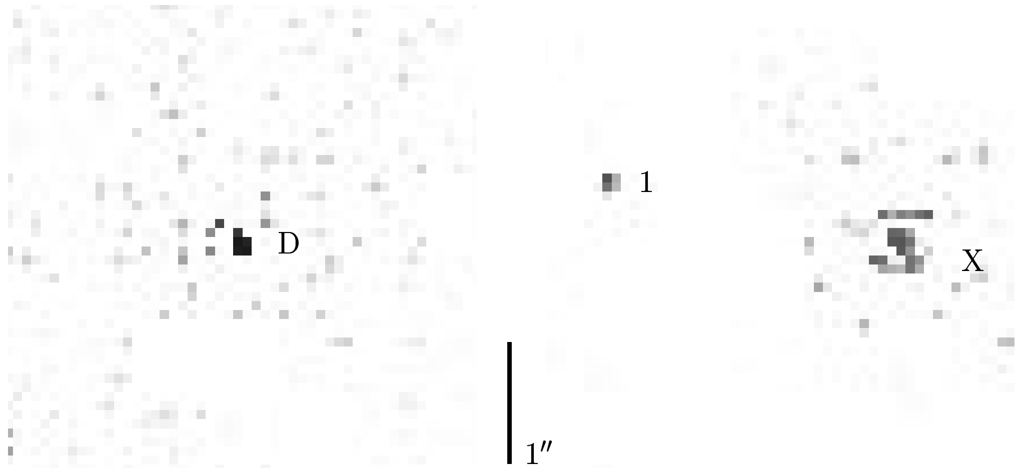

Figure 5. Deconvolved NIC-2 F187N Paα image using the image restoration scheme by Lucy and Richardson as implemented in MIDAS. The result shown is after 80 iterations; the results after 40 or 120 iterations look very similar. For the PSF the F190N image of Cyg X-3 was used. Left panel: The $4'' \times 4''$ region around star D. Right panel: The $4'' \times 4''$ region around Cyg X-3. This region also includes star 1 (seen at the left).

non-critical because the basic result, the extended structures to the east and west, is robust. The intensity in the east feature is comparable to that of star 1.

The extended nebular emission can also be detected in the original image. In Fig. 6 we plot a west-east cut through the profiles of Cyg X-3 in the F187N and F190N images. The lines represents the average of the 5 central columns. The excess emission detected by deconvolution algorithm in Fig. 5 can easily be seen $0\farcs2$–$0\farcs3$ east of the main peak; there is also a difference between the two profiles, although less pronounced, to the west. The uncertainties of the profiles at a level of 2 and 3 counts per second is 2% and 1%, respectively. (The total integration time was 4096 sec for the F187N exposure and 2048 sec in the F190N image.) Therefore, the difference between the two curves on the east side is at a level of about $10\,\sigma$. Because the F190N image has been used as the PSF template for the deconvolution, we also know that the Cyg X-3 F190N profile agrees well with that of star D and Z in the F187N exposure. Nevertheless, despite the high confidence level, it is still possible that the emission detected close to Cyg X-3 results simply from spatial and/or temporal variations of the PSF, and hence a mismatch between the true PSF for Cyg X-3 and the PSF used to perform the deconvolution.

6. Conclusions

In view of the importance of Cyg X-3 to the understanding of massive binary evolution — as the only representative of the c+WR class — we have searched for nebular emission that would testify to the events during its previous evolutionary phase. We suspect that the previous phase was a common envelope phase which implies that the non-degenerate star has lost a substantial fraction of its mass. This mass is expected to be still around the system, probably in a ring. To date, there have been no clear

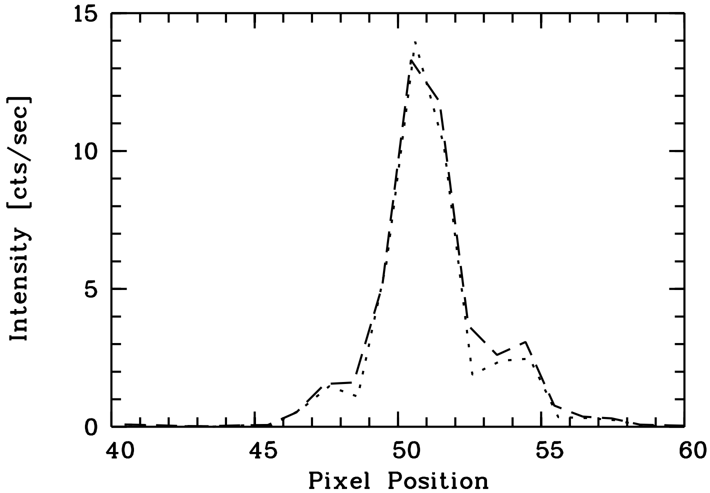

Figure 6. West-east crosscut, i.e. from bottom to top in Figs. 5, through the NIC-2 F187N image of Cyg X-3 (dashed) and of F190N (dotted). The 5 central columns are averaged and the central intensity of the F190N cut is scaled to that of the F187N. Excess emission in the east wing of Cyg X-3 is visible, at a distance of $0\farcs2$–$0\farcs3$ from the center (1 pixel= $0\farcs075$).

detections of emission around Cyg X-3. However, on the basis of the first part of our HST observations, we report here the *possible* detection of matter close to Cyg X-3. Our result is preliminary and at this stage of the analysis it is still not clear whether the features seen are artifacts produced by subtle imperfections in our PSF. Clearly, we need a better sampling of the profiles of the Cyg X-3 image and of the PSF. We hope to achieve this in an upcoming HST observation with NIC-1 camera. If the extended nebular emission is confirmed, we will estimate the mass lost from the donor star during the common envelope phase. This result could have a profound impact on models of binary evolution.

Acknowledgments. WS is grateful to R. Hook and S. Stolovy for enlightening discussions on the properties of NICMOS PSF. WDV is grateful to Alan Stockton for partial support. Support for this work was also provided by NASA through grant number G)-07838.01-96A from the Space Telescope Science Institute, which is operated by AURA, Inc., under NASA contract NAS5-26555.

References

Bonnet-Bidaud, J.M., & Chardin, G. 1988, Physics Reports, 170, 325

Dickey J.M. 1983, ApJ, 273, L71

Fender, R.P., & Bell Burnell, S.J. 1996, A&A, 308, 497

Garcia-Segura, G., & Mac Low M.-M. 1995, ApJ, 455, 160

Iben I., & Livio M. 1993, PASP, 105, 1373

Joyce, R.R. 1990, AJ, 99, 1891

Livio M., & Soker N. 1988, ApJ, 329, 764

Moffat, A.F.J. 1992, A&A, 253, 425
Moffat, A.F.J., Marchenko, S.V., & Bartzakos, P. 1996, RMxAAC, 5, 38
Ogley, R.N., Bell Burnell, S.J., & Fender, R.P. 1997, Vist. Astron., 41, 65
Schmutz, W., Geballe, T.R., & Schild, H. 1996, A&A 311, L25
St-Louis, N. et al. 1993, A&A, 267, 447
Terman, J.L., Taam, R.E., & Hernquist, L. 1994, ApJ, 422, 729
Tutukov, A. 1982, IAU Symp. 99, 485
Vacca, W., Schmutz, W., Close, L., & Geballe, T.R. 1998, AJ, submitted
van den Heuvel, E.P.J., de Loore, C. 1973, A&A, 25, 387
van Kerkwijk, M.H. 1993, A&AL, 276, L9
van Kerkwijk, M.H., Charles, P.A., Geballe, T.R., et al. 1992, Nature, 355, 703
Walder, R., Folini, D. 1998, A&AL, 330, L21
Willis, A.J. et al. 1989, A&AS, 77, 269

NICMOS and the VLT
Pula, Sardinia, May 26-27th 1998
Wolfram Freudling and Richard Hook, eds.

NICMOS Observes the Galactic Center

Marcia Rieke

Steward Observatory, University of Arizona, Tucson, AZ 85721, USA

Abstract. The NICMOS team has devised a comprehensive program of observations of the Galactic Center. The suite of observations include those aimed at measuring proper motions, at determining the spectral type at the tip of the main sequence from the last episode of star formation, at searching for variability near SgrA^*, and at looking at the distribution of ionized gas. Data in hand give a first look at variability and a detailed look at the search for the tip of the main sequence will be discussed where NICMOS has demonstrated adequate sensitivity and photometric precision to identify likely O8-B1 stars at the Galactic Center.

1. Introduction

The crowding of stars at the Galactic Center and their heavy obscuration makes the Galactic Center a very attractive target for NICMOS observations. From groundbased data, we already know that the Galactic Center harbors a massive black hole ($\sim 2\times10^6 M_\odot$) and that there are stars with ages significantly less than 50×10^6 years. The NICMOS instrument team has chosen to focus on projects that take advantage of the extremely stable point spread function which should permit both very accurate position measurements and very accurate photometry, even at the shortest wavelengths. The presence of a Pα filter is also of interest for studying the ionized gas at the Galactic Center. Because much of the NICMOS data on the Galactic Center has been taken recently with several projects still awaiting completion, this report will focus on describing the observing strategies and some of the problems that will need to be solved to extract the maximum return from the NICMOS data.

2. Proper Motion Studies

As originally planned, the NICMOS program to measure proper motions of Galactic Center stars would have been executed over the projected five- year lifetime of NICMOS. Because of the thermal short which has reduced the lifetime to two years, this program has had to change its observing strategy. The team had hoped to observe with the same stars always hitting the same pixels, but the desire to acquire a number of repeated observations has necessitated relaxing this requirement. Groundbased data suggest that some velocities may be as high as $\sim$ 1000 km/sec, much higher than the 100 km/sec that the program was designed to measure and so NICMOS may still contribute to this area in spite of its shortened lifetime.

The observing strategy is based on a compromise between trying to achieve the highest possible spatial resolution while still penetrating the dust that obscures the Center. A filter with a modest width to avoid as many color problems in the astrometric solutions was also desirable. The team has chosen the F145M filter with camera 1 which as .042" pixels as the optimum choice. As a check against possible systematic effects, a globular cluster, NGC4147, which lies at a distance which results in similar exposure times as for the Galactic Center, is also being observed. This cluster has a very small internal velocity dispersion so no proper motions should be seen. The first epoch data were taken in June, 1997, as the first NICMOS guaranteed time program to execute. The stars close to SgrA^* have S/N $\sim$ 50:1 in this data set. Four more sets of data will be taken before NICMOS exhausts its cryogen.

3. Variability Studies

Calibration programs with NICMOS are revealing that it is a very stable instrument from a photometric point of view with monthly repeats of standards showing less than 2% spread when flat fielded using NICMOS' internal lamp (Colina, this conference). The stable point spread function also will contribute to the ability to make accurate and repeatable measurements in crowded fields. The NICMOS team is looking for evidence of stellar variability, possible light flashes or variations due to variable accretion into SgrA^*, or variations due to micro-lensing. The data that have been obtained to date have not been examined carefully but do not reveal variations at the level of $\sim$ 30% or more in exposures 8 minutes in length repeated for nearly an hour. Much longer timescales will be probed when the completed data set is available.

4. Observations of Pα

The central $\sim$90" will be imaged using the Paschen α filter and its associated continuum filter. The data already returned reveal a similarity to the 5 GHz radio maps, but the key central 10" $\times$ 10" remains to be observed.

5. Search for the Tip of the Main Sequence

This portion of the Galactic Center program is the only part where data collection is complete, but it is the program requiring the highest degree of confidence in the flux calibration and the understanding of the NICMOS photometric system. This project is meant to probe the history of star formation at the Galactic Center. The presence of M supergiants such as IRS7 and Wolf-Rayet and/or LBV stars such as the IRS 16 stars strongly suggests that star formation has occurred recently. The strong and distributed Pα flux also suggest the widespread presence of hot stars. If NICMOS can be calibrated to the goal of 2% accuracy and if the interstellar extinction law can also be determined with adequate precision along this line of sight, then multi-color photometry with NICMOS can be used to deredden the stellar population and place the stars on a color magnitude diagram. The bluest stars representing the tip of the main sequence from the last epoch of star formation should be apparent – for example, O8-O9 stars should have an apparent magnitude around K $\sim 13-14$. The difficulty will be in proving that the colors are well enough determined, especially at the shortest wavelengths where such stars will be about 7 magnitudes fainter in the F110M filter.

Preliminary analysis of the data reveals a color magnitude diagram with both a clump of blue stars with the correct properties to be the tip of the main sequence and a clump of red stars which are likely to be red giants, another population expected at the Center. The stars closest to SgrA^* are all very blue, and only further work will resolve whether they have unusual properties due to being close to a black hole or whether their colors reflect their being ordinary O stars. This preliminary work has also shown that a careful determination of the extinction law in NICMOS filters will be required, with the IRS 16 stars playing a key role in this determination since their spectral types and hence intrinsic colors are now well understood.

Acknowledgments. The U.S. National Aeronautics and Space Administration is thanked for the funding which permitted the construction and operation of NICMOS.

NICMOS and the VLT
Pula, Sardinia, May 26-27th 1998
Wolfram Freudling and Richard Hook, eds.

NICMOS/HST H-band (F160W) Images of the 30 Dor Starburst Cluster

H. Zinnecker

Astrophys. Inst. Potsdam, Germany

A. Moneti

ISO Science Operations Centre, Villafranca, Spain

1. Introduction

We have taken diffraction-limited ($\sim$ 0.15") near-infrared F160W (henceforth H-band, for convenience) images with NICMOS on HST of the center of the R136 cluster (age 3.5 Myr) in the core of the 30 Dor giant HII region in the Large Magellanic Cloud.

The aim is to search for the low-mass ($M < 2M_\odot$) low-luminosity, pre-Main Sequence stellar population and to determine the H-band luminosity function, and eventually to determine whether the mass function is normal down to and below sub-solar mass stars, or whether there latter are missing. Note that the best available data so far (ground-based, Brandl et al. 1996, ApJ 466, 274) can sample only $M > 2M_\odot$, while previous V and I band HST images with WFPC2 (Hunter et al. 1995, ApJ. 448, 179) have reached down to masses $\sim 3M_\odot$ and could not answer the question if the the IMF is truncated at lower masses. Our initial tests on the data show that we reach H $\sim$ 22.5, which corresponds to $M=0.2M_\odot$, according to pre-Main Sequence evolutionary models, and it is not out of the question that we will be able to reach even deeper with some later recalibration. On the other hand, the faintest stars measured in the crowded central region will be much much brighter than this limit.

The answer to the question of whether sub-solar mass stars have formed in the R136 cluster is key to determining whether it is a prototype young globular cluster, in which case it must have lots of them, and should clarify whether the IMF in starburst clusters and starburst galaxies, is deficient in low-mass stars. The absence of low-mass stars would have far-reaching consequences for the chemical, dynamical, and photometric evolution of starburst galaxies (e.g. Charlot et al. 1993 ApJ. 419, L57).

2. Observations and Preliminary Analysis

The planned observations consisted of a 3x3 "core" mosaic centered on R136, two 3x1 "wings" extending from two adjacent sides of the core mosaic, and several sky positions located between 10' and 20' mostly north of the cluster. At each position four dithered images were obtained in order to remove cosmic rays, bad pixels, and the coronographic hole. The data were obtained in multiaccum mode, with SAMP-SEQ=STEP128, and using NSAMP=16 which gave a maximum integration time of 896 sec. The wings were planned in so that NIC-1 would cover the cluster core in one of the positions. Unfortunately a programming error caused the first wing to start at the wrong side and thus to move inward rather than outward, so that it resulted in an extra, and unnecessary

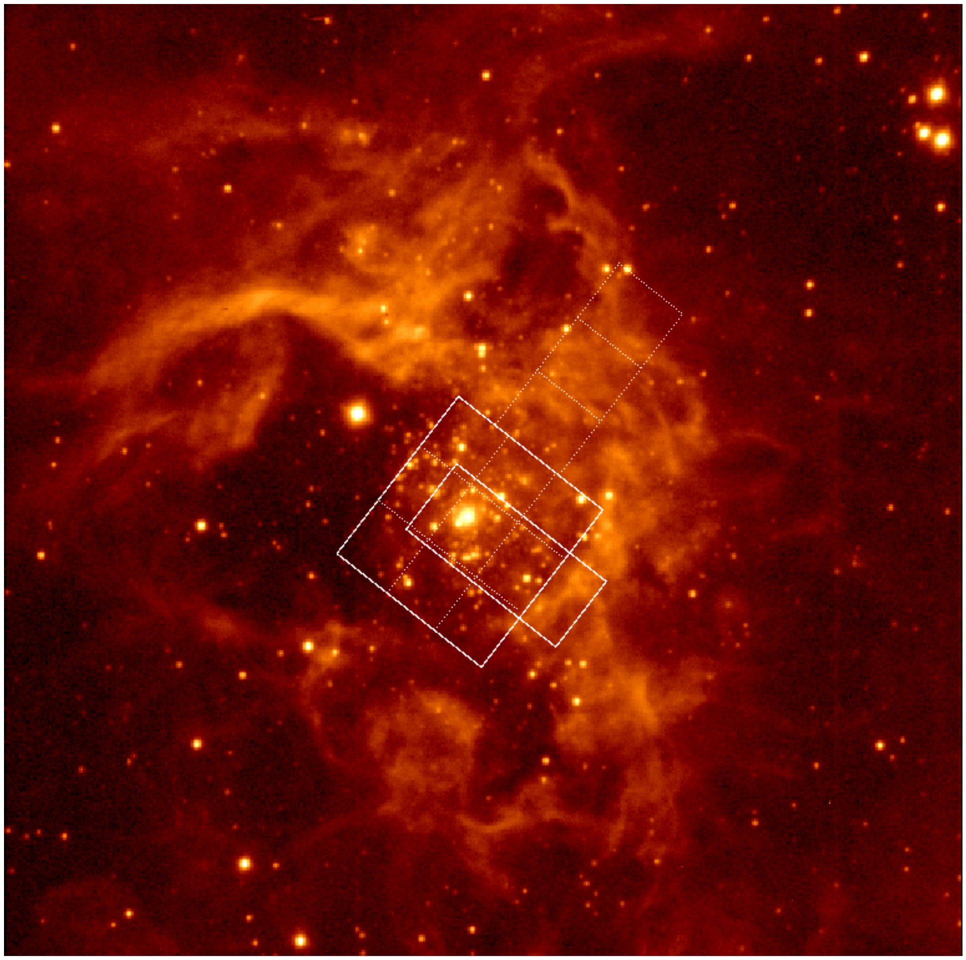

Figure 1. Layout of the 30 Dor NIC2 observations, superimposed on a 5x5' SOFI near-infrared image of the region (Moorwood et al., The Messenger 91, title page)

image of the core, and missed the NIC-1 images of the core The second wing has not been executed to date. Figure 1 shows the NIC2 frames overlaid on an infrared image of 30 Dor taken with SOFI.

All observations have been obtained after the August 97 fix, and no sign of the "pedestal" feature can be seen in our data. While the pedestal might be difficult to see on the crowded source images, the sky fields contain very few objects, and especially there we see no sign of this effect.

The raw data were processed with the standard pipeline, specifically with calnica 3.1, and various mosaics were constructed using calnicb 2.1.2. The maximum dynamic range (peak of brightest star [about 2500 DN] divided by the rms noise [0.01 DN]) is over 250,000. Our first attempts at doing photometry on these images were performed with DAOphot on selected single images and on selected 4-image mosaics of a single position; for these attempts we started with sky images and otherwise the least crowded regions of the cluster. In what follows we give a brief description of the images and of the problems encountered in running DAOphot.

The NIC-2 images are characterised primarily by an unusual PSF (by ground-based standards) consisting of (1) a central core which is close to Gaussian in shape, with a FWHM of about 1.75 pix, and with is thus somewhat undersampled, (2) a first Airy ring with extends between r = 2".4 and 3".5, peaking at about 3", and with a peak intensity of about 10% of the core, (3) a cloud of over twenty "dots" located between 4" and 8" from the core, and with peak intensity about 0.15% of the maximum, and (4) 12 long diffraction spikes, arranged in four groups of three, with changing intensity as a function of distance from the center. Secondly, the field is very crowded, and even extremely crowded in the centre.

First of all, it is important to give proper values to the gain and readnoise parameters ("epadu", and "readnoi"): since the data values are count rates, the effective gain is the true gain multiplied by the integration time in sec. The latter is actually pixel dependent (only a few multiaccum readouts, and thus a short integration time, are used on bright stars; we have used the full integration time. The read noise for a single read is about 30 electrons, but the effective read noise is lower since there are 16 reads on unsaturated pixels.

Determining the PSF with such high dynamic range and in a crowded region is a major challenge: overall there are very few stars that sufficiently bright and sufficiently away from other bright stars that they can be used for PSF determination, and secondly the "dots" around these stars are themselves identified as stars by the DAOfind algorithm, and even though they are often slightly elongated, the roundness and sharpness parameters in DAOfind are less useful than one would like given the undersampling (and also because they are designed primarily for sources elongated along the pixels). So far we have found no very good method of telling DAOphot that the "dots" are features of the PSF, and not nearby stars. Ideally one would like to convolve the image with a kernel more suited to the NIC-2 PSF, rather than one suited to a Gaussian PSF; this go a long way toward avoiding picking up the "dots" as stars.

A second method is to use a synthetic PSF. We have simulated a polychromatic PSFs using John Krist's Tiny Tim package, and using a 5000 K blackbody as the source spectrum. These PSFs have the advantage of not being contaminated by nearby stars, but in them they seem to leave somewhat higher residuals in PSF-subtracted images than empirically derived PSFs.

The undersampling problem has already been mentioned in the context of the DAOfind algorithm. A second problem it causes is that the "fitrad" parameter needs to be exceedingly small, i.e. 1.85 pix at most, or the fit will extend to the Airy ring, with poor results. This means that very few pixels are used, and large residuals remain after the fitting process. Note that so long as "fitrad" is small, the best fit analytical function for the core of the PSF is a Gaussian; for larger "fitrad", the fit extends into the region where the Airy ring's contribution is significant, and the best fit is given by the "penny1" function. In order to avoid this, we have run DAOphot on an expanded, or magnified (by a factor of 2, and with spline interpolation) image, so that more pixels can be used in the fit of the analytical core. The result showed a much better subtraction over the stellar cores.

3. Preliminary Results

In order to get a first idea of the kind of results we could expect, we went ahead with allstar using an empirically determined PSF on one of the “core” mosaic corner images. The results indicate that the observed H-band luminosity function increases at least to H = 20th mag. Here a very rough calibration was performed using H = 11.5 for the star Mk34, which was used as a reference (we have not yet compared this calibration to the ”standard” calibration derived by STScI). Stars as faint as H = 22.5 were detected, but the effects of completeness have to be assessed before we can make any statement about what really happens beyond 20th mag, i.e. below 2 $M_{\odot}$.

Acknowledgments. Our NICMOS 30 Dor team consists of B. Brandl, W. Brandner, A. Eckart, D. Hunter, R. Larson, M. McCaughrean, G. Meylan, A. Moneti, M. Rosa, N. Walborn, G. Weigelt, and H. Zinnecker (PI). We would like to thank the participants at this conference for fruitful discussions, in particular M. Rieke and S. Stolovy, G. de Marchi and R. Hook.

NICMOS and the VLT
Pula, Sardinia, May 26-27th 1998
Wolfram Freudling and Richard Hook, eds.

The Formation and Evolution of LMC Rich Star Clusters: NGC 1818

R.A.Johnson, R.A.W.Elson, G.Gilmore, S.Beaulieu, N.R.Tanvir

Institute of Astronomy, Cambridge, UK

B.Santiago

Universidade Federal do Rio Grande do Sul, Porto Alegre, Brazil

Abstract. The Large Magellanic Cloud (LMC) is uniquely suitable for the study of massive star clusters at all stages of evolution. By combining HST observations of these clusters with N-body models we hope to understand the origin and evolution of rich star clusters in our own Galaxy, in the LMC, and beyond. Here we give a brief overview of our large Cycle 7 HST project and present some preliminary results.

http://www.ast.cam.ac.uk/LMC

1. LMC Project Outline

Our LMC globular clusters sample contains 8 clusters. These are grouped into four age pairs, with ages of $10^7 - 10^{10}$ yr. They are among the richest clusters in the LMC and have masses $\approx 10^4 M_\odot$. Table 1 lists some important properties of the cluster sample.

Our observing strategy is to obtain HST images of two fields in each cluster, one field at the cluster core and one at the half mass radius. HST images of both regions are taken with WFPC2 (F555W and F814W) and NICMOS (F160W). STIS images are also taken at the half mass radius. We obtained 95 orbits of Cycle 7 HST time (PID 7307) and hope to have all the data by the end of the year.

Current N-body codes are now capable of modelling realistic systems with 10^4 stars. We aim to combine our HST observations with N-body models to understand the formation and evolution of globular clusters. A detailed discussion of the aims of this LMC project is given in Elson et al. (1998a). In brief, we will use the young clusters to constrain the star formation timescale (see below for an example) and also to look for evidence of sequential star formation (e.g. did low mass stars form first ?). Binaries play a crucial role in cluster evolution and we will be able to place firm observational constraints on the binary fraction at various evolutionary stages. Using our very deep STIS images we will construct initial mass functions (IMFs). If there is a universal IMF then a minimal expectation would be that the younger LMC clusters, with very little dynamical evolution, a wide range of stellar masses, and in some cases very similar metallicities, should have indistinguishable mass functions.

Table 1. The LMC globular cluster sample

Cluster	log(age/yr)	[Fe/H][1]	$R_g{}^{\circ 2}$	$R_c''^{3}$	Recent CMD
NGC 1805	7.2	...	3.7	...	...
NGC 1818	7.3	-0.8	3.4	9.4	Will et al. (1995)
NGC 1831	8.7	-0.3	4.6	15.7	Mateo (1998)
NGC 1868	8.8	-0.6	5.4	6.0	Corsi et al. (1994)
NGC 2209	9.1	-1.0	5.7	18.8	Corsi et al. (1994)
H14=SL506	9.2	...	4.4	9.4	none available
NGC 2210	10.1	-2.2	5.0	6.8	Brocato et al. (1996)
H11=SL868	10.1	-2.1	5.2	18.0	Mighell et al. (1996)

[1]The values of metallicity are quite uncertain; for many of the clusters widely differing values are quoted in the literature

[2]Distance from the LMC centre

[3]Core radius

2. NGC 1818 Initial Results

NGC 1818 is one of the two youngest clusters in our sample. It has an age of 20-40 Myr (Hunter et al. 1997) and a metallicity of [Fe/H]=-0.8 (Will et al. 1995). We have used WFPC2 (PC, F555W) and NICMOS (NIC2, F160W) observations of the centre of this cluster to search for evidence of age spreads. The NICMOS observations were taken as part of this project. However, as our new WFPC2 observations have not yet been taken we have used archive F555W data (PID 6277 PI J. Westphal). Unlike our own WFPC2 observations, the archive data has no exposures short enough not to saturate the brightest stars. Figure 1 shows the NIC2 F160W image.

The same procedure for obtaining the photometry was followed in the optical and in the near-infrared. The IRAF package DAOPHOT was used. Firstly the task DAOFIND was used to detect stars on the image, and aperture photometry was obtained for these stars. A point spread function (psf) was constructed from bright stars in the image. All the stars in the image were then fitted with the psf. The psf fitting diagnostics (chi and sharpness) were used to exclude non-stellar objects to produce the final star list. To construct the colour-magnitude diagrams we have used aperture photometry of this final star list.

The many diffraction spikes, especially in the NICMOS image, could be affecting the magnitudes of some of the stars and introducing a scatter in the colours. All the stars in the final star list have therefore been visually inspected on both the images. Those that appear to be affected by the diffraction spikes of bright neighbours, or that are very close to a bright star, have been removed.

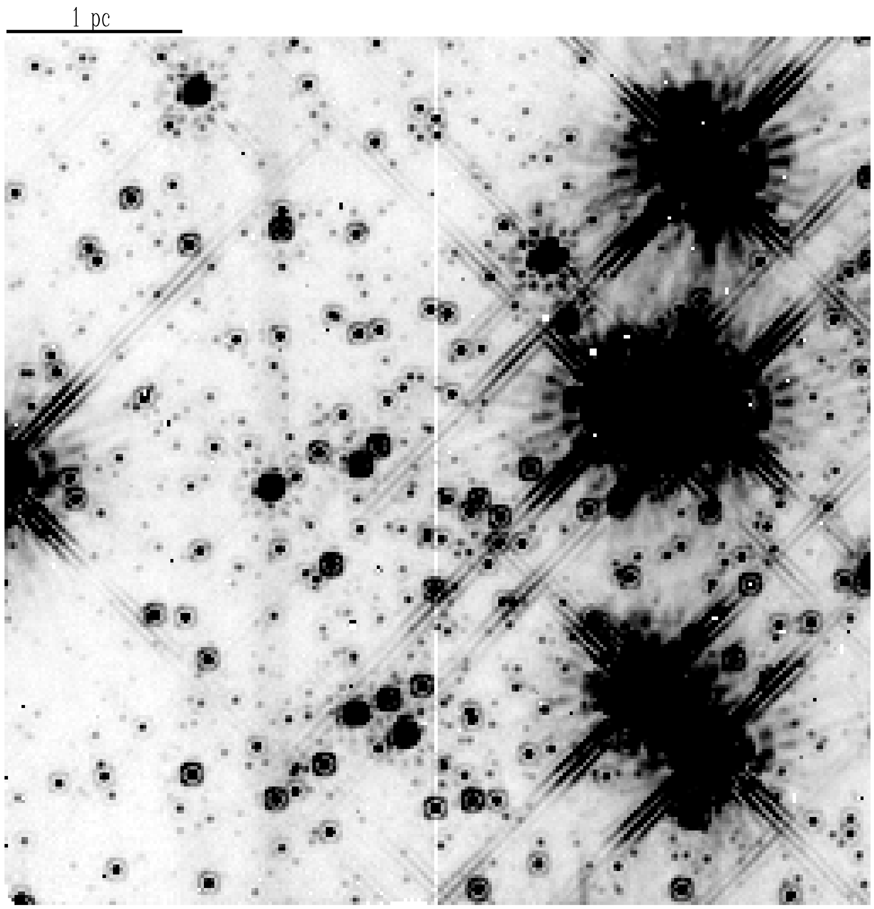

Figure 1. NIC2 F160W image of NGC 1818 central regions. Bad pixels are white.

An estimate of the maximum error in the H_{160} magnitude of the bright stars due to the varying underlying background showed that the psf fitting errors gave a good estimate of the error. The V_{555} errors are poisson errors.

Figure 2 shows the V_{555} vs. V_{555}-H_{160} colour-magnitude diagram for the central regions of NGC 1818. Overplotted on the data are isochrones for [Fe/H]=-0.7 with ages of 25, 40, 63 and 159 Myr. The isochrones are from Bertelli et al. (1994) with magnitudes calculated for the HST passbands (Worthey 1998) and have been shifted to a distance modulus of 18.5 and reddened by E(B-V)=0.05. The H_{160} data have not been photometrically calibrated and so an arbitrary x-axis shift has been applied to align the data with the isochrones. It can be seen from the position of the isochrones that age spreads in the cluster will be apparent for $V_{555} < 19$. Figure 3 zooms in on this region.

Other possible causes of a spread in the colour magnitude diagram are background field star contamination and the presence of cluster binaries. From the background field presented in Hunter et al. (1997) we estimate that one of the stars with $V_{555} < 18$, and one of the stars with $18 < V_{555} < 19$ could be background stars. For $V_{555} > 19$ it is not

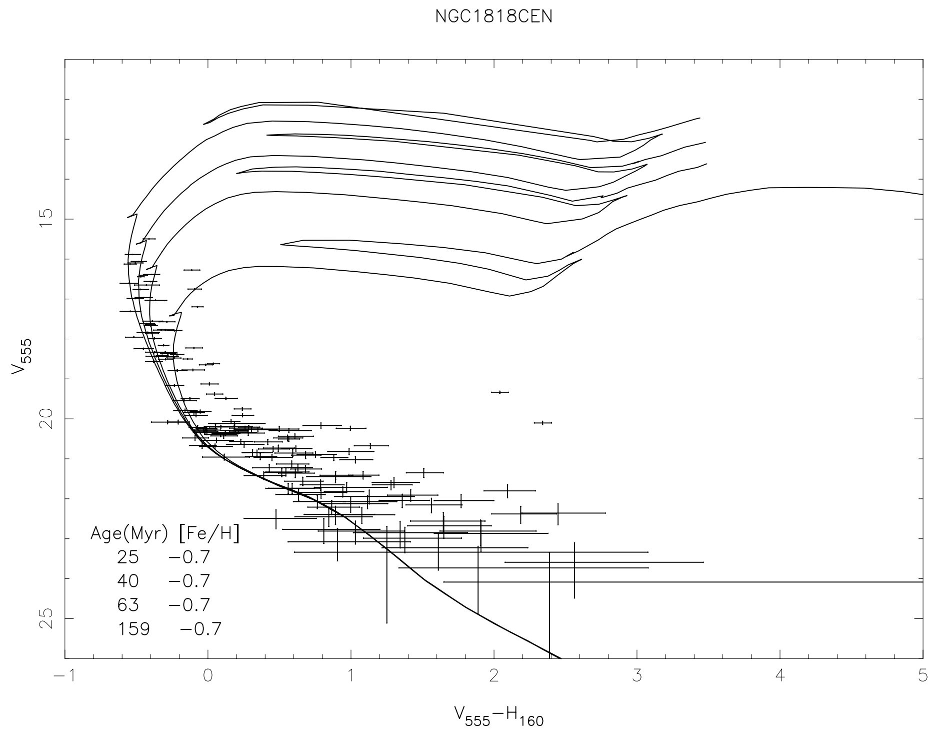

Figure 2. Colour magnitude diagram for NGC1818 central regions. Overplotted are isochrones for ages between 25 and 169 Myr.

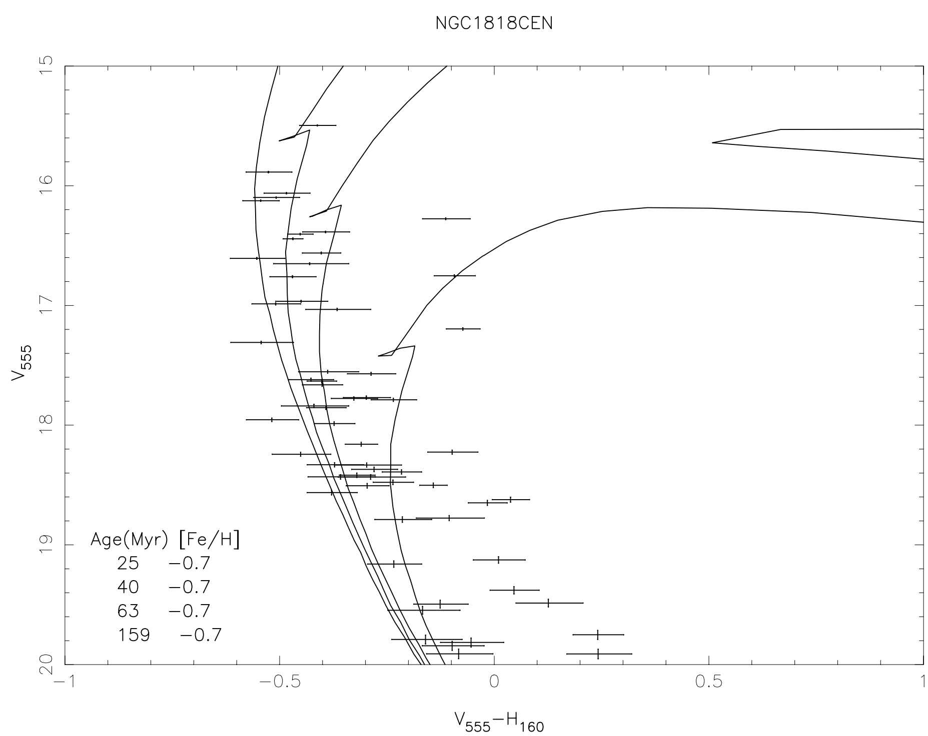

Figure 3. Colour magnitude diagram for NGC1818 central regions showing the area where age spreads are detectable.

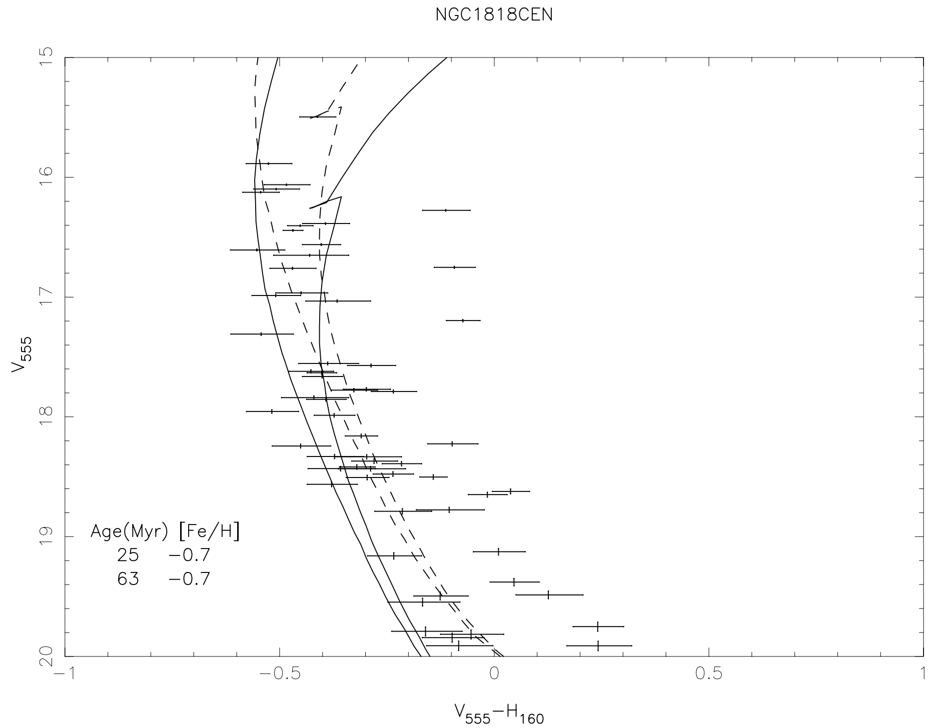

Figure 4. Position of equal mass binary sequence (dashed lines) for two isochrones of ages 25 and 63 Myr

possible to estimate the background star contamination from Hunter et al. (1997). NGC 1818 contains a binary star population (Elson et al. 1998b), with the majority of binaries having a secondary mass $>$ 70% of the primary mass. In this case the observed binary sequence lies along the equal mass binary sequence. Figure 4 plots the position of an equal mass binary sequence for the 25Myr and 63 Myr isochrones. Although some of the spread in stars with $V_{555} \approx 18$ could be due to binaries, this is not the case for the brighter stars.

Figure 3 contains three bright stars (V_{555} <18) which lie to the right of the 63Myr isochrone. As mentioned above these stars have been inspected in both the V_{555} and H_{160} images for underlying diffraction spikes or neighbouring bright stars which may be affecting their magnitudes. They lie close to the 169 Myr isochrone. This is much to old for them to be cluster members. As mentioned above the background field star contamination at these magnitudes should be negligible. However there is always the possibility that we are unfortunate enough to be looking at a background clump of stars. Analysis of our own background fields and parallel data will enable us to place better limits on the expected number of background stars at each magnitude.

There are several stars with V_{555} around 19 which have very red colours. Again, it is possible that these are field stars and/or background galaxies.

The rest of the stars with V_{555} <18 appear to lie mostly within the 20-63 Myr isochrones. There is tentative evidence here for an age spread of some 40Myr. However, we need to run simulations to quantify how much of this spread is due to photometric errors. The crossing time at the half mass radius of NGC1818 ≈10Myr. If the 40Myr age spread is real then it is several times greater than the crossing time which has implications for the process of star formation in the progenitor cloud. We explore these implications further in a future paper.

3. Future Improvements

There were a few bright stars which were saturated on the archive WFPC2 observations used here. Our own WFPC2 data will contain some very short observations which will allow us to place these bright stars on the CM diagram. Note that the brighter the stars the greater the separation between isochrones of different ages, so even a few bright stars are an important age spread indicator. We hope to reduce the errors on the H_{160} photometry by possible improvements in the NICMOS data reduction and also in the point spread fitting.

References

Bertelli, G., Bressan, A., Chiosi, C., Fagotto, F., Nasi, E. 1994, A&AS, 106, 275

Brocato, E., Castellani, V., Ferraro, F., Piersimoni, A., Testa, V. 1996, MNRAS, 282, 614

Corsi, C., Buonanno, R., Fusi Pecci, F., Ferraro, F., Testa, V., Greggio, L. 1994, MNRAS, 271, 385

Elson, R. A. W., 1998a, in prep.

Elson, R. A. W., Sigurdsson, S., Davies, M., Hurley, J., Gilmore, G. 1998b, MNRAS, submitted

Hunter, D. A., Light, R. M., Holtzman, J. A., Lynds, R., O'Neil, Jr., E. J., Grillmair, C. J. 1997, ApJ, 478, 123

Mateo, M. 1998, ApJ, 331, 261

Mighell, K. J., Rich, R. M., Shara, M., Fall, S. M. 1996, AJ, 111, 2314

Will, J., Bomans, C., de Boer, K. 1995, A&A, 295, 54

Worthey, G. A. 1998, priv. comm.

NICMOS and the VLT
Pula, Sardinia, May 26-27th 1998
Wolfram Freudling and Richard Hook, eds.

A Color Analysis of NICMOS Parallel Observations

Michael R. Corbin, Rodger I. Thompson, Elizabeth Stobie, & Irene Barg

NICMOS Group, Steward Observatory, The University of Arizona, Tucson, AZ, 85721, U.S.A.

Abstract. NICMOS observations made in parallel with the other HST instruments have produced an archive of over 2,000 images, covering a wide range of Galactic latitudes. The images obtained through the end of 1997 were taken with all three cameras, using the *JHK*-analog filters and the Camera 3 grisms. The maximum sensitivity of these images is approximately 0.1 μJy, which should allow the detection of such astrophysically interesting sources as brown dwarfs in the solar neighborhood and star-forming galaxies out to z $\sim$ 3. Using model and actual spectra, we have derived the colors of a variety of objects including stars, brown dwarfs, and high-redshift galaxies in the *JHK*-analog filters. We have also developed software designed to perform batch photometry on NICMOS images and measure the associated object colors. Follow-up optical and infrared spectroscopy of interesting sources can be obtained with 10-meter class telescopes such as the VLT. In this contribution we describe the NICMOS parallel images and our analysis software, and discuss our preliminary findings.

1. Introduction

An important benefit of the refurbished *Hubble Space Telescope* has been the routine acquisition of images by the NICMOS cameras when either the WFPC2 or STIS instruments are making pointed observations. These parallel observations are designed to supplement the NICMOS pointed observations, with the broad goals of probing the stellar population of the Galaxy and external galaxies, investigating regions of star formation, and assessing the distribution and evolution of galaxies and QSOs. To date, the volume of NICMOS observations released into the HST Archive exceeds two thousand images, with roughly double that amount expected by the end of Cycle 7. Such a database offers great potential for addressing the aforementioned issues, and we have undertaken to analyze it as thoroughly as possible, with an emphasis on the classification of objects by their colors in the NICMOS filters.

2. The NICMOS Parallel Program

NICMOS parallel observations were begun in 1997 June using all three NICMOS cameras, with Cameras 1 and 2 selected as prime due to the focus problem with Camera 3. Camera 3 was selected as prime in 1997 November as it came into better focus, due to its larger field of view and the availability of its grisms. Parallel observations of a given field were made in the *JHK*-analog filters F110W, F160W, and F222M in Camera 2, while observations in Cameras 1 and 3 were limited to the F110W and F160W filters, and the G096 and G141 grisms in Camera 3. Integration times range from a minimum of 192s to a maximum of 1280s, with associated 5σ detection limits of approximately 1 to 0.1 μJy. Through 1997 December, the approximate total areas covered in the usable observations of each camera were 23 arcmin^2 (Camera 1), 70 arcmin^2 (Camera 2), and 174 arcmin^2 (Camera 3). A small fraction of the images suffer blurring or streaking from spacecraft motion and contain no useful information, while a significant fraction of the images, particularly in Camera 1, contain no objects.

A sample set of Camera 2 parallel images in the F110W, F160W, and F222M filters is shown in Figure 1. The F222M image shows strong Airy rings in the object PSFs, which can be treated to a limited degree in the photometry software. Fields observed at low Galactic latitudes are often very rich, and a batch photometry approach is clearly necessary.

3. Analysis

Our first step in the analysis of the parallel images has been to re-calibrate them, by matching the raw images with the best available on-orbit dark current and flat-field frames. Comparison of the resulting images with those processed through the STScI calibration pipeline indicates a maximum improvement of approximately 3% in photometric accuracy. This increased accuracy should also improve our color classifications of the objects in the F110W, F160W, and F222M filters.

We have derived colors in these filters for a wide range of objects, including normal stars, brown dwarfs, young galaxies, ultraluminous infrared galaxies, and QSOs. We have found that in most cases there is a good separation of the different classes of object in the plane of the (F110W - F160W), (F110W - F222M) color indices, which can be measured for the Camera 2 observations. These colors were derived using model and actual spectra of the objects (e.g., Kurucz model spectra of stars; Kurucz 1992). The colors were derived by convolving the filter transmission curves (factoring in detector quantum efficiency) with these object spectra, and taking the ratio of the integrated fluxes of the resulting spectra. An illustration of this method is shown in Figure 2, which compares the Camera 2 F110W, F160W, and F222M filter transmission curves with a composite spectrum of several hundred QSOs discovered in the Large Bright Quasar Survey (Francis et al. 1991). The composite spectrum has been redshifted to z = 6, and we have derived colors for this spectrum over the range $3 \leq z \leq 10$. For active galaxies at low redshift, we have used the interpolated nuclear spectrum of the highly luminous Seyfert 2 galaxy Markarian 231 as a guide. Our efforts to derive object colors are not yet complete, and in particular we are currently working on deriving the colors of high-redshift supernovae using their optical and ultraviolet spectra.

Of particular current interest is the detection of brown dwarfs and very low-mass stars, and the determination of their mass function and space density. Burrows et al. (1997) have generated model spectra of brown dwarfs in the infrared and determined the detection thresholds associated with current and planned infrared space missions. While Burrows et al. find that the spectra of brown dwarfs depend in a complex way on their age, mass and composition, the 0.1 μJy sensitivity limit of the NICMOS parallel observations should allow the detection of a certain range of them out to a distance of approximately 10 pc. The spatial resolution of NICMOS could also lead to the detection

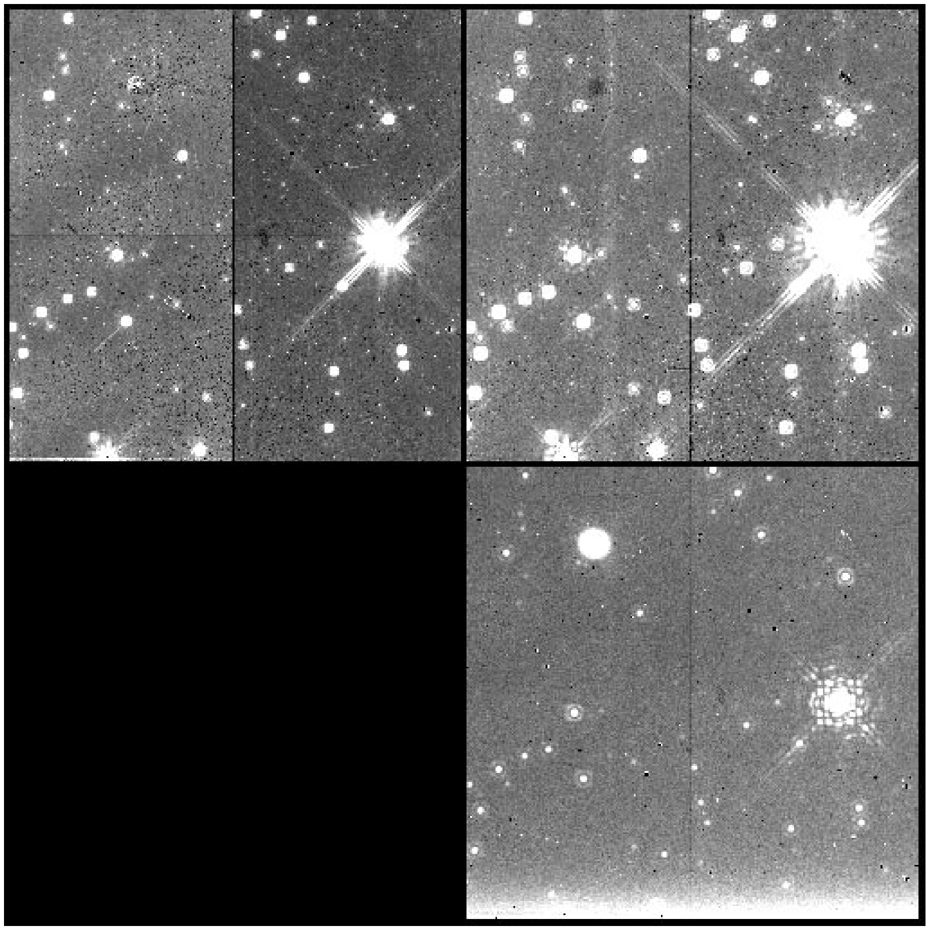

Figure 1. Sample NICMOS Camera 2 parallel images in the F110W, F160W, and F222M filters (clockwise from top left). The bright spot in the upper left of the F222M image is the coronagraphic hole, incompletely removed by the flat field frame.

of brown dwarfs in close binary systems such as Gl 229B, which is difficult from the ground.

Figure 3 shows the color-color diagram for Camera 2, for the spectra of point sources. The sensitivity limit of these observations should also allow the detection of the recently discovered population of young ($\sim$ 1 Gyr) star-forming galaxies at z $\sim$ 3 (Steidel et al. 1996), based on their K-band fluxes, as well as star-forming galaxies at lower redshifts. In Figure 4 we show the Camera 2 color-color plot for a 1 Gyr-old galaxy over a wide range of redshifts, using the population synthesis model of Bruzual & Charlot (1993). While the detection of such galaxies out to z $\sim$ 10 in these observations is not possible under normal circumstances, lensing of such sources by a foreground galaxy cluster could raise their fluxes to the detection level. The limitation of the Camera 1 and 3 wide-band observations to the F110W and F160W filters should

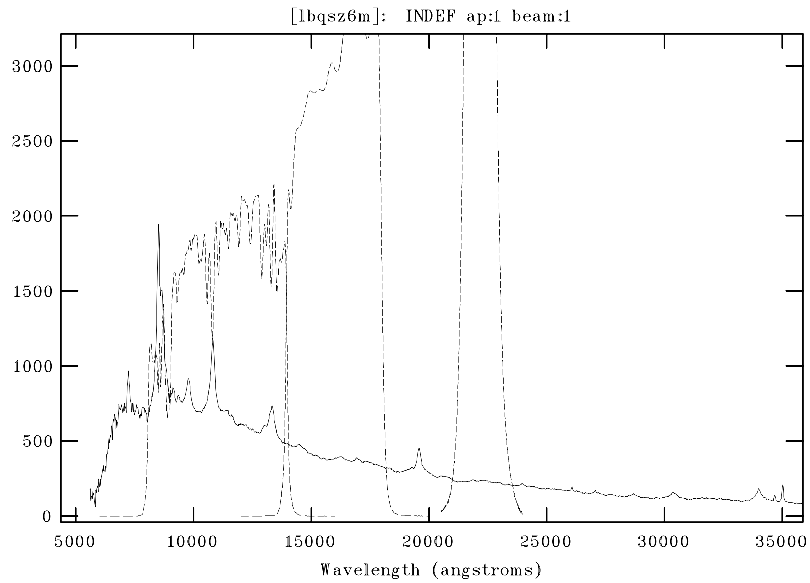

Figure 2. Comparison of NICMOS Camera 2 F110W, F160W, and F222M filter transmission curves (dotted lines) with the Large Bright Quasar Survey composite quasar spectrum, redshifted to z = 6. Flux units are arbitrary. Colors in this filter set were derived from the convolution of spectra such as this with the filter transmission curves.

still allow the identification of sources of interest such as infrared luminous galaxies and young galaxies at very high redshift, which as may be seen from Figures 3 and 4 have negative values of the (F110W - F160W) color index. Embedded young stellar objects also have spectra which peak in the far infrared (Green & Lada 1996), and as a result can also be identified by negative values of this index.

4. Software

We have developed an IDL-based interface for the batch photometry program DoPhot (Schechter, Mateo, & Saha 1993) designed specifically for the processing of NICMOS images. Compared to other photometry packages, DoPhot offers the advantages of being able to fit an empirical PSF, and has easily adjustable detection thresholds and aperture sizes. Our interface, called NICPHOT, operates on NICMOS images by first multiplying by the exposure time image to convert from adu/s, then allowing the interactive measurement of image background levels and PSFs. The DoPhot programs are then run, generating an output list of object positions, shape classifications, and instrumental magnitudes. We are developing a separate IDL program, NICCAT, to take these output files and determine object fluxes, colors (corrected for Galactic extinction), and the associated classifications. By applying NICPHOT and NICCAT together to the parallel images we expect to obtain fluxes and tentative classifications for all the objects they contain. The application of these programs is not limited to the parallel images,

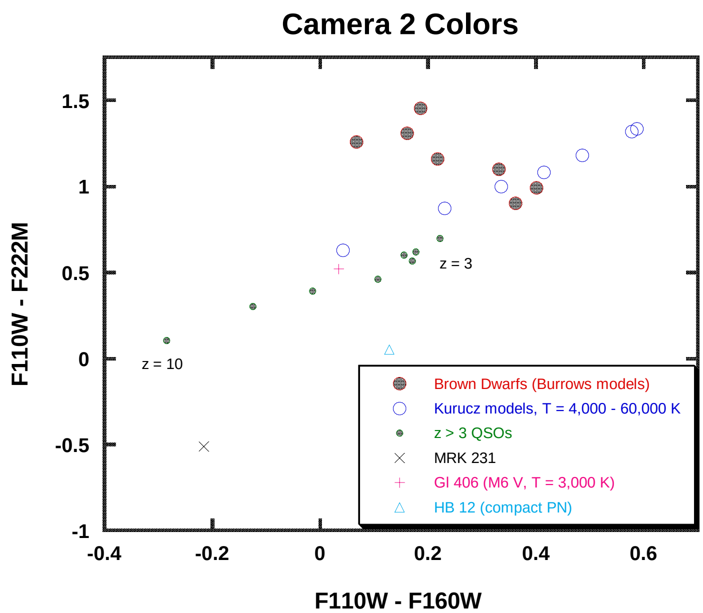

Figure 3. The expected color indices of point sources in the *JHK*-analog filters in Camera 2. The color indices are defined as the log of the ratio of fluxes in each filter. The points represent a combination of model and actual spectra, e.g. the values for the compact planetary nebula HB 12 were measured from low-resolution spectra obtained with the NICMOS grisms. For stars, Kurucz models were used due to their uninterrupted coverage through the near infrared. However, this region is poorly modeled at low temperatures, so we have used the near infrared spectrum of the M 6 star Gl 406 as a guide for such objects.

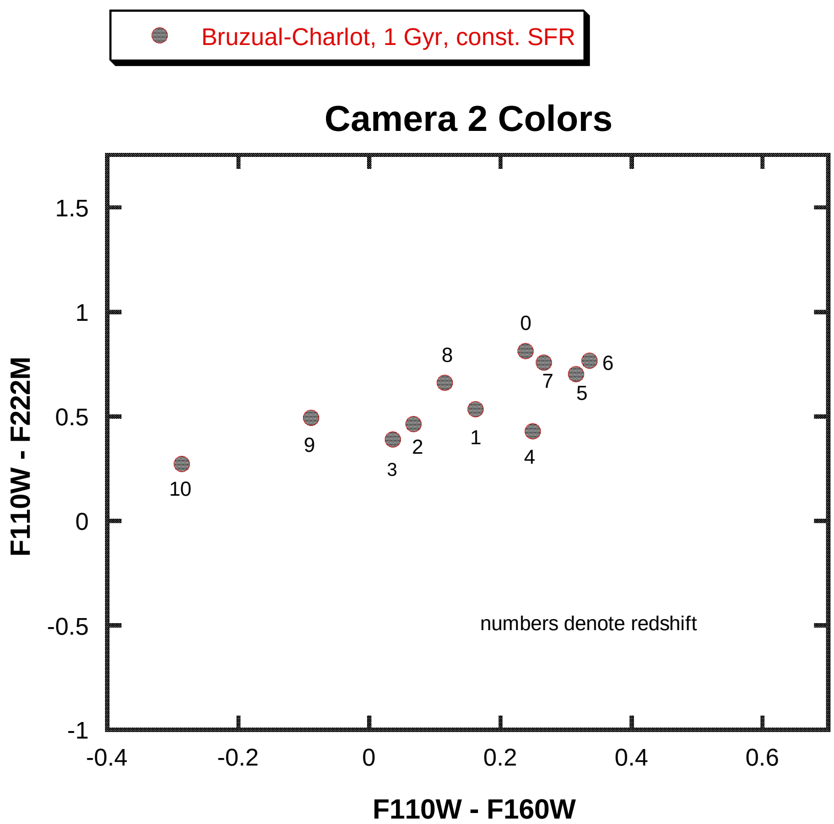

Figure 4. The expected color indices in Camera 2 for a Bruzual & Charlot model galaxy spectrum. The model age is 1 Gyr and assumes a constant star formation rate.

and we are making them available to the community. In particular, we encourage their application to background sources in deep pointed observations with NICMOS to allow the serendipitous discovery of interesting objects. NICPHOT does not treat grism images; this is best done by using the routine NICMOSlook (Freudling 1998).

5. Scientific Objectives and Preliminary Findings

The parallel observations are in no sense complete, and because of the small area of sky covered cannot be considered a survey from which reliable number counts can be made (see, however, McCarthy et al. 1998). However, the detection of *any* brown dwarf and very high redshift galaxy and QSO candidates is important. Specifically, in the case of the former, more examples are required to allow detailed study through follow-up spectroscopy, which is possible with 10m-class telescopes such as the VLT and Keck. In the case of QSOs, any detection of objects above $z \sim 5$ would run contrary to evidence that their space density above such redshifts drops nearly to zero (Shaver et al. 1996). The high angular resolution and dust penetration of NICMOS observations in the Galactic plane also holds promise for refinement of stellar number counts and population modeling towards the Galactic center. Finally, as with any observations of this type, there is always the possibility of detecting new classes of objects, and our classification algorithm is structured accordingly.

Full processing of the parallel images with the aforementioned software and the generation of a source catalog is expected to take several months. However, we have to date inspected all of the parallel images taken through 1997 December. In addition to the aforementioned blank fields and blurred images, we have noticed few galaxies relative to point sources, and among these several interacting systems, which are likely to be infrared-luminous. Inspection of the images also reveals a wide range in source density, ranging from the blank fields to fields at low Galactic latitude which are sufficiently rich that the photometry algorithm will be challenged to distinguish individual sources.

References

Bruzual, G., & Charlot, S. 1993, ApJ, 405, 538

Burrows, A. et al. 1997, ApJ, 491, 856

Francis, P.J., Hewett, P.C., Foltz, C.B., & Chaffee, F.M. 1991, ApJ, 373, 454

Freudling, W. 1998, in 1997 HST Calibration Workshop, ed. S. Casertano, R. Jedrzejewski, C.D. Keyes, & M. Stevens (Baltimore:STScI), 407

Green, T.P. & Lada, C.J. 1996, AJ, 112, 2186

Kurucz, R.L. 1992, in IAU Symposium 149, *The Stellar Populations of Galaxies*, ed. B. Barbuy & A. Renzini (Dordrecht:Kluwer), 225

McCarthy, P. et al. 1998, these proceedings

Shaver, P.A., Wall, J.V., Kellermann, K.I., Jackson, C.A., & Hawkins, M.R.S. 1996, Nature, 384, 439

Steidel, C.C., Giavalisco, M., Pettini, M., Dickinson, M., & Adelberger, K. 1996, ApJ, 462, L17

Schechter, P.L., Mateo, M., & Saha, A. 1993, PASP, 105, 1342

NICMOS and the VLT
Pula, Sardinia, May 26-27th 1998
Wolfram Freudling and Richard Hook, eds.

The Old Stellar Population of NGC 1569 from NICMOS data

A. Aloisi

Dipartimento di Astronomia, Università di Bologna, Bologna, I 40126, E-mail: aloisi@astbo3.bo.astro.it

L. Origlia and M. Tosi

Osservatorio Astronomico di Bologna, Bologna, I 40126

L. Greggio[1]

Dipartimento di Astronomia, Università di Bologna, Bologna, I 40126

M. Clampin, C. Leitherer and A. Nota[2]

Space Telescope Science Institute, Baltimore, MD 21218

M. Sirianni

Dipartimento di Astronomia, Università di Padova, Padova, I 40100

Abstract. To have a census of the old stellar populations of the dwarf irregular galaxies NGC 1569 and NGC 1705 and to trace the major episodes of star formation over a Hubble time in these starbursting systems, we have applied for and obtained HST/NICMOS observations in the F110W and F160W bands with the NIC2 camera. At the distance of these galaxies, the expected performances of NIC2 camera should allow one to reach and resolve with the required accuracy individual stars at the tip of the red giant branch (i.e. with an age spanning from 1 to 15 Gyr). NICMOS observations of NGC 1569 were already acquired in February 1998, while NGC 1705 will be observed in October 1998. Here we present some preliminary results on the photometric reduction of the available NICMOS data and some problems related to the use of this instrument.

1. Cosmological Background and Astrophysical Goals

Dwarf irregular galaxies (DIGs) and blue compact dwarf galaxies (BCDGs) are of crucial importance to understand galaxy formation and evolution. They are fundamental ingredients in common scenarios of galaxy formation, either as left-overs or as building blocks of the formation process (Silk 1987). They have also been suggested to be the

[1]Universitaets Sternwarte Muenchen, Muenchen, D 81679

[2]Affiliated with the Astrophysics Division, Space Science Department of the European Space Agency

equivalent at early epochs ($z \leq 1$) of the faint blue galaxies responsible for the count excess seen in deep photometric surveys.

Nearby galaxies of this type are ideal laboratories for such studies because their proximity allows us to examine in detail issues which are important to interpret the galaxy behavior with time, and therefore with redshift; among these the occurrence of galactic winds, the chemical enrichment of the interstellar medium and intergalactic medium, the photometric evolution. Besides, their low level of evolution, as indicated by the low metallicity and the high gas content, makes these systems the most similar to primeval galaxies, and thus the most useful to infer the primordial galaxy conditions and Big-Bang nucleosynthesis products. Understanding how the star formation (SF) proceeds in blue compacts and irregulars is then fundamental for astrophysical and cosmological purposes.

A quantitative comparison between observations and chemical evolution models has evidenced that the SF in blue compacts proceeds in few short and intense bursts (e.g. Matteucci & Tosi 1985, Marconi et al. 1994). The analysis of the color-magnitude diagrams (CMDs) of dwarf irregulars in the Local Group indicates a SF activity in the last ~ 0.5 Gyr occurred in long episodes separated by long quiescent intervals (e.g. Tosi 1994, Greggio 1995). On the other hand the analysis of the integrated light from giant irregulars is consistent with continuous, even constant SFR (Hunter & Gallagher 1985, 1986). All these evidences are consistent with the theory of Stochastic Self Propagating Star Formation (Gerola et al. 1980): the star formation level is directly related to the dimensions of the systems, the smallest ones having the longest quiescent phases and the shortest bursts of SF. Anyway, the question is still far from being settled and requires further studies of relatively nearby systems where it is possible to resolve single stars and study the stellar content with the required accuracy.

A crucial point to understand galaxy evolution is thus to check whether or not all the dwarf starburst galaxies contain an old stellar population, besides the youngest one, and trace back to early epochs the history of star formation. The best way to search for old stellar populations is to observe the resolvable galaxies in the infrared and construct the corresponding CMDs, where the old low mass stars on the red giant branch evolutionary phase are more easily visible and distinguishable from the younger, more massive objects.

2. Why choose NGC 1569?

In order to evaluate the contribution of blue compact dwarf galaxies to the galaxy counts at high redshift it is necessary to know their SF history in a wide range of epochs. Systems which show high values of SFRs, as the so-called Blue Compacts and Starbursting Dwarfs, should be the main contributors to galaxy counts at high redshift and NGC 1569 is the closest system of this type.

NGC 1569 is a blue dwarf irregular located at a distance of 2.2 Mpc, corresponding to a distance modulus $(m\text{-}M)_0$=26.71. Its total mass and hydrogen content are $M \simeq 3.3 \times 10^8\ M_\odot$ and $M_H \simeq 1.3 \times 10^8\ M_\odot$ respectively (Israel 1988). The average metallicity is $Z \simeq 0.25\ Z_\odot$. We are then dealing with a gas-rich system in a relatively early stage of its chemical evolution. Furthermore, the intrinsic blue colors and the Hα morphology, showing many filaments and arc-like structures, indicate that this galaxy is experiencing an intense SF process and related galactic winds.

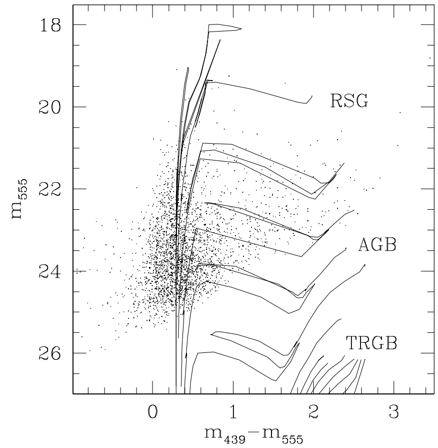

Figure 1. V vs (B–V) diagram of the stars detected in NGC 1569. The diagram contains $\sim$ 2800 objects with photometric error $\sigma < 0.2$ mag in both filters. Superimposed on the observational data are the theoretical stellar evolution tracks from 0.6 to 120 $M_\odot$ at Z=0.004 (Fagotto et al. 1994). As it is clear, with this diagram we are just able to sample the RSGs, but barely the AGB stars. We are not allowed at all to detect stars at the RGB tip.

Pre-Costar HST studies of the field population of NGC 1569 were done by O'Connell et al (1994) and Vallenari & Bomans (1996). These data have shown that the galaxy contains two so-called Super Star Clusters (SSCs), i.e. unresolved stellar systems suggested to be similar to globular clusters but of very young ages (a few Myr). With their observed I,(V–I) CMD Vallenari & Bomans reached a magnitude I$\sim$22.5, sampling a look-back time of $\sim$1.5 Gyr. Using the interpretative methods of isochrones and synthetic CMDs, they demonstrated that the galaxy has experienced a global burst of SF from 0.1 Gyr to 4 Myr ago. They found also some evidences of an older episode from 1.5 Gyr to 0.15 Gyr with a significantly lower SFR.

3. NGC 1569 as observed in the Optical Bands of HST/WFPC2

NGC 1569 was observed by our group with the WFPC2 on board HST on January 1996 (De Marchi et al. 1997, Greggio et al. 1998). Deep images were taken in the F555W and F439W broadband filters, while less deep frames in the F380W filter (corresponding indicatively to the standard ground-based V,B,U bands). The photometric reduction produced the V, (B–V) CMD plotted in Figure 1 for all objects with a photometric error $\sigma < 0.2$ in both bands ($\sim$2800 stars).

At the distance of 2.2 Mpc the optical data in the B and V filters sample only stars as young as 0.15 Gyr (V,B<26). The theoretical interpretation of this observed CMD with the method of synthetic diagrams has indicated a SF in the field stopped around 8 Myr ago, but rather continuous over the whole look-back time sampled (with quiescent periods no longer than 10 Myr) and 10^3 times higher than in the solar neighbourhood (Greggio et al. 1998). Thus in every respect this system has been a starburst galaxy with one of the highest estimated SFRs (4$\div$20 $M_\odot$ yr^{-1} kpc^{-2}).

4. The Need for Near-Infrared NICMOS Observations

The optical V, B-V CMD allows us to reconstruct the SF history of NGC 1569 only over the last 0.15 Gyr, giving an indication of a high SFR in this look-back time. The high SFR, the relatively low abundances measured and the high gas content revealed for this object seem to suggest that this galaxy is experiencing a strong SF activity just in recent epochs: its previous SFR should have been at a much lower level.

In their I vs (V–I) diagram sampling a look-back time of 1.5 Gyr, Vallenari & Bomans (1996) detected a well populated AGB, which indicates a previous episode of SF in NGC 1569 at intermediate ages (see their Figure 5), even if with a very low SFR. Recent measurements of the oxygen, nitrogen and helium abundances in the ISM of NGC 1569 (Kobulnicky & Skillman 1997), when compared to predictions of chemical evolution models for bursting dwarfs (Marconi et al. 1994), seem consistent with several bursts of SF, provided that strong galactic winds have occurred to loose part of the products of stellar nucleosynthesis. Considerations on the short gas exhaustion timescales suggest that these previous bursts cannot be as strong as the last one.

In Figure 1 superimposed on the observational optical data are the theoretical stellar evolution tracks from 0.6 to 120 $M_\odot$ at Z=0.004 (Fagotto et al. 1994). Due to the instrumental limits, the optical data allow one to analyse in great detail the blue (young) stars and only the more massive red ones. This implies that with the V, (B–V) diagram we are just able to sample the red supergiants (RSGs) but barely reach the asymptotic giant branch (AGB) stars. Even using the I, (V–I) diagram we can at best reach the brightest portion of the AGB (Vallenari & Bomans 1996).

In contrast, NIR CMDs are the best instrument to study properly not only the brightest red stellar populations (RSGs, AGB) in the age range from a few Myr to 1 Gyr, but also the red giant branch (RGB) stars with ages from 1 to 15 Gyr: since the RGB tip is predicted by all stellar evolution theories to be located at a constant luminosity $\log(L/L_\odot)=3.4$, the detection of objects in this phase would without doubts show the existence of stars in the mass range 0.6-2 $M_\odot$, while the RGB tip color distribution will give us the epochs of major SF episodes over a Hubble time. The absence of stars at the RGB tip will definitely show that the parent galaxy has been forming stars only in epochs more recent than 1 Gyr.

5. NICMOS Data in the Central Region of NGC 1569

We observed the field around the two SSCs of NGC 1569 with the NICMOS infrared detector in February 1998. Ten different frames with a spiral pattern dithering and a MULTIACCUM readout mode in the two F110W and F160W broadband filters (roughly J and H bands) were taken on NIC2 camera for a $19'' \times 19''$ field of view, a resolution of $0''.075$ per pixel and a total integration time of $\sim$ 5,100 s in each filter (4 orbits in total). The RGB tip in NGC 1569 is expected at J$\sim$23, as inferred from its position at V$\sim$26 in our optical diagram of Figure 1 and from the typical color of red giants (V-J$\sim$3). With the exposure times used NIC2 should be able to reach J,H=24$\div$25 with a S/N$\geq$10 and allow us to perform photometry 1$\div$2 mag below the RGB tip.

All frames were calibrated through the standard STScI pipeline which for dithered images makes use of the two different stages CALNICA (for instrumental calibration and cosmic ray rejection on each single frame) and CALNICB (for the reconstruction of the mosaic). The photometric reduction was performed using the PSF-fitting

DAOPHOT package on a 2 pixel aperture: all parameters involved were set at the values deduced from the HST Data Handbook (see Voit 1997 for more details) and from a statistical analysis of images. Instrumental magnitudes were then converted into the HST VEGAMAG system following the prescription of the Handbook.

The crowding of the infrared field and the difficulty in finding isolated stars to construct a good PSF brought us to try the simulation of theoretical PSFs with the *Tiny Tim* software (Krist & Hook 1997), but we encountered some difficulties in generating polychromatic PSFs. We thus searched for datasets of some calibration programs in order to build a template PSF in each filter for the reduction of our frames.

Figure 2 shows the mosaicked image in the F160W band with sumperimposed the coordinates of all stars fitted in both bands and plotted in the infrared CMDs of Figure 3 (a total of $\sim$1330 objects). These diagrams show few main sequence stars around (J–H)$\sim$0 and a large number of post-main sequence red stars.

6. How can we reach our Scientific Goal?

From a rapid analysis of our NIR CMDs it is immediately clear that however we choose the values of the parameters involved in the procedure of photometric reduction, we are not able to reach the predicted magnitude limits in J,H of 24$\div$25: we remain 2$\div$3 mag brighter and $\sim$1 mag above the RGB tip. An inspection of the position of stars fitted in the F160W image of Figure 2 indicates that the stars measured are only the brightest objects; there are fainter objects which appear resolved by eye but the standard photometric reduction seems unable to recognize and fit them.

The problem is not attributable to the estimate of the necessary exposure time. It could be instead that NICMOS performances have been somehow overestimated or that the instrumental calibration and frame combination of the associated images in the standard pipeline have not been appropriate. The complex procedures used yield also to a difficult estimate of parameters (as *gain* and *readout noise*) involved in the photometric reduction of the final mosaicked images. As these parameters are of primary importance in the detection of stars above a certain threshold and in the estimate of photometric errors and fit goodness, an erroneous value can lead to an incorrect result and to the difficulty in finding, fitting and retaining faint stars. This difficulty in fitting faint stars seems not due to the PSF used, as we tried with two different solutions: a PSF constructed with three quite isolated stars in our frames and a template obtained from the calibration program frames. On the other hand, we should also consider the extreme crowding of our central regions, which requires a very fine tuning of all the reduction parameters to resolve the fainter stars.

The CMDs in Figure 3 represent at the moment the best result we are able to obtain with the standard calibration pipeline and photometric reduction. They are clearly insufficient to reach the RGB tip at J$\sim$23. At this preliminary stage, we can conclude that *non standard* procedures for the data reduction appear to be necessary (and hopefully sufficient) to reach our scientific goal.

Acknowledgments. A.A. thanks the organizing committee of this workshop for the financial support.

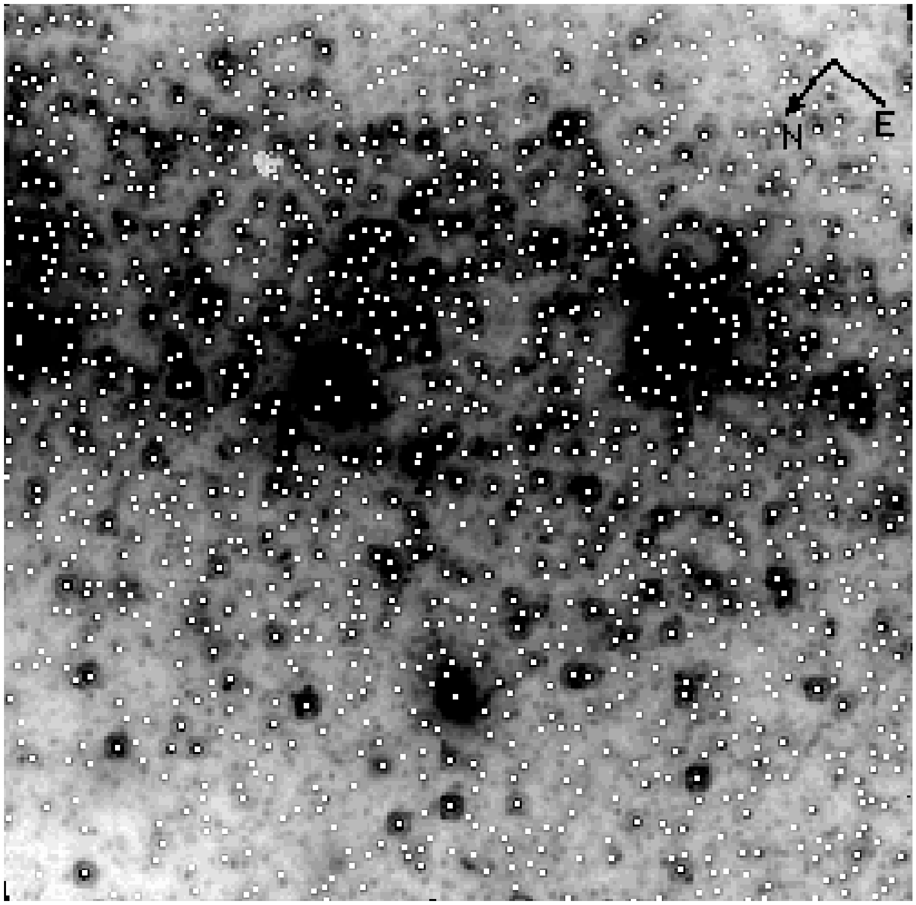

Figure 2. Deep combined image of NGC 1569 in the NICMOS F160W filter for a total exposure time of ∼5,100 s. The inner region of the galaxy is centered in the NIC2 field of view corresponding to $\sim 19'' \times 19''$ and yielding an effective plate scale of $0''.075$ per pixel. The ten dithered frames were combined into the mosaicked image for a total field of $\sim 19''.7 \times 19''.6$. Orientation is indicated in the figure. Superimposed to the image (white points) are the positions of all stars fitted in both NIR bands with the standard photometric reduction. An inspection of the figure clearly indicates that the stars measured are only the brightest ones: there are fainter objects which appear resolved by eye but that the procedure is unable to recognize and fit.

References

De Marchi, G., Clampin, M., Greggio, L., Leitherer, C., Nota, A., & Tosi, M. 1997, ApJ, 479, L27

Fagotto, F., Bressan, A., Bertelli, G., & Chiosi, C. 1994, A&AS, 105, 29

Gerola, H., Seiden, P. E., & Schulman, I. S. 1980, ApJ, 242, 517

Greggio, L. 1995, in The Local Group: Comparative and Global Properties, ed. J. Storm, A. Layden & C. Smith (Garching: ESO), 72

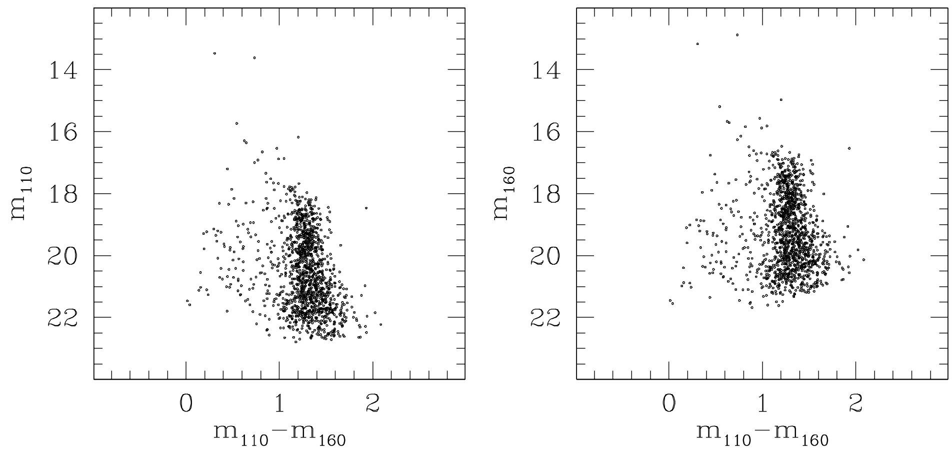

Figure 3. Infrared CMDs of the ∼1330 stars detected in the NIC2 field of NGC 1569: J vs (J–H) (left panel) and H vs (J–H) (right panel). By eye it is clear that the standard photometric reduction has not allowed us to sample stars at the RGB tip around J∼23: we are ∼1 mag brighter.

Greggio, L., Tosi, M., Clampin, M., De Marchi, G., Leitherer, C., Nota, A., & Sirianni, M. 1998, ApJ, in press

Kobulnicky, H. A., & Skillman, E. D. 1997, ApJ, 489, 636

Hunter, D. A., & Gallagher III, J. S. 1985, AJ, 90, 80

Hunter, D. A., & Gallagher III, J. S. 1986, PASP, 98, 5

Israel, F. P. 1988, A&A, 194, 24

Krist, J., & Hook, R. 1997, The Tiny Tim User's Manual, Ver. 4.4

Marconi, G., Matteucci, F., & Tosi, M. 1994, MNRAS, 270, 35

Matteucci, F., & Tosi, M. 1985, MNRAS, 217, 391

O'Connell, R. W., Gallagher III, J. S., & Hunter, D. A. 1994, ApJ, 433, 65

Silk, J. 1987, in High Redshift and Primeval Galaxies, ed. J. Bergeron, D. Kunth, B. Rocca-Volmerange & J. Tran Than Van (Gif-sur-Yvette; Editions Frontieres), 301

Tosi, M. 1994, in Dwarf Galaxies, ed. G. Meylan & P. Prugniel (Garching: ESO), 465

Vallenari, A., & Bomans, D. J. 1996, A&A, 313, 713

Voit, M. 1997, HST Data Handbook (Baltimore: STScI)

NICMOS and the VLT
Pula, Sardinia, May 26-27th 1998
Wolfram Freudling and Richard Hook, eds.

HST-NICMOS Observations of Galactic Bulges: Red Nuclei in Nearby Galaxies

Reynier F. Peletier[1]

[1]*Dept. of Physics, University of Durham, South Road, Durham, DH1 3LE, UK, E-mail: R.F.Peletier@dur.ac.uk*

Marc Balcells[2]

[2]*Instituto de Astrofísica de Canarias, Via Lactea, s/n, 38200 La Laguna, Tenerife, Spain. E-mail: balcells@ll.iac.es*

Abstract. We describe multi-color observations with NICMOS and WFPC2 of 20 nuclei of nearby galactic bulges of types S0-Sbc. We find that the centers of 19 out of 20 bulges are found to be dusty, with average extinction A_V between 0.6 and 0.9 mag. Our second result is that the stellar populations of galactic bulges of type S0-Sb show a very tight $B-I$ vs. $I-H$ relation, suggesting that the age spread among bulges of early-type spirals is small (at most about 2-3 Gyr).

1. Introduction

Bulges of spiral galaxies are generally seen as small elliptical galaxies in the center of a large spiral. For example, bulges fall on the fundamental plane of elliptical galaxies (Djorgovski & Davies 1987, Bender et al. 1992). Dynamically, bulges are hotter than disks, while colder than giant ellipticals. Their surface brightness profiles fall off as $\mu(r) \propto r^{1/n}$ (Andredakis et al. 1995), with n getting smaller towards later morphological types. In a series of papers (Balcells & Peletier 1994, Peletier & Balcells 1996, 1997) we have studied the stellar populations of bulges by taking a sample of highly inclined early-type spirals (type S0-Sbc), and analyzing optical and near-infrared colors of the side of the minor axis which is not obscured by the disk. This method avoids the need to address extinction corrections, which are very uncertain in inclined galaxies. That our minor axis color profiles are smooth suggests that dust effects are indeed minimal.

We found that dustfree colors of bulges are never redder than ellipticals of the same luminosity. This implies that their metallicities are lower than those of giant ellipticals. In addition we found that the colors of bulges are very similar to those of the inner disk, both for blue optical and for optical-infrared colors. Color differences from galaxy to galaxy are much larger than the differences between bulge and disk of the same galaxy. This implies that the inner disk (at 2 scale lengths) must have formed at most 3 Gyr after the bulge.

HST allows us to investigate the centers of bulges with a ten fold increase in spatial resolution. HST-based information on the colors of galaxy centers at scales of tens of parsecs is scarce. Colors contain useful information on the stellar populations of the galaxy centers. They also give clues about the amount of internal extinction due to dust. For ellipticals, unsharp masking techniques show that patchy dust is very common (van Dokkum & Franx 1995). Dust may affect the shapes of surface brightness profiles observed by eg. Lauer et al. (1995).

Here we show first results of a color study of the centers of galactic bulges. Since we are interested in disentangling the effects of extinction, metallicity and age, we have chosen to observe a sample of galaxies in 3 bands covering a large wavelength baseline. We observed in the NICMOS F160W band (H-band), F814W (I) and in F450W, a wider version of the B-band. With these three bands we can make the red $I-H$ color, primarily sensitive to extinction by dust and old stellar population gradients, and the $B-I$ color, especially sensitive to recent star formation. Examples of how these colors can be used are shown in e.g. Knapen et al. (1995). This is the first study of colors of early-type galaxies based on NICMOS data. In a following paper, the surface brightness profiles are presented in H, I and B, showing the effects of dust on the surface brightness profiles of bulges.

2. Sample and Observations

20 galaxies were observed with HST in Cycle 7 (Summer 1997) with WFPC2 (F450W and F814W) and NICMOS (F160W). They all are part of the original sample of Balcells & Peletier (1994), which is a complete, magnitude-limited sample in B of early-type spirals (type S0-Sbc) with inclinations larger than 50°. The galaxies observed with HST are all objects for which one side of the minor axis is more or less featureless as seen from the ground. We assume that this means that extinction by dust there is negligible (in general less than A_B = 0.05 mag). The subsample was chosen to include galaxies from all types S0-Sbc, excluding galaxies that are exactly edge-on, and is biased towards the nearest objects.

To reduce the optical data the normal HST-pipeline reduction was used. For NGC 7457 the I-band observations were taken from the HST Archive. For the H-band two MULTIACCUM NIC2-exposures of in total 256 s were taken, offset from each other by $1''$. The normal STSDAS CALNICA reduction package was used, after which a small fraction of the flatfield was subtracted from the reduced images, to account for a non-zero pedestal level in the raw image. This fraction was determined by requiring that the final image was smooth. Applying this step is only important for the lowest flux levels, but it improves the image considerably. The final sky background level was determined by comparing the image with the ground-based image in the same band. For the H-band a small correction was applied to the K-band image (a fit to Worthey (1994)'s models):

$$H-K \;=\; 0.105(I-K) \;-\; 0.0471$$

The images were calibrated to the STMAG system using Holtzmann et al. (1995), using a constant shift of 0.10 mag to correct to infinite aperture. After this, the same paper was used to iteratively account for the color term in the F450W filter. The colors were corrected for galactic extinction using the new dust maps of Schlegel et al. (1998), and the Galactic extinction law (Rieke & Lebofsky 1985). After this the bands were redshift-corrected. This small correction (from Persson et al. 1979) was ΔB = -5z, ΔI = –z and ΔH = 0.

To account for the difference in Point Spread Functions (PSF) when determining the $X-Y$ color profile, the X-band image was convolved with the Y-band PSF, and

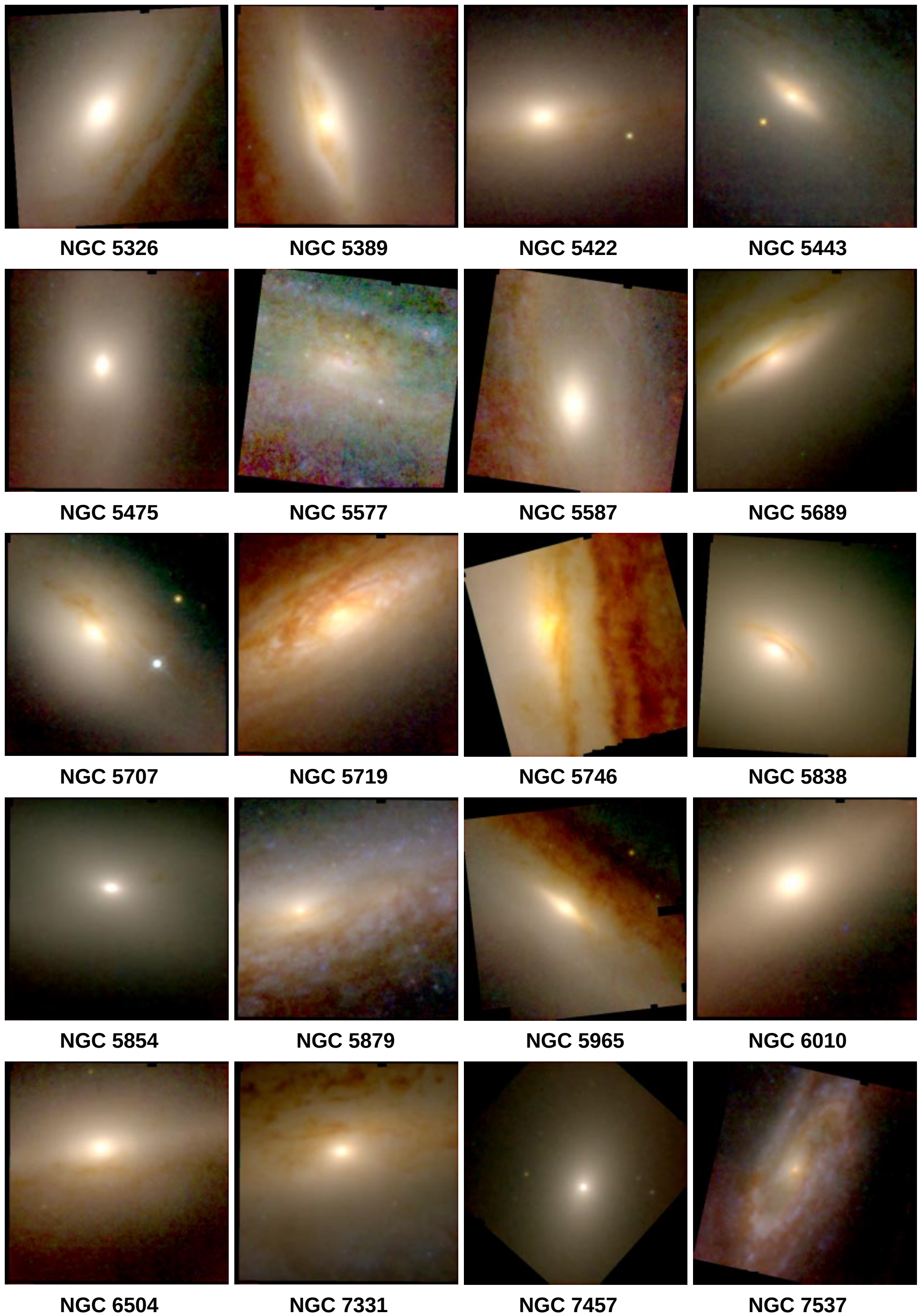

Figure 1. Real color images of the galaxies. The size of the images is about $20'' \times 20''$

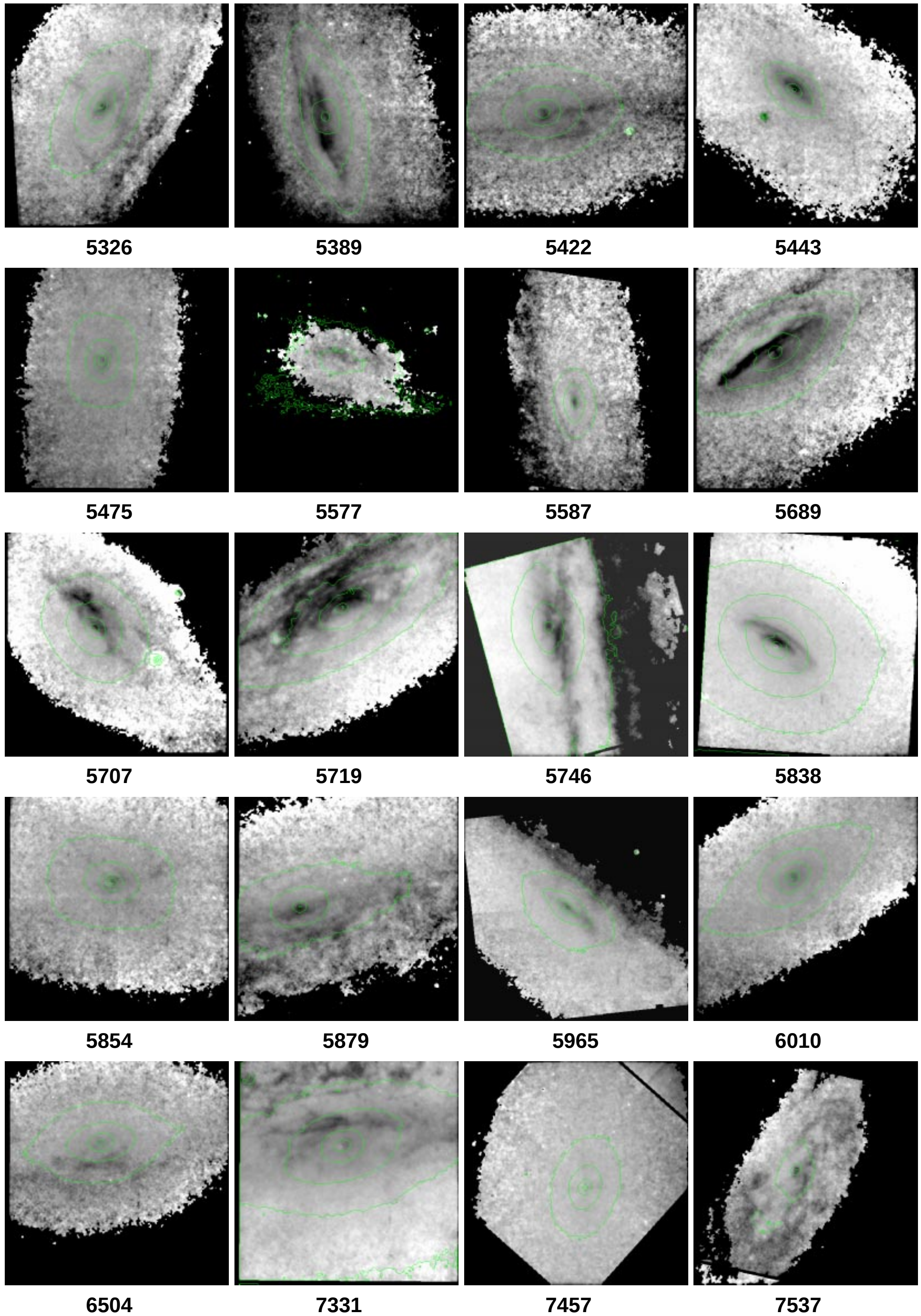

Figure 2. $I-H$ color maps of the galaxies on the same scale as Fig. 1. Superimposed are H-band contours.

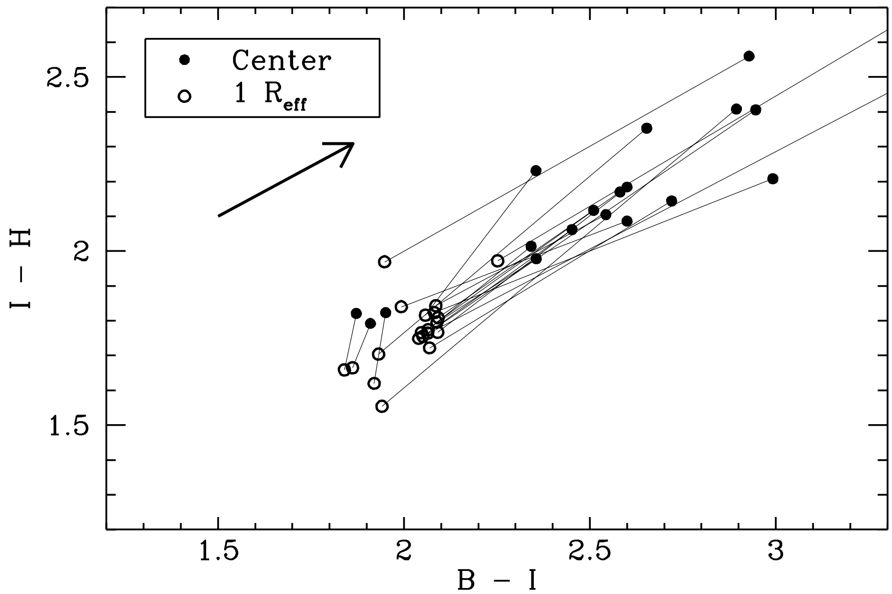

Figure 3. Color-color diagram for the 20 galaxies. Displayed are the positions of the center (filled) and 1 bulge effective radius on the minor axis (open circles). Also indicated is a reddening vector for a reddening of A_V = 0.5 mag.

the Y-band image with the X-band PSF. These PSFs were determined with the Tiny Tim package (Krist 1992). We then determined minor axis profiles in wedges of 22.5^o, centered on the H-band nucleus, and subtracted these wedges to get color profiles. Finally the color profiles were combined with the ground-based color profiles, to cover the whole range of the bulge, shifting the ground-based profile on top of the HST-profile. In this way absolute and relative accuracies of a few percent can be expected (Colina 1998). Real-color images of the galaxies are shown in Fig. 1.

3. The $B-I$ vs. $I-H$ color-color diagram

3.1. Dust in Nuclei of Galactic Bulges

In Fig. 2 we show the $I-H$ color maps of the 20 galaxies, superimposed on the H-band contour maps. The maps indicate the position of dustlanes. Comparing these images with those of Fig. 1 it is clear that many, maybe all, galaxies have red nuclei. We now try to estimate how much extinction they contain. In Fig. 3 we show the colors at the center and at one bulge effective radius in a $B-I$ vs. $I-H$ color-color diagram. The Figure shows indeed that in all cases the center is redder, by sometimes very large amounts. Since the vector indicating reddening by dust is almost parallel to the the vector indicating changes in metallicity (see Fig. 4), it is not possible to say exactly how much of the reddening is due to extinction. Lower and upper limits to the internal extinction may be estimated as follows.

We see in Fig. 3 that three blue galaxies in the bottom left corner of the diagram show small color differences. These are NGC 7457, NGC 5854 and NGC 5577. NGC 5577 is an Sbc galaxy with much lower surface brightness than the rest of the galaxies, with patches of dust and star formation everywhere in its central areas, clearly different from most other galaxies in the sample. For the other two galaxies, both semi-minor axis color profiles are smooth. A plausible *upper limit* to the reddening is derived by taking these profiles to be representative of the population-induced color gradients in our sample; assuming that the colors at one effective radius are dustfree, one obtains that the central $I-H$ colors are reddened by on the average 0.29 $\pm$ 0.05 mag, and the $B-I$ colors by 0.58 $\pm$ 0.10 mag. A *lower limit* to the reddening can be found if one assumes that the stellar populations are never redder than those of the central Virgo galaxy NGC 4472. Studies by e.g. Balcells & Peletier (1994) have shown that dustfree bulge colors at $r_e/2$ are never redder than ellipticals of the same size, making this assumption very likely. Using here $B-I$ = 2.30 and $I-H$ = 1.85, we find that in this case the $I-H$ colors would be reddened by on the average 0.37 $\pm$ 0.06 mag and $B-I$ by 0.44 $\pm$ 0.10 mag. Using the Galactic extinction law (Rieke & Lebofsky 1985) these numbers correspond to an average internal extinction A_V between 0.69 and 0.89 mag, if $I-H$ is used, and between 0.60 and 0.80 mag when one uses $B-I$.

For those galaxies for which no dust lanes or patches were found, we tried a more sensitive method, by carefully analyzing the isophote shapes. Dust generally causes patchy structures, which means that the galaxy isophotes are not symmetric any more, and that the third order Fourier terms C3 and S3 (Carter 1978) will be non-zero, and generally increasing when going to the blue. No dust lanes or patches were found for NGC 5475, 5854, 6504 and 7457. However, S3 and C3 in B and I were found to be significantly non-zero in all of these, except for NGC 7457.

3.2. Stellar Populations

Apart from providing high resolution, HST also has the advantage that the photometric conditions are very stable, so that accurate colors can be determined. For this reason we can use the color-color diagram to infer information about the age-spread in the sample, and about the cause of the stellar population gradients. In Fig. 4 our galaxies are plotted together with Single Stellar Population (SSP) models of Vazdekis et al. (1996). We see that for $I-H < 2.1$, in the region where reddening is not necessarily important, the color-color diagram is extraordinarily tight. Only NGC 5577, an Sbc galaxy, with much lower surface brightness than the rest, is much bluer in $B-I$ than the other galaxies. For a given $I-H$ the scatter in $B-I$ is $\sim$ 0.05 mag at $I-H$ = 1.9 and 0.08 mag at $I-H$ = 1.7. Independent of the amount of extinction, the tightness of the relation shows that the average age of the stars is very similar from bulge to bulge. According to the model the age-spread would be about 2-3 Gyr, although the ages in the outer parts of the bulge are somewhat younger than further inwards. An average age of about 8 Gyr is found. One should however keep in mind that this kind of stellar population model is generally not very good at determining absolute ages. No type-dependence of this result is found, except that for the latest type (Sbc) $B-I$ tends to be bluer for a given $I-H$, showing that the Sbc bulges are generally younger than earlier-type bulges.

4. Discussion

In the previous section we have shown that

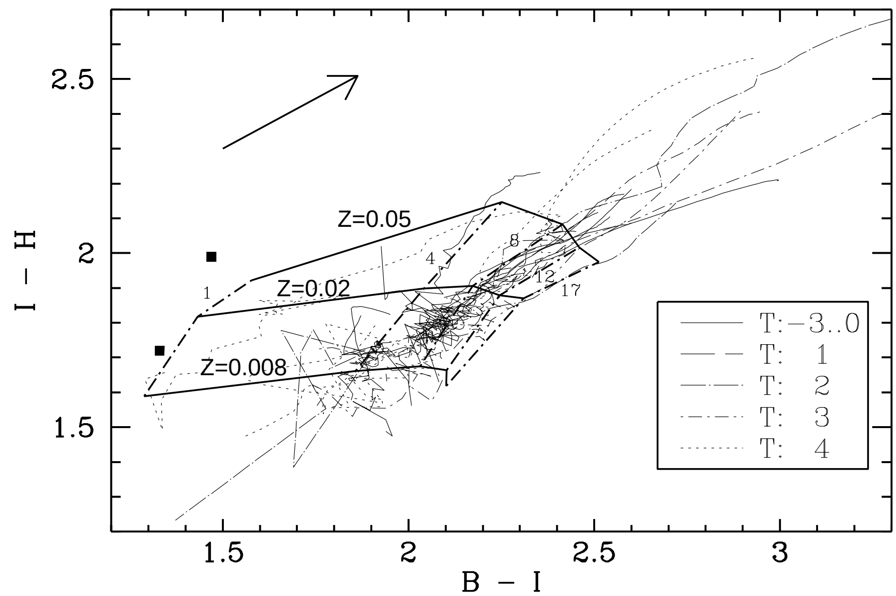

Figure 4. Individual color profiles for the sample galaxies. Each galaxy is represented by a line from the center to the point where the bulge contribution is as large as that of the disk. Superimposed are SSP models by Vazdekis et al. (1996). Drawn fat lines are lines of constant metallicity, dashed-dotted lines are loci of constant age. Also indicated is a reddening vector for a reddening of A_V = 0.5 mag. The two filled squares indicate the colors of knots A and C in the jet of M 87.

1. Centers of bulges of early-type spirals are generally dusty. We find that A_V on the average lies between 0.6 and 0.9 mag, which implies that A_H should be between 0.1 and 0.2 mag.

2. Galactic bulges show a very tight $B-I$ vs. $I-H$ relation, implying that the age spread among bulges of early-type spirals is small (at most about 2-3 Gyr).

The first conclusion shows one more similarity between bulges of early-type spirals and ellipticals. Van Dokkum & Franx, analyzing WFPC data of elliptical galaxies, give an average dust mass of 4×10^3 $M_\odot$. For the bulges analyzed here we find an average dust mass of $\sim 10^4$ $M_\odot$, i.e. a slightly larger number. We should however note that van Dokkum & Franx determined their dust masses only from one V-band image, so their numbers are very rough. If we assume a Galactic gas to dust ratio of 130 (see van Dokkum & Franx 1995) we find the galaxies analyzed in this paper have an average of 10^6 $M_\odot$ of interstellar material in their nuclear regions. This is generally much smaller than the stellar mass in these areas. Note that the amount of ISM in the galaxies outside the nuclear area in general is much larger, as shown by the large dustlanes etc.

Several of our bulges have central features which resemble the inner disk in the giant elliptical NGC 4261 (Jaffe et al. 1996). Examples are NGC 5326, NGC 5587,

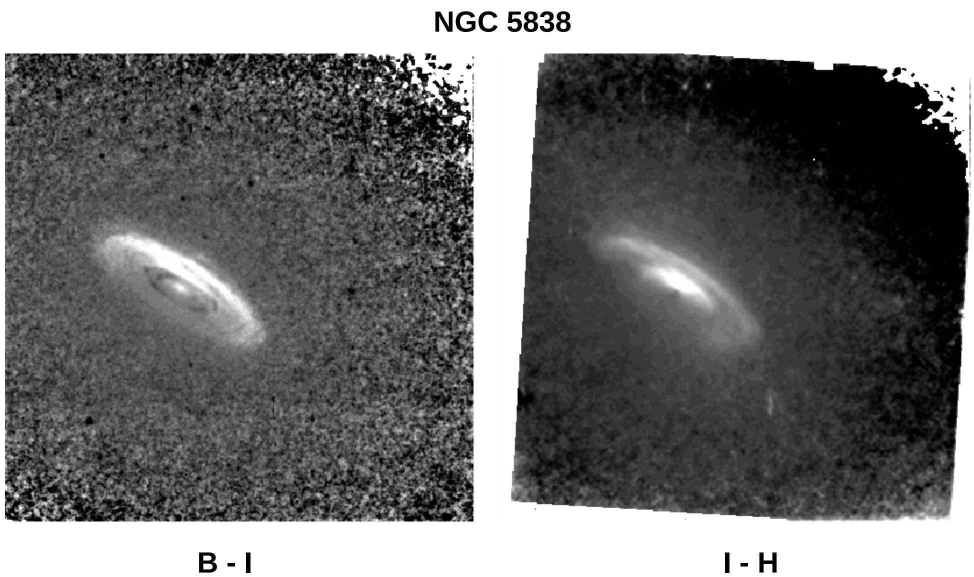

Figure 5. Color maps of the inner $20'' \times 20''$ of NGC 5838. White indicates redder colors.

and NGC 5838. NGC 4261 has a LINER spectrum in the center, and it is argued by Jaffe et al. that this inner disk might provide the fuel for the AGN. The objects studied in our paper however are not known to be active, and also their colors are consistent with being from stellar origin, extincted by dust. As a comparison, we have plotted the colors of two knots of the jet in M 87 in Fig. 4, for which the emission is thought to be due to synchrotron radiation (see Stiavelli et al. 1997). They are much bluer in $B-I$ than the nuclei of the bulges. We conclude that in general the material to fuel an AGN in our bulges is present, although it is not clear whether black holes are present. An indication that they are could be the fact that many bright nearby S0 galaxies harbor faint radio sources in their centers (Sadler et al. 1989).

The largest nuclear disk that we observe, in NGC 5838, shows another interesting feature. $B-I$ and $I-H$ color maps are shown in Fig. 5. Two dust lanes are visible, the outer having a diameter of $\sim$ 1 kpc. The central dust lane, very prominent in the $I-H$ map, is rather weak in the $B-I$ map. Furthermore, in the $B-I$ map several darker areas are seen, i.e. of bluer color. The fact that these features are only seen in a blue color indicates that we are seeing the presence of young stars being formed in the inner disk. This explains also why the inner dust lane is less strong in $B-I$. Although it is clear that the main body of the galaxy is old, we see that even at present the galaxy is forming stars, although at a very low rate. For the other galaxies unfortunately we don't have the resolution to detect the presence of young stars in this way, but it is likely that the dust and gas, which has been found in a large fraction of ellipticals and early-type spirals, is a suitable environment for the formation of young stars, and that galaxies, even early-types, are still forming stars in their nuclei right now.

In a recent series of papers Carollo and coworkers (Carollo et al. 1997b) divide bulges in three categories, on the basis of their R-band surface brightness profiles: the *Classical $R^{1/4}$ bulges, small exponential*, and *dominant exponential bulges*. Of the whole sample discussed here, only one galaxy, NGC 5577, would not fall into the category of $R^{1/4}$ bulges: Surface brightness profiles in the inner regions are very similar to ellipticals. This result supports the view that early type bulges have $R^{1/4}$ profiles, while late types have profiles which approach the exponential shape (Andredakis et al. 1995). Comparing color profiles is somewhat more difficult. The only paper presenting a reasonable sample of ellipticals is Carollo et al. (1997a), presenting V and I profiles of 15 galaxies observed with the refurbished WFPC2. It seems that the color gradients are similar, although they are difficult to compare, since Carollo et al. (1997a) masked out dusty areas before obtaining the color profiles.

The fact that the ages are all so similar indicates that there has been a major episode of star formation in the universe, in which most of these bulges were formed. This could be in agreement with the star formation history predicted by Madau et al. (1996) on the basis of data of the Hubble Deep Field, which shows a maximum between $z = 1$ and 3. Note that the objects studied here are generally field objects, which means that they do not necessarily have to have similar ages as galaxies in clusters, which must have formed beyond $z = 3$ (Ellis et al. 1997).

Acknowledgments. The authors acknowledge very useful support from Luis Colina, Massimo Stiavelli and Doris Daou at the STScI, and useful discussions with Ian Smail.

References

Andredakis, Y., Peletier, R.F. & Balcells, M., 1995, MNRAS, 275, 874

Balcells, M. & Peletier, R.F., 1994, AJ, 107, 135

Bender, R., Burstein, D. & Faber, S.M., 1992, ApJ, 399, 462

Carollo, C.M., Franx, M., Illingworth, G.D. & Forbes, D., 1997a, ApJ, 481, 710

Carollo, C.M., Stiavelli, M., de Zeeuw, P.T. & Mack, J., 1997b, AJ, 114, 2366

Carter, D., 1978, MNRAS, 182, 797

Colina 1998, this conference

Djorgovski, S. & Davis, M., 1987, ApJ, 313, 59

Ellis, R., Smail, I., Dressler, A., et al., 1997, ApJ, 483, 582

Holtzmann, J.A., Burrows, C.J., Casertano, S., Hester, J.J., Trauger, J.T., Watson, A.M. & Worthey, G., 1995, PASP, 107, 1065

Jaffe, W., Ford, H., Ferrarese, L., van den Bosch, F. & O'Connell, R.W., 1996, ApJ, 460, 214

Knapen, J.H., Beckman, J.E., Shlosman, I., Peletier, R.F., Heller, C.H. & de Jong, R.S., 1995, ApJ, 443, L73

Krist, J. 1992, Tinytim v2.1 User's Manual (STScI)

Lauer, T. R., et al. 1995, AJ, 110, 2622

Madau, P., Ferguson, H.C., Dickinson, M. et al., 1996, MNRAS, 283, 1388

Peletier, R.F. & Balcells, M., 1996, AJ, 111, 2238

Peletier, R.F. & Balcells, M., 1997, NewA, 1, 349

Rieke, G. & Lebofsky, M.J., 1985, ApJ, 288, 618

Sadler, E.M., Jenkins, C.R. & Kotanyi, C.G., 1989, MNRAS, 240, 591

Schlegel, D.J, Finkbeiner, D.P. & Davis, M., 1998, ApJ, in press

Stiavelli, M., Peletier, R.F. & Carollo, C.M., 1997, MNRAS, 285, 181
van Dokkum, P.G. & Franx, M., 1995, AJ, 110, 2027
Vazdekis, A., Casuso, E., Peletier, R.F. & Beckman, J.E., 1996, ApJS, 106, 307
Worthey, G., 1994, ApJS, 95, 107

NICMOS and the VLT
Pula, Sardinia, May 26-27th 1998
Wolfram Freudling and Richard Hook, eds.

HST/NICMOS Observations of the Interacting System Arp 299

Almudena Alonso-Herrero, Marcia J. Rieke, and George H. Rieke

Steward Observatory, the University of Arizona, Tucson, AZ 85721, E-mail: aalonso@as.arizona.edu, mrieke@as.arizona.edu, grieke@as.arizona.edu

Abstract.

Arp 299 (IC 694 + NGC 3690) is one of the nearest examples of interacting galaxies with a high infrared (IR) luminosity ($L_{\rm IR} = 5.4 \times 10^{11}\,{\rm L}_\odot$, for the assumed distance $D = 42\,$Mpc), close to the limiting value for ultraluminous IR galaxies. We present *HST*/NICMOS observations taken with all three cameras. We concentrate on the data reduction and analysis of the images taken with camera 3 through the narrow-band filters F164N and F166N. The [Fe II]1.644 μm morphology and properties are described in detail. The relative ages of the burst of star formation together with the supernova rate for the bright sources in the interacting system are derived.

1. Introduction

The existence of luminous and ultraluminous IR galaxies has long been known (Rieke & Low 1972), but it was with the launch of the IR satellite *IRAS* that this class of galaxies was detected in large numbers. Since then an intense debate started as to whether there is an evolutionary link between luminous IR galaxies, ultraluminous galaxies and optically selected quasars (see Sanders & Mirabel 1996 for a recent review). Among the ultraluminous IR class ($L_{\rm IR} > 10^{12}\,{\rm L}_\odot$, IR luminosity between 8 and 1000 μm), a large percentage is found to be interacting/merging systems containing active galactic nuclei. Sanders et al. (1988) proposed that the IR luminous phase is the initial stage for the appearance of a quasar. In this context the interacting system Arp 299 (NGC 3690+IC 694 or Mrk 171) is an interesting study case by itself, not only because of its high IR luminosity ($L_{\rm IR} = 5.4 \times 10^{11}\,{\rm L}_\odot$), close to the limiting value for ultraluminous IR galaxies, but also because it is one of the nearest examples of interacting starburst galaxies (distance $D = 42\,$Mpc for $H_0 = 75\,$km s^{-1} Mpc^{-1}).

A number of bright IR and radio sources have been detected from ground-based observations (see Gehrz et al. 1983, Wynn-Williams et al. 1991 and references therein). Following the notation introduced by Gehrz et al. (1983) for the interacting pair of galaxies Arp 299, the nucleus of IC 694 (eastern component) is referred to as source A, and the sources in NGC 3690 (western component) are called B1, B2, C and C$'$ (see Figure 1). One of the most remarkable characteristics of this interacting system (and other luminous IR galaxies) is the high concentration of molecular hydrogen within relatively small regions. From CO maps, Sargent & Scoville (1991) estimated the density of molecular gas $\simeq 8 \times 10^5\,{\rm M}_\odot$ pc^{-2} in IC 694, $\simeq 3 \times 10^4\,{\rm M}_\odot$ pc^{-2} in components B1 and B2 of NGC 3690 and $\simeq 2 \times 10^4\,{\rm M}_\odot$ pc^{-2} at the interface of both galaxies, region C+C'. Numerical simulations of collisions between gas-rich galaxies (see Barnes &

Hernquist 1996 and references therein) show that collisions are very efficient at transporting large quantities of molecular gas into the centers of galaxies; such large quantities are similar to those observed in IC 694 and other ultraluminous IR galaxies.

HST NICMOS images of the system together with MMT optical and IR spectroscopy are analyzed to derive the star formation properties of the system.

2. Observations

NICMOS on the *HST* observations of the interacting galaxy Arp 299 were obtained on November 4 1997 using all three cameras. Images were taken with the following filters and cameras: NIC1 F110M; NIC2 F160W, F222M, F237M, F187N, F190N, F212N and F215N; NIC3 F164N and F166N. The pixel sizes for NIC1, NIC2 and NIC3 are 0.045 arcsec pixel^{-1}, 0.076 arcsec pixel^{-1} and 0.20 arcsec pixel^{-1} respectively. In this paper we will concentrate on the data reduction and data analysis of the camera 3 narrow-band filter images. The observational strategy consisted of taking a spiral dither with a 5.5 pixel spacing, with two, three or four positions. The orientation of the images is PA = 90 degree. The FWMH of the point sources in the fully-reduced NIC3 F164N image is $0.29''$. It is important to note that the NIC3 images were not taken during the NIC3 observing campaign. Nevertheless the quality of the images is remarkable and most suitable for scientific purposes.

2.1. Reduction of narrow-band filter images taken with NIC3

The field of view of NIC3 ($\simeq 51.2'' \times 51.2''$) is large enough to cover both galaxies in the interacting system. Four images (spiral dither with a $1''$ separation) with a total integration time of 1,024 seconds were taken through filters F164N and F166N respectively.

Part of the reduction of the NICMOS images was performed with routines of the package NicRed (McLeod 1997). This data reduction package works within the IRAF environment. Darks with exposure times corresponding to those of our observations were obtained from other proposals close in time. Usually between 10 and 20 darks were averaged together for a given sample sequence after the subtraction of the first readout. The flatfields for the filters NIC3 F164N and F166N are in-flight flats kindly reduced by Dr. Rodger Thompson. The first steps in the data reduction (done with the task *nicfast* within Nicred) involve subtraction of the first readout, dark current subtraction on a readout basis, correction for linearity and cosmic ray rejection (using fullfit), and flatfielding. Since our NICMOS images were obtained after August 1997, no correction for the pedestal effect was necessary. The background was measured on blank regions of the flatfielded images and subtracted from each image.

As a first try to produce the final [Fe II]1.644 μm line emission image, the dithered galaxy images for a given filter were registered to a common position using fractional pixel offsets and cubic spline interpolation, and combined to produce the final images through filters F164N and F166N. Once the images were combined, the flux calibration was performed using the conversion factors based on measurements of the standard star P330-E during SMOV (Marcia Rieke 1997 private communication), which are: 6.43×10^{-5} Jy ADU^{-1} and 6.66×10^{-5} Jy ADU^{-1} for NIC3 F164N and F166N respectively. The combined continuum and line+continuum images were again shifted to a common position and finally the F164N was subtracted from the F166N to produce the [Fe II]1.644 μm line emission image (note that at the redshift of Arp 299 the

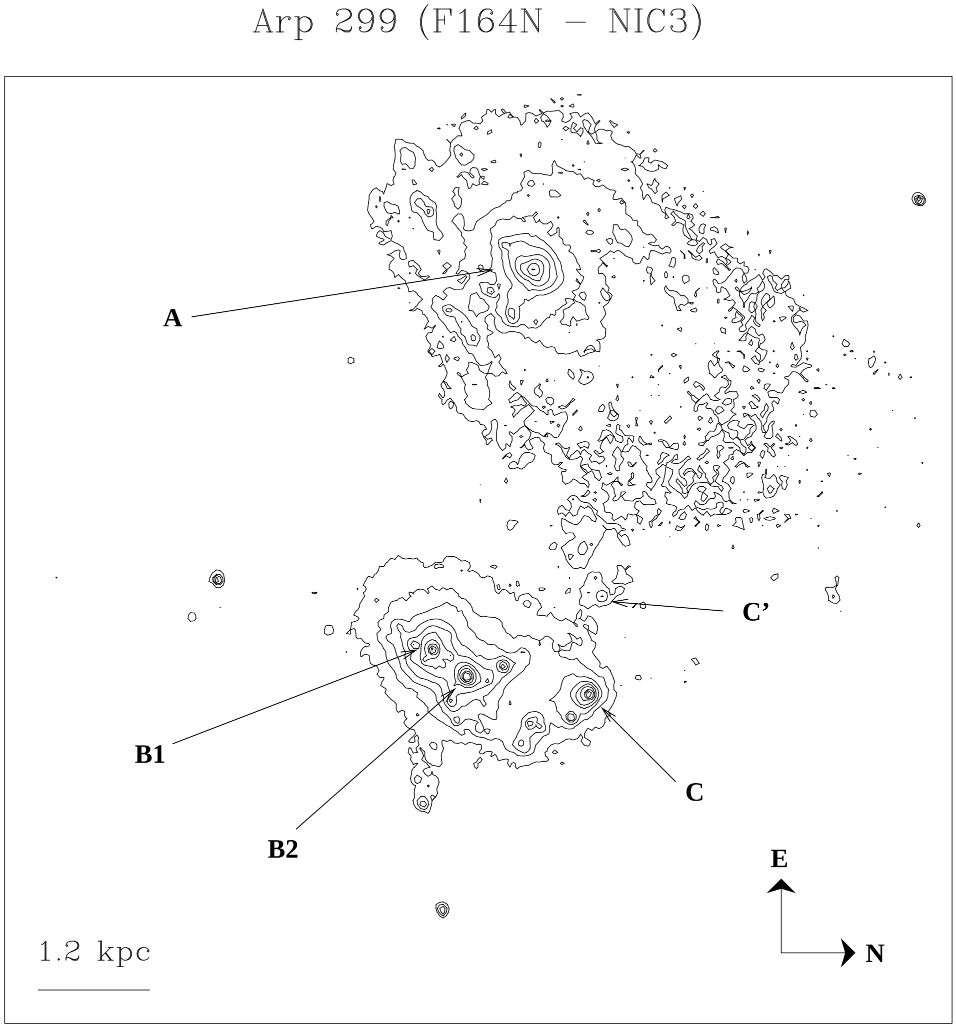

Figure 1. NIC3 F164N contour plot on a logarithmic scale of Arp 299. For the redshift of this galaxy the filter F164N contains the continuum adjacent to the [Fe II]1.644 μm line. The field of view is $51.2'' \times 51.2''$. The first contour corresponds to 0.08 mJy and the last contour to 0.64 mJy.

[Fe II]1.644 μm line gets shifted into the F166N filter). The resulting image showed some residuals produced by both the under-sampling of the point spread function (PSF) and the variation of the shape of PSF with wavelength. In addition it appears that for point-like sources and camera 3 there is a significant variation of the shape of the PSF depending on the position along the pixel.

To solve some of these problems we used a different strategy when subtracting the continuum images from the line+continuum images. Instead of combining all the images together prior to the continuum subtraction, we realigned both the F164N and F166N individual images for a given position (usually by less than a few tenths of a pixel), and subtracted the F164N individual images from the F166N individual images.

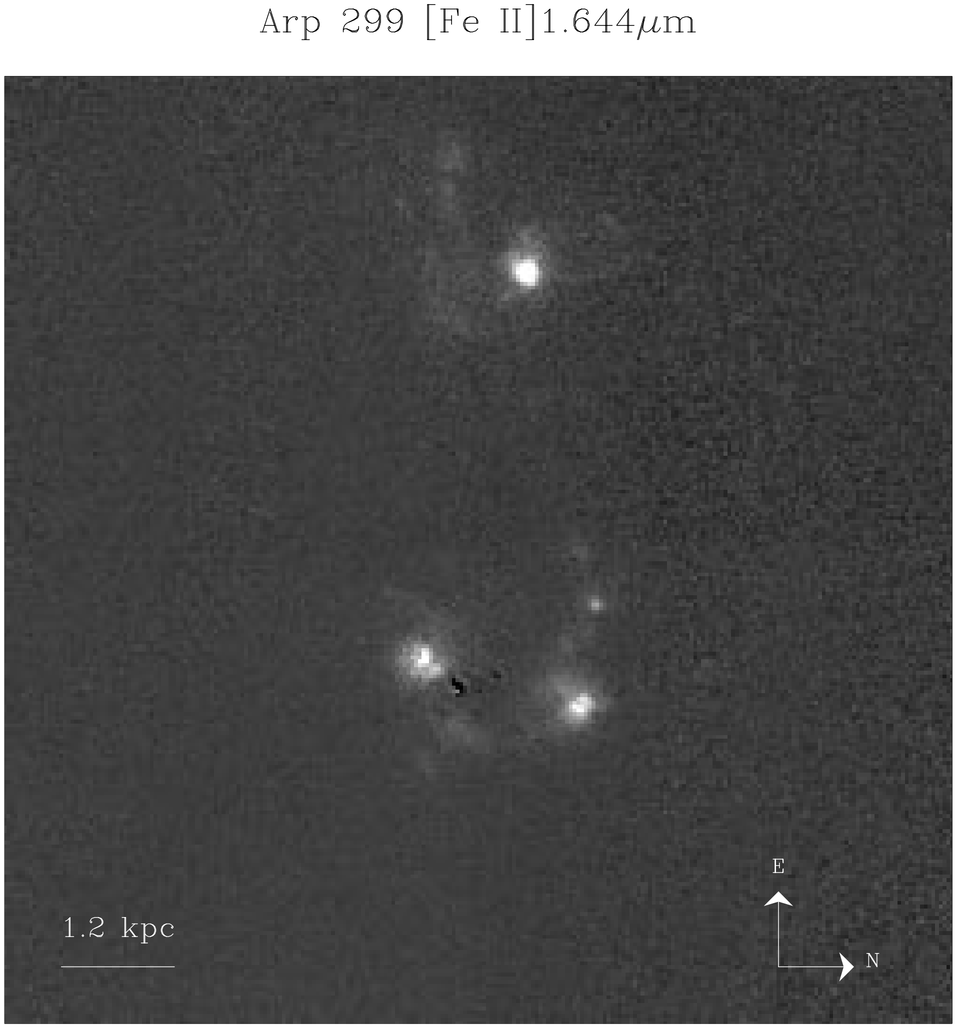

Figure 2. Gray-scale image (on a logarithmic scale) of Arp 299 taken through the NIC3 F166N filter. The image has been continuum subtracted to show the [Fe II]1.64 μm emission. The size is the same as in Figure 1.

The resulting individual continuum-subtracted F166N images were then shifted to a common position (using the offsets computed with the F166N images before continuum subtraction) and combined to the final line emission image. Even though we first dithered the images for a given filter and then changed filters, this method yielded better results. This is because the pointing of the *HST* is very accurate, and therefore after changing filter, the telescope goes back to the initial point of the dither sequence with a precision of less than one tenth of a pixel. The method described here would produce even better results for those cases in which for a given position both the continuum and the continuum+line images were taken before moving the telescope to the next position.

Finally we would like to point out that we performed a straight subtraction using the continuum at 1.64 μm, i.e., the continuum has not been converted to 1.66 μm, wave-

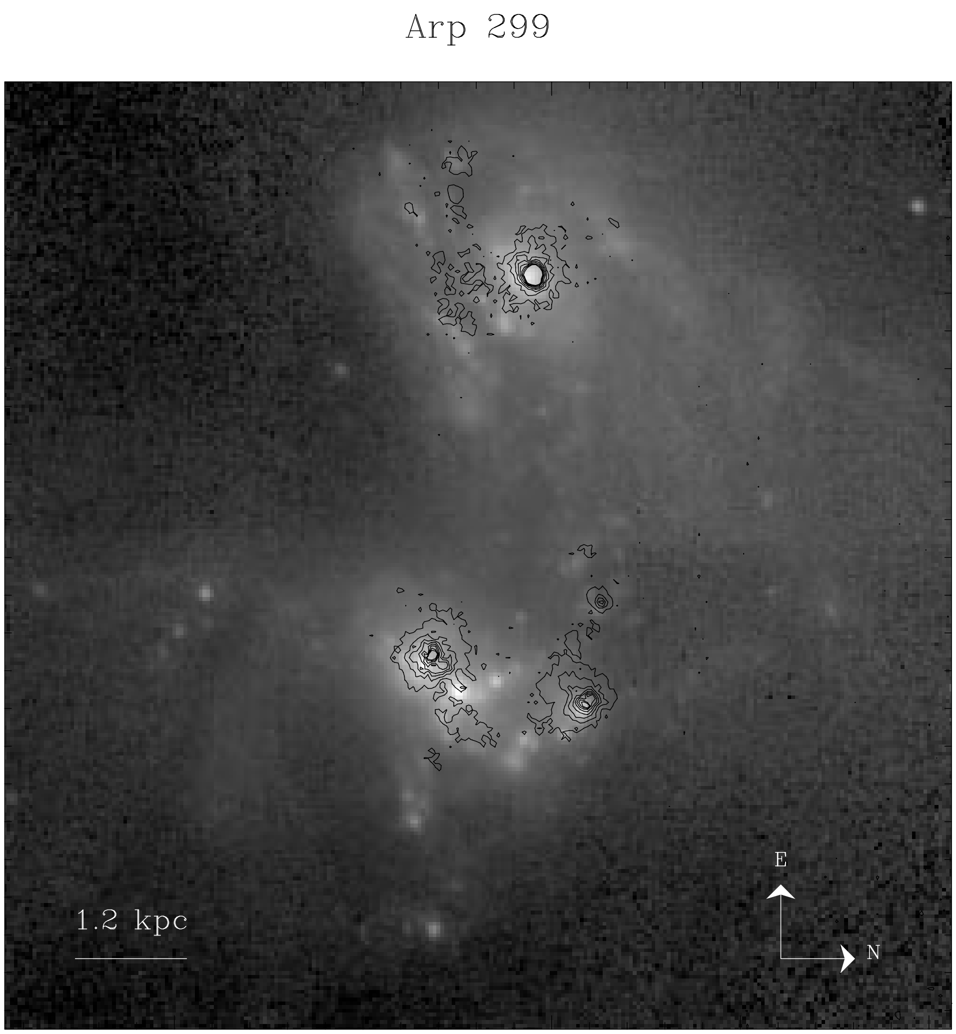

Figure 3. The grey-scale map is the F164N continuum image on a logarithmic scale. The contours are the continuum-subtracted [Fe II]1.64 μm emission on a linear scale. The field of view is the same as in Figure 1.

length of the underlying continuum of the [Fe II] line in Arp 299. For sources in which obscuration is patchy or/and very high, a better approach would be to fit the continuum between two different wavelengths, and construct an image in which the continuum has been interpolated to the line wavelength.

3. Morphology of the [Fe II] emission

In Figure 1 we show a contour plot of the interacting galaxy Arp 299 through the NIC3 F164N filter which contains the continuum adjacent to the [Fe II]1.644 μm emission line. Figure 2 is a grey scale map of the [Fe II]1.644 μm line emission (continuum-subtracted NIC3 F166N filter), and in Figure 3 we overlay the line emission contours on the grey scale map of the continuum emission (NIC3 F164N) for clarity.

The NIC3 F164N continuum image (Figure 1) of the system clearly shows not only the emission from the brightest sources (i.e., A, B1, B2, C and C') already known from ground-based images, but also reveals the spiral nature of IC 694 with a number of H II regions along the spiral arms, along with some compact sources in NGC 3690 surrounding B1, B2, and located south-west of C. In the large scales (better seen in Figure 3) Arp 299 shows the characteristic tidal tails common to interacting pairs extending south and west of NGC 3690.

Most of the [Fe II]1.644 μm line emission (Figure 2) originates from three regions, that is, source A (nucleus of IC 694), B1 in NGC 3690 and C+C' at the interface of both galaxies. These three regions are not compact but quite extended with linear projected sizes of about 1 kpc. In addition sources B1 and C show structure. It is remarkable that very little or no emission seems to be coming from source B2 (the brightest source at visible wavelengths). The same result was found by Fisher, Smith & Glaccum (1991) from their ground-based Brγ images. In addition to the emission from the bright sources the [Fe II] image traces the emission from H II regions located in the spiral arms south-east of IC 694. There is a number of H II regions northwest of B1, and east of C extending all the way to source C', and east of C. The resemblance in morphology with the our NIC2 Paα ($\lambda_{\rm rest} = 1.875\,\mu$m) images (not shown here, see Alonso-Herrero et al. 1998) is remarkable, although some differences are found. The [Fe II] emission is more extended in A, B1 and C than the Paα emission. If most of the [Fe II] emission is excited by shocks in supernova remnants (SNR) in the star-forming regions, then it is expected that the [Fe II] emission would be more extended as the shocks propagate outwards the H II regions, whereas the Paα emission will tend to be more concentrated toward the center where the young ionizing stars are located. The [Fe II]1.644 μm to Paα line ratio is found to vary radially within the star-forming regions, increasing by at least a factor of five for increasing radial distances. In addition, age effects will also contribute to differing line ratios (see next section). In contrast the H_2 morphology of Arp 299 is quite different with point-like emission originating from B1 and C in NGC 3690, whereas the nucleus of IC 694 is very bright in H_2 and shows some diffuse emission with a beautiful butterfly-like shape (see Alonso-Herrero et al. 1998). The lack of resemblance between the [Fe II] and the H_2 emission suggests that the scenario in which both emissions have a common origin may not be that simple, perhaps indicating that the nature of the shocks producing both emissions is different.

4. Discussion

We have measured both the [Fe II]1.644 μm and Paα line fluxes from five different regions in the interacting system through a 1 arcsec-diameter aperture ($\simeq 200$ pc for the assumed distance) to try to isolate the star-forming regions as much as possible. The Brγ fluxes were computed by assuming $f(\mathrm{Br}\gamma)/f(\mathrm{Pa}\alpha) = 0.082$ for easy comparison with values of f([Fe II]1.644 μm)/$f(\mathrm{Br}\gamma)$ usually reported in the literature. Results are given in Table 1, where the f([Fe II]1.644 μm)/$f(\mathrm{Br}\gamma)$ ratios have not been corrected for extinction (see below). By H II we refer to the H II regions located north-west of B1.

So far we have not discussed the effects of extinction. From the optical and near-infrared spectroscopy obtained for all the bright sources in the system, we have estimated the extinction using hydrogen recombination line ratios. However, the values of the extinction to the gas are quite dependent on the wavelength of the lines involved, the highest values obtained when using the $f(\mathrm{Br}\gamma)/f(\mathrm{Pa}\alpha)$ line ratio (indicating that some of the hydrogen lines may be still optically thick in the near-infrared). The observed f([Fe II]1.644 μm)/$f(\mathrm{Pa}\alpha)$ line ratios have to be corrected for extinction by a factor (assuming a simple model of foreground dust screen): $10^{0.4\times0.04\times A_V}$ where the term 0.04 accounts for the differential extinction between 1.6 μm and 1.9 μm. Note that we analytically fit the extinction curve of Rieke & Lebofsky (1985) for near-infrared wavelengths. The values of the extinction derived for the bright components are between $A_V = 10$ mag and at least $A_V = 17$ mag (assuming a foreground dust screen model).

Table 1. [Fe II]1.644 μm line fluxes, [Fe II]1.644 μm to Brγ line ratios and supernova rates for different components in Arp 299.

Component	f([Fe II]) (erg cm^{-2} s^{-1})	f[Fe II]/f(Brγ)	(SNr) (yr^{-1})
A	1.58×10^{-14}	1.08	0.13 – 1.86
B1	8.45×10^{-15}	1.33	0.11 – 0.53
C	6.35×10^{-15}	0.56	0.091 – 0.95
C'	2.21×10^{-15}	0.58	0.020 – 0.21
H II	6.35×10^{-16}	0.59	3×10^{-3}

Note. — Fluxes and line ratios for circular 1 arcsec-diameter apertures. The supernova rates correspond to 4 arcsec-diameter apertures for A, B1, C and C'.

In Alonso-Herrero et al. (1997) we showed that the f([Fe II]1.644 μm)/$f(\mathrm{Br}\gamma)$ line ratio in starburst galaxies is understood as transition from pure H II region (such as the Orion Nebula) to an increasing rôle of shock excitation by supernova remnants. The extinction-corrected values of this ratio are well apart from the typical value for pure ionization for all the sources indicating that an important fraction of the [Fe II] emission is produced by supernova remnants. Moreover, as the starburst ages the f([Fe II]1.644 μm)/$f(\mathrm{Br}\gamma)$ ratio will increase as the number of SNR grows and the ionization from very young stars decreases, making this line ratio a good age indicator. From the predictions of the models presented in Vanzi, Alonso-Herrero & Rieke (1998) we can estimate that the relative difference in ages between the bursts in both components A and B1, and components C and C' is approximately 3 million years assuming a Gaussian burst with FWMH = 1 Myr. From these models we derive an age (measured from the peak of star-formation) as young as 4 Myr for components C and C' in NGC 3690, indicating that the most recent star-formation is occurring at the interface of the two galaxies. A more detailed discussion of the star-forming properties of this system will be presented in Alonso-Herrero et al. (1998).

Finally the total [Fe II]1.644 μm fluxes can used to derive the supernova rate (SNr) using the calibration for M82 derived in Vanzi & Rieke (1996). For the (SNr) we measure the [Fe II]1.644 μm fluxes through a 4 arcsec-diameter aperture, except for the H II regions north-west of B1 for which we use the flux through the 1 arcsec-diameter aperture. The values of the supernova rate are presented in the last column of Table 1. The two values correspond to the supernova rates obtained from the [Fe II]1.644 μm fluxes not-corrected and corrected for extinction. Gehrz et al. (1983) estimated the supernova rate from their 20 cm radio measurements with a 5 arcsec beam. Their values are 4.2, 2.5, 1.9 and 0.9 yr^{-1} for components A, B1+B2, C and C'. Taking into account the uncertainty in the calibration for M82 for the (SNr) in terms of the [Fe II]1.644 μm flux (a factor of 2, Vanzi & Rieke 1996), the agreement between the two independent estimates is quite good for components A and C. The largest discrepancy occurs for B1. Given the fact that source B2 shows no [Fe II] emission it is possible that the radio emission from B2 is not related to SNR, but still included in Gehrz et al. (1983) calculations.

5. Conclusions

We have presented *HST*/NICMOS observations of the interacting system Arp 299 (IC 694 + NGC 3690). A detailed description of the reduction and analysis of narrow-band filters images taken with camera 3 (F164N and F166N) is given, demonstrating that although the NIC3 images were not taken during the NIC3 observing campaign, they are most suitable for science.

Most of the [Fe II]1.644 μm line emission is found to be originating from three bright sources, A (nucleus of IC 694) and B1 and C+C' in NGC 3690. Little or no emission is coming from B2 (the brightest source at visible wavelengths). The resemblance between the [Fe II]1.644 μm and Paα emission is remarkable, although the [Fe II]1.644 μm emission is extended to larger scales. The [Fe II]1.644 μm to Paα line ratio is a good age indicator, since as the starburst ages the number of SNR grows whereas the flux from young ionizing stars decreases. We find that the region C+C' at the interface of the two galaxies is undergoing the youngest star-formation process. Finally the [Fe II]1.644 μm fluxes are used to compute the supernova rate for each component.

Acknowledgments. During the course of this work AA-H was supported by the National Aeronautics and Space Administration on grant NAG 5-3042 through the University of Arizona. The work was also partially supported by the National Science Foundation under grant AST-95-29190.

References

Alonso-Herrero, A., Rieke, M. J., Rieke, G. H., & Ruiz, M. 1997, ApJ, 482, 747

Alonso-Herrero, A., Rieke, M. J., & Rieke, G. H. 1998, ApJ, in preparation

Barnes, J. E., & Hernquist, L. 1996, ApJ, 471, 115

Fischer, J., Smith, H. A., & Glaccum, W. 1991, in ASP Conf. Ser. Vol. 14 (San Francisco: ASP), p63

Gehrz, R. D., Sramek, R. A., & Weedman, D. W. 1983, ApJ, 267, 551

McLeod, B. 1997 in HST Calibration Workshop, ed. S. Casertano et al.

Sanders, D. B. et al. 1988, ApJ, 325, 74

Sanders, D. B., Mirabel, I. F. 1996, ARA&A, 34, 749
Sargent, A., & Scoville, N. 1991, ApJ, 366, L1
Rieke, G. H., & Low, F. J. 1972, ApJ, 176, L95
Rieke, G. H., & Lebofsky, M. J. 1985, ApJ, 288, 618
Vanzi, L., & Rieke, G. H. 1996, ApJ, 479, 694
Vanzi, L., Alonso-Herrero, A., & Rieke, G. H. 1998, ApJ, 503 (in press)
Wynn-Williams, C. G. et al. 1991, ApJ, 377, 426

NICMOS and the VLT
Pula, Sardinia, May 26-27th 1998
Wolfram Freudling and Richard Hook, eds.

NICMOS Camera 3 Parallel Imaging Observations: Number Counts, Sizes and Red Objects

P. McCarthy, L. Yan, L. Storrie-Lombardi, and R. J. Weymann

Carnegie Observatories, 813 Santa Barbara St.
Pasadena, CA, 91101 Email: pmc2@ociw.edu

Abstract.
We present results from our analysis of F160W images obtained with NICMOS Camera 3 operating in the parallel mode. Despite the less than optimal focus, we achieve depths that are very close to the nominal performance. With exposure times of 2,000 to 13,000 seconds we reach 3σ depths of H$= 24.3-25.5$. We derive the galaxy number counts in an area of roughly 9 square arc-minutes. The slope of the counts fainter than H $=$ 20 is 0.31, and the integrated surface density to H$\leq$ 24.75 is 4×10^5 galaxies per square degree. We transform the deepest K-band counts to our system and find good agreement. At H = 24.5 the observed surface density is roughly twice that predicted by non-evolving models. The half-light radii of the galaxies declines steeply with apparent magnitude and reaches our resolution limit of $0.''20$ at H = 23.5. Deep ground-based VRI imaging of one NICMOS field has revealed a very red galaxy with H = 18.8 and R - H $=$ 6.

1. Introduction

One of the key results to come from deep WFPC2 imaging was the realization that galaxies have very sub-arcsecond angular sizes at faint apparent magnitudes (e.g. Griffiths et al. 1994). The small sizes and, consequently high surface brightnesses, make space-based observations of faint galaxies, even with the relatively small aperture of HST, equally or more sensitive than similar observations with large collecting areas on the ground.

The large reduction in background achieved at wavelengths of 0.8 to 1.9μ and it's high angular resolution make NICMOS a very fast imaging device in the broad-band 1μ and 1.6μ filters. In the minimum background bandpass, F160W, the on-orbit background is more than 7 magnitudes fainter than what is typically achieved on the ground. NICMOS faces two challenges in surveying the population of faint field galaxies: its small field of view and finite lifetime. Observations made in parallel with one of the other science instruments offer a means of surveying significant areas at faint magnitudes while maximizing the use of the limited on-board cryogen.

The simplest analysis of deep imaging observations is the number magnitude relation. Galaxy counts as a function of apparent magnitude probe both the geometry of the Universe and the dynamical and luminosity evolution of galaxies. Evolutionary effects dominate the departures of the counts from the Euclidean expectation. The near-IR pass-bands, however, are particularly well suited to galaxy count studies as they are only mildly sensitive to extinction and uncertainties in the K-correction.

2. Observations

2.1. NICMOS Imaging

The deformations of the NICMOS internal optical configuration resulted in poor images in camera 3 for much of 1997. As a result the parallel observations that were carried out before November 1997 were done with cameras 1 and 2. These cameras have small fields of view and their small pixel sizes lead to significant contributions from read noise. Teplitz et al. (1998) and Corbin (these proceedings) describe early results from examinations of these data. We have concentrated on the images obtained with Camera 3 after the movement of the field offset mirror to removed the vignetting associated with distortions of the optical bench. With the pupil adjustment mirror set to its extreme position camera 3 now yields images that are quite close to the performance achieved with a refocusing of the HST secondary mirror. Each camera 3 image covers 3/4 of one square arc-minute with pixels that are $0.''2$ on a side. The FWHM that we realize from our dithered nominal focus images is $0.''25$.

We have reduced the deepest F160W parallel images obtained in the period from November 1997 to January 1998. The approach that we have taken to the processing of the multiaccums data is independent of the STScI pipeline and relies heavily on McLeod's NICREDv1.5 package (McLeod 1997). We formed observed sky+dark frames for each read in the multiaccums sequence by computing the median of all of the independent high galactic latitude fields available at that time. These median sky+dark images were subtracted from each read and each pixel was then corrected for nonlinearities and cosmic ray events. The individual linearized and cleaned images were then corrected for the flat field response, block replicated to a 2×2 finer scale, shifted by integer ($0.''1$) pixel shifts and combined with a final 3-σ cosmic ray rejection applied. The deepest of our camera 3 parallel images reaches a 1σ surface brightness limit of 26 H magnitudes per square arcsecond. The 3σ point-source detection limits for our fields range from H = 24.3 to 25.5

2.2. Ground-based Optical Imaging

We have obtained optical follow-up imaging of several of our fields using the 2.5m du Pont telescope at the Las Campanas Observatory. The observations were made using a SITE 2048×2048 CCD, Johnson V & R filters and a Cousin's I filter. The pixel scale of the SITE CCD at the Cassegrain focus of the 2.5m is $0.''278$. The observations were made in February of 1998 and the seeing ranged from $0.''6$ – $0.''8$ FWHM. The exposure times were typically 6000 seconds in each filter, although one field, 0457-0456 was only observed for 3600 seconds in R. The telescope was offset several tens of arc seconds between each exposure and standard techniques were used to calibrate and reduce the images. These images allow us to to determine colors of objects in the NICMOS images with a factor of 3 range in wavelength.

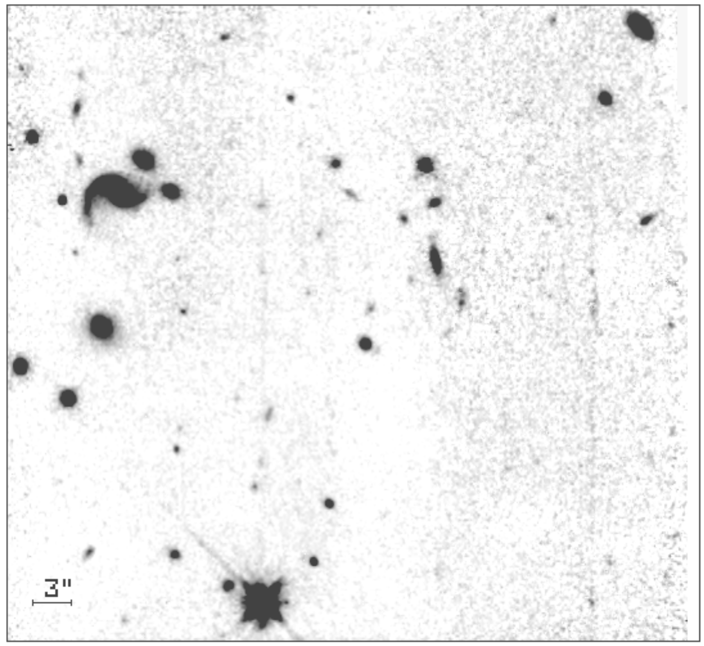

Figure 1. A NICMOS Camera 3 F160W parallel field. The field shown is $52'' \times 50''$

3. Results and Discussion

In Figure 1 we show a typical image from the parallel program. It contains 4500 seconds of integration in two dither positions and reaches a 1σ surface brightness limit of $H = 25.7$. Our deepest field to date, 1120+1300 is shown in Yan et al. (1998) and has an additional 0.5 magnitudes of depth. We carried out the object detection and photometry with SExtractor version 1.2b10b (Bertin & Arnout 1996) using a photometric zero point for camera3/F160W provided by M. Rieke (priv. comm). The uncertainty in the zero-point is roughly 5%. The object detection was performed with a gaussian kernel with FWHM $= 0.3''$ and a 2.0σ detection threshold. The softer images delivered by camera 3 at the nominal telescope focus actually improve the reliability of the object detection algorithm and the photometric precision for small objects, at the cost of some loss of sensitivity. The isophotal magnitudes were measured to an isophotal level equal to 1σ above the global sky noise.

We define the total magnitude in a manner similar to those used by Smail et al. (1995) and Djorgovski et al. (1995). The philosophy is to measure isophotal magnitudes where possible and to correct these to $2''$ aperture magnitudes using an aperture correction that is a function of the isophotal magnitude. For the faintest and smallest objects the isophotal sizes are smaller than the $0.''6$ primary photometry aperture and

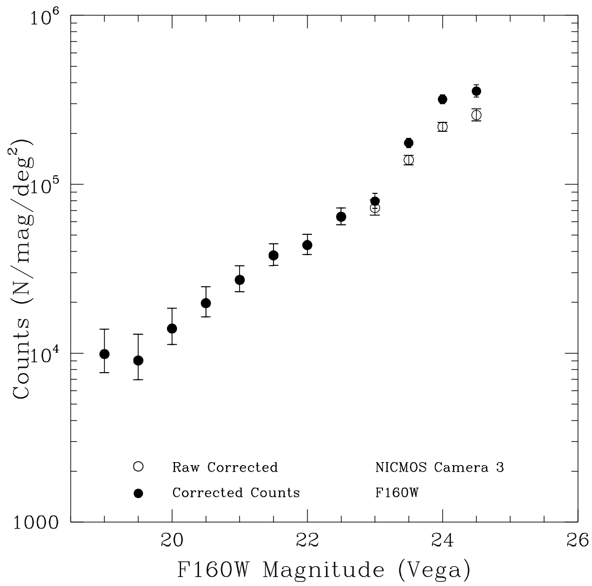

Figure 2. Raw and corrected galaxy counts. The raw counts are shown as open symbols, the corrected counts as filled. The error bars are derived from the variance within each bin averaged over all fields.

isophotal magnitudes are subject to large uncertainties. For these objects we apply an aperture correction to convert the $0.''6$ magnitudes to a $2''$ aperture. The magnitude of this correction was determined from the average profile of 20 faint galaxies and was found to be indistinguishable from that derived from stars with H$\sim$ 18. The details of the aperture correction for galaxies with isophotal sizes larger than $0.''6$ are given in Yan et al. (1998).

3.1. Incompleteness Modeling

The principal sources of systematic error in deriving galaxy number counts are the aperture correction and the incompleteness and false detection corrections. The aperture corrections, described above, where chosen to be robust in the face of low signal-to-noise ratio and under-sampled data. More sophisticate approaches are possible (e.g. Petrosian 1998) but generally require high quality data. The completeness determination, however, must be tailored to the specific data set. In our data we suffer from low spatial frequency errors in the dark+bias corrections that impact the detection efficiency locally. This source of uncertainty operates in addition to the effects of crowding and Poisson noise. Yan et al. (1998) carried out an extensive series of simulations to quantify the incompleteness effects. We adopt a 50% completeness level as our cutoff and the simulations show that this corresponds to depths of H$=$ 23.8 to 24.8 for our chosen fields. As described in Yan et al. the rate of false detections is of the order of 5%.

In Figure 2 we plot our raw and corrected galaxy counts. The error bars represent the statistical uncertainty in each magnitude bin, averaged over all the fields that contribute to that bin. The slope of the differential counts is 0.31 ± 0.02. This slope is

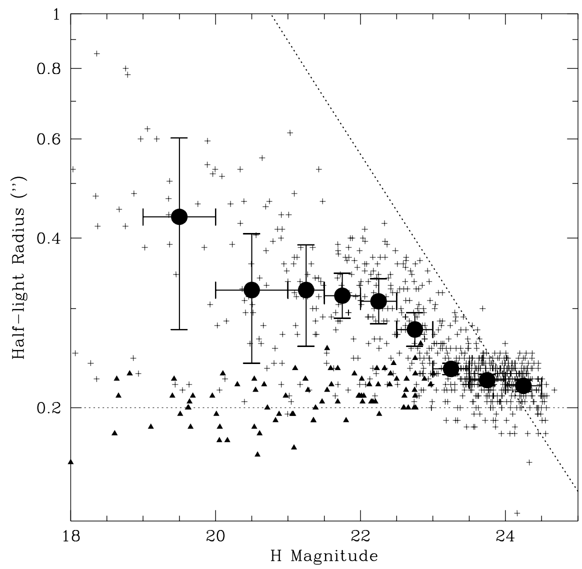

Figure 3. The derived half-light radii for all of the detected objects in 12 high latitude fields, plotted as crosses. The median sizes are plotted with heavy filled symbols, the locus of stellar points are shown as filled triangles.

quite close to the observed slope in the K-band counts for K$>$ 18 (Gardner et al. 1993; Djorgovski et al. 1995; Moustakas et al. 1997).

3.2. Object Sizes

We characterize the size of the detected objects in terms of their half-light radii. The image of each object was extracted and regrided with 10$\times$ finer sampling. The enclosed flux was then computed in half pixel steps until 50% of the total flux was enclosed, the total flux being derived from the total magnitude as described above. We used the same algorithm as that used by Smail et al. (1995). In Figure 3 we plot the derived half-light radii for all of the objects detected in 12 high galactic latitude fields. We also plot the median size in one or half magnitude bins. The filled triangles are the results of the same analysis applied to a globular cluster field over the magnitude range $16 < H < 23$.

4. Implications of the Galaxy Counts

Because the near-IR counts are, in comparison to the visible-band counts, less sensitive to uncertainties in the K- and evolutionary corrections they have attracted considerable attention in recent years. There have been suggestions that the K-band counts can be used to discriminate between various world models (e.g. large or small q_o, zero or non-zero Λ_o) as well as some well considered cautions to such goals (e.g. Djorgovski et al. 1995). Nevertheless, it is fair to say that until recently no clear evidence of departure from non-evolving models had been seen in the K-band counts (e.g. Metcalf et al. 1995). Recently Bershady et al. (1998) presented evidence for significant excesses

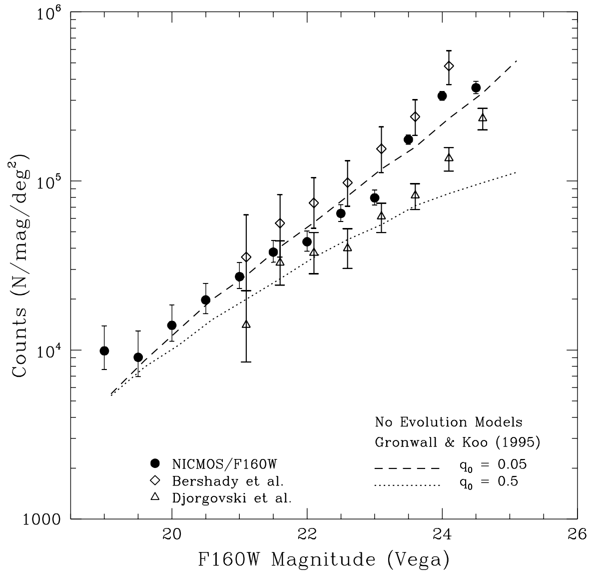

Figure 4. NICMOS F160W counts compared to Keck K counts and models. The K-band counts are from Bershady et al. and Djorgovski et al. and have been transformed to F160W by applying F160W = K + 1.1. The curves are non-evolving models from Gronwall & Koo (1995) transformed to F160W as above.

over the Gronwall & Koo (1995) no evolution models for K magnitudes fainter than ~ 23.

We would like to be able to directly compare our F160W counts to those observed at K. To do this we use the transformation given by Gardner (1998). In the magnitude range of interest this transformation is well approximated by a simple offset of 1.1 magnitudes. In Figure 4 we plot our counts along with those of Bershady et al. (1998), Djorgovski et al. (1995), and the Gronwall & Koo (1995) models, with the latter data sets transformed to F160W as described above. Our counts fall midway between the Bershady et al. and Djorgovski et al. counts.

The counts shown in Figure 4 show a departure from the low density zero Λ_o no-evolution model of Gronwall & Koo. Averaging our counts with Bershady's yields a factor of 2 excess over no evolution at $H = 24$. The run of half-light radii versus magnitude displayed in Figure 3 shows that this excess of counts is dominated by objects with angular sizes $< 0.''25$. As our detection efficiency at faint magnitudes is clearly impacted by our surface brightness limits, our number counts at these magnitudes should be treated as lower limits. Like Bershady et al.'s K-band counts, our F160W counts are systematically higher than the counts reported by Djorgovski et al. (1995), after allowing for the transformation from K to F160W. Bershady et al. attribute this discrepancy to differing approaches to the aperture corrections. Our methodology in deriving and applying the aperture corrections is very similar to that used by Djorgovski et al., the primary difference being that our primary measurement aperture size, $0.''6$ is larger, in terms of the instrumental response FWHM, than that used by Djorgovski et al.. The differences in the various counts may reflect field-to-field variations rather than differences in the photometry. In all but the last magnitude bin ($24.25 < H < 24.75$) our measurements cover an area 6× larger than that covered in either the Bershady et al. or Djorgovski et al. studies. The slopes derived from all three programs are in close agreement.

5. Extremely Red Objects

Near-IR images of high latitude fields by a number of groups have revealed a population of objects with colors that are as red or redder than evolved extinction-free stellar populations at plausible redshifts (e.g. McCarthy, Persson, & West 1992; Hu & Ridgway 1994 etc.). These Extremely Red Objects (EROs) begin to appear at K magnitudes of approximately 17 (see Ellis 1997, Figure 5b) and are usually defined by R - K > 6, although some authors use a more strict criterion. The nature of these objects remains unclear at this time. Hu & Ridgway argued that they were $\sim 10L_*$ ellipticals at $z \sim 2$ on the basis of their spectral energy distributions. Graham & Dey (1996) obtained a redshift for one of the red Hu & Ridgway objects and argued that it was a dusty star-forming object. The recent sub-mm detection of this object by Cimatti et al. (1998) strongly supports the starburst model for this particular object. NICMOS offers the potential for high resolution imaging of such objects. The difficulty is that in the absence of pointed observations one must cover substantial area to detect such objects. Our ground-based visible-light imaging of the NICMOS parallel fields has revealed one such object and a small number of similar objects are within the camera 2 or camera 3 images of distant radio galaxies and quasars. In Figure 5 we show a set of 4 images of a sub-portion of the field shown in Figure 1. The ERO is clearly visible and is well resolved. With an H-band magnitude of 18.8 it is well detected and its morphology is fairly concentrated, in contrast to the distorted morphology reported for HR10 by Graham & Dey. The spectral energy distribution of this object can be fit with a dust-free galaxy model, but it requires both a large redshift and age. Similar objects in the radio galaxy fields can be fit with less extreme models and these may well represent a population of $z > 1$ ellipticals with old stellar populations.

6. Summary

We have analyzed a modest fraction of the NICMOS camera 3 imaging parallels. These data offer a unique combination of depth and resolution at wavelengths that were heretofore unavailable from space. These low-cost low-impact images already probe as deep or deeper than the deepest K-band images obtained with large apertures on the ground. We have shown that the galaxy counts continue with a slope of 0.31 to H$\sim$ 25 and that there is a likely excess of counts above non-evolving models. This excess is dominated by objects with small angular sizes. Ground-based followup imaging has revealed a number of extremely red objects and has provided our first high-resolution images of the ERO population at wavelengths beyond 1μ.

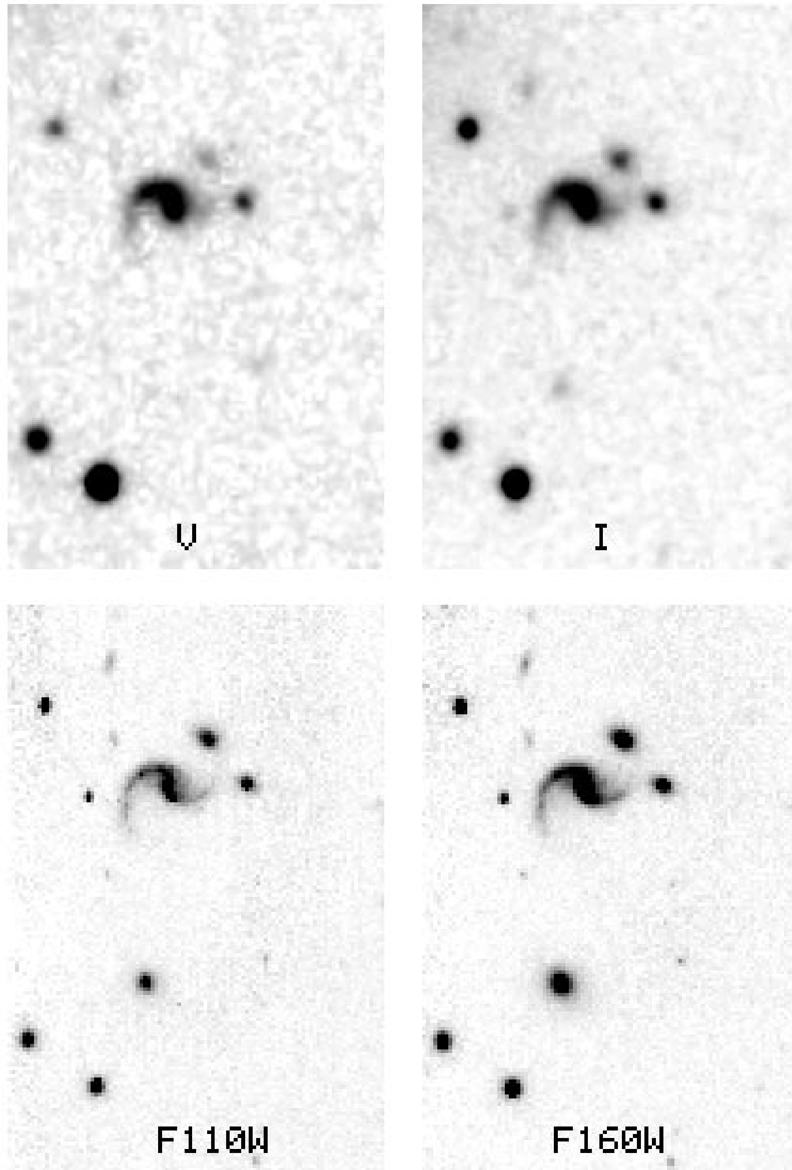

Figure 5. V,I, F110W, & F160W images of a portion of the field shown in Figure 1. Each image is $20'' \times 30''$ in size. The very red object near the center has H = 18.8.

7. Acknowledgments

We thank the staff of the Space Telescope Science Institute, and J. Mackenty in particular, for their efforts in making this parallel program possible. We acknowledge useful discussions with J. Gardner, H. Teplitz, R. Thompson, & M. Rieke. B. McLeod and I. Smail are thanked for generously allowing the use of their software for the data reduction and scale length measurements. This research was supported, in part, by grants from the Space Telescope Science Institute, GO-7498.01-96A and P423101.

References

Bershady, M., Koo, D. C., & Lowenthal, J. 1998, ApJ, in press

Bertin, E., & Arnouts, S. 1996, A&AS, 117, 393

Cimatti, A., Andreani, P., Rottgering, H., & Tilanus, R. 1998, Nature, 392, 895

Djorgovski, S., et al. ApJ, 438, L13

Ellis, R. 1997, ARA&A, 35, 389

Gardner, J. P. 1998, PASP, 110, 291

Gardner, J.P., Cowie, L.L., & Wainscoat, R.J. 1993, ApJ, 415, 9

Graham, J. R., & Dey, A. 1996, ApJ, 471, 720

Griffiths, R. et al. 1994, ApJ, 435, L19

Gronwall, C., & Koo, D. C. 1995, ApJ, 440, L1

Hu, E., & Ridgway, S. E. 1994, AJ, 107, 1303

McCarthy, P. J., Persson, S. E., & West, S. 1992, ApJ, 386, 52

McLeod, B. 1997, proceedings of the 1997 HST Calibration Workshop, eds. S. Casertano, R. Jedrzejewski, C. D., Keyes, & M. Stevens (STScI), 281

Metcalf, N., Shanks, T., Campos, A., Fong, R. & Gardner, J. P. 1995, Nature, 383, 236

Moustakas, L. A. , Davis, M. , Graham, J. R. , Silk, J. , Peterson, B. , Yoshii, Y. 1997, ApJ, 475, 445

Petrosian, V. 1998, ApJ, submitted

Smail I., Hogg D.W., Yan L. & Cohen, J.G. 1995, ApJ, 449, L105

Teplitz, H. Gardner, J. P., & Heap, S. 1998, ApJ, submitted

Yan, L., McCarthy, P. J., Storrie-Lombardi, L. J., & Weymann, R. J. 1998, ApJ, in press

NICMOS and the VLT
Pula, Sardinia, May 26-27th 1998
Wolfram Freudling and Richard Hook, eds.

The Structure and Composition of High Redshift Radio Galaxies

R. A. E. Fosbury[1]

ST-ECF, Garching bei München, Germany, (rfosbury@eso.org)

J. Vernet

ESO, Garching bei München, Germany

M. Villar-Martín

Department of Physics & Astronomy, University of Sheffield, UK

M. H. Cohen

Astronomy Department, California Institute of Technology, Pasadena, USA

A. Cimatti, S. di Serego Alighieri

Osservatorio Astrofisico di Arcetri, Firenze, Italy

P. J. McCarthy

The Observatories of the Carnegie Institution, Pasadena, USA

Abstract. Keck spectropolarimetry, giving spectral coverage from Ly-α to beyond CIII], and HST imaging of a sample of powerful radio galaxies with $z \sim 2.5$ has been obtained. These data are giving us a clear picture of the nature of the 'alignment effect' and are revealing new correlations between polarization and emission line ratios which may be interpreted in the context of the stellar evolutionary histories of these massive galaxies. In particular, we see the 2200Å dust absorption feature in the radio galaxy continua and a large variation in the NV/CIV line ratio amongst objects having a similar ionization level. VLT infrared spectroscopy of this and similar samples will give us a view of a period of galaxy history during which rapid chemical evolution was taking place.

1. Introduction

This is a short progress report on a rather extensive programme we are carrying out to study the structure and composition of high redshift radio galaxies (HzRG) — and, by implication, the host galaxies of radio quasars — using observations in the optical, IR and mm bands. A separation of the stellar and the AGN-related components is

[1] Affiliated to the Astrophysics Division, Space Science Department, European Space Agency

made using a combination of Keck spectropolarimetry and high resolution WFPC 2 imaging in the rest-frame UV (below the 4000Å break), NICMOS imaging in the rest-frame optical, and photometric measurements of cool dust thermal emission at longer wavelengths. The relevance to this meeting is the use of NICMOS to image the evolved stellar population in these galaxies (see the following talk by McCarthy) during the epoch when powerful AGN were most common. In addition, we plan to use VLT (ISAAC) IR-spectroscopy to measure the rest-frame optical emission line spectrum, allowing us to perform the kind of detailed ionization/composition analysis which has already been carried out on local objects.

2. The Sample

We have selected RG with $z \sim 2.5$ which allow us to study the strong UV emission lines from Ly-α to CIII], the UV continuum, resonance absorption lines and the 2200Å dust feature in the optical band and to straddle the 4000Å break in the 1–2$m\mu$ region.

Our principal sample consists of eight objects (six of which have already been analysed) with $2.3 < z < 2.9$ and this is supplemented by three sources from the literature having similar quality data but extending the redshift range to $1.8 < z < 3.8$. More data are currently being obtained on sources with $z > 3$.

3. Observations

The Keck spectropolarimetric observations for the first two sources in the programme are described in Cimatti et al. (1998). Four more sources have been observed and reduced and three further objects were observed during the period of this Workshop. An example of the spectropolarimetry is shown in Figure 1. The HST WFPC 2 and NICMOS images, where available, were taken from the public archive at the ST-ECF and from the McCarthy et al. program (ID 7498). An example of the NICMOS and WFPC 2 imaging is shown in Figure 2. Some deep groundbased imaging data have been taken from the literature to complement the higher resolution but shallower HST images.

4. Principal Results

Here we summarise the principal results to date. These will be described more fully in papers in preparation.

- All sources show a strong 'alignment effect' between their UV and radio morphologies although the structures are complex. One case, 4C 23.56 (Knopp & Chambers 1997), shows a beautiful 'ionization cone' in Ly-α. The brightest UV emission is extended and does not necessarily coincide with the nucleus (radio core).

- The continuum colours are remarkably similar to one another and can be fitted by a power law absorbed by a standard Galactic (in the RG rest-frame) extinction law with $E_{B-V} \sim 0.1$, which corresponds to $\tau \sim 1$ at 1500Å. Example fits to three of the sources are shown in Figure 3.

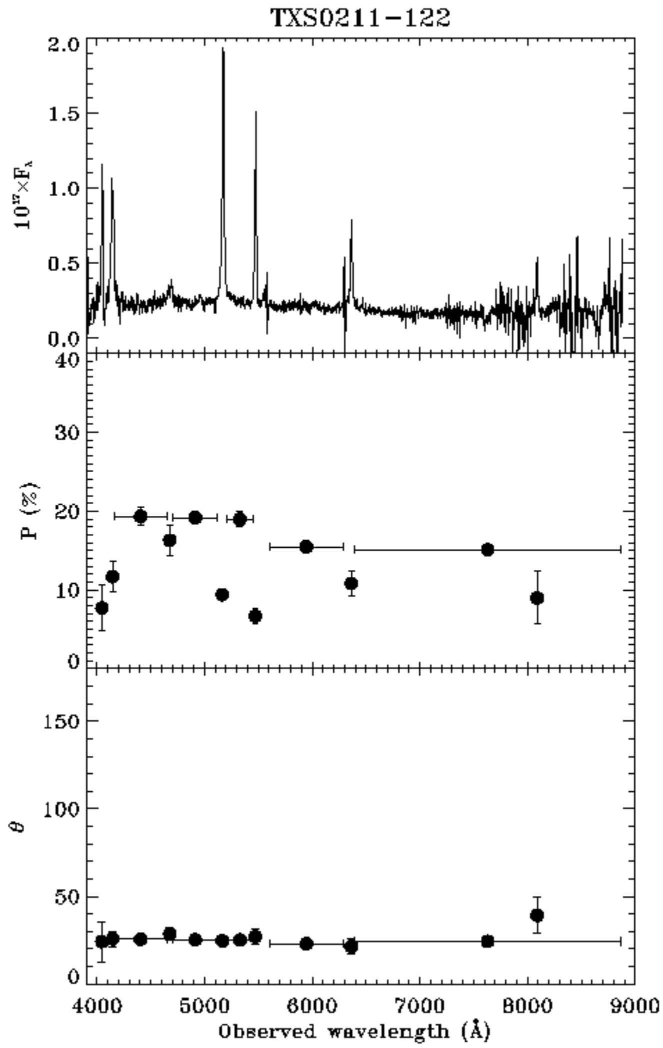

Figure 1. A Keck II, LRISp spectropolarimetric observation of the radio galaxy TXS 0211-122. The three panels show respectively the total flux (in 10^{-17} erg cm^{-2} s^{-1} Å^{-1}), the fractional polarization in continuum (wide horizontal bars) and line bands and the position angle of the E-vector. The strong emission lines are, from short wavelengths, Ly-α, NV, CIV, HeII and CIII].

- Interstellar absorption lines are seen and, in some objects, there is evidence for wind and photospheric absorption lines from hot stars. Several sources show complex, spatially extended absorption structures at Ly-α (see also van Ojik et al., 1997).

- The emission lines are spatially extended (up to $\sim$ 20 arcsec or $\sim$ 150 kpc for Ly-α) and show complex kinematic structures extending over $\pm$2000 km s^{-1}.

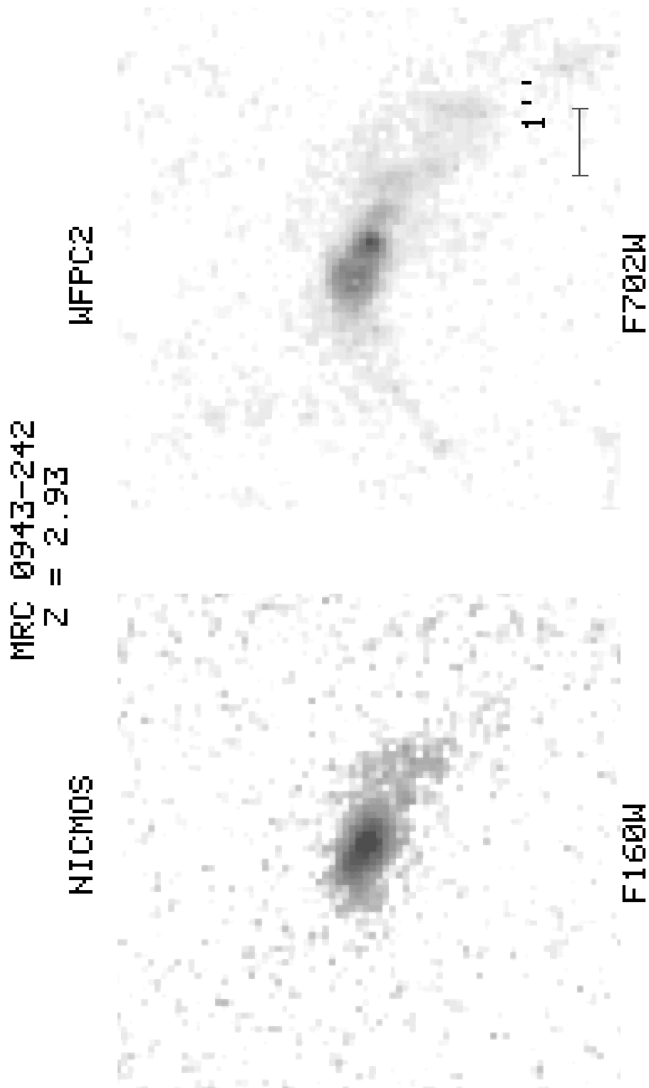

Figure 2. Images from NICMOS/F160W and WFPC 2/F702W of the $z = 2.93$ radio galaxy MRC 0943-242 represented at the same scale. This object has an aligned component which still dominates in the H-band. Although bluer than the underlying galaxy, the aligned light is somewhat redder than usual in these objects although the range in UV colours is small (see text). There is a prominent Ly-α absorption component.

- The continuum linear polarization, measured just longward of Ly-α/NV, ranges from $< 3\%$ to $\sim 20\%$. The E-vector is perpendicular to the UV extension as seen at HST resolution (but not necessarily precisely to the radio axis).

- The emission line spectra indicate a rather constant level of ionization with a small range in the observed CIII]/CIV and HeII/CIV line ratios.

- Amongst the spatially integrated properties, the strongest correlations, shown in Figure 4, are observed to be:

  1. between continuum polarization, P, and the Ly-α/CIV emission line ratio (anticorrelation)
  2. between P and the NV/CIV ratio

5. Discussion

The conclusions we are drawing from these studies can be summarised as follows:

- Powerful radio galaxies contain (hidden) QSO nuclei whose EUV emission ionizes the extended gas along the radio axis and whose FUV emission we see scattered by extended dust structures.

- The scattered component can — but does not always — dominate the observed UV continuum and there is evidence for an unpolarized hot stellar component in addition to a nebular continuum contribution from the emission line gas. The presence of an old, red stellar population becomes apparent above the 4000Å break, although this does not always dominate the observed flux in the infrared bands.

- There is a direct connection between the scattering mechanism (which produces the polarization) and the destruction of Ly-α photons. This could simply result from the abundance and spatial distribution of dust, although orientation effects may be important as well.

- The continuum exhibits dust extinction signatures in the form of the 2200Å dip and a peak at the position of the extinction minimum around 1400Å. Some of the extinction may arise in an extended halo outside the regions which see the QSO radiation field directly. This would be consistent with the absence of the 2000Å dip in radio quasars.

- There appears to be strong connection between the dominance of scattered light (dust abundance and/or intrinsic quasar luminosity) and nitrogen/carbon ratio. The behaviour of the NV/CIV, NV/HeII diagram indicates that the effect is due to nitrogen abundance variations and not to carbon depletion. This may be related to the suggestion of a relative overabundance of nitrogen in high redshift QSOs (Hamann & Ferland 1993).

These objects are telling us the story of the formation of massive galaxies and their quasar nuclei during the epoch when AGN had their maximum space density. The UV emission lines can give us some clues to the chemical composition of the extended nebulosity but to make inferences with more confidence, we need to measure the optical forbidden line spectrum in the infrared with ISAAC at the VLT.

Acknowledgments. We thank Laura Pentericci for making available to us the reductions of the NICMOS images. We are grateful to Bob Goodrich for frequent help with the polarimetric observations and many discussions. Our Keck programme is supported by NATO Collaborative Research Grant number 971115. This paper is based partially on observations made with the NASA/ESA Hubble Space Telescope, obtained at the Space Telescope Science Institute, which is operated by the Association of Universities for Research in Astronomy, Inc., under NASA contract NAS 5-26555.

References

Cimatti, A., di Serego Alighieri, S., Vernet, J., Cohen, M. H. & Fosbury, R. A. E. 1998, ApJ, 499, L21

Hamann, F. & Ferland, G. 1993, ApJ, 418, 11

Knopp, G. P. & Chambers, K. C. 1997, ApJS, 109, 367

van Ojik, R., Röttgering, H. J. A., Miley, G. K. & Hunstead, R. W. 1997, A&A, 317, 358

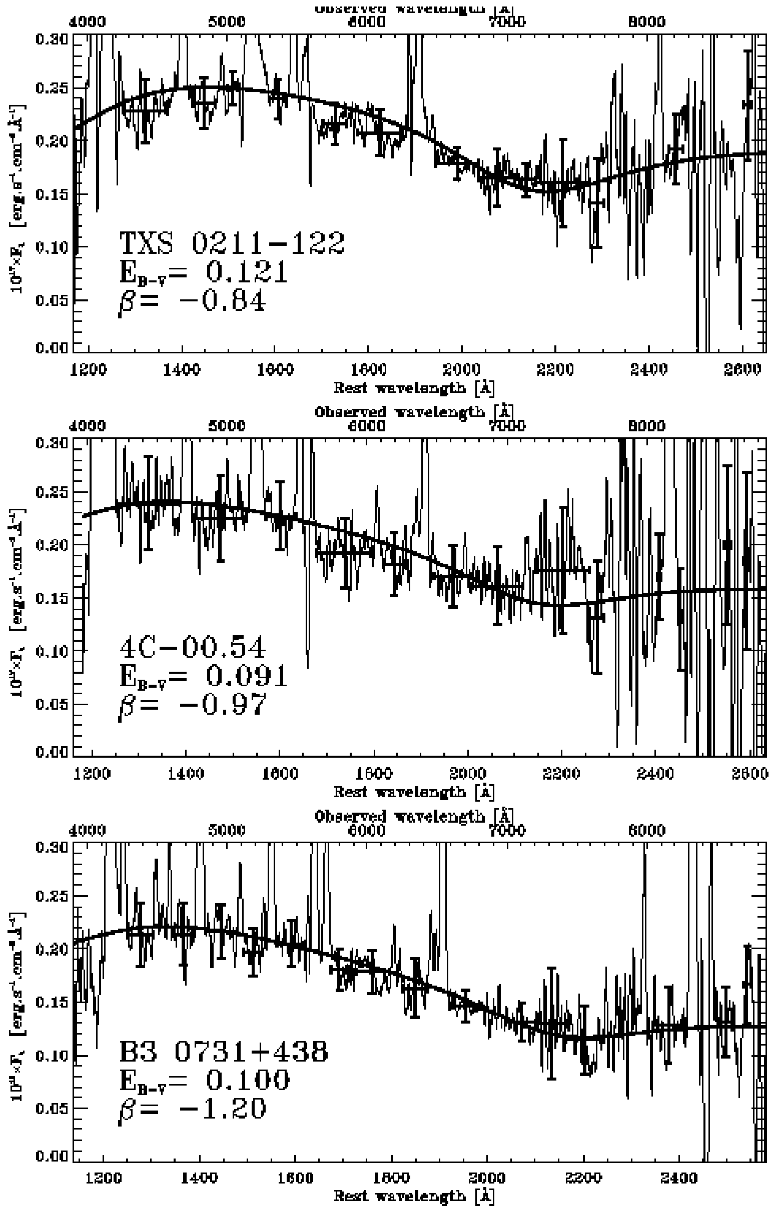

Figure 3. Total flux spectra of three of the radio galaxies scaled to show the continuum. The crosses mark continuum bins chosen to be free of emission lines and atmospheric absorption features with the vertical bars representing one sigma statistical errors. The fitted curves are two parameter fits of a power law (with index β in F_λ) absorbed by a Galactic extinction curve in the rest-frame of the RG. The derived values from $1/\sigma^2$ weighted fits are shown in the labels.

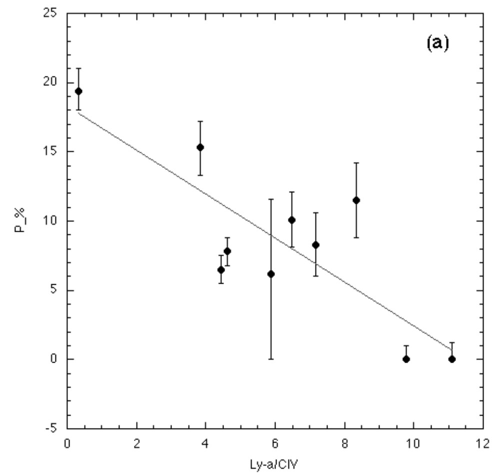

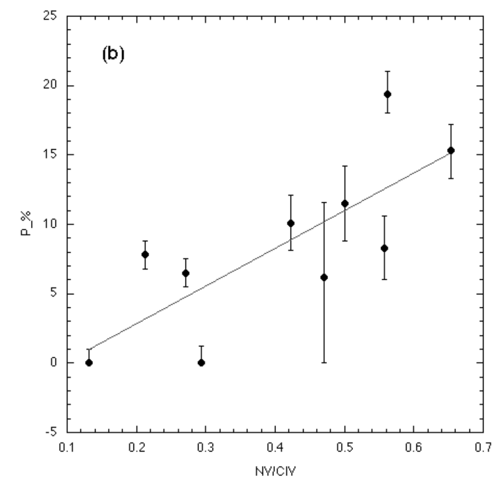

Figure 4. Plots of the fractional continuum polarization against (a) the Ly-α/CIV emission line ratio and, (b) the NV/CIV ratio. The sources in the plots are: 4C 23.56 (components a and b, $z = 2.482$), 4C -00.54 ($z = 2.366$), TXS 0211-122 ($z = 2.338$), B3 0731+438 ($z = 2.429$), USS 0828+193 ($z = 2.572$) and MRC 0943-242 ($z = 2.93$) from our own observations and 4C 41.17 ($z = 3.798$), MRC 2025-218 ($z = 2.63$) and 3C 256 ($z = 1.824$) from the literature.

NICMOS and the VLT
Pula, Sardinia, May 26-27th 1998
Wolfram Freudling and Richard Hook, eds.

Investigating the Evolution of Quasar Host Galaxies with NICMOS

Marek J. Kukula[1]

Space Telescope Science Institute, 3700 San Martin Drive, Baltimore, MD 21218, USA

James S. Dunlop and David H. Hughes

Institute for Astronomy, University of Edinburgh, Royal Observatory, Edinburgh EH9 3HJ, UK

Lance Miller

Nuclear and Astrophysics Laboratory, University of Oxford, Keble Road, Oxford OX1 3RH, UK

Christopher P. O'Dea and Stefi A. Baum

Space Telescope Science Institute, 3700 San Martin Drive, Baltimore, MD 21218, USA

Abstract.
We present the preliminary results of our Cycle 7 program to study the evolution of the host galaxies of radio-loud and radio-quiet quasars out to a redshift of 2. By careful choice of filters, and careful quasar sample selection we have ensured that (1) we sample the same spectral region at all redshifts (2) our images consist purely of starlight, uncontaminated by emission lines, and (3) our results are not biased by quasar luminosity correlating with redshift. With this data we can investigate the cosmological evolution of the luminosity, scale-length, and degree of disturbance in quasar hosts and thus obtain insights into several key questions about quasar activity including the mechanism behind the dramatic evolution in the quasar luminosity function. An initial, very crude analysis of our NICMOS images shows that we are detecting the hosts out to a redshift of ~ 2. The estimated galaxy luminosities are consistent with the values obtained for low-*z* quasars of the same luminosity.

1. Introduction

In recent years the study of quasar host galaxies has become increasingly important and it is now recognized that an understanding of their properties and evolution has the potential to resolve some long-standing mysteries concerning nuclear activity in galaxies. Conversely, quasar surveys provide an easy method of locating galaxies at large

[1] on leave from the Institute for Astronomy, University of Edinburgh

redshifts, so knowledge of the properties of quasar hosts offers a means of investigating the history and evolution of galaxies themselves.

The problems inherent in observing quasar host galaxies from the ground are too well-known to require detailed explanation but considering the enormous difficulties involved in separating faint, diffuse galaxy light from the point spread function (PSF) of a bright quasar, it is perhaps surprising that so much progress has been made to date using ground-based techniques. Although such studies are effectively limited to $z \leq 0.3$, at these low redshifts a combination of ground-based and HST programs is beginning to piece together a clear picture of the properties of quasar hosts in the local universe.

However, the local universe is not the most representative region in which to study the quasar population: arguably the epoch of greatest importance to quasar research occurred at a redshift of ~ 2, when quasars were 100 times more numerous than they are today. Although simulations show that it is impossible to derive the properties of quasar hosts at such high z from the ground with any degree of confidence, numerous attempts have been made with - not surprisingly - confusing results.

In this paper we describe the preliminary results of a project designed to exploit the unique capabilities of the HST+WFPC2+NICMOS combination. Coupled with rigorous sample selection our HST data should enable us to study how the luminosities, sizes and morphologies of the hosts of both RLQs and RQQs have evolved from the 'golden era' of quasar activity at $z \sim 2$ to the present day.

2. Previous work

The advent of NICMOS offers the first realistic hope of determining the properties of quasar hosts at high redshifts, and so a brief summary of the current state of our knowledge of host galaxies at low and high z is perhaps worthwhile at this point. Since the subject of this paper is our own NICMOS program we will focus on work which we ourselves have carried out, and of which our NICMOS study is the natural extension. However this is not to diminish the impact of the many other ground-based and HST studies which have been carried out in recent years.

2.1. The host galaxies of low-z quasars

At low z, attention has been focused on determining the luminosities, scalelengths, morphologies and interaction histories of the host galaxies, and investigating the extent to which these properties are correlated to the optical and radio luminosity of the quasar (Véron-Cetty & Woltjer 1990; Dunlop et al. 1993; McLeod & Rieke 1994a,b; Bahcall, Kirhakos & Schneider 1995; Hutchings & Morris 1995; Disney et al. 1995; Bahcall et al. 1996). For example, it has long been known that low-luminosity AGN display marked preferences in terms of host type, with (radio-quiet) Seyferts favoring spiral hosts whilst (radio-loud) Radio Galaxies are found exclusively in massive ellipticals, but the evidence for or against such a distinction for the hosts of radio-loud and radio-quiet *quasars* has until recently been unclear.

In our own ground-based K-band study of RLQ and RQQ hosts at $z \simeq 0.2$ we found that almost half of the RQQs, as well as all of the RLQs, lie in spheroidal galaxies rather than exponential discs (Dunlop et al. 1993, Taylor et al. 1996). We also found that all of the host galaxies are large, with half-light radii ≥ 10 kpc, luminous, with $L \geq L^{\star}$ at

K, and display a $\mu_{1/2} - r_{1/2}$ (surface brightness - half-light radius) relation identical in both slope and normalization to that displayed by the brightest cluster galaxies.

Through a follow-up program of off-nuclear spectroscopy (Kukula et al. 1997; Hughes et al. 1998) we have also shown that the SEDs of these host galaxies can be described by a two-component spectrum, consisting of a well-behaved, old stellar population and a strong blue component which can be interpreted as an ongoing starburst, scattered quasar light from the nucleus or some combination of both. But the result most relevant to our HST program is that, longwards of the 4000Å break, our spectroscopy demonstrates that the host galaxy spectrum is almost entirely dominated by light from the passive, underlying stellar population - *i.e.* directly related to the galaxy itself rather than to processes which might be linked to the active nucleus.

2.2. *R*-band imaging of low-*z* quasar hosts with WFPC2

It was this fact which persuaded us to choose *R*-band (F675W) for a WFPC2 host galaxy imaging proposal in Cycle 6. With matched RLQ and RQQ samples covering the redshift range $0.1 \leq z \leq 0.25$ the F675W filter samples the starlight from the host galaxies longward of the 4000Å break, whilst simultaneously avoiding strong emission lines such as [O III] and Hα (impossible to achieve with a wider filter). As a result, compared to previous HST studies of quasar hosts, our WFPC2 observations are uniquely sensitive to the *stellar continuum* of the host and exclude many contaminating sources of emission which may have caused confusion in the past.

At the time of writing our low-*z* WFPC2 observing program is half complete. The data obtained so far are of extremely high quality, and we have been able to follow the host galaxy light to within $\sim 1''$ of the quasar, and thus to place tight constraints on the luminosity of the galaxy. When the observations are complete we will be able to rigorously examine the relationship between quasar optical luminosity/radio-loudness and the properties of the host at redshifts of $\simeq 0.2$.

However, in the context of our Cycle 7 NICMOS study these Cycle 6 WFPC2 observations will allow us to determine the *rest-frame R*-band luminosities, scalelengths and morphologies of the *starlight* in low-redshift quasar hosts. We can therefore use them to establish a crucial ‘here-and-now’ baseline against which to judge the results of our near-infrared observations at higher redshifts.

2.3. High-redshift quasars.

Given that the host galaxies of low-redshift quasars have properties consistent with the products of successive galaxy mergers, and given the dramatic cosmological evolution seen in the quasar population (see below) one of the key aims of new quasar research must be to investigate the cosmological evolution of their hosts. In particular we would like to determine how the luminosities, scalelengths, and the degree of morphological disturbance seen in quasar host galaxies varies with cosmological epoch between the peak of quasar activity at $z \simeq 2$ and the present day, and whether the hosts of radio-loud and radio-quiet quasars differ in their luminosity/morphological evolution.

However, the difficulties involved in such studies are far more formidable than at low z and this is reflected in the current state of confusion surrounding the interpretation of recent ground-based attempts to observe quasar hosts at $z \simeq 2$.

Several groups have attempted such observations and have succeeded in detecting extensions around high-redshift quasars (Hintzen, Romanishin & Valdes 1991; Heckman et al. 1991; Lehnert et al. 1992; Aretxaga, Boyle & Terlevich 1995). These studies suggest that the host galaxies of quasars at $z \simeq 2$ are ~ 2.5 to 3 magnitudes brighter than those of low-redshift quasars, a result which is at least consistent with common scenarios for elliptical galaxy evolution. However, the usefulness of any such direct comparison is hampered by the fact that these high-redshift quasars are typically 5 magnitudes more luminous than the low-redshift objects studied to date. In addition, the situation is somewhat confused since other workers have failed to detect extended emission around high-redshift RQQs (Lowenthal et al. 1995). Hutchings (1995) also concludes that the hosts of RQQs are considerably fainter than those of RLQs at high redshift, a result which may simply indicate that much of the light detected around high-redshift RLQs may not be due to stars, but rather to processes associated with the extreme radio activity (as is found for high-z radio galaxies (Tadhunter et al. 1992), and for low-z RLQs (Stockton & MacKenty 1987). This emphasizes the importance of avoiding emission lines and sampling the spectrum longwards of the 4000Å break.

3. Motivation: host galaxies and quasar evolution

One of the main motivating factors in the study of quasar hosts at high redshifts is the hope that a knowledge of these galaxies might help to us to understand the physical origin of quasar evolution.

The strong cosmological evolution in comoving space density of quasars of a given luminosity has been known quantitatively for 30 years. However, although much work has gone into empirical fits of the evolution (Schmidt & Green 1983; Boyle, Shanks & Peterson 1988; Hewett, Foltz & Chaffee 1993; Goldschmidt et al. 1998) its causes remain a mystery. Hierarchical growth models such as CDM may be able to explain the rapid rise in QSO numbers with time at early epochs ($z > 4$) as a consequence of the rate of galaxy mergers, but as yet they cannot account for the decline by a factor 100 in quasar numbers from $z = 2$ to the present day without invoking some rather *ad hoc* assumptions (Carlberg 1990; Haenhelt & Rees 1993).

Clearly more observational evidence is required. Host galaxy studies are currently one of the most promising avenues of inquiry since they hold out the hope of linking quasars into the latest models of galaxy formation and evolution. At low redshifts there does appear to be a link between quasar luminosity and galaxy mass, at least for AGN in the luminosity range $-20 > M_H > -26$, in the sense that there appears to be a lower limit to the host luminosity which increases with quasar luminosity (MacLeod & Rieke 1994a,b; 1995). With HST/NICMOS it will be possible for the first time to study quasar hosts at the key epoch of quasar activity: $z = 2$, the period at which the rate at which quasars were being created was overtaken by the rate at which quasars fade or disappear.

There is one crucial question to be answered: is the decline in quasar numbers caused by a form of luminosity evolution (LE) of long-lived quasars, or does it in fact reflect a more complicated balance between birth and death of short-lived quasars which is a function of quasar luminosity (luminosity-dependent density evolution, LDDE)?

Host galaxies offer a means of distinguishing between these two hypotheses. In the LE model, individual quasars decrease in luminosity with time. If we create test samples covering a narrow range of quasar luminosity over the range of redshifts from $z = 2$ to the present epoch, we should see quasars of a fixed luminosity occupying a progressively wider range in mass of host galaxy.

In the LDDE model with short-lived quasars, quasar evolution has implicitly little to do with the physics of the active nucleus, and is linked to cosmological evolution of massive structures. We expect that there should be no redshift-dependence of quasar host luminosity (other than passive evolution) for quasars of a given luminosity. This result would tell us that quasar evolution is indeed directly linked to galaxy formation and the subsequent merger and interaction probabilities. It would tell us that the epoch $z = 2$ was a key epoch for *galaxies*, not just active galaxies, and we can use N-body simulations of galaxy formation and hierarchical merging to test whether different galaxy-formation models can explain the observed quasar evolution.

By comparing the hosts of RLQs and RQQs and the way in which they evolve with time we will also gain insights into the way in which environment and history influence the 'radio loudness' of quasars.

4. This project: studying host galaxy evolution with WFPC2 and NICMOS

The potential rewards of a program to determine the properties of quasar hosts from redshifts of $z \simeq 0.2$ out to the peak in the quasar number density at $z \simeq 2$ are clearly quite far reaching and provided the impetus for our Cycle 7 study. However, the lesson of previous ground-based attempts has clearly shown that the only way to succeed in such an endeavor is to adopt a thorough and carefully thought-out approach.

Our Cycle 7 program therefore relies heavily on our previous experience with ground-based and Cycle 6 HST studies of low-z quasar hosts, and uses many of the same strategies in order to avoid potential problems. Fundamental to this approach is the selection of appropriate quasar samples and the use of carefully chosen filter-redshift combinations to maximize the chances of detecting starlight from the host galaxies.

4.1. Sample Design

We therefore now list and explain the selection criteria which we have used to define the samples of RQQs and RLQs for our Cycle 7 study of host-galaxy evolution. We stress that such sample control is *essential* if the aim is to obtain clean, meaningful results and advance our understanding of the cosmological evolution of the hosts of RQQs and RLQs.

- From simulated images of quasars and their hosts it is clear that it is essential, particularly at high-redshift, to confine our study to quasars of moderate-low optical luminosity if we are to derive reliable luminosities and scalelengths for their host galaxies (see Taylor et al. 1996). Accordingly we have confined our selection of high-redshift quasars to absolute magnitudes $-24 > M_V > -25$.

- Having defined the luminosity bin at high redshift, it is vital to break the flux-density–redshift correlation which inevitably arises in flux limited samples, and to make sure we sample a comparable range of luminosities at all intermediate redshifts. In our Cycle 6 study of quasar hosts at $z \sim 0.2$ (using the F675W filter in WFPC2) there are 5 RQQs and 5 RLQs with $-24 > M_V > -25$. These 10 objects form the low$z$ baseline against which we will test the results of our high-z observations. Thus we will be able to compare the host galaxies of quasars of the same *intrinsic optical luminosity* from $z \sim 0.2$ to ~ 2.

- To ensure that we detect *starlight* from the host galaxies at all redshifts it is necessary to make sure that, as in our Cycle 6 WFPC2 study at $z \simeq 0.2$, the spectrum of the host galaxy is always observed at $\lambda_{rest} > 4000$Å and yet is uncontaminated by either [OIII] or Hα line emission. This cannot be done with the somewhat more sensitive 'Wide' filters such as F110W and F160W on NICMOS, but can be achieved over a wide range of redshifts by using the F814W filter (for WFPC2), and the F110M and F165M filters in NICMOS Camera 1, provided the quasar redshifts are restricted to lie within the following redshift bins: $0.32 < z < 0.43$, $0.83 < z < 1.00$, $1.36 < z < 1.69$ and $1.67 < z < 2.09$.

- In order to perform a clean comparison of the hosts of RLQs and RQQs at each epoch it is necessary to ensure that the RLQs are genuinely radio-loud ($P_{5GHz} > 10^{25}\mathrm{WHz}^{-1}\mathrm{sr}^{-1}$), that the RQQs are genuinely radio quiet ($P_{5GHz} < 10^{24.5}\mathrm{WHz}^{-1}\mathrm{sr}^{-1}$), and that within each redshift bin their optical luminosity distributions are well-matched. This is not a trivial task. It requires that we select only RQQs which have been observed and have not been detected with sufficient sensitivity at the VLA, and requires that we confine our RLQ sample to steep-spectrum objects whose intrinsic radio luminosity cannot be artificially boosted by relativistic beaming.

The simultaneous application of these 4 constraints is sufficiently stringent that the resulting quasar sample, illustrated in Figure 1, is virtually unique (primarily because there are relatively few optically-faint steep-spectrum RLQs, and because relatively few RQQs have been observed with sufficient sensitivity in the radio). Also shown in Figure 1 is the low-redshift ($z \sim 0.2$) sample from our Cycle 6 WFPC2 program. It can be seen that this low-z sample spans almost 3 magnitudes in optical luminosity in a narrow redshift range whereas the samples selected for the Cycle 7 study are confined to only 1 magnitude in luminosity but span the bulk of the history of the Universe. This figure thus emphasizes how these two complementary samples will allow us to unambiguously separate the effects of cosmological epoch from any relation between host galaxy properties and quasar luminosity.

4.2. PSF determination

Accurate knowledge of the form of the PSF is essential in order to decouple the quasar contribution from that of its host. Synthetic PSFs, though often an excellent match to the inner regions of the profile, sometimes fail to reproduce the shape of the PSF at larger radii and this can be disastrous for the detection of host galaxy light.

We therefore devoted two entire orbits of our Cycle 7 allocation to obtaining empirical PSFs using our chosen filter/camera combinations (F110M and F165M with NICMOS Camera 1). Two different stars were used, to safeguard against the possibility that one of them might possess Vega-like dust shells which would compromise the PSF, and by using a sequence of exposures in MULTIACCUM mode we were able to obtain deep, unsaturated images of very high dynamic range.

5. Preliminary NICMOS results

The acquisition of NICMOS data for our Cycle 7 program was completed in February 1998, and the remaining WFPC2 F814W observations of objects in our $z \sim 0.4$ subsample are currently scheduled for the first half of 1999.

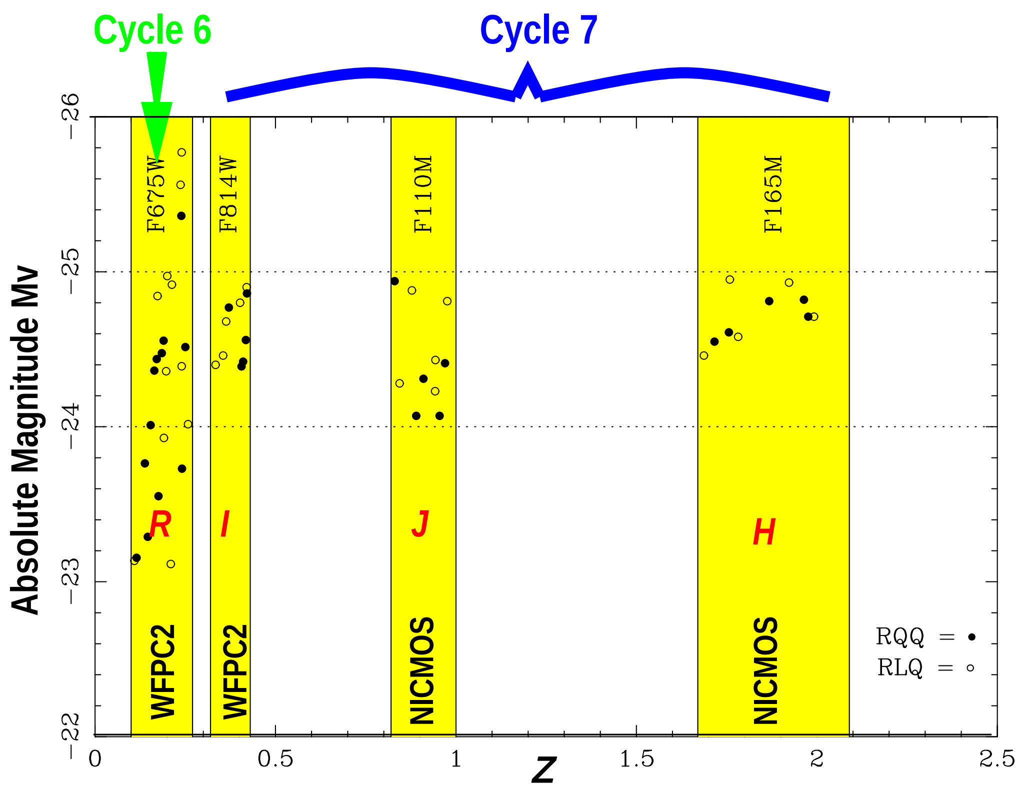

Figure 1. Redshift regimes in the current sample of RQQs (filled circles) and RLQs (open circles), with the appropriate NICMOS/WFPC2 filters indicated. Also shown are the quasars from our Cycle 6 WFPC2 F675W imaging study, to emphasize that these objects will provide the low-*z* baseline against which to measure any cosmological evolution in the current sample. Each redshift-filter combination samples the same region of the galaxy's restframe spectrum (roughly restframe *R*-band) and avoids both Hα and [OIII]λ5007 emission.

Pedestal removal and recalibration using the most recent reference files have resulted in significant improvements in image quality, although several problems, such as CR persistence, remain to be dealt with. Full 2-D modeling of the images would be premature at this stage. However, we have been able to carry out a preliminary analysis of the data, the results of which we describe here.

We have limited ourselves to an aperture 20 pixels (0.86 arcsec) across, centered on the quasar. By comparing the total flux within this region with that of an appropriately scaled empirical PSF we have been able to estimate the contributions of the quasar and its host to the light within a radius of ~ 4 kpc of the quasar. This method is extremely crude and inevitably leads to an underestimation of the total galaxy luminosity. However, the initial results are extremely encouraging:

- The measured J and H magnitudes of the quasars in our $z \sim 1$ (F110M) and $z \sim 2$ (F165M) samples are close to the predicted values.
- In almost every case we detect a significant excess flux with respect to the empirical PSF, which we attribute to the host galaxy. This component typically accounts for $\sim 25\%$ of the light in our 0.87-arcsec aperture. This implies quasar:host ratios and galaxy luminosities which are consistent with the values obtained for low-z objects, although the uncertainties are currently too large to allow the testing of specific models of galaxy evolution.

We are therefore confident that, as the remaining issues of image processing are resolved, our NICMOS images will begin to provide the first clean measurements of host galaxy sizes and luminosities for quasars spanning a large fraction of the history of the Universe.

References

Aretxaga, Boyle & Terlevich, 1995, MNRAS, 275, L27
Bahcall, Kirhakos & Schneider, 1995, ApJ, 450, 486
Bahcall et al., 1996, ApJ, 457, 557
Boyle, Shanks & Peterson 1988 MNRAS, 235, 935
Carlberg, 1990, ApJ, 350, 505
Disney et al., 1995, Nat, 376, 150
Dunlop, Taylor, Hughes & Robson, 1993, MNRAS, 264, 455
Goldschmidt, Kukula, Miller & Dunlop, 1998, ApJ, in press
Haenhelt & Rees, 1993, MNRAS, 263, 168
Heckman et al., 1991, ApJ, 370, 78
Hewett, Foltz & Chaffee, 1993, ApJ, 340, L5
Hintzen, Romanishin & Valdes, 1991, ApJ, 366, 7
Hughes, Kukula, Dunlop & Boroson, 1998, in preparation
Hutchings, 1995, AJ, 110, 994
Hutchings & Morris, 1995, AJ, 109, 1541
Kukula, Dunlop, Hughes, Taylor & Boroson, 1997, in ‘Quasar Hosts’, Clements & Pérez-Fournon eds, p177
Lehnert et al., 1992, ApJ, 393, 68
Lowenthal et al., 1995, ApJ, 439, 588
McLeod & Rieke, 1994a, ApJ, 420, 58
McLeod & Rieke, 1994b, ApJ, 431, 137
McLeod & Rieke, 1995, ApJ, 441, 96
Schmidt & Green, 1983, ApJ, 269, 352
Stockton & MacKenty, 1987, ApJ, 316, 584
Tadhunter et al., 1992, MNRAS, 256, 53P
Taylor, Dunlop, Hughes & Robson, 1996, MNRAS, 283, 930
Véron-Cetty & Woltjer, 1990, A&A, 236, 69

NICMOS and the VLT
Pula, Sardinia, May 26-27th 1998
Wolfram Freudling and Richard Hook, eds.

NICMOS Imaging of QSO Host Galaxies at $0.1 < z < 4.4$

L. J. Storrie-Lombardi and R. J. Weymann

Carnegie Observatories, Pasadena, CA 91101, email: lisa@ociw.edu

K. K. McLeod

Wellesley College, Wellesley, MA 02181

G. H. Rieke, J. Hill, and V. Kulkarni

Steward Observatory, Tucson, AZ 85719

Abstract.

We present preliminary results from two programs to image the host galaxies of radio-quiet quasars in 1.6 micron light using NICMOS camera 2 on HST. The high redshift program consists of QSOs covering the redshift range $0.8 < z < 4.4$ and a range of QSO luminosities. Of the six objects for which data have been obtained the results range from no host galaxy detected, to an obvious galaxy with an interacting companion, to a possible high redshift galaxy cluster. The low redshift program covers QSOs with $0.1 < z < 0.4$. A host galaxy is detected in all 12 objects for which data have been obtained.

NICMOS and the VLT
Pula, Sardinia, May 26-27th 1998
Wolfram Freudling and Richard Hook, eds.

Limits on the Star Formation Rates of $z > 2$ Damped Lyα Systems from Hα Spectroscopy

Andrew J. Bunker[1]

Department of Astrophysics, University of Oxford, OX1 3RH, UK

Stephen J. Warren

Imperial College, Department of Physics, Blackett Laboratory, Prince Consort Road, London SW7 2BZ, UK

D. L. Clements

Institut d'Astrophysique Spatiale, Bâtiment 121, Université Paris XI, F-91405 Orsay CEDEX, France

Gerard M. Williger

NASA Goddard Space Flight Center, Code 681, Greenbelt, Maryland 20771, USA

Paul C. Hewett

Institute of Astronomy, Madingley Road, Cambridge CB3 0HA, UK

Abstract. We present the results of a long-slit K-band spectroscopic search with CGS4 on UKIRT for Hα emission from the objects responsible for high-redshift ($z > 2$) damped Lyα absorption systems. The objective was to measure the star-formation rates in these systems. However, no Hα emission was detected above our 3σ limits of $f \lesssim 10^{-19}\,\mathrm{W\,m^{-2}}$, corresponding to star formation rates $\lesssim 10\,h^{-2}\,\mathrm{M_{\odot}\,yr^{-1}}$ ($q_0 = 0.5$). These upper limits are more meaningful than those from searches for Lyα emission because the Hα line is unaffected by resonant scattering. For $q_0 = 0.5$ our limits are in conflict with the star formation rates predicted under the assumption that the high-z DLAs are the fully-formed galactic-disk counterparts of today's massive spiral galaxies. Deeper spectroscopy is needed to test this picture for $q_0 = 0.0$. A programme of NICMOS imaging observations currently underway, combined with VLT spectroscopy, will provide a detailed picture of the link between DLAs and young galaxies.

---

[1] *Present address:* NICMOS Postdoctoral Researcher, Department of Astronomy, University of California at Berkeley, 601 Campbell Hall, Berkeley CA 94720, USA
email: `bunker@bigz.Berkeley.EDU`

1. Introduction

The history of star formation in the Universe is a topic of enormous current interest (*e.g.*, Madau *et al.* 1996). The damped Lyα absorption systems (DLAs, Wolfe *et al.* 1986) contain most of the neutral gas in the Universe, and from their redshift distribution, and the measured column densities, the evolution in the co-moving density of neutral gas Ω_g can be measured (*e.g.*, Lanzetta *et al.* 1991). Then the analysis of the variation of Ω_g with redshift allows the measurement of the history of star formation in the Universe (Pei & Fall 1995) provided the consequences of dust obscuration are accounted for.

This approach to the history of star formation unfortunately tells us nothing about how galaxies are assembled. One school of thought has DLAs being the (large) progenitors of massive spiral disks (*e.g.*, Lanzetta *et al.* 1991; Prochaska & Wolfe 1997). However, Møller & Warren (1998) have recently shown that the impact parameters of the few detected galaxy counterparts of high-redshift DLAs are small (in the context of this debate) and that the space density of the DLAs at high-redshift is probably much higher than the space density of spiral galaxies today.

2. Searches for Star Formation in Damped Systems

Here we present the results of a spectroscopic survey for H$\alpha\,\lambda\,656.3$ nm emission from 8 damped absorption systems at $2.0 < z < 2.6$, along the line-of-sight to 6 high-redshift quasars. At these redshifts Hα appears in the near-infrared K-window. The results are relevant to the debate on the nature of the DLAs, for if the DLAs are the counterparts of today's spiral galaxies the associated Hα emission should be detectable. The rate of depletion of the cosmic density of neutral gas can be used to compute a universal star formation rate. The average star formation rate in each DLA depends then on their space density, so that high measured rates of star formation would provide support for the view that the DLAs are massive galaxies already in place at high-z. A low measured star formation rate on the other hand would be in agreement with the hierarchical picture.

There have been extensive searches for Ly$\alpha\,\lambda\,121.6$ nm emission from DLAs but with limited success (*e.g.*, Smith *et al.* 1989; Hunstead, Pettini & Fletcher 1990; Lowenthal *et al.* 1995). This is generally thought to be due to the fact that resonant scattering greatly extends the path length of Lyα photons escaping through a cloud of neutral hydrogen so that even very small quantities of dust can extinguish the line (Charlot & Fall 1991). Because the effective extinction can be extremely large this has the consequence that non-detections do not provide any useful information on the star formation rates in the DLAs. The Hα line, although intrinsically weaker by a factor ~ 10, lies at a longer wavelength where the extinction is smaller, and is not resonantly scattered. In consequence a search for Hα emission from DLAs may be more efficient than a search for Lyα.

3. Our Near-IR Spectroscopic Survey

With the CGS4 spectrograph on the 3.8-m UK Infrared Telescope (UKIRT) we have undertaken a search for line emission from 8 high-redshift DLAs ($2.0 < z < 2.6$) near the expected wavelength of Hα. The observations and data reduction are detailed in Bunker

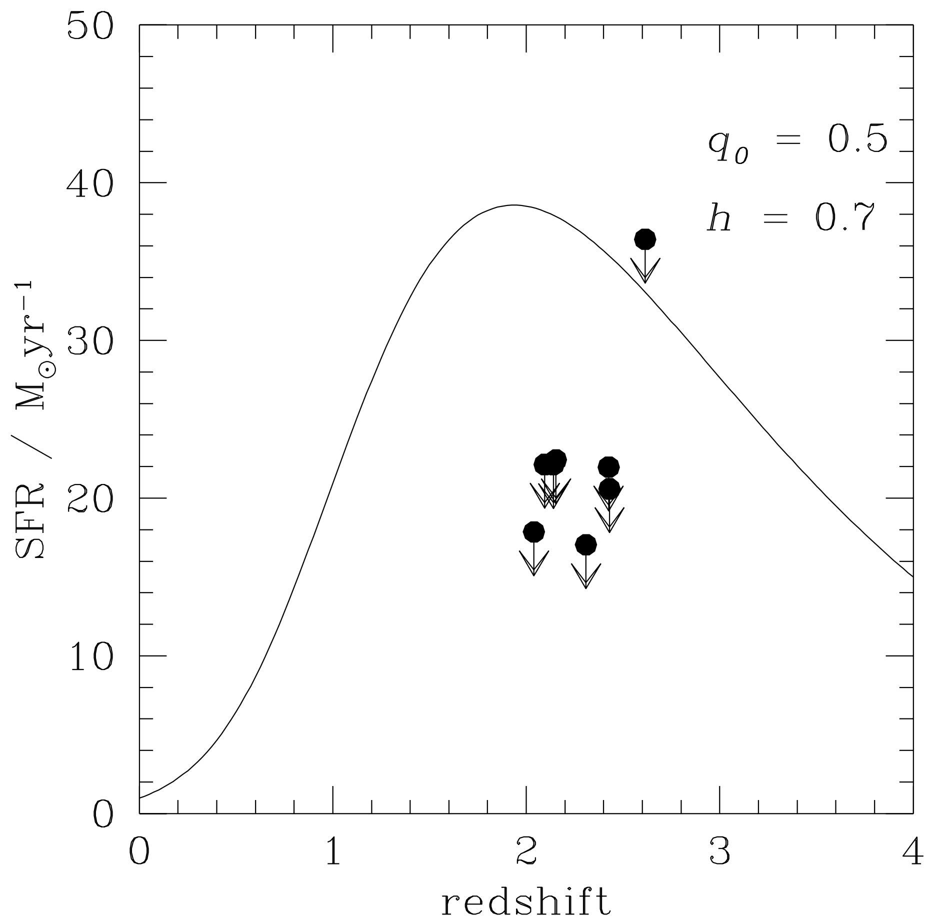

Figure 1. The measured 3σ upper limits to the SFRs in $M_\odot\,yr^{-1}$ for the sample of 8 DLAs for $q_\circ = 0.5$. The curves are the predicted survey-averaged SFRs from the closed-box models of Pei & Fall (1995), under the assumption that the DLAs are the progenitors of present-day spiral galaxy disks. The predictions of the hierarchical picture will lie below these curves in proportion to the ratio of the space density of galaxy sub-units at any redshift to the space density of spiral galaxies today.

(1996). No lines were detected at $> 3\sigma$ significance above the quasar continuum. Our long-slit K-band spectra were typically 1-hour each and used the 2.5-arcsec wide slit ($10\,h^{-1}$ kpc at $z \approx 2.3$, $q_0 = 0.5$ & $h = H_0\,/\,100\mathrm{km\,s^{-1}\,Mpc^{-1}}$ throughout). With a 3-arcsec extraction width, the 3σ upper-limits lie in the range $(1.0-1.6)\times 10^{-19}\ \mathrm{W\,m^{-2}}$ for spectrally-unresolved line emission. The resolution of CGS4 in this configuration is $650\,\mathrm{km\,s^{-1}}$ FWHM.

We use the upper limits on Hα line luminosities to constrain the star formation rates in these systems, based on the prescription of Kennicutt (1983), where a star formation rate (SFR) of $1\,M_\odot\,yr^{-1}$ generates a line luminosity in Hα of 11.2×10^{33} W. The limits to the SFRs lie in the range $(8.4 - 18)\,h^{-2}\,\mathrm{M_{\odot}\,yr^{-1}}$, although the conversion between Hα line luminosity and SFR is somewhat uncertain and depends on the assumed IMF.

4. Testing the Large Disk Hypothesis

We compare the measured upper limits to the star formation rates in our sample against predictions based on the assumption that DLAs are the progenitors of today's spiral galaxies. We begin with the analysis by Pei & Fall (1995) of the observed rate of decline of the cosmic density of neutral gas $\Omega_g(\mathrm{obs})$ measured from surveys for DLAs. At any redshift $\Omega_g(\mathrm{obs})$ will be an underestimate of the true cosmic density $\Omega_g(\mathrm{true})$ because quasars lying behind DLAs will suffer extinction, and may therefore drop out of the samples of bright quasars used to find the DLAs. Pei & Fall correct for this bias, accounting in a self-consistent manner for the increasing obscuration as the gas is consumed and polluted as star formation progresses. In this way they determine the evolution of $\Omega_g(\mathrm{true})$, and so the SFR per unit volume.

Although the analysis of Pei & Fall provides the SFR per unit volume at any redshift, it gives no information on the SFR in individual galaxies. For the hypothesis of large disks of constant co-moving space density, assuming that the SFR in a DLA is proportional to the present-day galaxy luminosity $L(0)$, we can predict the SFRs in the population of DLAs at any redshift. Figure 1 plots the results of this calculation, showing the predicted survey-averaged star formation rate for a sample of DLAs for $q_{\circ} = 0.5$. Seven of the eight DLAs lie below the curve in this plot. The significance of this result is reduced by the fact that the solid angle over which we have searched for Hα emission is smaller than the expected solid angle of the large disks. Despite this we would still have expected to detect 2 or 3 systems with average SFRs twice as large as our upper limits. These results then provide support for the hierarchical picture. For $q_{\circ} = 0.0$ deeper limits are required to distinguish between the two pictures. A more detailed treatment of this survey and its implications is given in Bunker *et al.* (1998).

5. Future Work

A decisive test can be made with the latest generation of near-IR instrumentation. Deep *H*-band imaging with HST/NICMOS (Warren *et al.*, GO-7824) will reveal whether the galaxies responsible for damped absorption are indeed in sub-L^* pieces, and the opportunities afforded by the largest ground-based telescopes such as the VLT should enable the accurate measurement of star formation rates in these systems. Combined with spectroscopy of metal lines, in this way we will build up a picture of the history of assembly, gas depletion, and chemical evolution in the population of damped absorbers.

Acknowledgments. We would like to thank the Organizing Committee of the "NICMOS & the VLT" Sardinia meeting. We are grateful for the excellent support we received while observing at UKIRT. We thank Mike Fall, Palle Møller & Hy Spinrad for useful discussions, and Max Pettini & Richard McMahon for details of some of the damped systems included in our survey. AJB was supported by a PPARC studentship while at Oxford, and a NICMOS-IDT postdoctoral position at U.C. Berkeley.

References

Bunker A. J. 1996, D. Phil. Thesis, University of Oxford, "Searches for Distant Galaxies", WWW address `http://astro.berkeley.edu/~ bunker/thesis.html`

Bunker A. J., Warren S. J., Clements D. L., Williger G. M., Hewett P. C. 1998, MNRAS, *submitted*

Charlot S., Fall S. M. 1991, ApJ, 378, 471

Hunstead R. W., Pettini M., Fletcher A. B. 1990, ApJ, 365, 23

Kennicutt R. C. 1983, ApJ, 272, 54

Lanzetta K. M., Wolfe A. M., Turnshek, D. A., Lu L., McMahon R. G., Hazard C. 1991, ApJS, 77, 1

Lowenthal J. D., Hogan C. J., Green R. F., Woodgate B. E., Caulet A., Brown L., Bechtold J. 1995, ApJ, 451, 484

Madau P., Ferguson H. C., Dickinson M. E., Giavalisco M., Steidel C. C., Fruchter A. 1996, MNRAS, 283, 1388

Møller P., Warren S. J. 1998, MNRAS, *in press* (astro-ph/9804205)

Pei Y. C., Fall S. M. 1995, ApJ, 454, 69

Prochaska J. X., Wolfe A. M. 1997, ApJ, 487, 73

Smith H. E., Cohen R. D., Burns J. E., Moore D. J., Uchida B. A. 1989, ApJ, 347, 87

Wolfe A. M., Turnshek D. A., Smith H. E., Cohen R. D. 1986, ApJS, 61, 249

Part 4. Future Technology

NICMOS and the VLT
Pula, Sardinia, May 26-27th 1998
Wolfram Freudling and Richard Hook, eds.

Design and Status of the NICMOS Cryocooler

John W. MacKenty

Space Telescope Science Institute, Baltimore MD 21210 USA
Email: mackenty@stsci.edu

Edward S. Cheng

NASA Goddard Space Flight Center, Greenbelt MD 20771 USA
Email: ec@cobi.gsfc.nasa.gov

Abstract.
NASA is developing the NICMOS Cooling System (NCS) to provide operation of NICMOS beyond the exhaustion of its stored solid nitrogen cryogen. It is planned that the NCS will be installed into HST in early 2000 during the Third HST Servicing Mission (SM3). This development was motivated by the development of a thermal short within the NICMOS dewar which has reduced the cryogen lifetime from a planned 4.5+ years to slightly less than 2 years. While the acceleration of the the NICMOS observing program and the selection of a second round of General Observer proposals will permit NICMOS to obtain up to 70 percent of its originally anticipated observations, the extension of the NICMOS operational period will both enable additional science programs and provide HST with a near infrared capability potentially until the end of the HST mission.

The NCS combines an external radiator identical in design to the ACS/STIS Aft Shroud Cooling System (ASCS) planned for SM3, a Creare, Inc. reverse-Brayton cycle turbine cooler, and an EVA installed neon loop to the NICMOS dewar's cooling coil. This system has been assembled and is undergoing system level testing in May 1998. A validation flight on the HOST pallet onboard STS-95 in October 1998 is planned. We discuss the design of the NCS and the expected post-SM3 performance of NICMOS with the NCS.

1. Motivations

1.1. Extending the NICMOS Lifetime

The Near Infrared Camera and Multi-Object Spectrometer (NICMOS) was installed on board the Hubble Space Telescope (HST) by NASA during the Second HST Servicing Mission to provide a near infrared capability. Scientifically useful operation of NICMOS requires that its HgCdTe focal plane detector arrays (FPAs) be maintained at temperatures below approximately 80K. By design, the NICMOS FPAs are operated between 58 and 62 Kelvins with cooling provided by an expendable supply of solid nitrogen. The dewar containing the FPAs and solid nitrogen supply was designed for an on-orbit of lifetime of 4.5 to 5 years with the exhaustion of the nitrogen cryogen being the limiting factor. Unfortunately, internal stresses in the dewar caused physical motions shortly following the deployment of NICMOS into HST. These motions resulted in direct contact developing between baffles on the innermost cold solid nitrogen dewar and its surrounding cooled shell. The planned long lifetime of the nitrogen supply was to be achieved by a series of well isolated cold shells placed in hard vacuum around the inner nitrogen container. The innermost shell was cooled by the vented nitrogen gas and provided the cooling for the filters and spectral dispersing elements. This vapor cooled shell is known as the VCS. (The outer two shells are cooled using thermal electric coolers.)

The result of this physical contact between the inner dewar and the VCS was a thermal short which approximately doubles the heat flux into the solid nitrogen cryogen. The anticipated on-orbit lifetime of NICMOS was thereby reduced to approximately 22 months. Considering the initial commissioning period, this will reduce the period of NICMOS science observations to about one third of the original goal.

With the advice of outside committees, NASA and STScI have accomplished a partial recovery of the NICMOS science opportunity by accelerating the NICMOS observing program at the expense of observations with other science instruments on HST. By assigning NICMOS 40-50 percent of the total HST time available until mid-November 1998, STScI will be able to complete all GTO, and GO Cycle 7 and 7-NICMOS TAC approved programs. This, with the inclusion of the additional Cycle 7-NICMOS Call for Proposals, will result in the acquisition of 60-70 percent of originally anticipated NICMOS science return.

1.2. Other Considerations

Beyond the recovery of the NICMOS capability, the addition of the NICMOS cooling system and its associated aft-shroud cooling system provides two other benefits.

First, the HST aft-shroud thermal situation will limit simultaneous Science Instrument operations starting in the 2001 timeframe. This is the result of increasing power demands of the new generations of instruments (*e.g.* STIS and ACS) and the normal aging of the outer surfaces of the spacecraft. A second radiator of the same design adopted for NICMOS and a shared control electronics subsystem provides a means of directly cooling ACS, STIS, and potentially COS together with the ASCS itself.

Second, the NCS permits a flight demonstration of long life cryocooler system which is desirable for future space missions. For example, the Creare cryocooler system within NCS is the leading technology candidate to provide the Next Generation Space Telescope (NGST) with sufficient cooling to support a mid-infrared (thermal) IR instrument.

2. Expected NICMOS Performance after HST Servicing Mission 3

In general, the NCS is expected to restore NICMOS approximately its condition prior to the exhaustion of the nitrogen cryogen. The temperature at the FPA detectors will be 72-75 Kelvins (compared to 61 Kelvins in June 1998). This will increase the dark current from 0.05 e-/s to 0.5 or 1.0 e-/s. Even for fairly long exposures, the readout noise of approximately 30 electrons will dominate the dark current. Only very long narrow band exposures at wavelengths shorter than 1.8 microns have a significant potential loss in performance. As a minor benefit, the quantum efficiency of the detectors at short wavelength will increase by perhaps one third. The filters, which are viewed by the entire wavelength response of the detectors, are expected to be cooled below 160 Kelvins (which is actually closer to their original design temperature than their present 100 Kelvins). Therefore, background from filters is expected to remain undetectable.

Image quality is expected to be equivalent to that obtained during late 1997 and 1998 (with Camera 3 remaining several mm out of focus). Although considerable uncertainties regarding the behavior and state of the dewar structure remain, it appears very unlikely that Camera 3 will be recovered into the internal focus adjustment range of the NICMOS pupil alignment mechanism (PAM). Therefore additional "NIC3 campaigns" in which the telescope focus is shifted may still be required to obtain the very best possible image quality in NICMOS Camera 3.

During NCS operation, the temperature stability of the detectors will be an important parameter. The goal is stability of 0.05K during one orbit and 0.2K long term. Temperature variations will create bias shifts (similar to the pedestal effect) and may require similar calibration efforts. Although the NCS requires consider power to operate (equivalent to approximately 1.5 science instruments), present indications are that full time operation will be possible until at least 2003 (at Servicing Mission 4) and potentially beyond although NICMOS+NCS campaigns may be required.

3. NICMOS Cooling System Design

The NCS Requires 5 distinct elements: (1) a flexible neon loop connection between the NICMOS dewar cooling coil and the NCS heat exchanger, (2) the Creare Cryocooler, (3) the Power Conversion Electronics, (4) the Electronics Support Module, and (5) two externally mounted radiators. Figure 1 shows the main elements as they will be installed inside HST.

3.1. Flex Lines

The actual cooling of the interior of the NICMOS dewar is accomplished by circulating 65 to 70 Kelvins neon gas through the cooling coil at the aft end of the dewar. This coil was originally used to solidify the nitrogen cryogen within the dewar by passing cold Helium gas through it during ground assembly of NICMOS. This coil is accessible via two bayonet fittings on the side of NICMOS to which the "flex Lines" will be attached by an astronaut during SM3. The requirement on the cooling system is to provide 400 milliwatts of cooling power into the dewar.

3.2. Creare Cryocooler

The Creare, Inc. mechanical cryocooler system uses a reverse-Brayton cycle turbine design which provides several major advantages for this application. First, this closed loop system operates with extremely high speed –7 kHz– turbines so the potential for mechanical coupling to the HST is very small. Since HST has very demanding pointing requirements (7 milliarcseconds with actual performance frequently better than 3 milliarcseconds), avoiding disturbances is crucial. Second, this system can provide the degree of cooling required. Since the parasitic losses within the astronaut installed flex lines and the bayonet couplings are rather large, delivering 400 mW into the NICMOS dewar is expected to require 7 to 8 Watts from the cooler. Third, the Creare design is sufficiently compact in physical size to fit within presently unused space between the aft end of the NICMOS instrument's enclosure and the aft bulkhead of the HST.

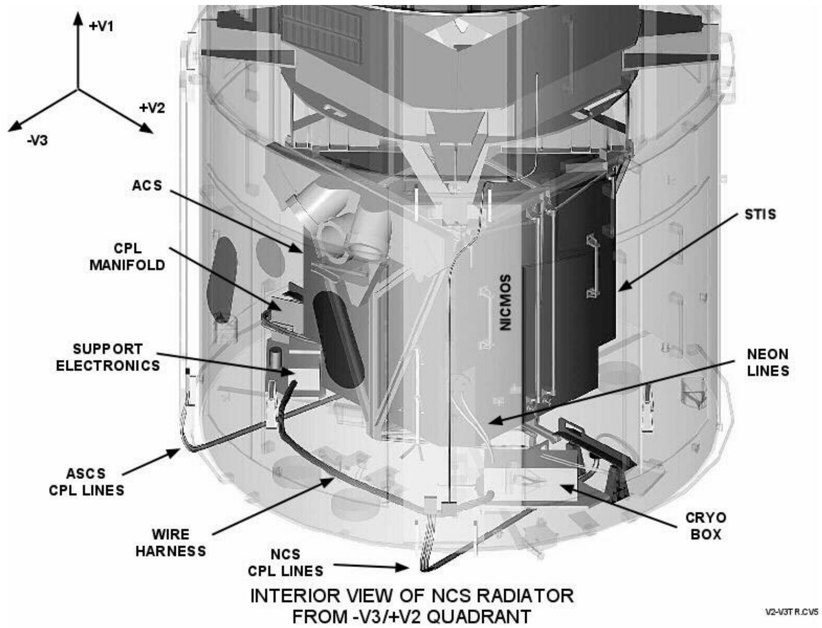

Figure 1. Cutaway view of the NICMOS Cryocooler and ASCS showing the various modules and their interconnections.

The Creare cryocooler is connected to the flex lines cooling loop by means of a heat exchanger operating at 62 Kelvins. It is contained in the NICMOS CryoCooler (NCC) enclosure together with gas storage bottles to purge, pressurize, and –if necessary– re-pressurize the external neon loop. A cutaway view of the NCC is shown in Figure 2 and the assembled unit (minus its external thermal blankets is shown in Figure 3. Note the MLI blanket encased flex lines extending from the box on the left side.

3.3. Power Conversion Electronics

The Power Conversion Electronics (PCE) is required to produce the AC power required by the Creare cryocooler and is located within the same enclosure as the Creare cooler (the NCC box). The cooler will require up to 400W during the initial cooldown phase.

3.4. Electronics Support Module

The Electronics Support Module (ESM) contains a microprocessor to control both the NCS and the Aft-Shroud Cooling System (ASCS). This system is commanded via an HST remote interface unit (RIU), the same path used by each science instrument. Even in the absence of the NCS, the ESM would be required to control the ASCS cooling support for ACS and STIS.

3.5. Aft-Shroud Cooling System

The Aft-Shroud Cooling System (ASCS) consists of two externally mounted radiators as illustrated in Figure 4. One is dedicated to NICMOS+NCS while the other supports all other SIs and the ESM. Heat is transferred to these radiators by Capillary Pumped Loop (CPL) lines to be installed by the astronauts. Heat flow along CPL lines is reg-

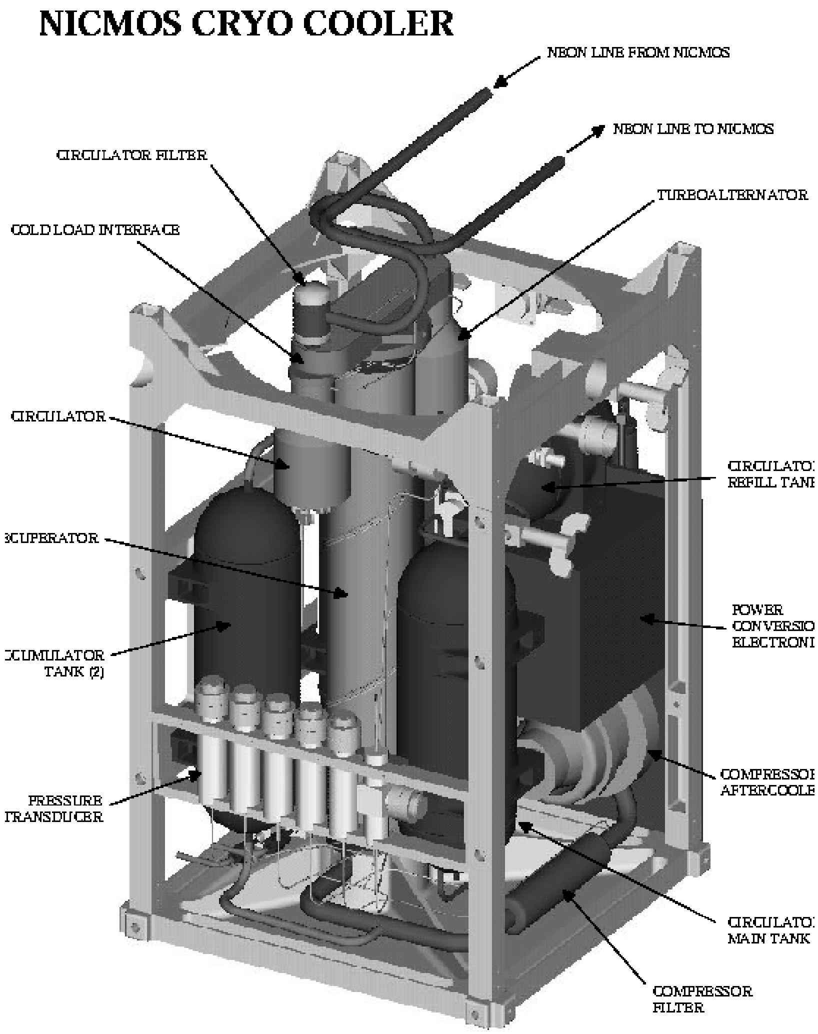

Figure 2. NICMOS CryoCooler Enclosure

ulated by the ESM by means of heaters attached to each end of a CPL line. The CPL lines are connected to the ACS and STIS instruments at interface plates. A view of the NICMOS radiator under construction is shown in Figure 5

4. Testing and Reviews Prior to Flight on Servicing Mission 3

The NCS poses several challenges for the HST Servicing process. First, the entire system is not available for testing since NICMOS is presently installed in HST. Second, the time available for the development of the NCS is very short (ar the start of the NCS development effort in mid-1997 SM3 was scheduled for November 1999 – it is now scheduled for May 2000 due to events external to the HST project). And third, the Creare cryocooler system has not yet been tested under zero gravity conditions.

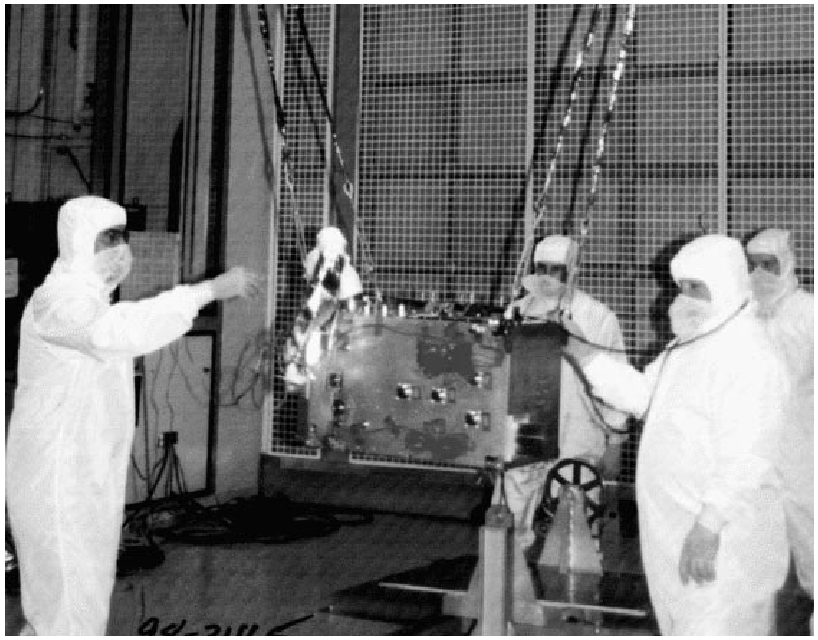

Figure 3. Assembled NICMOS Cryocooler

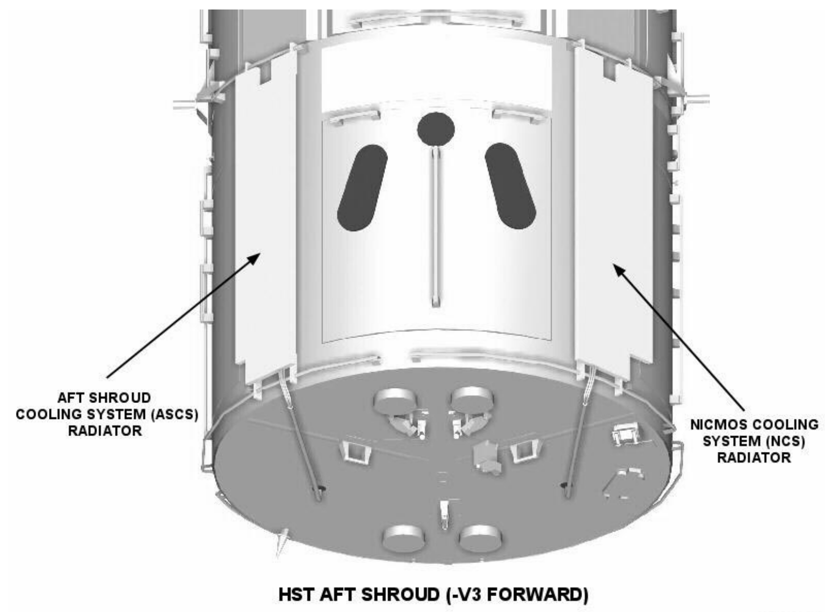

Figure 4. Schematic view of the ASCS Radiators installed on HST

To address these factors, the NCS development process includes plans to test the flight-NCS in space during STS-95 as part of the Hubble Orbital System Test (HOST) payload. This space shuttle flight is currently scheduled for October 1998. A thermal simulator of the NICMOS dewar with a high fidelity replica of the cooling coil and

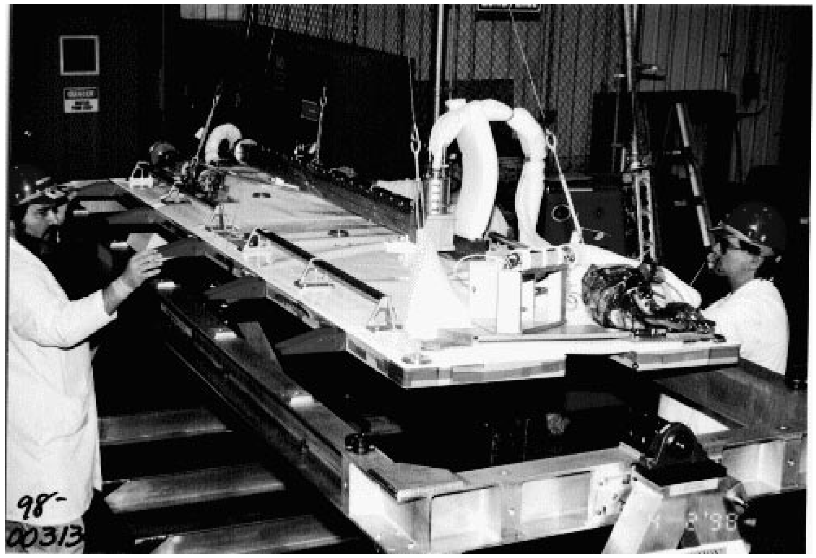

Figure 5. ASCS NICMOS Radiator under construction at GSFC

its interface plate has been constructed to support this testing both on the ground and during the HOST flight.

Previous testing of the Creare cryocooler has demonstrated operation for more than 1.5 years with the most critical turbine component having over 13 years of life testing. During the first half of 1998, the NCS flight components have been integrated and are presently undergoing testing in thermal vacuum chambers at Goddard Space Flight Center (Figure 6). The development of the NCS and the ongoing evaluation of the technical and scientific performance of NICMOS has been, and will continue to be, reviewed by an Independent Science Review board. The final decision to proceed with installation of the NCS into HST will depend upon the outcome of the ground and HOST mission testing and the findings of this review board.

Figure 6. The placement of the NCS and the NICMOS thermal simulator into a thermal vacuum chamber at GSFC in early May 1998 is shown. The large diameter tubes connecting the two boxes are the flex lines.

NICMOS and the VLT
Pula, Sardinia, May 26-27th 1998
Wolfram Freudling and Richard Hook, eds.

2048 x 2048 HgCdTe Arrays for Astronomy at Visible and Infrared Wavelengths

Donald N.B. Hall

Institute for Astronomy, University of Hawaii

Abstract. In collaboration with the European Southern Observatory and the Subaru project, the University of Hawaii Institute for Astronomy has entered into a partnership with Rockwell International Science Center to develop 2048 x 2048 format HAWAII-2 HgCdTe arrays for low background ground based astronomical applications. Present plans call for production of 2048 x 2048 multiplexers late in 1998 and hybrid arrays utilizing 2.5 μm PACE HgCdTe in 1999.

However Rockwell has recently achieved a breakthrough in HgCdTe material quality through use of new detector growth technologies which utilize p/n double layer planar heterostructure arrays grown by MBE on lattice matched CdZnTe substrates. Initial tests of this material have demonstrated near theoretical dark current as a function of temperature and cutoff wavelength.

UH IfA and Rockwell plan to evaluate arrays utilizing this new material for use in the Next Generation Space Telescope. The primary goal would be to directly compare the performance of $\lambda c = 5$ μm cut off wavelength 2048 x 2048 HgCdTe arrays with that of 1024 x 1024 InSb arrays. However HgCdTe offers the advantage that λc can be tailored to any value from 1.2 to 17 μm; a second goal of the investigation would be to fabricate, test and demonstrate 2048 x 2048 HgCdTe arrays with λc values of 1.8 and 2.5 μm Although the investigation would focus primarily on 1 - 5 μm detectors, the same multiplexers could also be hybridized to Si PIN diode arrays, providing sensitivity down through the visible into the ultraviolet.

These large format arrays offer potential advantages for both space and ground based applications.

1. Introduction

Over the last two decades, dramatic improvements in the performance of 1 - 5 μm infrared detector materials combined with the leap from single detectors to million pixel arrays have led to a billion-fold improvement in our ability to observe astronomical sources at these wavelengths. These advances, along with those in lightweight mirror and adaptive optics technologies, have already revolutionized ground based infrared astronomy and now pave the way for the science program of NGST.

InSb has long been the detector material of choice for ground based astronomical observations spanning the 1 - 5 μm region and also has space heritage as the detector material chosen for ISO and SIRTF. However HgCdTe is now an attractive alternate technology which offers very significant advantages as a detector in the 1 - 5 μm region. 2048 x 2048 format arrays - over four million pixels (Mpxl) - are now under development and the first are scheduled for delivery in the last quarter of 1998. New molecular beam epitaxial (MBE) HgCdTe material offers potentially superior detector performance to InSb along with the additional flexibility to tailor the band-gap to set the long wavelength cutoff (λc) to any value from 1.2 to 17 μm. This is particularly valuable under low background conditions as the theoretical dark current is reduced by more than an order of magnitude for each 10% reduction in λc; diode capacitance and hence read noise is also reduced with λc.

Over the last decade the University of Hawaii (UH) Institute for Astronomy (IfA) and Rockwell International Science Center (Rockwell) have collaborated in a series of programs to develop large format HgCdTe arrays optimized for low background astronomical applications. UH now has three years of experience operating 1024 x 1024 format, 2.5 μm HAWAII arrays at telescopes on Mauna Kea. Rockwell has already delivered 30 pairs of engineering and science grade HAWAII arrays to other customers and is in the process of filling orders for a similar number. Read noises of 12 e^-, reduced to 3 e^- with multiple reads, and dark currents below 1 e^- per minute have been demonstrated for these HAWAII arrays.

Rockwell has recently achieved a breakthrough in HgCdTe material quality through use of new detector growth technologies which involve p/n double layer planar heterostructure arrays grown by MBE on lattice matched CdZnTe substrates. Initial tests of 256 x 256 arrays of this material have demonstrated near theoretical dark current as a function of temperature and cutoff wavelength (Figure 2). The new material is lattice matched to the CdZnTe substrate, eliminating the lattice defects of earlier PACE material which are thought to be responsible for both its reduced quantum efficiency at short wavelengths and also image persistence effects. In contrast to the low index sapphire substrate used in PACE material, the refractive index of CdZnTe is well matched to the HgCdTe detector material; the exposed surface of the CdZnTe substrate can thus readily be anti reflection coated and Rockwell is now routinely achieving quantum efficiencies in excess of 80% with this technology.

In November 1997, IfA entered into a contract with Rockwell for the development of a 2048 x 2048 format, 18 μm pitch, low noise HAWAII-2 multiplexer (mux) based on the proven HAWAII technology; the European Southern Observatory and the Subaru Telescope have also joined this effort. The first run of this 4 Mpxl mux will take place late summer in the same Rockwell production foundry where high yields of the HAWAII muxes have been consistently achieved. This contract specifies early 1999 delivery of two science grade arrays to UH; they will consist of the 4 Mpxl muxes hybridized to traditional 2.5 μm PACE HgCdTe. Rockwell intends to subsequently offer arrays utilizing this mux to the broad astronomical community. The 37 mm physical dimensions of the 4 Mpxl HgCdTe arrays are only fractionally (one third) larger than the corresponding 27mm of the 1024 x 1024 ALADDIN InSb arrays and the 18 μm pixel size reduces the rate of ionizing events per pixel by better than a factor of two.

The same muxes can also be readily hybridized to both to Si diode arrays and to MBE HgCdTe material with cutoff wavelengths as long as17 μm, thus providing the option of wavelength coverage from the ultraviolet through much of the MIR. For many applications this offers the flexibility of extended wavelength coverage with the operational simplicity of using the same multiplexers at the same operating temperature..

The planed NGST investigation would consist of the following tasks:

1. Fabricate 2048 x 2048 muxes for this program by augmenting the silicon foundry runs already planned under the HAWAII-2 subcontract.
2. Produce $\lambda c = 1.8$, 2.5 and 5 μm HgCdTe wafers utilizing p/n double layer planar heterostructure MBE material on CdZnTe substrates.
3. Initially hybridize 256 x 256 HgCdTe sub arrays with these three cutoff wavelengths to high quality sections of engineering grade 2048 x 2048 muxes. Later in the program full 2048 x 2048 hybrid devices would be produced.
4. Test and demonstrate the performance of these arrays as they relate to NGST requirements down to a temperature of 30 K. The performance of the $\lambda c = 5$ μm devices will be specifically characterized relative to available 1024 x 1024 InSb devices. Initial measurements at Rockwell will be followed up with detailed evaluation in the laboratory and at the telescope in Hawaii.
5. Evaluate the visible wavelength sensitivity of thinned HgCdTe at temperatures of 30 - 50 K relative to available data on thinned InSb and demonstrate the performance of 2048 x 2048 HAWAII-2 muxes hybridized to Si PIN diode sub-arrays.
6. Evaluate, and subject to availability of funding, demonstrate incorporation of these arrays into mosaic focal planes.
7. Assess the resources needed to deliver significant numbers of these arrays.

2. Multiplexer

The HAWAII-2 mux represents only a modest jump from the 1024 x 1024 HAWAII mux developed under a similar contract in late 1993 and early 1994. The HAWAII devices have been characterized in great detail and continue to provide unparalleled results in astronomical applications worldwide.

Although the 2048 x 2048 device will be, by a factor of four, the largest device yet fabricated in deep submicron CMOS technology, Rockwell extrapolates high yields based on previous experience with their world-class foundry. The yield of the HAWAII muxes has increased 400% over the last two years and, on the basis of ongoing improvements driven by worldwide competition, we anticipate a defect free yield approaching 30% for the larger muxes.

Operation at the 30K temperature of the NGST focal plane represents a significant extrapolation of the 60 - 77K temperatures at which HAWAII muxes have been operated. The lower operating temperature was not anticipated to be a problem and we have confirmed that two critical parameters, gain and read noise, for an engineering grade HAWAII array show no significant change between 78 and 30 K. The results, shown

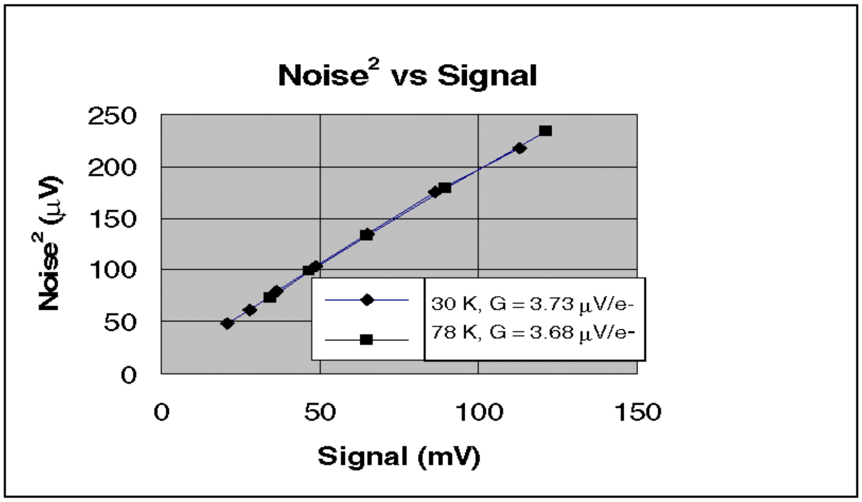

Figure 1. Noise squared vs. signal shows no discernable change between 78 and 30 K.

in Figure 1, demonstrate a change of less than 1.5% in mux gain and no measurable change in read noise (23 vs. 22.7 electrons). The performance of both muxes and hybrid arrays at temperatures down to 30k will be fully evaluated during the proposed investigation as described in Section 5..

3. 1 - 5 μm HgCdTe Detector Material

Rockwell will utilize molecular beam epitaxy (MBE), the highest performance HgCdTe detector growth technology available, to fabricate the 2048 x 2048 arrays. Based on this proven, flexible and highly reproducible technology, we expect that the focal plane arrays produced will provide excellent performance and operability. The key attributes of MBE HgCdTe detectors are:

- low dark current consistent with theoretical diffusion-limited operation
- high uniformity of key characteristics, particularly breakdown voltage and 1/f noise
- sharp, well-defined spectral characteristics
- elimination of image persistence and poor short wave quantum efficiency seen in earlier PACE material through lattice matching of the HgCdTe to the CdZnTe substrate
- the opportunity to anti reflection coat the surface of the CdZnTe substrate to achieve high quantum efficiency

Rockwell's MBE technology has been shown to produce the best HgCdTe FPA's in the industry spanning cutoff wavelengths from 1.85 to 17.3 μm.

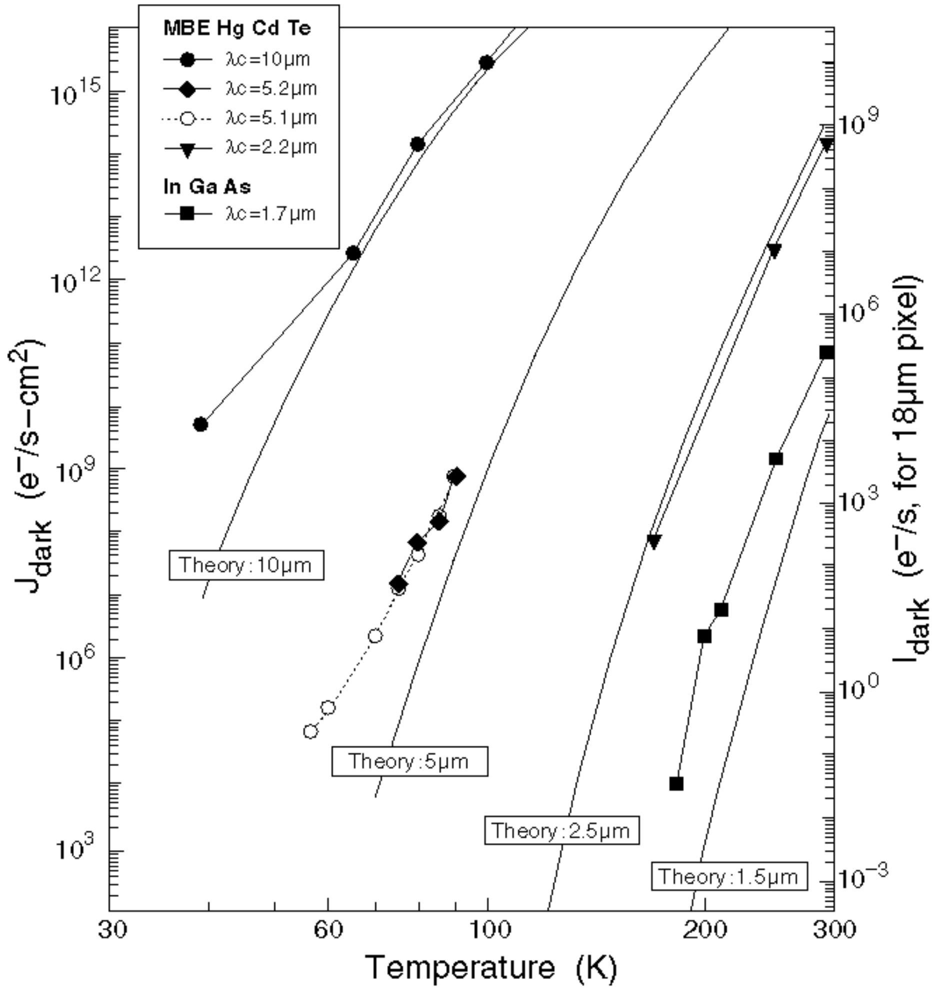

Figure 2. The measured temperature dependence of dark current of MBE HgCdTe with λc's near 2.2, 5 and 10 μm tracks theoretical predictions far better than traditional PACE material.

Tailoring λc to shorter wavelengths also improves read noise as the junction capacitance decreases with λc. Figure 3 shows the modeled junction capacitance plus input capacitance vs. λc for an HgCdTe/CdZnTe MBE double layer planar heterostructure (DLPH) diode. The figure shows that the junction + input capacitance is reduced from 37 to 32 fF as λc is reduced from 5 to 2.5 μm and that there is no change in read noise from 78 to 30K.

4. Hybridization of 2048 x 2048 Arrays

The hybrid mating of the 2048 x 2048 NGST FPA will be based on techniques proven in the fabrication of the 1024 x 1024 HAWAII devices. The proposed layout of the

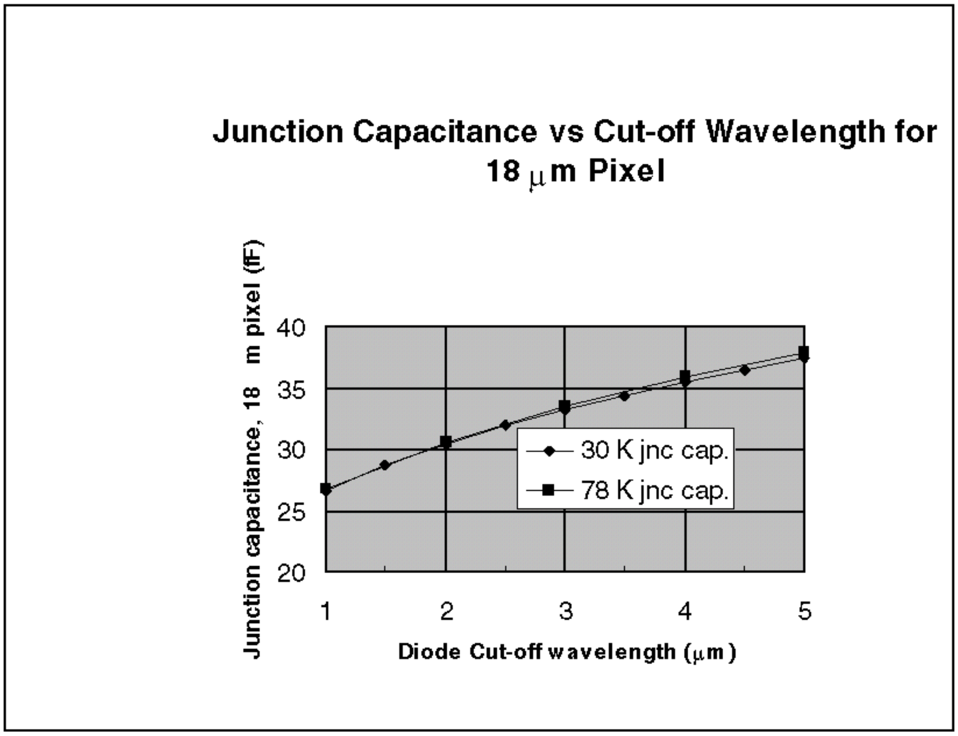

Figure 3. Modeled junction capacitance vs. cut-off wavelength λc.

2048 x 2048 hybrid is basically a 4X scale-up of the 1024 x 1024 arrays, with very similar pixel size (18 vs. 18.5 μm) and the same interconnect dimensions. The use of CdZnTe as the detector substrate should enhance hybridization as the material is easier to polish than the sapphire substrate of the PACE material used in the HAWAII FPAs and produces flatter detector die.

The main challenge in scaling up the hybrid mating method is the need to apply four times the force to the hybrid components to produce a robust indium interconnect bond. Rockwell's current mating machine is capable of mounting and aligning the larger die of the 2048 x 2048 device, but is not designed to apply the required loads. Our plan for hybridization of the HAWAII-2 arrays is to use this mating machine to align and attach the hybrid components at the load currently used for the 1024 x 1024 arrays, then transfer the hybrid to a very rigid air gimbal in a load frame. Such a compressive apparatus can be made much more rigid than a mating machine, since there is no need to accurately control the movement and orientation of the mounting surfaces. The hybrids will then be compressed to the final load, with the air gimbal ensuring that the load is evenly distributed. The air gimbal and other components for this mating method are in house at Rockwell: the first 2048 x 2048 hybrids are scheduled for fabrication under the HAWAII-2 program late in 1998. Mask sets have also been procured for the fabrication of 2048 x 2048 test structures. The 2048 x 2048 hybrid mating technology should be relatively mature and have been fully demonstrated under the HAWAII-2 program well

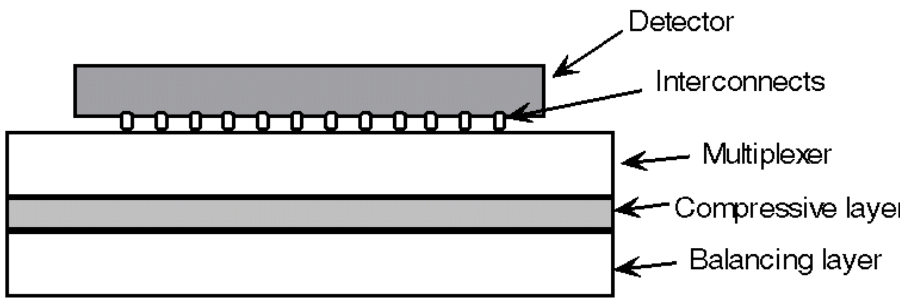

Figure 4. The BCS design compresses the mux to match the thermal contraction of the detector without bending the FPA.

before 2048 x 2048 arrays would be required for the NGST program.

The difference in thermal expansion between the detector and the silicon mux has the potential to create large thermally induced stresses on the indium interconnects and the detector material. With repeated thermal cycling this can result in failure of the interconnects or lead to damage to the detector pixels. Rockwell has developed the Balanced Composite Structure (BCS) design to produce reliable hybrids and applied it to a variety of FPA designs, including the 1024 x 1024 HAWAII FPA. This design relieves the stress at the hybrid interface by compressing the mux to match the thermal expansion of the detector material. The thickness and composition of the compressive layer is adjusted to produce the desired compression of the multiplexer. A balancing layer below the compressing layer prevents bending of the FPA (Figure 4) The BCS design has been successfully applied to a number of FPA's with CdZnTe-substrate detectors and Rockwell does not anticipate the need for any modifications in going to the 2048 x 2048 format hybrids.

5. Test and Evaluation of Performance Down to 30 K

Both Rockwell and the IfA have existing test facilities capable of characterization of focal plane arrays down to 30 K. We propose to utilize these facilities for initial screening and evaluation of muxes and arrays produced under the proposed investigation. However the verification of full device performance at read noise levels of 2 e and dark currents as low as 4 e / Ksec will require a specialized ultra-low background test facility.

We plan to carry out initial characterization of HAWAII-2 engineering grade muxes hybridized to 256 x 256 sub arrays of 5.0, 2.5 and 1.8 μm MBE HgCdTe material on lattice matched CdZnTe substrates and to Si PIN diode arrays. Later we intend to demonstrate and characterize full scale 2048 x 2048 array technology. By that time there will exist a substantial body of data on HAWAII-2 muxes hybridized to traditional PACE material.

6. Options for Extension to Visible Wavelengths

The sensitivity of the proposed 2048 x 2048 devices can be extended through visible wavelengths either by thinning the CdZnTe substrate or by hybridizing an array of Si PIN diodes to the same multiplexer.

Typical HgCdTe FPA's are not sensitive to visible wavelengths due to absorption in the CdZnTe substrate layer short of 0.8 μm. It is possible to achieve detector response comparable to InSb in the visible by removing the CdZnTe substrate with a selective etch. At least two standard etches are available that remove the CdZnTe substrate but do not affect the layer containing Hg. This process would remove the entire CdZnTe substrate leaving only the very thin active layer of HgCdTe hybridized to the multiplexer. This material would be sensitive to visible wavelengths.

Several issues would need to be addressed in this approach:

1. The hybrid gap must be back filled with an epoxy or similar material to support the thin HgCdTe layer, but the backfill material must resist the etch
2. The multiplexer, including the exposed wirebond pads, must resist the etch
3. The exposed HgCdTe surface must be passivated to avoid large leakage currents.

Rockwell has established technologies which would address all of these issues.

However, the alternate of hybridizing a back-illuminated Si PIN diode array to the 2048 x 2048 mux appears far more attractive. By utilizing this hybrid focal plane array approach, it is possible to produce a visible imager which will operate at 30K with a combination of performance and other features not attainable with either HgCdTe or InSb in the visible. In this hybrid approach, the detector will be independently optimized for visible quantum efficiency, speed and dark current outside of the standard CMOS process, but will use standard high-volume silicon processing techniques. Due to the maturity of silicon and the available material quality, the cosmetic quality of this device should be very high. The fully-depleted architecture provides low cross-talk and reduces any resistivity variations to improve uniformity of response. This hybrid approach allows for a fill factor of nearly 100%; with an anti-reflection coating of SiO2 tailored to the appropriate thickness, quantum efficiencies exceeding 80% throughout the visible should be achievable. If lower dark current than the thinned wafer approach is required, a bonded-wafer approach in which a thin (10 - 75 μm) silicon layer is transferred to the multiplexer through bump-bonding with the later removal of the thicker bonded substrate can be employed. In this approach dark currents at the levels of CCD's are attainable, while providing the advantages of operation at 30K, utilization of the same 2048 x 2048 multiplexer and non destructive readout.

7. Mosaic Focal Planes

Although the primary goal of the proposed investigation is the demonstration of 2048 x 2048 FPAs optimized for NGST core program 1 - 5 μm requirements, with potential

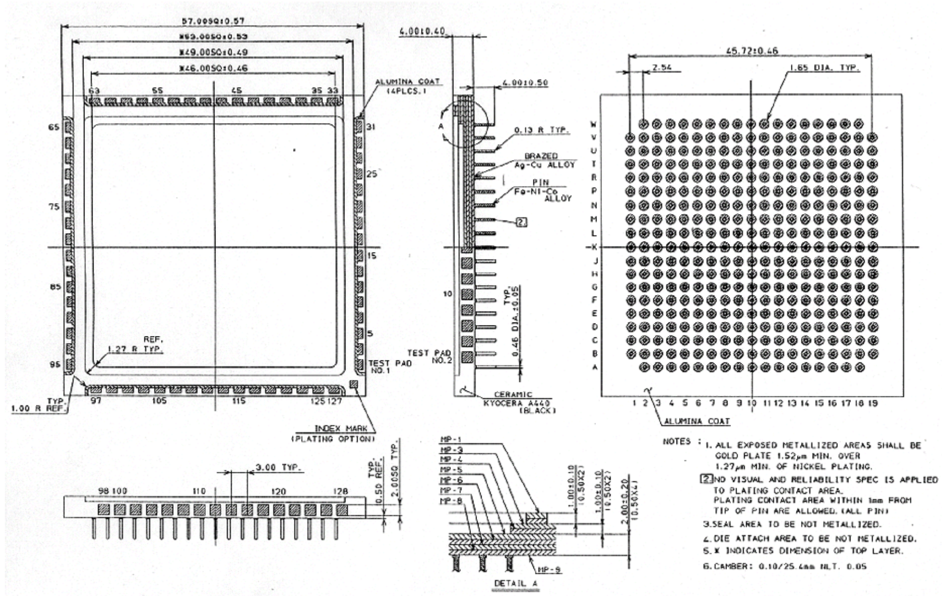

Figure 5. The proposed package for the HAWAII-2 arrays.

extension through visible wavelengths, the eventual NGST goal is an 8 k x 8 k mosaic imager. This will require the assembly of sixteen 2048 x 2048 FPAs with precision packaging designed to minimize the dead space between the arrays. Both Rockwell and UH have extensive experience with such mosaic focal plane technology.

At UH Gerald Luppino has pioneered the development of several generations of CCD mosaic focal planes for wide field visible imaging. He has extensive experience in the packaging for large CCD focal planes and has developed the first 8192 x 8192 CCD mosaiced from eight 2048 x 4096, three side buttable, devices; similar mosaics are now in routine astronomical use and have been widely duplicated. They utilize an Aluminum Nitride (AlN) ceramic which is an ideal thermal expansion match to silicon and is also a superb thermal conductor. The same techniques are readily applicable to IR array mosaics and involve technology very comparable to the proposed NGST mosaics.

Rockwell has extensive experience mounting large FPAs in the pin grid array commonly used to package large microprocessors. These packages connect to zero insertion-force (ZIF) sockets through an array of pins on the back surface, eliminating the need to clamp the package from the front or sides. This approach lends itself to closer acking of the FPAs in the mosaic.

Figure 5 shows the package designed for the HAWAII-2 2048 x 2048 FPA. This package provides a 46mm well for mounting the FPA and 128 electrical connections that are routed to probe pads on the outer edges and also to the outer two rows of pins on the backside. The central pins in the pin grid array are dedicated to thermal contacts. Rockwell proposes to utilize these packages in the fabrication of initial NGST FPA's.

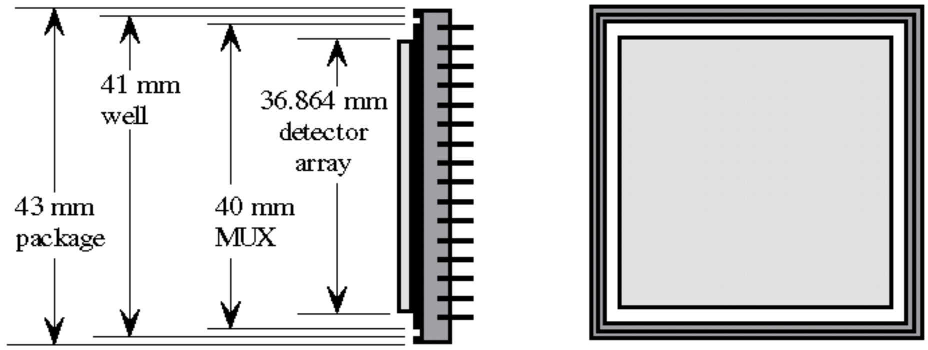

Figure 6. Conceptual design for a PGA package optimized for assembly of a mosaic array.

The budget constraints of the current program require us to utilize existing tooling available from the package vendor to minimize cost and is therefore not fully optimized for assembly of a close packed mosaic array. The outer edges of the PGA packages are 57 x 57 mm, resulting in a gap of approximately 20 mm between active areas. The package could be optimized by shrinking the well and outer edges of the package to the minimum dimensions shown in Figure 6, allowing the dead space between arrays to be reduced to 7 mm (most of this gap would be occupied by wirebond pads on both the mux and package). A single custom ZIF socket for all sixteen FPAs would allow exact positioning of the arrays and provide denser packing of the arrays by eliminating the some of the gap due to butting of the socket perimeters.

8. Production Approaches

8.1. MBE HgCdTe Capability at Rockwell Science Center

The science objectives of the NGST program require near-theoretical performance from very large arrays. This means that only a single array can be processed on each standard 4 cm substrate. This requires detectors that are not only very high performance but are also high yield so as to be produced in relatively large numbers. Rockwell is confident that these requirements can be met utilizing MBE technology.

The ability to fabricate MBE HgCdTe with a variety of λc's matched to the science requirements is a key advantage of HgCdTE over fixed band-gap materials. An important attribute of Rockwell's process is the ability to precisely control the band-gap for any run and to rapidly modify it from one run to another. This is illustrated in Figure 7 which documents the growth of a series of LWIR, MWIR and SWIR layers which were grown sequentially demanding the high composition control flexibility inherent to this technology.

Rockwell is currently using MBE processes to produce many arrays. These include all LWIR FPA's (λc up to 17.3 μm), key MWIR deliverables for operation at

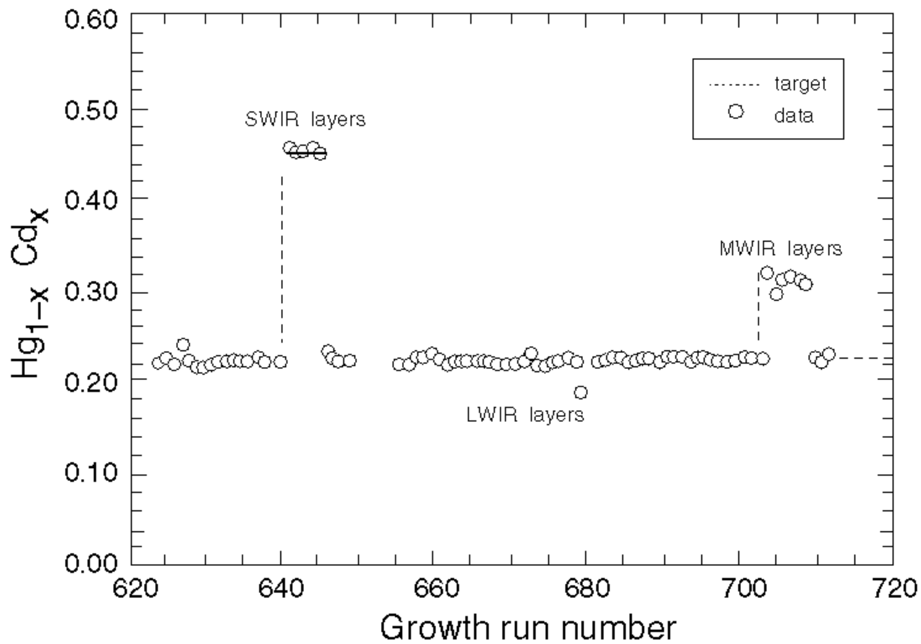

Figure 7. An important attribute of Rockwell's MBE growth technology is the ability to rapidly modify the composition of the Hg1-x Cdx Te material. The figure illustrates this capability where a series of LWIR, MWIR and SWIR layers were grown sequentially.

elevated temperatures and all NIR (1.8 to 2.3 μm) prototypes. The performance benefits of the DLPH MBE HgCdTe detector technology are illustrated by the dark current density data shown in Figure 2 for recent devices with λc from 2.2 to 16 μm. The MBE dark current is far superior to traditional PACE material and is in good agreement with the theoretical limit for conventional (unthinned) p/n HgCdTe detectors.

9. Conclusion

In the next several years we expect to develop and evaluate visible and infrared 2048 x 2048 hybrid focal plane arrays optimized for extremely low background astronomical applications. They will be specifically optimized for the Next Generation Space Telescope. However Rockwell intends to make these arrays available to the broad astronomical community. They offer major opportunities for large ground based telescopes such as the VLT, particularly in spectroscopic applications.

10. Acknowledgements

The author wishes to acknowledge the substantial contributions of K. W. Hodapp and G. Luppino at the University of Hawaii Institute for Astronomy and K.Vural, J.T. Montroy and L. J. Kozlowski at Rockwell International Science Center to the planning of this project.

Author Index